MATERIALS SCIENCE

A. Planes
L. Mañosa
A. Saxena (Eds.)

Magnetism and Structure in Functional Materials

Springer

Springer Series in
MATERIALS SCIENCE 79

Springer Series in

MATERIALS SCIENCE

Editors: R. Hull R. M. Osgood, Jr. J. Parisi H. Warlimont

The Springer Series in Materials Science covers the complete spectrum of materials physics, including fundamental principles, physical properties, materials theory and design. Recognizing the increasing importance of materials science in future device technologies, the book titles in this series reflect the state-of-the-art in understanding and controlling the structure and properties of all important classes of materials.

71 **Dissipative Phenomena in Condensed Matter**
Some Applications
By S. Dattagupta and S. Puri

72 **Predictive Simulation of Semiconductor Processing**
Status and Challenges
Editors: J. Dabrowski and E.R. Weber

73 **SiC Power Materials**
Devices and Applications
Editor: Z.C. Feng

74 **Plastic Deformation in Nanocrystalline Materials**
By M.Yu. Gutkin and I.A. Ovid'ko

75 **Wafer Bonding**
Applications and Technology
Editors: M. Alexe and U. Gösele

76 **Spirally Anisotropic Composites**
By G.E. Freger, V.N. Kestelman, and D.G. Freger

77 **Impurities Confined in Quantum Structures**
By P.O. Holtz and Q.X. Zhao

78 **Macromolecular Nanostructured Materials**
Editors: N. Ueyama and A. Harada

79 **Magnetism and Structure in Functional Materials**
Editors: A. Planes, L. Mañosa, and A. Saxena

80 **Ion Implantation and Synthesis of Materials**
By M. Nastasi and J.W. Mayer

81 **Metallopolymer Nanocomposites**
By A.D. Pomogailo and V.N. Kestelman

82 **Plastics for Corrosion Inhibition**
By V.A. Goldade, L.S. Pinchuk, A.V. Makarevich and V.N. Kestelman

83 **Spectroscopic Properties of Rare Earths in Optical Materials**
Editors: G. Liu and B. Jacquier

84 **Hartree–Fock–Slater Method for Materials Science**
The DV–X Alpha Method for Design and Characterization of Materials
Editors: H. Adachi, T. Mukoyama, and J. Kawai

85 **Lifetime Spectroscopy**
A Method of Defect Characterization in Silicon for Photovoltaic Applications
By S. Rein

86 **Wide-Gap Chalcopyrites**
Editors: S. Siebentritt and U. Rau

Volumes 20–70 are listed at the end of the book.

A. Planes L. Mañosa A. Saxena
(Eds.)

Magnetism and Structure in Functional Materials

With 129 Figures (8 in color)

Springer

Professor Antoni Planes
Professor Lluís Mañosa
Universitat de Barcelona, Facultat de Física
Departament d'Estructura i Constituents de la Matèria
Diagonal 647, 08028 Barcelona, Catalonia, Spain
E-mail: toni@ecm.ub.es, lluis@ecm.ub.es

Dr. Avadh Saxena
Los Alamos National Lab, Theoretical Division, T-11, MS B262
Los Alamos, NM 87545, USA
E-mail: avadh@lanl.gov

ISSN 0933-033X

ISBN-10 3-540-23672-4 Springer Berlin Heidelberg New York

ISBN-13 978-3-540-23672-6 Springer Berlin Heidelberg New York

Library of Congress Control Number: 2004117013

Typesetting by the Authors and SPI Publisher Services using a Springer TEX macro package
Cover concept: eStudio Calamar Steinen
Cover production: *design & production* GmbH, Heidelberg

Printed on acid-free paper SPIN: 10948583 57/3100/SPI 5 4 3 2 1 0

In Memorium

James Arthur Krumhansl

(August 2, 1919–May 6, 2004)

Preface

This book is based on the emerging notion that a thorough and fundamental understanding of the interplay of magnetism and structure is needed if a wide variety of functional materials are to be efficiently used in applications. The intent is to foster interaction between researchers in three distinct but related topics: (i) magnetoelastic materials such as magnetic martensites and magnetic shape memory alloys, (ii) magnetocaloric effects related to magnetostructural transitions, and (iii) colossal magnetoresistance (CMR) manganites and related perovskites. The goal is to identify common underlying principles in these three classes of materials that are relevant to optimize various functionalities. The interplay between structure and magnetic properties is sensitive to disorder and manifests itself at multiple length scales in a cross-correlated and hierarchical fashion.

Functional materials are becoming a major theme of the XXI century research. The emergence of apparently different magnetic/structural phenomena in disparate classes of materials (mentioned above) clearly points to a need to integrate common concepts in order to achieve a broader understanding of the interplay between magnetism and structure in this general class of functional materials. This book represents the first steps toward this goal and we hope it reflects this at least in spirit. The idea for this book was born at the workshop *Interplay of Magnetism and Structure in Functional Materials* held at the Benasque Center for Science in the Pyrenees mountains during February, 9–13, 2004.

The topics covered here are interdisciplinary in nature and the chapters are written by expert researchers, who are from physics, materials science, applied mathematics and engineering backgrounds. Therefore, the book is addressed to both the experts and researchers getting into the field of magnetic functional materials including graduate students.

The eleven chapters are arranged as follows. The first two chapters (respectively by Shenoy et al. and Castán et al.) focus on the general aspects of phase transitions in multiferroic materials such as the role of elastic compatibility and long-range interactions, coupling between strain and other impor-

tant physical variables, e.g. magnetization, polarization, orbital ordering, etc., role of disorder in pretransitional phenomena and transition kinetics, local structure probes and phonon anomalies. The next two chapters by Morellon and Ibarra, and by Egami, cover a broad variety of magnetoresistive, magnetostrictive and superconducting materials where the authors discuss the role played by the interplay of spin, charge, orbital and lattice degrees of freedom on their properties. The chapters by Shapiro, Venkateswaran and De Graef, and Brown et al., review and provide exciting new results concerning the anomalous phonon behavior, structural and magnetic precursors and techniques for imaging them. James and Zhang provide an applied mathematical perspective on the problem of martensites as well as the conditions for the coexistence of ferroelectricity and magnetism. The century old (but still not fully understood) problem of the Invar as well as anti-Invar effects are reviewed by Wasserman and Acet. Finally, Pecharsky and Gschneider Jr. and Casanova et al. elaborate on the magnetocaloric effects and emerging new materials and applications. The last chapter by Prof. P.-A. Lindgård nicely summarizes the workshop held in Benasque and provides perspectives for the future.

We would like to dedicate this book to the memory of Prof. James A. Krumhansl who passed away while writing the Introductory chapter. This unfinished chapter with his thoughts on the complex functional materials is also included in the beginning of this book. Over six decades Prof. Krumhansl inspired many generations of scientists in the multidisciplinary field of complex materials and brought the concept of (elastic) solitons in materials science as simply being domain walls or twin boundaries. He also popularized the physicist's notion of phonons among metallurgists which has undoubtedly helped the interpretation of many experimental observations.

Finally, we gratefully acknowledge financial support from MCyT (Spain), AGAUR (Catalonia), University of Barcelona, Los Alamos National Laboratory, the U.S. Department of Energy and Benasque Center for Science. We specially thank Prof. Pere Pascual (Director of Benasque Center) for gracefully providing the conference facilities at Benasque.

Antoni Planes
Lluís Mañosa
Avadh Saxena

Barcelona and Los Alamos,
October 2004

Contents

List of Contributors

M. Acet
Experimentalphysik
Universität Duisburg–Essen
D-47048 Duisburg, Germany
macet@ttphysik.uni-duisburg.de

X. Batlle
Departament de Física Fonamental
Universitat de Barcelona
Diagonal 647
08028 Barcelona, Spain
xavier@ffn.ub.es

P.J. Brown
Institut Laue Langevin
38042 Grenoble, France and
Department of Physics
Loughborough University
Loughborough LE11 3TU, UK
Brown@ill.fr

F. Casanova
Departament de Física Fonamental
Universitat de Barcelona
Diagonal 647
08028 Barcelona, Spain
felixcas@ffn.ub.es

T. Castán
Departament d'Estructura
i Constituents de la Matèria
Facultat de Física
Universitat de Barcelona
Diagonal 647
08028 Barcelona, Spain
teresa@ecm.ub.es

M. De Graef
Department of Materials Science
and Engineering
Carnegie Mellon University
5000 Forbes Avenue
Pittsburgh, PA 15213-3890, USA
degraef@cmu.edu

T. Egami
University of Tennessee
Departments of Materials Science,
Engineering, Physics,
and Astronomy
Knoxville, TN 37996, USA

Oak Ridge National Laboratory
Oak Ridge, TN 37831, USA
egami@utk.edu

K.A. Gschneidner, Jr.
Ames Laboratory
US Department of Energy
Department of Materials Science
and Engineering
Iowa State University
Ames, IA 50011-3020, USA
cagey@ameslab.gov

M.R. Ibarra
Departamento de Física
de la Materia Condensada and
Instituto de Ciencia
de Materiales de Aragón
Universidad de Zaragoza
and Consejo Superior
de Investigaciones Científicas
50009 Zaragoza, Spain
ibarra@posta.unizar.es

R.D. James
Department
of Aerospace Engineering
and Mechanics
University of Minnesota
Minneapolis, MN 55455, USA
james@umn.edu

T. Kanomata
Faculty of Engineering
Tohoku Gakuin University
Tagajo 985, Japan
kanomata@tjec.tonoku.
gakuin.ac.jp

A. Labarta
Departament de Física Fonamental
Universitat de Barcelona
Diagonal 647
08028 Barcelona, Spain
amilcar@ffn.ub.es

P.-A. Lindgård
Materials Research Department
Risø National Laboratory
4000 Roskilde, Denmark
P.A.Lindgard@RISOE.DK

T. Lookman
Theoretical Division
Los Alamos National Lab
Los Alamos, NM 87545, USA
txl@lanl.gov

J. Marcos
Departament d'Estructura
i Constituents de la Matèria
Universitat de Barcelona
Diagonal 647
08028 Barcelona, Spain
jmarcos@cells.es

L. Mañosa
Departament d'Estructura
i Constituents de la Matèria
Facultat de Física
Universitat de Barcelona
Diagonal 647
08028 Barcelona, Spain
lluis@ecm.ub.es

M. Matsumoto
IMRAM, Tohoku University
Sendai 980-8577, Japan
mma@tubero.tohoku.ac.jp

L. Morellon
Departamento de Física
de la Materia Condensada
and Instituto de Ciencia
de Materiales de Aragón
Universidad de Zaragoza
and Consejo Superior
de Investigaciones Científicas,
50009 Zaragoza, Spain
morellon@unizar.es

K.-U. Neumann
Department of Physics
Loughborough University
Loughborough LE11 3TU, UK
K.U.Neuman@lboro.ac.uk

V.K. Pecharsky
Ames Laboratory
US Department of Energy
Department of Materials Science
and Engineering
Iowa State University
Ames, IA 50011-3020, USA
vitkp@ameslab.gov

A. Planes
Departament d'Estructura
i Constituents de la Matèria
Facultat de Física
Universitat de Barcelona
Diagonal 647
08028 Barcelona, Spain
toni@ecm.ub.es

A. Saxena
Theoretical Division
Los Alamos National Laboratory
Los Alamos, NM 87545, USA
abs@viking.lanl.gov

S.M. Shapiro
Department of Physics
Brookhaven National Laboratory
Upton, NY 11973, USA
shapiro@bnl.gov

S.R. Shenoy
International Centre
for Theoretical Physics
Trieste, Italy
shenoy@ictp.trieste.it

S.P. Venkateswaran
Department of Materials Science
and Engineering
Carnegie Mellon University
5000 Forbes Avenue
Pittsburgh, PA 15213-3890, USA
spv@andrew.cmu.edu

E. Vives
Departament d'Estructura
i Constituents de la Matèria
Facultat de Física
Universitat de Barcelona
Diagonal 647
08028 Barcelona, Spain
eduard@ecm.ub.es

E.F. Wassermann
Experimentalphysik
Universität Duisburg–Essen
D-47048 Duisburg, Germany
waterman@ttphysik.uni-duisburg.de

Z. Zhang
Department
of Aerospace Engineering
and Mechanics
University of Minnesota
Minneapolis, MN 55455, USA
zhang@aem.umn.edu

K.R.A. Ziebeck
Department of Physics
Loughborough University
Loughborough LE11 3TU, UK
K.R.Ziebeck@Lboro.ac.uk

1

Complex Functional Materials

J.A. Krumhansl

[Based on notes provided by Prof. J.A. Krumhansl to the editors.]

To begin with, I want to say that the idea that complex functional/adaptive materials are a new, recent discovery displays a shallow knowledge of metallurgy, last century's condensed matter physics, and electrical engineering. But to get on to the point of the title: Some ten years ago when many *complex... materials* were being widely publicized for new funding, Dick Slansky, then Director of the Theoretical Division at Los Alamos National Laboratory, was complaining to me: "What good does 'complex', defined as non-simple, do for us scientifically? What kind of a guiding principle for science is that?"

To our great surprise we found that the main definition of "complex" has a well-defined meaning and is very useful to generalize to materials. Simple, we found the answer in most dictionaries! To me it is a most conceptually useful definition, and I hope you find it so too:

Complex (def. 1): "Composed of interconnected or interwoven parts"... This is the main meaning.

And it clearly describes many early Complex Functional Materials, such as a ferromagnet. That early work identified multiple domains which moved at the mesoscopic scale in response to an applied field by motion of magnetic domain walls. The effect is to change the average macroscopic magnetization. So this definition describes an array of interwoven microscopic phases which move, respectively, to change a macroscopic condition. Not surprisingly the same ideas apply to ferroelectrics and ferroelastics (martensites) and shape memory materials. The materials discussed in this book now can also be thought of in this context.

I offer some miscellaneous remarks on modern materials science. An important reference is "Renormalization Group Theory: Its basis and formulation in statistical physics", Michael E. Fisher, Reviews of Modern Physics **70**, p. 653 (1998). Read particularly pp. 653–655 and consider the following questions (1) Is the Renormalization Group (RG) a fundamental principle or a calculation method? (2) What fraction of all phase transitions are second order? Is Renormalization Group needed generally in Materials Science? (3) Is there really such a thing as First Principles calculations (at finite temperature)? What

is an effective Hamiltonian in modern condensed matter physics? I provide a few hints and partial answers. A vast majority (more than 90%) of all phase transitions in nature are of first order. Renormalization Group is essentially a calculational procedure. However, the Landau theory is of fundamental importance in materials science and so forth.

The key word for modeling is multiscale. Physically realistic models can start at the mesoscopic scale where the notion of an order parameter and the corresponding Ginzburg–Landau free energy (for phase transitions) are essential. The coefficients of this free energy must be determined from experimental data such as structural, phonon dispersion, and thermodynamic response functions. Alternatively, these coefficients can be determined from microscopic calculations, e.g., electronic structure calculations and molecular dynamics simulations. The single crystal Ginzburg–Landau models can be extended to polycrystals and then suitably coarse grained to serve as input for continuum level constitutive response models.

Over the past half century I have had spirited discussions and shared many ideas with most of the authors in this book, and my own understanding of complex materials and multiferroics, using martensites as a prototypical example, has evolved. Understanding is always a relative word and I believe that the younger generation of scientists will take it to the next level by exploiting the modern tools of computational science, high resolution microscopies, and a suite of characterization techniques. The path to new ideas and applications in the field of functional materials is multidisciplinary – a synergy between metallurgists, materials scientists, physicists, applied mathematicians, engineers, and even biologists. We have to learn a lot from biology in terms of how evolution has optimized biological functionality.

2

Spin, Charge, and Lattice Coupling in Multiferroic Materials

S.R. Shenoy, T. Lookman, and A. Saxena

2.1 Introduction

Functional materials are those with technologically useful properties that can be sensitively controlled by external parameters. The need to understand and to use functionalities of shape memory alloys, relaxor ferroelectrics, colossal magnetoresistance manganites, superconducting cuprates and other materials, is one motivation for their intense current study [1–11]. Of course, applied stress, magnetic field or voltage will, respectively, induce *direct-variable* changes in strain, magnetization and electric polarization. More interestingly, in multifunctional materials with mutually coupled variables, there is also a *cross-variable* response, so a given field could control two or more variables, or a variable can be switched by two or more external fields.

Thus in magnetic shape memory alloys, with coupled strain and magnetization, the external shape can be controlled both by pressure and by magnetic field; and stress changes magnetization, while magnetic field affects structure [12]. In colossal magnetoresistance manganites [3], the conductance (that is related to magnetization), rises by many orders of magnitude in response to uniform magnetic fields as well as to hydrostatic pressure; while voltage induces changes in local structure and conductance [13, 14]. In ferroelectric manganites, polarization can be switched by a magnetic field [15]. In cuprates [7] the superconductivity is suppressed as usual by a magnetic field, but is also controlled by stress [16]; shape memory-like effects can occur [17]; and surprisingly (for these doped antiferromagnets), an external uniform magnetic field can rotate elastic domain walls [18]. Thus a variety of materials show cross-variable response in their macroscopic multifunctionalities, implying strong coupling of magnetic spin, electronic charge and lattice strain.

Finescale local probes have revealed something surprising, however. Many transition metal oxides spontaneously form *nonuniform* complex patterns of charge, spin and strain variables at scales of a nanometer and upwards [4–6, 19–26]. The multivariable patterning includes structural stripes,

magnetic droplets and conducting filaments, and there has been much experimental and theoretical interest in this "nanoscale phase separation" or "intrinsic heterogeneity" [4–6]. There is also a remarkable *cross-scale* response: a uniform or *macro*scale magnetic field can induce *meso*scale structural changes, or *nano*scale conductance variations [18, 19].

An understanding of these multiscale, multivariable textures is crucial to tailoring multifunctionalities on the macroscale [10]. Clearly, a uniform order parameter (OP) Landau model is insufficient. The *spatially varying* patterns of charge, magnetization, and strain must emerge as the locally stable minimum of some multivariable, nonlinear, free energy functional.

Spatial variation as a preferred state is not new, of course. Purely ferroelastic materials with a *strain tensor* order parameter, such as shape memory alloys like FePd, show mesoscale "twins" or bands of coexisting unit-cell variants, below the structural transition [27]; or woolen-fabric-like "tweed" of oriented criss-cross striations on a finer nanoscale, above the transition [28]. In martensites, interfaces can also be dynamic, with acoustic emission on quenching, from domains advancing at sound speeds [29]. Superconducting cuprates are also doped ferroelastics [30], and show both twinning and tweed, as emphasized by Krumhansl [7]. Magnetoresistant metallic glasses exhibit mesoscale tweed [31]. Relaxor ferroelectrics/magnetoelastics also show twins and tweed in electric polarization/magnetization [12, 32].

The similarity and ubiquity of textures in very different materials prompts a search for a common link. Competition between short- and long-range forces, and/or sign-varying frustration effects are known to generically favour patterning [33]. Since all variables live on a discrete, d-dimensional crystal lattice, it follows that local deformation or strain of the lattice both affects spin and charge, and in turn is influenced by them. It turns out that in ferroelastics, generic lattice-integrity *constraints* on the $\frac{1}{2}d(d+1)$ components of the symmetric strain tensor [34] can induce effective long-range interaction *potentials*, with sign-varying angular variation, and power-law decay. Working in a strain representation, rather than in the more conventional displacement representation, reveals these hidden, texture-inducing correlations. The origins of intrinsic inhomogeneities could lie in the ubiquitous strain tensor: its power-law interaction, its nonlinearity, and its coupling to other variables.

We focus on this emerging viewpoint [35–42], without giving a proper review of other approaches, or any more than illustrative references. In Sect. 2.2 we consider coupled "multiferroic" order parameters. Section 2.3 discusses the St Venant compatibility constraint that induces the effective long-range potential. Intrinsic inhomogeneities in proper ferroelastics and multiferroic oxides, are discussed in Sects. 2.4 and 2.5, respectively. Section 2.6 outlines the modelling of oxides, with charge and spin acting as local stresses and temperatures. A summary, with speculations on further work, is given in Sect. 2.7.

2.2 Order Parameters and Multiferroics

The order parameter is a basic concept in phase transitions [43]: a variable whose thermal average becomes nonzero below a transition temperature or pressure either continuously (second-order) or discontinuously (first-order). The free energy lowering can involve a global dominance of a uniform state: only one out of $N_{\rm V}$ competing, lower symmetry, degenerate minima or "variants" is finally present. Nonlinearity of the free energy functional in such second order transitions is manifest close to the transition, where renormalizations occur due to nonuniform critical fluctuations of competing variants.

Structural phase transitions involve a change in the discrete symmetry of the unit cell, with lattice points shifting on cooling (or application of stress) to new lower-symmetry positions. Ferroelastic displacive structural transitions [1] are those for which the symmetry of the low-temperature unit cell is a *subgroup* of the high-temperature unit cell symmetry. The order parameters (OP) for first-order ferroelastic transitions are $N_{\rm OP} \leq d$ independent components of the strain tensor, that can exhibit strain hysteresis under applied stress. The free energy lowering can involve a global coexistence of nonuniform states: all the $N_{\rm V}$ lower symmetry variants are finally present. Nonlinearity of the free energy functional in such first-order transitions is manifest for temperatures all the way below, and for a range above, the transition. Structural static domain walls such as in twins or tweed, and dynamic excitations, are elastic solitons [27,28,44], and the nonuniformity is a signature of nonlinearity.

Domains and hysteretic switching occur, of course, in several types of materials – indeed the very name "ferroelastic" and "ferroelectric" derive from the analogy with ferromagnets: they all have such behaviour in common (but not the element of Fe, ironically!) These three materials classes can be grouped under the common rubric of "ferroics" as they all "undergo nondisruptive phase transitions that alter their point group symmetry" with strain, electric polarization, or magnetization as the respective order parameters [9]. Materials with two or more ferroic OPs, and a sequence of nested phase transitions, are *multiferroics*, that can have mutually *coupled nonlinearities*. A primary order parameter at its transition temperature (or composition), can drive the other, secondary OPs; with roles exchanged at the other, nested transitions. For example cuprates have a ferroelastic structural transition [30], with strain as the primary OP, that can be followed on cooling by a Néel transition, with staggered magnetization as the primary OP [7]. In manganites depending on the doping, there is a complex phase diagram, with ferromagnetic, charge-order, ferroelastic and Jahn-Teller transitions [3, 6].

As illustrated in later sections, cuprates and manganites could be regarded as examples of *complex* multiferroics in the sense of Krumhansl, who speaks in this volume of complex materials as composed of interconnected parts, with interwoven microscopic phases moving relatively, to change a macroscopic condition. This picture of annealed-variable texturing

is complementary to quenched-disorder effects, certainly also present [6]. The multiferroic conceptual umbrella, and an approach that studies cuprates in the context of manganites and other oxides [23], might have pleased Krumhansl, who also remarked that "by and large, the physics literature on high T_c seems to be unfortunately disjoint from much earlier work on displacive phase transitions, or other areas of materials science, notably ferroelectricity and metallurgy" [7].

2.3 Strain Tensor and Elastic Compatibility

In this section we focus on "proper" ferroelastics that have only a strain tensor order parameter [1] and later consider couplings to other variables, in "improper" ferroelastics. Suppose we only consider those deformations of the crystal lattice that do not create dislocations and vacancies. Then the central point is that this seemingly innocuous "no-defect" constraint, of lattice integrity maintained at every instant, implies the existence of anisotropic, power-law (APL) correlations between order-parameter strains.

2.3.1 Levels of Description

The unit cell sets the minimum scale for strain variations. More generally, it is useful to define levels of description for probe distances R, as in Fig. 2.1. *Level 0* or $L_0 \sim R \gg a_0$ (lattice constant) is the macroscopic regime of engineering strains, and of system size and shape. *Level 1* is the regime of unit-cell strains, that can have meso- and nanoscale variations within the large range $L_0 > R > a_0$. The intracell regime of *Level 2* involves the bond angles and lengths, $a_0 > R \sim \ell_0$, of the atomic basis whose deformation

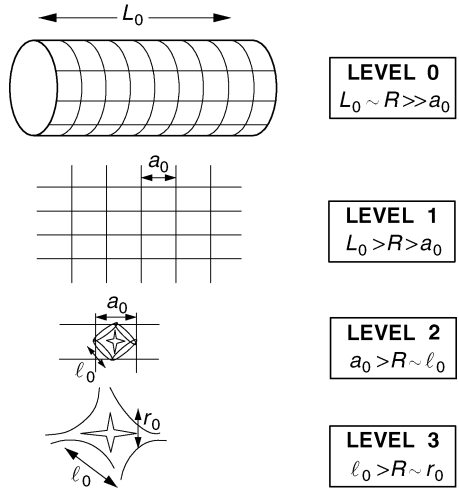

Fig. 2.1. Levels of description. See text, Sect. 2.3.1

may be termed as the "microstrain", e.g. Jahn–Teller-like distortions of perovskite octahedra [21]. Finally, *Level 3* is the Ångstrom-scale regime of the electron occupancies/spin states of individual-atom wavefunctions on scales $\ell_0 > R \sim r_0$, e.g. d-wave orbitals or core spins. Of course, the levels are coupled. The Level 1/Level 2 interface is where the elastic physics meets the structural chemistry. Jahn–Teller Hamiltonians [3] link Level 3 orbital occupancies to Level 2 octahedral "Q_2, Q_3" stretchings; these in turn represent Level 1 unit-cell strain distortions.

The material specifics of the multiferroics are in the detailed nature of the charge/polarization/spin variables; their symmetry-dictated couplings to each other and to strains; and the values and signs of the coupling constants as well as energy scales. But for materials with strong elastic anisotropy (from directional Level 2 bonding, or basis atoms with widely different sizes), the common key is the Level 1 strain. Its APL elastic correlations, nonlinearities, and couplings to other variables, could possibly induce domain-wall patterned states, as local minima of a multivalley free energy landscape. The power-law correlations are in a certain sense, scale-free, and could link widely separated variables at finer levels of description.

2.3.2 Definition of Unit-Cell Strain Tensor

Engineering strain is a Level 0 description of distortions of a medium, with derivatives of a continuous displacement $\boldsymbol{u}(\boldsymbol{r}')$, labelled by a continuum position $\boldsymbol{r}'$ [43,45]. On the other hand, unit-cell strain in a crystal lattice with lattice points $\boldsymbol{r}_i$ can be defined as a Level 1 continuous variable, that is a *discrete difference* of lattice-point displacements $\boldsymbol{u}(\boldsymbol{r}_i)$. It reduces to macroscopically varying engineering strains in the continuum limit of lattice constant $a_0 \to 0$, when the discrete differences become derivatives. Consider for simplicity, a cubic lattice with atoms at lattice points $\boldsymbol{r}_i$ (scaled in a_0) interacting through a two-body potential V that depends only on the magnitude of their separation $\boldsymbol{r}_{i,j} = \boldsymbol{r}_i - \boldsymbol{r}_j$. Then for a deformed lattice with points at $\boldsymbol{R}_i = \boldsymbol{r}_i + \boldsymbol{u}(\boldsymbol{r}_i)$, the energy change $\Delta V = V(|\boldsymbol{R}_{i,j}|) - V(|\boldsymbol{r}_{i,j}|)$ is

$$\Delta V = V(|\boldsymbol{r}_{i,j} + \boldsymbol{u}(\boldsymbol{r}_i) - \boldsymbol{u}(\boldsymbol{r}_j)|) - V(|\boldsymbol{r}_{i,j}|)\,. \tag{2.1}$$

For nearest-neighbour lattice points, $\boldsymbol{r}_i = \boldsymbol{r}_j + \hat{\mu}$ (where $\hat{\mu} = \hat{x}, \hat{y}, \hat{z}$) the discrete difference [46] of the displacement-vector components naturally appears, $\Delta_\mu u_\nu(\boldsymbol{r}_j) \equiv u_\nu(\boldsymbol{r}_j + \hat{\mu}) - u_\nu(\boldsymbol{r}_j)$. More specifically, in changes of the squared separations

$$|\boldsymbol{R}_{j+\hat{x},j}|^2 - |\boldsymbol{r}_{j+\hat{x},j}|^2 = 2E_{xx}\,, \tag{2.2}$$

the differences appear as $\frac{1}{2}d(d+1)$ components of a unit-cell, symmetric strain tensor that is *defined* by

$$E_{\mu\nu} \equiv \frac{1}{2}\left[\Delta_\mu u_\nu(\boldsymbol{r}_i) + \Delta_\nu u_\mu(\boldsymbol{r}_i) + G_{\mu\nu}\right]\,. \tag{2.3}$$

Here the last term $G_{\mu\nu} \equiv \Delta_\mu \boldsymbol{u}(\boldsymbol{r}_i) \cdot \Delta_\nu \boldsymbol{u}(\boldsymbol{r}_i)$ is the "geometric nonlinearity". An expansion, $\Delta V = \frac{1}{2} \sum_{\mu\nu} \sum_i K_{\mu\nu} E^2{}_{\mu\nu}(\boldsymbol{r}_i) + \cdots$ will include harmonic strain terms, with $K_{\mu\nu}$ an appropriate spring-constant matrix.

All this is simply to motivate the definition of the unit-cell strain tensor (2.3) of Level 1, that appears in the Ginzburg–Landau free energy expansion below. Although here only the static case is considered, the dynamic case has also been treated [37]. In a Lagrangian approach, expressing the displacement kinetic energy in terms of strain rates yields a strain-representation nonlinear dynamics for ferroelastic transitions; dynamic compatibility kernels can be of a resonant form to drive nonequilibrium interfaces at sound speeds [37].

The six physical strains that transform according to irreducible representations of the point group for the 3D cubic case, are one compressional, two deviatoric, and three shear strains, defined by linear combinations [38]

$$e_1 = \frac{1}{\sqrt{3}}(E_{xx}+E_{yy}+E_{zz}),\ e_2 = \frac{1}{\sqrt{2}}(E_{xx}-E_{yy}),\ e_3 = \frac{-1}{\sqrt{6}}(E_{xx}+E_{yy}-2E_{zz}),$$

$$e_4 = E_{yz}, \quad e_5 = E_{zx}, \quad e_6 = E_{xy}\,. \tag{2.4}$$

The three physical strains in 2D for the square lattice are one compressional, one deviatoric and one shear strain

$$e_1 = \frac{1}{\sqrt{2}}(E_{xx} + E_{yy}), \quad e_2 = \frac{1}{\sqrt{2}}(E_{xx} - E_{yy}), \quad e_3 = E_{xy}\,, \tag{2.5}$$

and we focus on this illustrative case, in Sect. 2.3.3.

A simplifying approximation is useful. The displacement differences can be scaled in a typical strain value λ through $\Delta u \to \lambda \Delta u$ or $E \to \lambda E(\lambda)$, with λ determined in terms of material parameters, e.g. for FePd, $\lambda \sim 0.02$ [37]. The last term in (2.3) is smaller by a relative factor of $\lambda \ll 1$ and can be neglected as a first approximation, setting $\lambda G_{\mu\nu} = 0$. (The geometric nonlinearity can later be included perturbatively, or by using the second-order compatibility equations [45].) For now, we take strain as the defined linear symmetric tensor. A Ginzburg–Landau expansion in quadratic and higher invariants of $\lambda E(0)$ is then formally a power series in λ.

2.3.3 Strain Free Energy

To describe structural transitions, with free energy nonlinearities to drive the finite-temperature transition, a partition function partial trace over Level 2 variables will yield a variational free energy F_{strain} in terms of the Level 1 strains. The coefficient of the OP harmonic term, that decreases linearly on cooling is $A^{(0)}(T - T_{\text{c}})$, and the nonlinear terms generate a first-order phase transition, at some temperature $T_0 > T_{\text{c}}$, that pre-empts the full softening on cooling to T_{c}. There are also non-OP harmonic terms. Scaling all strains in a typical value λ and all energy densities in a typical value D_0, and with scaled OP strains notationally distinguished through, e.g. $\varepsilon \equiv e_2$ for a deviatoric OP,

the free energy $F_{\rm strain} = D_0 \sum f$. The dimensionless scaled free energy density $f = f_0(\varepsilon) + f_{\rm grad}(\boldsymbol{\Delta}\varepsilon) + f_{\rm non}(e_1, e_3)$ can be expanded in symmetry-allowed invariants, that for the 2D square–rectangle case are

$$f = [(\tau-1)\varepsilon^2 + \varepsilon^2(\varepsilon^2-1)^2] + {\xi_0}^2(\boldsymbol{\Delta}\varepsilon)^2 + \frac{1}{2}(A_1{e_1}^2 + A_3{e_3}^2)\,. \tag{2.6}$$

Here the dimensionless ξ_0 sets a domain-wall thickness. The scaling of the Landau free energy $f_0(\varepsilon)$ to a factorized form as in the square brackets can be done for all ferroelastic transitions in 2D and 3D [37,47], generalizing a procedure of Barsch and Krumhansl [48]. The important dimensionless temperature variable $\tau = (T - T_{\rm c})/(T_0 - T_{\rm c})$ is unity at a temperature T_0, when all nonzero free energy minima in OP space fall on a "unit sphere" of radius $|\varepsilon| = 1$, and are degenerate with the $\varepsilon = 0$ high-temperature minimum. Dimensionless elastic parameters are elastic constant anisotropy ratios, related to the unscaled values by $A_{1,3} = A^{(1,3)}/[A^{(0)}(T_0 - T_{\rm c})]$, that can in principle be determined from experiment, molecular dynamics simulations, or electronic structure calculations. The scaled values can be large for anisotropic systems (e.g. for FePd parameters, $A_1 = A_3/2 = 150$), that has consequences discussed later.

It is tempting to say that since the non-OP free energy terms in (2.6) are harmonic, the optimization must set $e_1 = e_3 = 0$ at the outset, so that (for $\tau < 1$) a uniform $\varepsilon = \bar{\varepsilon}(\tau) \neq 0$ minimum determined by the Landau free energy alone, is picked out. However, this procedure incorrectly treats all strain components with wavevector $\boldsymbol{k} \neq 0$ as independent, and misses nonuniform states that are also local minima.

Simulations in a displacement representation of (2.6) minimize f in the d-dimensional variable $\boldsymbol{u}(\boldsymbol{r})$ at each lattice site. If instead, we want to work in terms of the physical unit-cell variables of compression, shear and deviatoric strain, then in fact, we have too many variables! The $\frac{1}{2}d(d+1)$ variables must be reduced in number by $N_{\rm c} = \frac{1}{2}d(d-1)$ constraints, to yield the required number of $\frac{1}{2}d(d+1) - N_{\rm c} = d$ degrees of freedom. Such constraints exist [34], and are implicit in the very definition (2.3) of the strain tensor.

2.3.4 St Venant Compatibility Constraints

In a "dyadic" notation, the strain tensor in real and Fourier space (without geometric nonlinearity) can be written as

$$\begin{aligned} \underline{\underline{\boldsymbol{E}}} &= \frac{1}{2}\left[\boldsymbol{\Delta u}(\boldsymbol{r}) + (\boldsymbol{\Delta u}(\boldsymbol{r}))^{\rm T}\right], \\ \underline{\underline{\boldsymbol{E}}}(\boldsymbol{k}) &= \frac{\rm i}{2}\left[\boldsymbol{K u}(\boldsymbol{k}) + \boldsymbol{u}(\boldsymbol{k})\boldsymbol{K}\right], \end{aligned} \tag{2.7}$$

where T is "transpose", and in Fourier space, the difference operator is effectively $\Delta_\mu \to {\rm i}\, K_\mu \equiv {\rm i}\, 2\sin(k_\mu/2)$. (The differences are bond-midpoint variables [46], and the physical strains can be assigned to the unit-cell centres, i.e. the dual lattice.)

Since Curl(Grad) acting on a single-valued function is zero, manifestly:

$$\begin{aligned} \mathrm{Inc}[\underline{\underline{\boldsymbol{E}}}] \equiv \boldsymbol{\Delta} \times [\boldsymbol{\Delta} \times \underline{\underline{\boldsymbol{E}}}]^{\mathrm{T}} = 0\,; \\ \boldsymbol{K} \times \underline{\underline{\boldsymbol{E}}} \times \boldsymbol{K} = 0\,. \end{aligned} \tag{2.8}$$

This *compatibility* constraint was obtained, in the continuum limit, by St Venant [49] in an 1864 commentary on a work of Navier, and its importance was emphasized more recently by Baus and Lovett [34]. It expresses the physical requirement that if a unit-cell is deformed, then the neighbouring and further-off cells must also deform in a decreasing way, so the cells all fit together in a smoothly "compatible" manner. Clearly, even if the cell that initiates these knock-on effects [1] is a pure deviatoric strain say, the compression/shear strains could still be needed, to maintain lattice integrity [37].

In (2.8), Inc$[\cdots]$ defines an "incompatibility" operation on tensor fields, such as the Div$[\cdots]$ or Curl$[\cdots]$ operations on vector fields. In fact Inc$[\boldsymbol{E}] = 0$ is a zero-incompatibility, no-defect condition analogous to the zero-divergence, no-monopole field equation Div$[\boldsymbol{B}] = 0$ in electromagnetism. In terms of single-valued auxiliary variables, i.e. displacements or vector potentials $\boldsymbol{u}, \boldsymbol{A}$, both are trivial mathematical identities; but in terms of the physical variables, i.e. unit-cell strain or magnetic field $\boldsymbol{E}, \boldsymbol{B}$, both are physical field equations.

In 1D there is only a single strain $\varepsilon = \Delta_x u_x(x)$ and there are no compatibility constraints: $N_{\mathrm{c}} = \frac{1}{2}d(d-1) = 0$. In 2D, the explicit difference equation with $N_{\mathrm{c}} = 1$ is

$$\frac{1}{\sqrt{2}}\,\Delta^2 e_1 - 2\Delta_x\Delta_y e_3 - \frac{1}{\sqrt{2}}(\Delta_x^2 - \Delta_y^2)e_2 = 0\,. \tag{2.9}$$

In 3D with $N_{\mathrm{c}} = 3$ we have [38, 45]

$$\begin{aligned} 2\Delta_y\Delta_z E_{yz} &= \Delta_z^2 E_{yy} + \Delta_y^2 E_{zz}\,, \\ 2\Delta_z\Delta_x E_{zx} &= \Delta_x^2 E_{zz} + \Delta_z^2 E_{xx}\,, \\ 2\Delta_x\Delta_y E_{xy} &= \Delta_y^2 E_{xx} + \Delta_x^2 E_{yy}\,. \end{aligned} \tag{2.10}$$

There are also three other equations that emerge,

$$\begin{aligned} \Delta_y\Delta_z E_{xx} + \Delta_x^2 E_{yz} &= \Delta_z\Delta_x E_{xy} + \Delta_x\Delta_y E_{zx}\,, \\ \Delta_z\Delta_x E_{yy} + \Delta_y^2 E_{zx} &= \Delta_y\Delta_z E_{xy} + \Delta_x\Delta_y E_{yz}\,, \\ \Delta_x\Delta_y E_{zz} + \Delta_z^2 E_{xy} &= \Delta_y\Delta_z E_{zx} + \Delta_z\Delta_x E_{yz}\,, \end{aligned} \tag{2.11}$$

but solving for shears in Fourier space, or applying appropriate difference operators, one gets identities.

2.3.5 Compatibility Potentials

The derivations of the St Venant compatibility potentials for a given transition are straightforward, as the interested reader can easily confirm by working through the square–rectangle case below. (The uninterested one can skip directly to (2.14), and conceptual comments.)

There are $\frac{1}{2}d(d+1)$ physical strains, of which $N_{\rm OP}$ are order parameters, and the other $n = \frac{1}{2}d(d+1) - N_{\rm OP}$ components are non-OP strains. One can use $N_{\rm c}$ Lagrange multipliers for the constraints [35–37]. More simply [42]:

1. Solve the $N_{\rm c}$ compatibility equations for n non-OP strains in Fourier space and substitute into the harmonic non-OP free energy, thus guaranteeing compatibility. The free energy now has $d = (d/2)(d+1) - N_{\rm c}$ strains.
2. Then further minimize (freely) with respect to the remaining $n - N_{\rm c} = d - N_{\rm OP} \geqslant 0$ non-OP strains, that are harmonic or bilinear in the free energy.

This procedure converts the harmonic, local, non-OP free energy $f_{\rm non}$ to a harmonic, *non-local* OP free energy $f_{\rm compat}$.

For the square–rectangle transition, $N_{\rm OP} = 1$, $n = 2$ and from (2.9), the $N_{\rm c} = 1$ compatibility equation in fourier space is

$$e_1(\boldsymbol{k}) = -[O_2(\boldsymbol{k})\,\varepsilon(\boldsymbol{k}) + O_3(\boldsymbol{k})\,e_3(\boldsymbol{k})]/O_1(\boldsymbol{k})\,, \tag{2.12}$$

where $O_1(\boldsymbol{k}) = -\frac{1}{\sqrt{2}}|\boldsymbol{K}|^2$, $O_2(\boldsymbol{k}) = \frac{1}{\sqrt{2}}(K_x^2 - K_y^2)$, $O_3(\boldsymbol{k}) = 2K_xK_y$. By substituting for e_1 and minimizing in e_3, the final result yields the compressional and shear strains as proportional to the OP deviatoric strain, $e_{1,3}(\boldsymbol{k}) = B_{1,3}(\boldsymbol{k})\,\varepsilon(\boldsymbol{k})$. Here $B_1 \equiv -O_1\,O_2/D$, $B_3 \equiv -(A_1/A_3)\,O_3\,O_2/D$, whereas $D \equiv [O_1^2 + (A_1/A_3)\,O_3^2]$, and it is seen that the compatibility constraint (2.12) is satisfied as an identity. Note that for an equilibrium $\varepsilon(\boldsymbol{k})$ texture peaking at diagonal orientations $\hat{k_x} = \hat{k_y}$, the non-OP strains $e_{1,3}$ vanish, as the coefficients $B_{1,3} \sim O_2 = 0$.

The non-OP harmonic free energy density becomes [35–37, 42]

$$f_{\rm non}(e_1, e_3) = f_{\rm compat}(\varepsilon) = \frac{A_1}{2}|e_1|^2 + \frac{A_3}{2}|e_3|^2 = \frac{A_1}{2}\,U(\boldsymbol{k})\,|\varepsilon(\boldsymbol{k})|^2\,, \tag{2.13}$$

where $U(\boldsymbol{k}) = |B_1|^2 + (A_3/A_1)|B_3|^2$. The free energy $F_{\rm strain}(\varepsilon)$ is obtained in terms of the OP alone, with the non-OP strains as derived quantities

$$F_{\rm strain} = \sum_{\boldsymbol{r}}[(\tau-1)\varepsilon^2 + \varepsilon^2(\varepsilon^2-1)^2] + f_{\rm grad}(\boldsymbol{\Delta}\varepsilon) + \frac{A_1}{2}\sum_{\boldsymbol{r},\boldsymbol{r}'}\varepsilon(\boldsymbol{r})\varepsilon(\boldsymbol{r}')\,U(\boldsymbol{r}-\boldsymbol{r}')\,. \tag{2.14}$$

This is a central conceptual result. In the usual displacement representation, every term in the free energy (2.6) involves anisotropic, nearest-neighbour differences of a d-dimensional variable $\boldsymbol{u}$ defined at the lattice points, e.g. $e_1^2 = (1/2)(\Delta_x u_x + \Delta_y u_y)^2$, while $\epsilon^6 = (1/8)(\Delta_x u_x - \Delta_y u_y)^6$. On the other hand, in the OP *strain representation*, the free energy of (2.14), in the spirit of Landau, depends only on the $N_{\rm OP} \leq d$ order parameters (on the dual lattice), and there is now an explicit, far-neighbour, potential that carries all the anisotropies [36, 37].

The Landau part in square brackets is diagonal in coordinate space, while the compatibility potential is diagonal in Fourier space. The St Venant kernel $U(\boldsymbol{k}) = O_2^2/2D \sim (K_x^2 - K_y^2)^2/K^2$, and the lattice Green's function

$G(\boldsymbol{k}) = [K_x^2 + K_y^2]^{-1}$, both reflect the discreteness of the lattice in their anisotropy at short wavelengths. However, at long wavelengths $U(\boldsymbol{k}) \to U(\hat{k})$ is still anisotropic and moreover, independent of the wavevector magnitude, in contrast to the isotropic $G(\boldsymbol{k}) \to 1/k^2$ that depends (only) on $|\boldsymbol{k}|$. This generic feature of U arises from solving the compatibility equation in terms of factors O_i/O_1 $(i = 2, 3)$, that depend on ratios $K_\mu^2/K^2 \to k_\mu^2/k^2 = \hat{k}_\mu^2$.

As an important consequence, $U(\boldsymbol{R})$ is *asymptotically anisotropic*, with a numerator that reflects the symmetry of the unit cell multiplying a *power-law decay* whose exponent is the dimensionality. By contrast, $G(\boldsymbol{R}) \sim 1/R^{d-2}$ is asymptotically isotropic. Explicitly, the $d = 2$ square-lattice kernel in coordinate space, at distances beyond a lattice scale is [35–37]

$$U(\boldsymbol{R}) \to \int \mathrm{d}^d k \, \mathrm{e}^{\mathrm{i}\boldsymbol{k}\cdot\boldsymbol{R}} U(\hat{k}) \sim \cos(4[\theta - \theta'])/R^d \,, \tag{2.15}$$

where $\hat{r} \cdot \hat{r}' = \cos(\theta - \theta')$ and the fourfold symmetry is manifest. Clearly, the asymptotic power-law decay has nothing to do with proximity to a second-order critical point: it arises from a change of variables $(k \to k/R)$ and wavevector phase space, with no contribution from the $|\boldsymbol{k}|$-independent, long wavelength kernel. The strain at a site can receive sign-varying, conflicting instructions from the other strains around it, in *elastic frustration*. While the spatial integral of the truly long-range $G(\boldsymbol{R})$ diverges as a power of system size, and that of an isotropic power-law $1/R^d$ is logarithmically divergent, the integral is zero over the sign-varying $U(\boldsymbol{R})$ power-law potential.

The compatibility kernels are different for different ferroelastic transitions, as they encode the transition symmetries. They have been evaluated for the case of 2D transitions, including square–rectangle ($N_{\mathrm{OP}} = 1$, $N_V = 2$), triangle to centered rectangle ($N_{\mathrm{OP}} = 2$, $N_{\mathrm{V}} = 3$), triangle-oblique ($N_{\mathrm{OP}} = 2$, $N_{\mathrm{V}} = 6$) [37]. For 3D transitions, evaluated kernels include cubic–tetragonal ($N_{\mathrm{OP}} = 2$, $N_{\mathrm{V}} = 3$), cubic–trigonal ($N_{\mathrm{OP}} = 3$, $N_{\mathrm{V}} = 4$) and so on [40, 47].

2.3.6 Other Approaches

There are many other complementary approaches to elastic textures, and we can merely list some of them.

1. Simulations in the displacement representation: This is widely used [35, 50]. Strains are derived from the equilibrium displacement-vector texture.
2. Sharp-interface minimizers: In the limit $\xi_0 \to 0$ the gradient cost tends to zero, yielding sharp-step domain walls. The applied mathematics problem is then to find distributions of domain walls with positive/negative constant-strain regions in between them, such that the nonlinear free energy is a local minimum [51, 52].
3. Simulations in morphological variables: This "phase-field" method focuses on atomic-basis morphological variables coupled to the strain, to describe the variants, with the inhomogeneous strain treated as a local-inclusion.

The effective free energy is nonlinear in the morphological variables, and has an anisotropic power-law potential between their squares. Strains are derived quantities [53].

Nonperiodic or disordered elastic systems, such as network glasses, can be studied through a discrete approach to their rigidity, that finds floppy, intermediate and rigid phases, as the average number of local bonding constraints varies [54].

In contrast to the above approaches, we describe here a representation that directly works with the strain, using derived compatibility kernels specific to each transition and an anisotropic power-law between OP strains (not their squares). The displacement vector can then be obtained from the strain field [34]. This approach is easily extended to include strain coupling to other variables, as discussed in the following sections. Complementary models for charge, spin or lattice texturings include those that invoke Coulombic forces and/or polaronic lattice couplings; charge states as Eshelby inclusions; quenched-disorder Griffiths models with locally suppressed transition temperatures; Ising-spin toy models; or inhomogeneities linked to trapped stresses [6, 55, 56].

2.4 Inhomogeneities in Ferroelastics

The local minima of the free energy $F_{\rm strain}$ of (2.14) are found by longtime $\varepsilon(\boldsymbol{r}, t)$ states emerging from a relaxational dynamics (that can be obtained in some limit from an underdamped dynamics),

$$\dot{\varepsilon} = -\partial F_{\rm strain}(\varepsilon)/\partial\varepsilon \tag{2.16}$$

with random $\varepsilon(\boldsymbol{r}, t = 0)$ initial conditions. The non-OP strains e_1, e_3 are obtained as derived quantities. With additional free energy terms, as discussed below, the asymptotic states can show equal-width twins, and tweed.

Twins

Figure 2.2a shows, for large anisotropies $A_1 = 100$, the final state of oriented domain walls. The preferred orientation follows from the compatibility kernel $U \sim (\hat{k}_x^2 - \hat{k}_y^2)^2$ that favours diagonal domain walls, but does not set a mesoscale domain wall separation length. The costly non-OP strains $e_{1,3}(\boldsymbol{k})$ vanish at diagonal orientations, as mentioned, in a kind of "elastic Meissner effect" [36]. (This is not true for all textures – e.g. the triangle to centred rectangle transition has states with three degenerate structural domains meeting at a point, where compatibility forces the $e_1(\boldsymbol{r})$ non-OP strain to be nonzero [37].) Figure 2.2b shows that for smaller $A_1 \simeq 1$ and other parameters the same, we get multiscale domains. These are qualitatively similar to martensites, that Krumhansl has termed a paradigm for the multiscale concept [10].

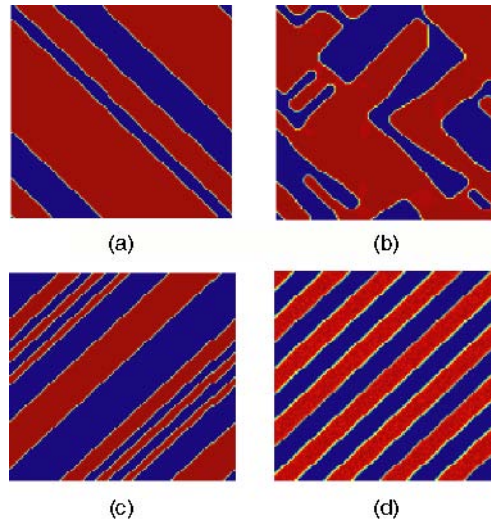

Fig. 2.2. Ferroelastic domain walls, below the square-to-rectangle transition temperature. (**a**) Large coefficient of the (bulk) compatibility potentials $A_1 = 100 \gg 1$. (**b**) Smaller coefficient of the (bulk) compatibility potentials, $A_1 \sim 1$. (**c**) Same as (**a**), but with different initial random seed, showing different quasidegenerate final state. (**d**) Same as (**a**), but with an added surface compatibility potential setting a length scale for equal-width twins

Why do such domain-wall states occur? After all, since the coefficient ξ_0^2 of the squared-gradient term in the free energy is positive, domain walls always cost energy. Figure 2.2c shows that with the *same* parameters as Fig. 2.2a, but a different initial-state random seed, the number $N_{\rm dom}$ of domain walls changes; although with the free energy density $f = F/L_0^2$ almost unchanged. This is easily understood: if the uniform case $\varepsilon = \bar{\varepsilon}(\tau)$ has a free energy density $f = -|f_0(\bar{\varepsilon})|$, then a state with walls of width ξ_0 will have a nearly degenerate $f = -\left[|f_0(\bar{\varepsilon})| - (\xi_0/L_0)N_{\rm dom}\,\bar{\varepsilon}^2\right]$. And once an elastic soliton (or domain wall) is oriented by the compatibility potential $A_1 U$ (that vanishes at a preferred angle), then the free energy barrier to a deviating segment of finite-fraction L_0 length will be $F_{\rm barrier} \sim A_1(\xi_0 L_0)\,\bar{\varepsilon}^2$. Thus one has the possibility of multiple wells separated by macroscopic barriers, in a rugged "free energy landscape" sculpted by the St Venant lock-in of multiple domain-wall segments, with all preferred orientations present. It would be interesting to make this "configurational strain-glass" picture more quantitative [57]. The $N_{\rm dom} = 0$ uniform state may be the lowest in energy, but only marginally so; moreover it has many competitors, and so is hard to find!

Of course, all this is with periodic boundary conditions. However, finite systems or nonperiodic boundary conditions can also be handled in principle. Consider an $L_0 \times L_0$ square martensite embryo within a sea of austenite.

The austenite/martensite interface (habit plane) at $x = 0$ say, can be treated by including decaying surface strains $\tilde{\varepsilon}(\boldsymbol{r})$, in the austenite; and also adding on to a "bulk" strain $\bar{\varepsilon}(\boldsymbol{r})$ deep inside the martensite. We demand continuity of the total strain on either side, plus strain–gradient matching as dictated by integrating the St Venant equation across the boundary. Then the surface strain amplitudes [in a Laplace–Fourier expansion for $\tilde{\varepsilon}(\boldsymbol{r})$] can be written in terms of the bulk amplitudes [in a Fourier expansion for $\bar{\varepsilon}(\boldsymbol{r})$]. The simulations can be performed in terms of the periodic boundary condition bulk strains in an $L_0 \times L_0$ surrogate system, with the surface strain contributions integrated out to yield a surface compatibility potential that adds on to the bulk compatibility potential. The necessarily nonzero decay constant in the positive x direction in the austenite side, then forces a modulation wavevector or martensitic twinning in the y direction inside the embryo. Explicitly, this elastic fringing-field energy is $F_{\text{surf}} \sim (1/L_0)A_3 \sum_{\boldsymbol{k}} |\bar{\varepsilon}(k_x, k_y)|^2/|k_y|$, in agreement with a displacement representation calculation. Figure 2.2d shows that F_{surf} clearly does set a mesoscopic length scale (has long wavelength $|\boldsymbol{k}|$ dependence), yielding equal-width "true" twins, and inducing a width–length scaling $W \sim {L_0}^{1/2}$, as in early experiments [27, 36].

Tweed

In (some) martensites above the structural phase transition, nanoscale crisscross domains are seen, that have been called "tweed" textures by Tanner [28]. Tweed (and twins) has been seen in cuprates, giant magnetoresistance (GMR) manganites, and relaxor ferroelectrics [7, 31, 32]; and magnetic tweed can also be imaged and modelled [58]. Its ubiquity suggests an explanation in terms of a common variable, e.g. strain. For ferroelastics, tweed has been linked [28] to an incipient softening on cooling of the elastic constant coefficient $C' = C_{11} - C_{12}$ of the harmonic deviatoric strain ε^2, that is τ in scaled form. Since compositional disorder is almost always present in alloys (and the transition temperature varies sharply with it), models that couple strains to the local composition $\eta(\boldsymbol{r})$ have been considered. These f_{tweed} terms include: (i) $\eta(\boldsymbol{r})\varepsilon^2(\boldsymbol{r})$ or spatially local structural transition temperature [35]; (ii) $\eta(\boldsymbol{r})e_1(\boldsymbol{r})$ or local compressional stress [59]; (iii) $[(\Delta_x^2 - \Delta_y^2)\eta(\boldsymbol{r})]\varepsilon(\boldsymbol{r})$ or local deviatoric stress [36]. Simulations with a fixed disorder realization show diagonally oriented tweed-like domains. For model (ii), an infinite anisotropy ($A_1 \to \infty$) yields a spin-glass picture of tweed [7, 35].

If $\eta(\boldsymbol{r})$ is treated like an annealed disorder random variable with distribution $P = \mathrm{e}^{-\eta^2/2\sigma^2}$ in the partition function, then the average of the Boltzmann factor $\mathrm{e}^{-\beta F_{\text{tweed}}}$ for models (i) and (ii) yields just renormalization of the ε^4 or ${e_1}^2$ terms, respectively. However, model (iii) yields the nontrivial term $f_{\text{cross}} \sim -\beta\sigma^2[(\Delta_x^2 - \Delta_y^2)\varepsilon]^2$, that favours crossings/steps in the domain-walls (being nonzero at intersections/corners). Since $\eta(\boldsymbol{r})$ is actually a quenched-disorder random variable, averages must be performed through replicas and the $n \to 0$ trick. Then including only Gaussian replica correlations, we obtain

the effective tweed term $f_{\text{tweed}} = [1 - (T_{\text{tweed}}/T)^2] f_{\text{cross}}$ with an extra temperature factor, that favours tweed only at temperatures $T > T_{\text{tweed}} \sim \sigma$.

2.5 Inhomogeneities in Multiferroic Oxides

High-resolution microscopies on complex oxides have revealed multiscale heterogeneities on scales from hundreds to a few lattice spacings. These include stripes, conducting filaments, superconducting islands and so on [4–6]. Cuprates like LaSrCuO undergo tetragonal to orthorhombic ferroelastic transitions with strain as the primary order parameter, and a Néel transition of the antiferromagnetic (AF) state at lower temperatures. Both structural and AF transition temperatures vary sharply with doping, e.g. substitution of one rare earth element by another of a different valency. The superconducting and pseudogap temperatures show large isotope effects over a range of dopings [60]; and there can be a downward cusp close to 1/8 doping. Angle-resolved photoemission shows lattice signatures [61]. Shape memory effects have been reported [17]. Diffuse X-ray, and neutron scattering show stripes of competing unit-cell structures at nanoscales, and staggered-magnetization domain walls [21, 22]. Scanning tunneling microscopy (STM) in the superconducting state shows a gap magnitude that varies over regions from 1 nm upwards [20]. Remarkably, a uniform magnetic field can couple to mesoscale elastic twin boundaries, and rotate their orientation [18]. Hence it is clear that cuprates can show both *cross-variable* and *cross-scale* response, and are complex multiferroics with strong charge/spin/strain coupling.

Colossal magnetoresistance (CMR) manganites like LaCaMnO show a complex phase diagram as a function of doping, with the transition temperatures between phases showing cusps close to multiples of 1/8 [3, 6]. At high and low dopings, there are AF insulator, and charge/orbital ordered regions. At intermediate dopings there is a ferromagnetic metal region that goes over into a paramagnetic insulator as the temperature is raised, with the Curie and metal–insulator temperatures quite close, and a resistivity peak around these temperatures. The Curie temperature has a strong isotope effect [60]. Theoretical double exchange models link the electron mobilities to orderings of the core level ferromagnetic spins [3]. With resistance changing by orders of magnitude, the "colossal" cross-variable responses include magneto-resistance in a magnetic field $\sim$ T [3]; stresso-resistance under external pressure $\sim$ GPa [13]; nonlinear resistance with switching/memory, under a voltage $\sim$ kV [14]; and photoconductance under laser power $\sim$ mW [62]. In short, here too, there is strong charge/spin/strain coupling and complex multiferroic behaviour.

STM probe studies by Faeth et al. [19] on CMR manganites reveal that the above macroscopic functionalities conceal a hidden nanoworld of spatial variations. Although STM is a surface probe, they found that the integrated STM resistivity versus temperature closely tracks the measured bulk resistivity peak, implying the intrinsic inhomogeneity is not just superficial.

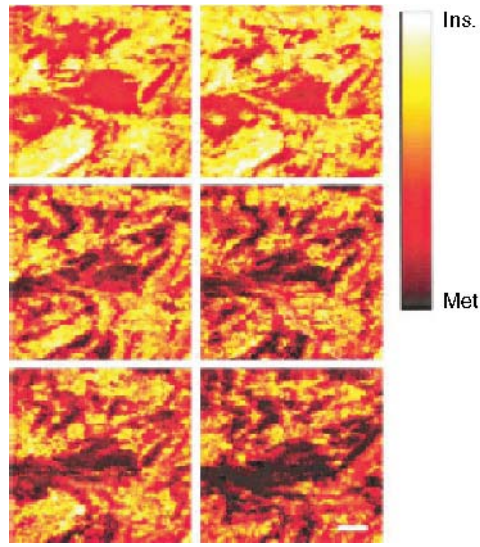

Fig. 2.3. STM picture in coordinate space of manganite local conductance near the ferromagnetic transition [19]. Insulator/metal denoted as light/dark. Panels, reading left to right from the top, show cross-scale responses in meso- and nanoscale texturing, with increasing uniform magnetic field in Tesla: 0, 0.3; 1.0, 3.0; 5.0, 9.0. Scale bar in the lower-most right panel (9 T) is 100 nm

Figure 2.3 shows the local conductance at a few volts. The dark (light) areas are metallic (insulating). The upper left panel shows that the zero field resistivity is already intrinsically inhomogeneous, from nano- to mesoscales. With increasing strength of magnetic field, the meandering high-conductance channels expand, and the resistivity drops: the global CMR is associated with the magnetic field or temperature controlling a *percolative metallicity*, that adaptively coexists with insulating regions [26]. This is a remarkable cross-scale response, as it is uniform fields that produce these nanoscale, "cloud-like" conductance variations [19]. It would be interesting to see how STM images vary with applied uniform voltage, stress, or illumination.

Analogies between manganites and martensites [10] have been noted in lenticular domain-wall texturings; or in their dynamics, with long incubation times, or avalanche-type acoustic emissions; and noise spectroscopy can be a state diagnostic [25, 29, 56, 63]. Multiferroics with a ferroelectric-polarization order parameter have not been emphasized here, but they can also show tweed and twins [32]. Piezoresponse force microscopies have revealed meandering mesoscale channels [64] reminiscent of manganites [19]. Magnetic fields can switch electric polarization in TbMnO ferroelectric manganites [15]. Early work has indicated ferroelectric signatures in cuprates [65] (and there are Level 2 models for pairing based on paraelectric fluctuations [66]).

With the nonlocality already inherent in the anisotropic and unruptured lattice, the viewpoint is that these complex textures are the adaptive responses of nonlinear media to simple *local* couplings of strain to other variables.

2.6 Charge and Spin as Local Stresses and Transition Temperatures

2.6.1 Coupling of Variables

The charges and spins couple in symmetry-allowed ways to strain tensor components. When coupled to linear (or quadratic) powers of strains, they act as local stresses (or local elastic constants). Conversely, when strains are coupled to quadratic powers of the magnetization (whether staggered or direct), then they act as local magnetic transition temperatures (whether Curie or Néel). Compatibility-induced power-law correlations then spread the influences of charge and spin states over large distances, and nonlinearities can mix scales. The magnetization contribution is (with $\xi_{\rm m}$ being the magnetic domain wall width)

$$F_{\rm mag} = g_0 \sum_{\boldsymbol{r}} \left[(T - T_{\rm cm}) m^2 + \frac{1}{2} m^4 \right] + \sum_r \xi_{\rm m}^2 (\boldsymbol{\Delta} m)^2 \,, \tag{2.17}$$

where $g_0 < 1$ is a ratio of magnetic to elastic energy densities. The charge carrier–lattice interaction is in general, a symmetry-allowed coupling to a specific physical strain. For harmonic, isotropic solids, it is often sufficient to write displacement as $\boldsymbol{u}(\boldsymbol{q}) = \hat{u}\, u(\boldsymbol{q})$ where $\hat{u}$ is a polarization direction, and then angular average the coupling to $\langle \alpha(\boldsymbol{q}) \rangle \equiv \alpha$ to get an "electron–phonon" interaction, $-\alpha \sum_{\boldsymbol{q}} n(\boldsymbol{q})\, u(\boldsymbol{q})$. However for anisotropic multiferroics, nonlinearities single out the OP strains; and spins/charges have different symmetry-dictated couplings to the different physical strains, that have unequal elastic constants. It is preferable to remain in the strain representation, and avoid truncations.

A charge state in a directional d-wave orbital can act as a deviatoric stress, while an isotropic "mobile" [67] charge state can act as a compressional stress. To focus on the anisotropy from the compatibility potentials, we consider an s-wave number density $n(|\boldsymbol{r}|) > 0$ of the charge. Ignoring higher order magnetoelastic terms such as $A_{m\varepsilon} m^2 \varepsilon^2$, the charge/spin/strain couplings [39]

$$F_{\rm coupling} = \sum_{\boldsymbol{r}} A_{n1} n e_1 + A_{m1} m^2 e_1 + A_{n\varepsilon} n \varepsilon^2 + A_{nm} n m^2 \tag{2.18}$$

act on strains as local stress "$p_1\, e_1$" terms, or local shifts in the structural transition temperature "$\tau \varepsilon^2$". Note that the m^2 terms can be combined with the $(T - T_{\rm cm}) m^2$ term of (2.17) to define a Curie or Néel *local transition temperature*, enhanced/suppressed essentially by the annealed local strain

$$T'_{\rm cm}(\boldsymbol{r}) \equiv T_{\rm cm} - [A_{m1} e_1(\boldsymbol{r}) + A_{\rm nm} n(\boldsymbol{r})]/g_0 \,. \tag{2.19}$$

The signs of the coupling constants are chosen to mimic some aspects of cuprates and manganites [39]. Thus $A_{m1} > 0$ implies that compression $e_1 < 0$, that brings spins closer, favours magnetization, where m is the direct (staggered) magnetization for manganites (cuprates). Since doping reduces the structural transition temperature, $A_{n\varepsilon} > 0$, and for cuprates $A_{n\varepsilon} \gg 1$. For manganites we take $A_{\rm nm} < 0$ to mimic double exchange, where the presence of a mobile hole favours local ferromagnetism $m(\boldsymbol{r})$ of the core spins. For cuprates, $A_{\rm nm} > 0$, as doping dilutes spins, and in fact strongly suppresses the Néel temperature, $A_{\rm nm} \gg 1$.

2.6.2 Simulations

We use a coupled relaxational dynamics with random initial conditions in strain and magnetization, to find the free energy local minima through

$$\dot{m} = -\partial F/\partial m; \quad \dot{\varepsilon} = -\partial F/\partial \varepsilon\,, \tag{2.20}$$

where we drop $F_{\rm tweed}$ and $F_{\rm surf}$ of Sect. 2.4 for simplicity:

$$F = F(\varepsilon, n, m) = F_{\rm strain} + F_{\rm mag} + F_{\rm coupling}\,. \tag{2.21}$$

The number-densities of the charges are normalized exponentials $\sim \mathrm{e}^{-2r}$, placed randomly, with fixed positions and profiles. It would be interesting to introduce a charge-density (ordering) dynamics, as considered elsewhere [68].

The bare Curie (Néel) transition temperatures are taken to be $T_{\rm cm} = 0$ ($T_{\rm cm} \neq 0$) for manganite (cuprate) parent compounds treated as paramagnets (antiferromagnets). We take [39] $A_1 = 50 = A_3/2$, $\xi_0^2 = \frac{1}{8}$, $\xi_m^2 = \frac{1}{2}$, $T_0 = 1$, $T_{\rm c} = 0.8$, $g_0 = 0.3$, $A_{m1} = +5$. The other, "manganite" parameters are $T_{\rm cm} = 0$, $A_{\rm nm} = -1$, $A_{n1} = +5$, $A_{n\varepsilon} = +2$. The "cuprate" parameters are $T_{\rm cm} = 0.6$, $A_{\rm nm} = +9$, $A_{n1} = -5$, $A_{n\varepsilon} = 20$. This is a regime of globally weak magnetism, relatively strong lattice couplings, and dominant compatibility forces.

Figure 2.4a shows the $e_1(\boldsymbol{r})$ strain of two textured manganite polarons, that are large and floppy, and deform each other [39]. These are multivariable *p*olaronic *e*lasto-*m*agnetic *t*extures or *pemt*ons, and finite-doping textures are multipemton states. Note that although the local stress $A_{n1}n$ has a given sign, compatibility induces quadrupoles, with both signs of strain (compression and expansion). Figure 2.4b shows that $x = 0.15$ produces large $m^2 \neq 0$ magnetization variations at multiple scales, but only in those regions where the temperature is below the strain-induced local transition temperature, $T < T'_{\rm cm}(\boldsymbol{r})$; whereas $m^2 = 0$ in $T > T'_{\rm cm}(\boldsymbol{r})$ regions. The ferromagnetic formation of a symmetry-breaking average $\langle m \rangle \neq 0$ on this (conducting) backbone will also have a percolative character. For cuprates Fig. 2.4c shows a more compact, smaller pemton, while Fig. 2.4d shows stripe-like structural variants for $x = 0.1$. The multipemton strain structure factors $|\varepsilon(\boldsymbol{k})|^2, |e_1(\boldsymbol{k})|^2$ reveal the fourfold symmetry hidden in the apparently disordered coordinate-space

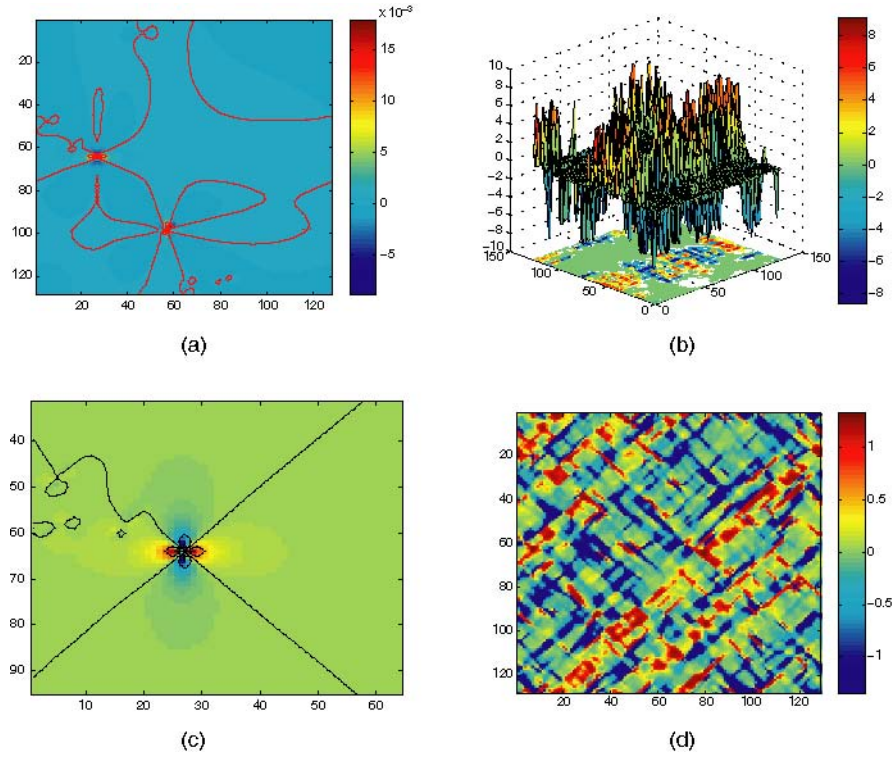

Fig. 2.4. "Manganite" parameters: see text. (**a**) Two charges showing compressional strain of two textured polarons. (**b**) Multipolaron magnetization for random-position doping fraction $x = 0.15$. "Cuprate" parameters: see text. (**c**) Single textured polaron. (**d**) Multipolaron deviatoric strain for doping fraction $x = 0.1$ showing stripe-like texturing

textures [39,42], showing butterfly-shape contours reminiscent of experimental diffuse scattering plots [69].

The application of long-wavelength external magnetic fields and stresses produces delicate short-wavelength "cloud-like" variations [39]. Note that in linear response, e.g. $m(\boldsymbol{q},\omega) = \chi(\boldsymbol{q},\omega)h(\boldsymbol{q},\omega)$, the response wavevector/frequency is the same as that of the applied field, and increasing the field strength merely magnifies the response. However, very different modes can be mixed by the nonlinear free energy strain $\varepsilon^6(\boldsymbol{r},t) \to \prod_{i=1}^{6} \varepsilon(\boldsymbol{q_i},\omega_i)$ and magnetization $m^4(\boldsymbol{r},t) \to \prod_{i=1}^{4} m(\boldsymbol{q_i},\omega_i)$ terms. Hence *cross-scale* responses in length and time are another signature of *nonlinearity* [19,44].

Thus simulations show multivariable, multiscale texturing, with textured single polarons, and stripe or channel-like multipolaronic states. There is one conceptual problem, however. The textures are supposedly from the generic feature that doping does not produce dislocations. But then complex textures

should always be seen – the picture is "too generic"! A further analysis [70] shows that the key response function is the *compliance* describing the strain from local internal stresses, $e_1(\boldsymbol{k}) = \chi_{11}(\boldsymbol{k})\, p_1(\boldsymbol{k})$. It contains the compatibility kernel in the denominator, and has a power-law tail in coordinate space, $\chi_{11}(\boldsymbol{R}) \sim 1/R^d$, beyond an onset length $\xi = \xi_0/\sqrt{A_1}$. Hence if $\xi \gg 1$, the compliance is already negligible before the power-law sets in; while for materials with $\xi \sim 1$ there is power-law behaviour over most of the range. For FePd, we have $\xi = 1.2$.

Although we have emphasized annealed-variable adaptive texturing, it is clear that quenched variables play an important and complementary role. Quenched compositional disorder acting as local stresses at random sites will have nonlocal compliance effects on the strain even at far-off sites, with total random-stress correlations showing APL decays. This could additionally motivate effective random-field, correlated disorder models as studied by Dagotto and coworkers [6]; or nonequilibrium stress-trapping scenarios of inhomogeneities [56].

It would be interesting to extend various Level 2, models for CMR behaviour or cuprate pairing [66, 71] to include Level 1 strain compatibility potentials and annealed-variable/quenched-disorder internal stresses, that induce multivariable heterogeneity. Parameter regimes where electronic states are sensitive to local quenched disorder [72], could be relevant for such strain-induced wavefunction texturing. The inhomogeneous states will have their own electronic and lattice excitations, e.g. domain-wall ripplings ("dyadons") [27].

2.7 Summary and Further Work

Intrinsic heterogeneities in multiferroics are both multivariable and multiscale, and can have cross-variable and cross-scale responses. As noted by Krumhansl, the simultaneous presence of multiple, distinct scales could require novel approaches to materials science that treat Ginzburg–Landau functionals as effective field theories [10]. Although there are different levels of description as in Fig. 2.1, the viewpoint outlined here regards the unit-cell strain tensor as a central factor in multiferroic texturings, that involve three elements: symmetry, compatibility, and nonlinearity.

The *symmetry* of the discrete point group of the unit-cell dictates the series expansion of the strain free energy in allowed invariant combinations of physical strain-tensor components. It also determines allowed local couplings of strain components to other variables like charge density, magnetization, and electric polarization, that can induce strain-driven local variations of (other) multiferroic transition temperatures. *Compatibility* constraints on strain components become effective interaction potentials with (symmetry-specific) sign-varying anisotropies and (dimensional) power-law decays, when some strains are eliminated. And the coupled order-parameter *nonlinearity* that is present over wide temperature ranges supports solitonic domain walls

(elastic or otherwise), that under orienting compatibility potentials, can lock in to complex patterns, as local minima of a multivalley free energy landscape: a multiferroic configurational glass. Further texturing, or a stabilization of inhomogeneous states relative to uniform states, could occur from compositional quenched disorder, that is nonlocally magnified by compatibility effects.

A microscopic treatment of the ideas would clearly be useful. If we integrate out the strains in Gaussian approximation, the effective free energy for the remaining variables in Fourier space $F_{\rm eff} = D_0 \sum_{\boldsymbol{k}} f_{\rm eff}$ is

$$f_{\rm eff} = \left\{ A_{\rm Coul} |n|^2 / k^2 \right\} + \frac{1}{2} \chi_{11} |A_{n1} n + A_{m1} m^2|^2 + \cdots , \tag{2.22}$$

where we have added a charge–charge Coulomb interaction, and have not shown the implicit higher-order in n–n, n–m^2, and m^2–m^2 interactions, from strain nonlinearities. Even for large isotropic Coulomb strength $A_{\rm Coul} \gg (A_{n1}, A_{m1})$, the treatment of correlated electrons [73] could more generally include these qualitatively distinct anisotropic interactions between charges and spins; and the consequent intrinsic inhomogeneities. One might conjecture that whereas Mott and Anderson localizations involve metal-insulator transitions across the system, there is a possibility here of "St Venant localization", i.e. inhomogeneous multipolaronic trapping, that coexists with the metallicity of electrons self-focussed into channels, as they propagate through a nonlinear, anisotropic, elastic medium, with mobility edges in coordinate space.

The emerging viewpoint is speculative and undoubtedly needs modification in detail, but seems worth exploring further. The unifying concept is of annealed order parameters that are adaptively complex in the sense of Krumhansl, whose insights have helped bring conceptual order to so many issues in condensed matter physics and materials science.

Acknowledgements

It is a pleasure to thank A.R. Bishop for fruitful collaborations. Partial support of this work is gratefully acknowledged, by SRS from ICTP, Trieste; and TL, AS from the US Department of Energy.

References

1. E.K.H. Salje: Phase Transformations in Ferroelastic and Coelastic Solids (Cambridge University Press, Cambridge, UK, 1990)
2. Z. Nishiyama: Martensitic Transformations (Academic, New York, 1978)
3. B. Raveau, C.N.R. Rao (Eds.): Colossal Magnetoresistance and Related Properties (World Scientific, Singapore, 1998); A.J. Millis: Nature **392**, 147 (1998)
4. A.R. Bishop, S.R. Shenoy, S. Sridhar (Eds.): Intrinsic Multiscale Structure and Dynamics in Complex Electronic Oxides (World Scientific, Singapore, 2003)

5. A. Bianconi (Ed.): Symmetry and Heterogeneity in High Temperature Superconductors (Plenum, New York, 2004)
6. E. Dagotto (Ed.): Nanoscale Phase Separation and Colossal Magnetoresistance (Springer, Berlin Heidelberg New York, 2003); J. Burgy, A. Moreo, E. Dagotto: Phys. Rev. Lett. **92**, 097202 (2004)
7. Y. Bar-Yam, T. Egami, J. Mustre-de Leon, A.R. Bishop (Eds.): Lattice Effects in High-T_c Superconductors (World Scientific, Singapore, 1992)
8. E.K.H. Salje, A.S. Alexandrov, W.Y. Liang: Polarons and Bipolarons in High T_c Superconductors (Cambridge University Press, Cambridge, UK, 1995)
9. V.K. Wadhawan: Introduction to Ferroic Materials (Gordon and Breach, Amsterdam, 2000)
10. J.A. Krumhansl: Mater. Sci. Forum **327–328**, 1 (2000)
11. E.F. Wassermann, M. Acet: this volume
12. Y. Murakami, D. Shindo, K. Oikawa, R. Kainuma, K. Ishida: Acta Mater. **50**, 2173 (2002); A.N. Bogdanov, A. deSimone, S. Muller, U. Rossler: J. Mag. Magn. Mater. **265**, 204 (2003)
13. H. Huang, T. Palstra, S.W. Cheong, B. Batlogg: Phys. Rev. B **52**, 15046 (1995)
14. S.B. Ogale, V. Talyansky, C.H. Chen, R. Ramesh, R.L. Greene, T. Venkatesan: Phys. Rev. Lett. **77**, 1159 (1996)
15. T. Kimura, T. Goto, N. Shintani, K. Ishizaka, T. Arima, Y. Tokura: Nature **426**, 55 (2003); H. Hur, S. Park, P.A. Sharma, J.S. Ahn, S. Guha, S.-W. Cheong: Nature **429**, 392 (2004)
16. P.H. Hor, L. Gao, R.L. Meng, Z.J. Huang, Y.Q. Wang, K. Forster, J. Vassilious, C.W. Chu, M.K. Wu, J.R. Ashburn, C.J. Torng: Phys. Rev. Lett. **58**, 911 (1987)
17. R. Tiwari, V.K. Wadhawan: Phase Transitions **35**, 47 (1991)
18. A.N. Lavrov, S. Komiya, Y. Ando: Nature **418**, 385 (2002)
19. M. Faeth, S. Friesen, A.A. Menovsky, Y. Tomioka, J. Aarts, J.A. Mydosh: Science **285**, 1540 (1999)
20. K.M. Lang, V. Madhavan, J.E. Hoffman, E.W. Hudson, H. Eisaki, S. Uchida, J.C. Davis: Nature **415**, 412 (2002)
21. A. Bianconi, N.L. Saini, A. Lanzara, M. Missori, T. Rosetti, H. Oyanagi, H. Yamaguchi, K. Oka, T. Ito: Phys. Rev. Lett. **76**, 3412 (1996)
22. J.M. Tranquada, B.J. Sternleich, J.D. Axe, Y. Nakamura, S. Uchida: Nature **375**, 561 (1995)
23. T. Egami: this volume
24. S.J.L. Billinge in [4]; E.S. Bozin, G.H. Kwei, H. Takagi, S.J.L. Billinge: Phys. Rev. Lett. **84**, 5856 (2000)
25. V. Podzorov, B.G. Kim, V. Kiryukhin, M.E. Gershenon, S.-W. Cheong: Phys. Rev. B (Rapid Commun.) **64**, 140406 (2001); V. Hardy, S. Majumdar, S.J. Crowe, M.R. Lees, D.McK. Paul, L. Hervé, A. Maignan, S. Hébert, C. Martin, C. Yaicle, M. Hervieu, B. Raveau: Phys. Rev. B **69**, 020407 (2004)
26. C. Renner, G. Aeppli, B.G. Kim, Y.A. Soh, S.W. Cheong: Nature **416**, 518 (2002)
27. B. Horowitz, G.R. Barsch, J.A. Krumhansl: Phys. Rev. B **43**, 1021 (1991); Phys. Rev. B **36**, 8895 (1987)
28. L.E. Tanner, A.R. Pelton, R. Gronsky: J. de Physique (Paris) Colloque **C4**, 169 (1982); T. Castán, A. Planes, A. Saxena: Phys. Rev. B **67**, 134113 (2003)
29. E. Vives, J. Ortín, L. Mañosa, I. Ràfols, R. Pérez-Magrané, A. Planes: Phys. Rev. Lett. **72**, 1694 (1994); T. Cástan, E. Vives, L. Mañosa, A. Planes, A. Saxena: this volume

30. V.K. Wadhawan: Phys. Rev. B **38**, 8936 (1988)
31. L. Yiping, A. Murthy, G.C. Hadjipayanis, H. Wan: Phys. Rev. B **54**, 3033 (1996)
32. O. Tikhomirov, H. Jiang, J. Levy: Phys. Rev. Lett. **89**, 147601 (2002); S.P. Venkateswaran, M. De Graef: this volume
33. M. Seul, D. Andelman: Science **267**, 476 (1995)
34. M. Baus, R. Lovett: Phys. Rev. Lett. **65**, 1781 (1990); Phys. Rev. A **44**, 1211 (1991)
35. S. Kartha, J.A. Krumhansl, J.P. Sethna, L. Wickham: Phys. Rev. B **52**, 803 (1995)
36. S.R. Shenoy, T. Lookman, A. Saxena, A.R. Bishop: Phys. Rev. B **60**, 12537 (1999)
37. T. Lookman, S.R. Shenoy, K.Ø. Rasmussen, A. Saxena, A.R. Bishop: Phys. Rev. B **67**, 024114 (2003); D.M. Hatch, T. Lookman, A. Saxena, S.R. Shenoy: Phys. Rev. B **68**, 104105 (2003)
38. A. Saxena, T. Lookman, A.R. Bishop and S.R. Shenoy in [4]
39. A.R. Bishop, T. Lookman, A. Saxena, S.R. Shenoy: Europhys. Lett. **63**, 289 (2003); cond-mat/0304198
40. K.Ø. Rasmussen, T. Lookman, A. Saxena, A.R. Bishop, R.C. Albers, S.R. Shenoy: Phys. Rev. Lett. **87**, 055704 (2001)
41. T. Lookman, A. Saxena, A.R. Bishop, S.R. Shenoy: J. Phys. (Paris) Coll. IV **112**, 195 (2003)
42. S.R. Shenoy, T. Lookman, A. Saxena and A.R. Bishop, in [4, 5]
43. P. Chaikin, T. Lubensky: Principles of Condensed Matter Physics. 2nd edn. (Cambridge University Press, Cambridge, UK, 2000)
44. S.N. Behera, A. Khare: Pramana (Bangalore) **15**, 245 (1980); F. Falk: Z. Phys. B **51**, 177 (1983); A. Bussmann-Holder, A.R. Bishop: J. Phys.: Condens. Matter **16**, L313 (2004)
45. S.F. Borg: Fundamentals of Engineering Elasticity, 2nd edn. (World Scientific, Singapore, 1990)
46. B.H. Chirgwin, C. Plumpton: A Course of Mathematics for Scientists and Engineers. Vol. 1, 2nd edn. (Pergamon, London, 1970), p. 321
47. S.R. Shenoy, T. Lookman, A. Saxena: unpublished
48. G.R. Barsch, J.A. Krumhansl: Metallurg. Trans. A **18**, 761 (1988); Proc. ICOMAT-92 (1992) (Monterey Inst. Adv. Stud., Monterey, CA, 1993), p. 53
49. `http://www-gap.dcs.st-and.ac.uk/~history/Mathematicians/Saint-Venant.html`
50. A.E. Jacobs: Phys. Rev. B **61**, 658 (2000)
51. J.M. Ball, R.D. James: Arch. Ration. Mech. Anal. **100**, 13 (1987)
52. R.D. James, Z. Zhang: this volume
53. Y. Wang, A. Khachaturyan: Acta Mater. **45**, 749 (1997)
54. M.F. Thorpe, D.J. Jacobs, M.V. Chubynsky, J.C. Phillips: J. Non-Cryst. Sol. **266–269**, 859 (2000); M. Micoulat, J.C. Phillips: Phys. Rev. B **67**, 104204 (2003); D. Selvanathan, W.J. Bresser, P. Boolchand: Phys. Rev. B **61**, 15061 (2000)
55. J. Zaanen, O. Gunnarsson: Phys. Rev. B **40**, 7391 (1989); S.A. Kivelson, V.J. Emery: Physica C **235**, 189 (1999); F. Kusmartsev: Europhys. Lett. **57**, 567 (2000); D.I. Khomskii, K.I. Kugel: Europhys. Lett. **55**, 208 (2001); M.B. Salomon, P. Lin, S.H. Chun: Phys. Rev. Lett. **88**, 197203 (2002)
56. S.S. Saxena, P.B. Littlewood: Nature **119**, 279 (2001); N. Mathur, P. Littlewood: Phys. Today (Jan.) **56**, 25 (2003)

57. P. Welch, M. Muthukumar: Phys. Rev. Lett. **87**, 218302 (2001); J. Schmalian, P.G. Wolynes: Phys. Rev. Lett. **85**, 836 (2000)
58. A. Saxena, T. Castán, A. Planes, M. Porta, Y. Kishi, T.A. Lograsso, D. Viehland, M. Wuttig, M. De Graef: Phys. Rev. Lett. **92**, 197203 (2004)
59. A. Onuki: J. Phys. Soc. Jpn. **68**, 5 (1999)
60. G.-M. Zhao, K.K. Singh, D.M. Morris: Phys. Rev. B **50**, 4112 (1994); D. Zech, H. Keller, K. Conder, E. Kaldis, E. Liarokapis, N. Poulakis, K.A. Müller: Nature **371**, 681 (1994); D. Rubio-Temprano, J. Mesot, S. Jansen, K. Conder, A. Furrer, H. Mutka, K.A. Müller: Phys. Rev. Lett. **84**, 1990 (2000); G.-M. Zhao, K.A. Müller: Nature **381**, 676 (1996)
61. A. Lanzara, P.V. Bogdanov, X.J. Zhou, S.A. Kellar, D.L. Feng, E.D. Lu, T. Yoshida, H. Eisaki, A. Fujimori, K. Kishia, J.I. Shimayama, T. Hoda, S. Uchida, Z. Hussain, Z.X. Shen: Nature **412**, 510 (2001)
62. M. Fiebig, K. Miyano, Y. Tomioka, Y. Tokura: Science **280**, 1925 (1998); J. Gump, I. Finkler, H. Xia, R. Sooryakumar, W.J. Bresser, P. Boolchand: Phys. Rev. Lett. **92**, 245501 (2004)
63. V. Hardy, A. Maignan, S. Herbert, C. Yaicle, C. Maitin, M. Hervieu, M.R. Lees, G. Rowlands, D.McK. Paul, B. Raveau: Phys. Rev. B **68**, 220402 (2003); V. Podzorov, C.H. Chen, M.E. Gershenon, S.-W. Cheong: Europhys. Lett. **55**, 411 (2001); A.K. Raychaudhuri: Proc. SPIE **5112**, 144 (2003)
64. I.K. Bdikin, V.V. Shvartsman, A.L. Kholkin: Appl. Phys. Lett. **83**, 4232 (2003)
65. D. Mihailovic, A.J. Heeger: Solid State Commun. **75**, 319 (1990); D. Mihailovic, I. Poberaj, A. Mertelj: Phys. Rev. B **48**, 16634 (1993)
66. S.R. Shenoy, V. Subrahmanyam, A.R. Bishop: Phys. Rev. Lett. **79**, 4657 (1997)
67. E.L. Nagaev: Principles of Magnetic Semiconductors, 2nd edn. (Cambridge University Press, Cambridge, UK, 2000)
68. T. Lookman, S.R. Shenoy, G.V. Pai, A. Saxena: unpublished
69. S. Shimomura, N. Wakabayashi, H. Kuwahara, Y. Tokura: Phys. Rev. Lett. **83**, 4389 (1999); I. Vasiliu-Doloc, S. Rosenkranz, R. Osborn, S.K. Sinha, J.W. Lynn, J. Mesot, O.H. Seeck, G. Preosti, A.J. Fedro, J.F. Mitchell: Phys. Rev. Lett. **83**, 4393 (1999); Z. Islam, X. Liu, S.K. Sinha, J.C. Lang, S.C. Moss, D. Haskel, G. Srajer, P. Wochner, D.R. Lee, D.R. Haeffner, U. Welp: cond-mat/0312622; S.K. Sinha: Z. Kristall. **219**, 143 (2004)
70. S.R. Shenoy, G.V. Pai, T. Lookman, A. Saxena: unpublished
71. T.V. Ramakrishnan, H.R. Krishnamurthy, S. Hassan, G.V. Pai: Phys. Rev. Lett. **92**, 157203 (2004)
72. D. Heidarian, N. Trivedi: Phys. Rev. Lett. **93**, 126401 (2004)
73. G. Kotliar, D. Vollhardt: Phys. Today (Mar.) **57**, 53 (2004); M.L. Kulic: Phys. Rep. **338**, 1 (2000)

3

Disorder in Magnetic and Structural Transitions: Pretransitional Phenomena and Kinetics

T. Castán, E. Vives, L. Mañosa, and A. Planes, and A. Saxena

3.1 Introduction

According to standard textbooks on thermodynamics [1], first-order phase transitions occur abruptly at given values of external control parameters such as temperature, pressure or applied field (stress, magnetic or electric). In real materials, however, these transitions rarely show such an ideal behaviour. Commonly, the expected sharp change of the order parameter is smoothed out and thus the transition spreads over a certain range of the external control parameter. Moreover, in a number of systems the transition is even preceded by anomalies, typically detected in the response to certain excitations, which may arise from local symmetry breaking perturbations. Actually, all the anomalies which originate from the tendency of the system to perform anticipatory visits to the low-symmetry phase are related to the so-called pretransitional effects which can be defined as phenomena that announce that the system is preparing for a phase transition before it actually occurs. In what follows, transitions exhibiting the behaviour described above will be denoted *extended* first-order transitions.

Nowadays, it is accepted that the influence of disorder in the form of randomly quenched defects or impurities, almost always present in any solid system, is at the origin of all these deviations with respect to the ideal first-order behaviour. In this sense, there is an emerging point of view in materials physics that disorder, understood in a broad sense (as imperfections, inhomogeneities, point defects, boundaries, etc.), is intrinsic to real materials. In fact, a wide variety of interesting properties in materials have only been understood when considering disorder as something inherent to the system [2]. There are two essential issues that enable us to account for the above-mentioned deviations from the ideal first-order transitions. On one side, the system must sensitively respond to quenched defects by, for instance, giving rise to variations of the effective local transition temperature. On the other side, as already pointed out by Imry and Wortis [3], when the transition starts the growth of the correlations is blocked by defects. More recently, the existence of an associated

disorder induced transition related to the change from a sharp to a smooth transition has been predicted [4]. It is worth noting that in all cases long-range interactions, as arising from surface (or interface) effects through compatibility conditions [5,6], play a fundamental role. They enable a cooperative response of the system to occur in the pretransitional regime by connecting the different perturbed regions. Moreover, they provide the necessary conditions for the transition kinetics to be athermal as opposed to thermally activated [7].

In the present chapter we will discuss and try to establish the general requirements for magnetic and structural materials to show pretransitional effects. Furthermore, the effect of disorder on the transition kinetics will also be analysed. The observed phenomenology will be illustrated with examples for magnetic and non-magnetic materials undergoing martensitic transitions (MTs). In addition, the possibility of simultaneous structural and magnetic precursors will be shown in the case of materials displaying magnetostructural transitions.

3.2 Disorder Distribution

As mentioned earlier, the point of view adopted in this work is that disorder is intrinsic to real materials. Generically, one might characterize the disorder in terms of a distribution such as sketched in Fig. 3.1. Intuitively the effects of the tails can be separated from the center of the disorder distribution as follows: The typical disorder affects the central values and fluctuations of most of the bulk properties, and will be important in determining the properties and kinetics of the transition. The tails of the distribution include non-typical disorder in the sense of non-dominant contributions such as from boundaries and extreme values, and become more relevant for small systems. It is expected that the properties affected by this kind of disorder will be much more sample dependent than in the case of typical disorder. We suggest that pretransitional effects are mainly determined by non-typical disorder. Based on this viewpoint, in this chapter we separately discuss the transition kinetics and pretransitional effects.

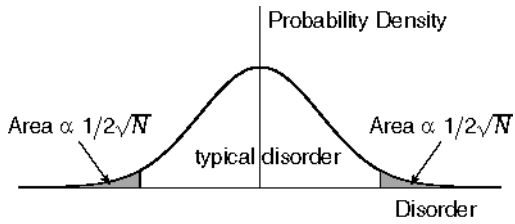

Fig. 3.1. Schematic representation of the disorder distribution in materials. N is the size of the system

3.2.1 Pretransitional Phenomena

Pretransitional effects have been observed in a wide variety of materials. Typical examples include elastic constant and phonon anomalies in High T_c superconductors [8], ferroelectrics [9], manganites [10, 11] and shape memory alloys [12]. In addition, many of these anomalies are associated with precursors such as satellites in diffraction patterns and modulated structures [13–17]. It must be noted that these structures cannot be understood as a coexistence of different phases but rather as a mesoscopic texture within a single thermodynamic phase because variations in the physical properties occur over very small distances (at the nanometer scale) [18]. Here, we shall focus on solids (magnetic and non-magnetic) undergoing MTs and we begin by clarifying what we mean by pretransitional phenomena.

The high temperature phase of most materials undergoing an MT exhibits a cubic bcc-based open structure. This turns out to be of crucial importance in the *pretransitional* behaviour of the material already well above the (martensitic) transition temperature (T_M). Among *pretransitional* effects, we shall call *precursors* those that involve structural changes – either dynamic or/and static – and consequently might influence the way in which the system approaches the incoming MT. To describe pretransitional effects that do not involve structural changes we shall use the term *premonitory*. These originate from the existence of low restoring forces along specific directions related to the symmetry of the high temperature cubic phase. More precisely, in bcc systems to the low resistance against distortions of the $\{110\}$ planes along the $\langle 1\bar{1}0\rangle$ directions which is a signature of the intrinsic instability of the lattice already pointed out by Zener [19] and Friedel [20]. Such a low resistance is reflected by the low energy of the corresponding transverse acoustic phonon branch TA_2 and the low value of the shear elastic constant $C' = (C_{11} - C_{12})/2$. It naturally follows that premonitory effects are inherent to the cubic structure rather than to the MT itself. They are even observed in materials that do not transform martensitically [16]. Nevertheless, they are at the origin of a wide variety of observed precursors and in the case of martensitic materials they participate actively in the structural instability.

3.2.2 Premonitory Behaviour: Temperature Softening

The response of a solid to long wavelength vibrational excitations is given by the elastic constants. A quite general characteristic of bcc materials is the low value of the elastic constant C' compared with other elastic moduli. Often, this is accompanied by a low value of the energy of phonons propagating along the [110] direction with $[1\bar{1}0]$ polarization (i.e. the TA_2 phonon branch) over the entire Brillouin zone. In effect, these two features are a consequence of the open character of the bcc structure which enables easy motion of the $\{110\}$ planes. This incipient mechanical instability provides an easy channel for the MT. On the other hand, the low energy of the overall TA_2 phonon branch

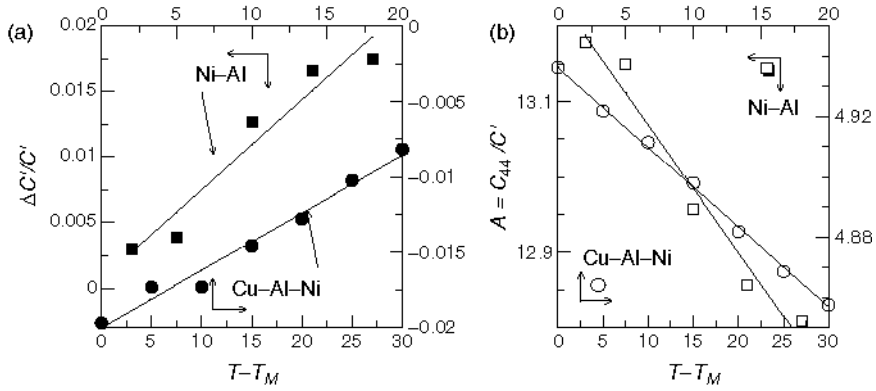

Fig. 3.2. (**a**) Temperature softening of the elastic constant C' in $Ni_{63}Al_{37}$ and $Cu_{2.742}Al_{1.105}Ni_{0.152}$. (**b**) Corresponding behaviour of the elastic anisotropy A. Data from [23, 24]

results in a high vibrational entropy which, from a thermodynamical point of view, is responsible for the stability of the bcc phase [12, 21]. Regarding MT the relevant aspect is the softening of both C' and the TA_2 phonon branch with cooling. In addition, there appears to be an intimate relationship between the value of the elastic anisotropy $A = C_{44}/C'$ and the structural instability in the sense that the value of A at T_M has some degree of universality [12, 22]. Figure 3.2 illustrates the temperature softening of C' (a) for Cu–Al–Ni and Ni–Al crystals and the corresponding increase in the elastic anisotropy A and (b) when approaching the transition T_M from above.

Eventually, certain martensitic materials might exhibit a dip on the TA_2 phonon branch. That is, the phonon branch shows a minimum at a particular value of the wave vector $q \neq 0$. This dip is particularly noticeable when the energy of the whole branch is not very low (although still lower than the other branches). Examples are presented in Fig. 3.3 for Ni–Al, Cu–Al–Be and NiTi(Fe) crystals. In that case, the dip becomes more pronounced when cooling which means that the anomalous phonon(s) soften more than the rest. The origin of this phonon dip anomaly is not intrinsic to the cubic symmetry but is due to the particular shape of the Fermi surface which has nesting features at specific wave vectors [25]. It is worth noting that for alloys, the position of the dip depends on composition [26].

Since at T_M there is no complete softening of any of the phonons (including the elastic limit $q = 0$), it has been suggested that the transition is due to a highly anharmonic coupling between both homogeneous ($q = 0$) and inhomogeneous ($q \neq 0$) distortions [28].

It is worth remarking that the presence of a dip on the TA_2 branch is not a necessary condition for the subsequent MT. Nevertheless, the existence of low energy excitations in the system should affect the actual transformation

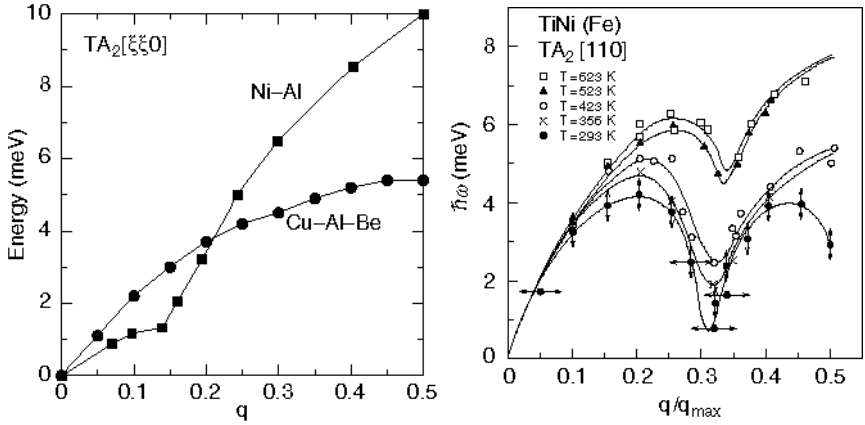

Fig. 3.3. TA_2 phonon branch in $Ni_{0.625}Al_{0.375}$, $Cu_{0.7373}Al_{0.2272}Be_{0.0355}$ and NiTi (Fe). *Right* panel shows the temperature softening of the phonon dip anomaly for NiTi(Fe). Lines are guides to the eyes. Data from [26, 27]

path. In this sense it has been suggested [26] that the wave vector of the dip anomaly is related to the periodicity of the close-packed planes in the martensitic structure. This is, however, an open issue since there are materials for which such stacking periodicity does not seem to be related to the dip anomaly (if there is any significant softening) [12].

3.2.3 Structural Precursors

The signature of the softening behaviour described in Sect. 3.2.2 is seen in the form of diffuse scattering. Actually, the low value of C' will produce strong ridges of thermal diffuse scattering running in the [110] directions [29]. Anisotropic thermal scattering has been observed in electron [17, 30–34], X-ray [35] and neutron [26] diffraction experiments. As an example, we show in Fig. 3.4 the electron diffraction (ED) patterns obtained for Ni–Al and Cu–Zn–Al crystals [33]. It is worth noting that Cu–Zn–Al, which has larger elastic anisotropy (A) [12], exhibits stronger anisotropic diffuse scattering than Ni–Al. In agreement with the ideas exposed above, diffuse scattering is observed in a wide variety of cubic materials with large values of A, independently of whether or not they exhibit a MT at finite temperatures.

In some cases, additionally to the thermal displacement fluctuations mentioned above, there exist static or long-lived fluctuations. As will be stated later, these fluctuations originate from the presence of quenched-in disorder (imperfections, inhomogeneities, etc.) that pin the fluctuations and are at the origin of the so-called tweed precursor strain modulations or simply structural tweed. It is the natural long-range elastic response to local disorder in cubic systems with large elastic anisotropy. Below we shall generalize this concept to other systems with modulations in other physical variables.

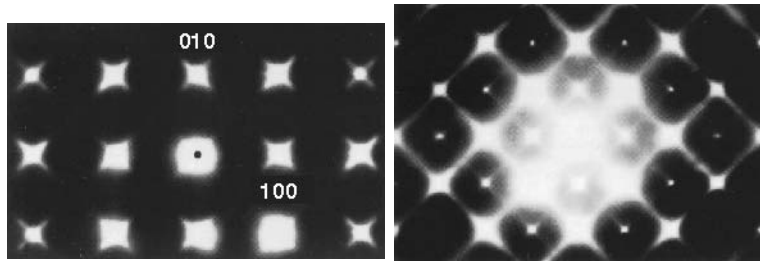

Fig. 3.4. ED pattern of samples with [001] normal of Ni–Al (*left*) and Cu–Zn–Al (*right*). Data from [33]

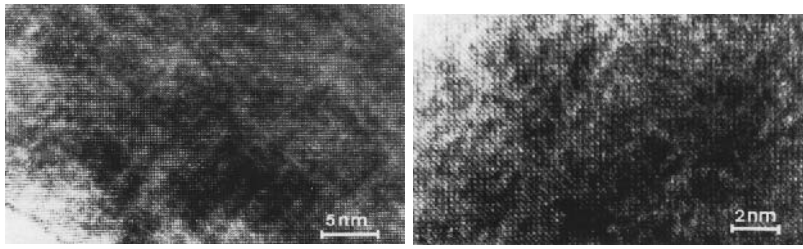

Fig. 3.5. HTEM strain contrast of samples with [001] normal for Ni–Al (*left*) and Cu–Zn–Al (*right*). Data from [33]

The contribution of such static (or long-lived) displacement fluctuations to the diffuse streaking shows up in real space strain contrast TEM images [16,30, 33,36,37]. It consists of a dense array of quasi-periodic striations lying parallel to {110} plane traces giving rise to the tweed pattern which is cross-hatched with correlations along the diagonals. The tweed striations are perpendicular to the [110] diffuse streaking and have been identified to correspond to strain waves of $[110]\langle 1\bar{1}0\rangle$ displacements [16].

It is very interesting to compare the characteristics of tweed in Ni–Al with that observed in Cu–Zn–Al, both shown in Fig. 3.5. We remind that whereas Ni–Al shows a significant dip accompanied with satellites in diffraction experiments, Cu–Zn–Al does not show any significant phonon anomaly but the whole TA_2 branch is very low lying in energy [38]. In both the materials the elastic anisotropy is quite large and the characteristics of the underlying modulation are the same. Nevertheless, whereas in Ni–Al tweed is mostly static, in Cu–Zn–Al the dynamic component is predominant [33]. We suggest this difference is due to a local coupling between the strain and the anomalous phonon in the case of Ni–Al.

For those materials exhibiting a significant dip anomaly one observes elastic scattering at the same wave vector as the phonon softening. This is the central peak reported in neutron scattering experiments and corresponds to the satellites observed in either X-ray [39], or electron [33, 40, 41] or neutron [42]

diffraction patterns. These satellites are broad peaks which indicate that they come from correlations which do not attain true long-range order. Nevertheless, there is an underlying structural modulation, either static or dynamic, whose wavelength is predicted by the dip anomaly and that eventually might correspond to the stacking fault periodicity of the martensitic phase.

3.2.4 Coupling to Magnetism

Recently, magnetic shape memory alloys have received an increasingly high interest because of the possibility of inducing large deformations by application of an external magnetic field. This effect was first discovered in Ni–Mn–Ga [43]. The corresponding phase diagram is shown in Fig. 3.6 as a function of the electron concentration per atom (e/a).

An extensive amount of research has been devoted to finding alternative materials showing magnetic shape memory effect. Among others some examples include Co–Ni–Al, Co–Ni–Ga, Ni–Mn–Al, Fe–Mn–Ga, etc. The pretransitional behaviour of these materials shows specific features which are due to coupling between structural and magnetic degrees of freedom. Although, up to now, experimental data of vibrational properties are only available for Ni_2MnGa, these bcc-based alloys should conform to the general scenario described above: The temperature softening of the TA_2 phonon branch at $q = 0$ and eventually a dip at $q \neq 0$. In the case of Ni–Mn–Ga, a dip anomaly is observed at a value of q which depends on composition [44, 45] as illustrated in Fig. 3.7 for $e/a = 7.56$ (left panel) and $e/a = 7.71$ (right panel) crystals.

Associated with the dip anomaly, structural precursors such as broad satellite peaks are observed. The signature of the coupling to magnetism is primarily observed as an enhancement of the softening of the anomalous phonon (dip)

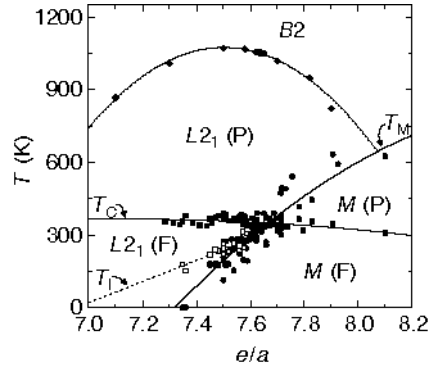

Fig. 3.6. Phase diagram of Ni–Mn–Ga as a function of the electron concentration per atom (e/a). P stands for paramagnetic, F, ferromagnetic and M, for martensitic. The *dotted line* denotes the intermediate transition (T_I), T_M is the martensitic transition and T_C is the Curie line

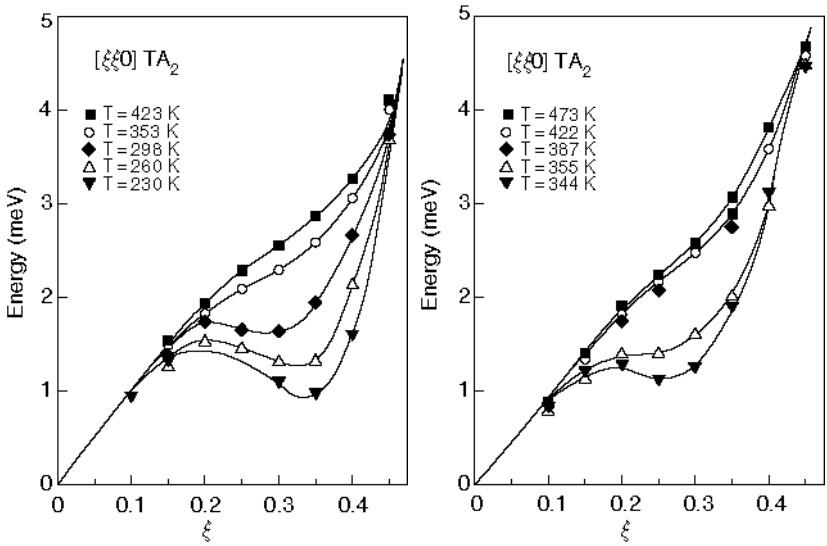

Fig. 3.7. Phonon dip anomaly for $Ni_{52.0}Mn_{23.0}Ga_{25.0}$ (*left*) and $Ni_{50.5}Mn_{29.5}Ga_{20.0}$ (*right*) crystals, which transform, respectively, to different modulated structures. Note the difference in the location of the dip. Lines are guides to the eye. Data from [44]

below the Curie point (T_C) [44,46]. This is shown in Fig. 3.8 for the same samples as before (left panel of Fig. 3.7).

Concerning the long wavelength limit (Fig. 3.8b), apparently, there is no change in the temperature dependence of C' when crossing the Curie point (T_C) [47]. It has been suggested that, in the absence of external magnetic field, the magnetic domain structure below T_C results in an almost zero magnetization and therefore no significant change in the macroscopic elastic response is expected [47]. The magnetoelastic coupling is revealed in this case by an increase of the elastic constants with applied magnetic field [48]. We now focus on a new feature, that is the upturn observed in both the anomalous phonon and in C' at a temperature (T_I) slightly above the MT for the low e/a crystal. This is the signature of a phonon condensation which gives rise to the development of a modulated phase, which in turn is evidenced by the fact that the broad satellites become true Bragg peaks [49]. Such an intermediate phase consists of a micromodulated domain structure without resulting in a macroscopic deformation so that the cubic symmetry is preserved on average. It has been shown that magnetoelastic coupling is responsible for the occurence of such intermediate phase [50] and that the associated phase transition (T_I) is of first order [51,52]. This behaviour is characteristic of multi-stage structural transformations [53]. For the large e/a crystal the phonon condensation (and therefore the intermediate phase) is suppressed by the occurrence of a structural instability which leads (directly) to the low temperature martensitic phase.

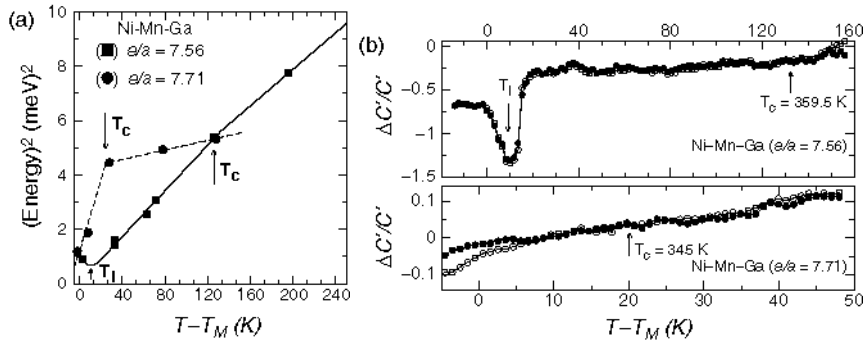

Fig. 3.8. (**a**) Energy of the anomalous phonon (dip) as a function of temperature for two Ni–Mn–Ga crystals. Lines are guides to the eye. Note the change in slope at T_C for the two cases and the upturn for the sample (low e/a) with the intermediate phase transition at T_I. Data from [44]. (**b**) Relative change of shear elastic constant C' as a function of temperature for the same two Ni–Mn–Ga crystals. Data from [47]. Again, note the upturn at T_I in C' for the low e/a crystal

Note the remarkable kink observed in the softening of the anomalous phonon at T_C (see Fig. 3.8a) for the sample with high value of e/a. From Fig. 3.6, it follows that this intermediate modulated phase exists only for low e/a, that is in the region where the MT is far below the Curie point.

3.2.5 Ferroic Precursors: Magnetic and Others

In this section we generalize the tweed concept to other systems than purely structural, and special attention is given to magnetic systems. The starting point is a general framework aimed to understand precursor modulations in the so-called ferroic materials [54], that is, modulations in either strain, or magnetization or polarization observed above the ferroic transition. We remark that since such modulations occur prior to a phase transition one expects the properties of the incoming phase to be affected by the actual initial state of the system.

Recent advances in high resolution imaging of magnetic domain patterns, such as magnetic force microscopy [55] and Lorentz transmission electron microscopy (LTEM) [56], have revealed fascinating modulated magnetic patterns both above and below the Curie temperature in certain magnetic alloys. In contrast to the structural tweed discussed above, the magnetic modulations that occur as precursors to the magnetic transition give rise to a stripe-like pattern. Figure 3.9 shows the magnetic pattern observed by Lorentz microscopy in Co–Ni–Al above the Curie point.

Very recently [58], TEM observations in Co_2NiGa alloys showing both strain and magnetic modulations have been presented, and a model that explains these observations has been proposed. From the observation of the

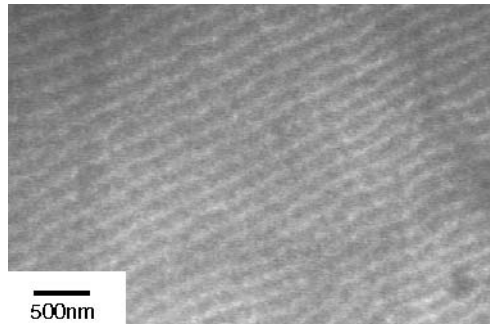

Fig. 3.9. Magnetic tweed-like modulations observed by Lorentz microscopy in $Co_{0.380}Ni_{0.330}Al_{0.290}$ above the Curie point. Data from [57]

magnetic modulations it naturally follows that the tweed concept is not just structural but applicable to a much broader class of materials. In addition, it is shown that, independently of specific details of the pattern or the physical variable involved in modulation, the origin of tweed lies in very general requirements, likely to be fulfiled in quite different systems undergoing phase transitions. For instance, polar (or dielectric) tweed has been observed in ferroelectrics [15, 59]. Extending ideas put forth earlier by other authors in the context of (purely) structural tweed [5, 60], we suggest that the tweed-like modulations above the transition (structural, magnetic or other) are a natural cooperative response in systems that are sensitive (in the sense of, e.g. phonon softening, "susceptibility" or other response functions) to local symmetry breaking perturbations (e.g. due to statistical disorder) assisted by anisotropic long-range interactions. The long-range nature of such interactions (elastic, magnetic or other) connects the different perturbed regions while the anisotropy determines the specific modulations of the resulting pattern. We note that statistical compositional disorder is intrinsic to alloys and therefore they are the most probable candidates to exhibit such phenomena.

The magnetic tweed-like modulations could conceivably arise in two different ways: (1) Purely due to magnetic disorder without any structural degrees of freedom being involved. This can be called *purely magnetic tweed* or simply *magnetic tweed*. It has been observed [57] above the Curie temperature (T_C) in $Co_{0.38}Ni_{0.33}Al_{0.29}$ alloys, see Fig. 3.9. (2) Due to structural or compositional disorder which produces a structural tweed above the structural transition temperature (T_M) in magnetic alloys undergoing a MT. A coupling of strain with magnetism can then lead to a magnetic modulation both above and/or below T_C. This kind of tweed is termed *magnetoelastic tweed*. It has been observed by LTEM in ferromagnetic (Heusler) Ni_2MnGa [61, 62] and Co_2NiGa alloys [63]. By using two-dimensional models on a square lattice it can be shown [58] that *magnetic tweed* patterns are stripe-like whereas *magnetoelastic tweed* produces cross-hatched patterns.

The concept of a structural or a magnetic tweed can be generalized to a "ferroelastic tweed". A "proper" ferroelastic tweed would correspond to strictly the structural tweed [5, 6]. However, magnetic tweed (in magnetic or magnetoelastic materials) and polar tweed in ferroelectrics [15, 59, 64] would correspond to an "improper" ferroelastic tweed because both the disorder and the long-range interaction may arise from a physical variable other than strain, e.g. magnetization or polarization. Improper ferroelastic tweed may also be observable in Jahn–Teller distorted colossal magnetoresistance (CMR) materials, giant magnetoresistance compounds [65], high T_c superconductors [66] and other perovskites with disorder in, for instance, octahedral tilts. The origin of the anisotropic long-range interaction in proper ferroelastic (or structural) tweed is the elastic compatibility constraint [5, 6] whereas polar or magnetic dipole interaction can arise from the crystal surface.

3.3 Transition Kinetics

In the previous sections, we have dealt with the effect of the non-typical disorder in materials undergoing *extended* first-order phase transitions. We now turn our attention to the effect of typical disorder on these transitions. The most evident effect is that, instead of occurring at a given point of the phase diagram, they spread in a certain region of the control parameters. In this region there is a coexistence of the high and low temperature phases. Usually these driving parameters are the temperature or conjugated fields of the order parameters. In practice, distinction between pretransitional effects and the actual transition process is not always evident. We propose, as a general criterion, that significant hysteresis occurs in the transition region, whereas pretransitional effects are almost reversible.

3.3.1 Athermal Transitions

The transitions to be considered are always associated with the existence of high energy barriers, which separate the parent and product phases that must be overcome for the transition to proceed. Figure 3.10 shows schematically a phase diagram for such systems as a function of temperature T and a generic driving field H. We indicate the region of pretransitional effects and the hysteresis region, that typically has a width ΔH (or ΔT). Indeed, in the irreversible region the actual state of the system is metastable and history dependent. It is also worth noting that, although we have plotted a single axis for the field, in multiferroic materials (such as those with two or more coupled ferroic properties, e.g. magnetoelastic materials) there can be more than one different external fields coupled to the relevant order parameters.

The following main characteristics of such *extended* first-order phase transitions must be emphasized:

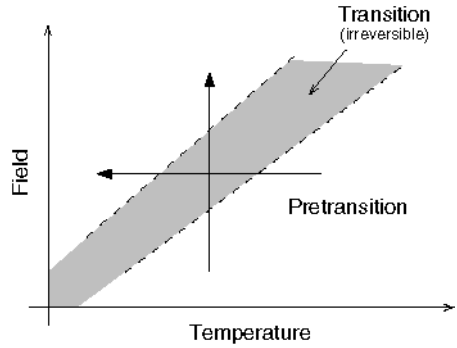

Fig. 3.10. Schematic phase diagram of an *extended* first-order phase transition as a function of the conjugated field and temperature. Pretransional and transitional regions are indicated. *Arrows* denote that the transition can be induced either by cooling or by applying an external field

- The existence of long-range forces of elastic, magnetic or electric nature arising from compatibility conditions (or dipolar forces) associated with the system boundaries and/or interfaces. The external force driving the transition must then compete with the whole system and not only with a small microscopic domain. Thus thermal fluctuations play, in general, only a minor role, which means that the time scale of the thermal activation processes $\tau_{\rm th}$ is very large. This time scale is proportional to $\exp[-E_{\rm b}/k_{\rm B}T]$, where $E_{\rm b}$ is a measure of the free-energy barriers.
- The existence of quenched disorder. In the scenario described in the previous paragraph it is clear that any perturbation that locally modifies the profile of the energy landscape will be crucial for the transitions to proceed. Therefore, as a consequence of quenched disorder the energy barriers are inhomogeneously distributed in the system. This gives rise to the existence of a complex energy landscape with multiple energy minima where almost divergent barriers may coexist with low energy paths. Thus, in this class of transitions quenched disorder of any kind (dislocations, vacancies, composition fluctuations, impurities, etc.) is expected to strongly modify the transition path and the hysteresis features. In many cases disorder cannot be considered strictly quenched, since their characteristics (amount of disorder and spatial distribution) can be modified by cycling through the transition. In this case modification of disorder enables to establish an optimal transition path that avoids high energy barriers which arise from long-range forces. Moreover, in some cases aging effects have been reported (for instance, associated with reordering processes [67]), but on time scales of $\tau_{\rm th}$.
- As a consequence of these complex free-energy landscapes, the intermediate and the final state of the transition exhibit a mesoscopic domain pattern which in some cases displays self-similar properties and a lack

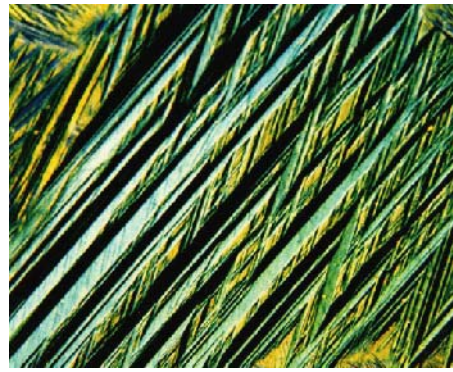

Fig. 3.11. Optical micrograph with polarized light on the surface of a Cu–Al–Zn sample after cooling through MT. Domains corresponding to different martensite variants with many different characteristic lengths coexist

of characteristic scales. An example is presented in Fig. 3.11, that corresponds to the final structure of a MT in a Cu–Zn–Al single crystal. Note the multiple lengthscales of the martensitic domain structure.

- The response of the system to the driving parameter shows, in a broad range of driving rates, avalanche behaviour [68]. Different experimental detection techniques reveal that the evolution of the transition is characterized by burst-like events separated by inactivity periods. Such events correspond to jumps from one metastable state to another involving dissipation of energy. In many cases the properties of the avalanches reveal a lack of characteristic scales within a broad range of time, sizes and energies. Although this makes it difficult to properly define a characteristic time scale associated with the avalanches, the duration of the longest detected avalanche event τ_{av} is typically much smaller than the time scales associated with thermal activation processes τ_{th}.
- The last common feature is the dependence of the hysteresis properties and the avalanche behaviour on the driving rate $\dot{H}$. A convenient way to describe the dependences with the driving rate is by defining a third time scale τ_{dr} which is given by $\Delta H/\dot{H}$. In most cases, when τ_{dr} is much larger than τ_{av}, the avalanche response of the system is essentially deterministic and reproducible (rate independent hysteresis), but in other cases when τ_{dr} and τ_{av} compete, rate dependent hysteresis effects are observed.

These factors may simultaneously exist in MT [69, 70] and in some ferromagnetic systems [71] at low enough temperatures. Interestingly, similar behaviour is also observed in perovskite manganites [72–74]. The dynamics of such transitions have been termed as *athermal*. In practice, this means that the transition driven by a temperature change shows similar kinetic effects as compared to those observed in the transition driven by an external field (applied stress, magnetic field, etc.). These two paths are indicated in Fig. 3.10.

Note that the case of a simple uniaxial ferromagnetic material is a particular case in which the phase transition region in Fig. 3.10 is horizontal and symmetric with respect to the temperature axis. Thus the *athermal* transition can only driven by external (magnetic) field.

3.3.2 Modelling Athermal Transitions

From a more fundamental point of view, *athermal* represents a limiting case in which the time scale of thermal activation τ_{th} is much larger than τ_{av} and τ_{dr}. A first attempt to analyse this situation has been recently considered by Pérez-Reche et al. [7, 70]. The proposed model enables a good understanding of the possible interplay of the three time scales introduced above. However, since the existence of spatial inhomogeneities which arise from disorder are not explicitly included in the model, it only allows for the description of the onset of the transition but it is not appropriate for the study of its subsequent evolution. Therefore, one of the main drawbacks of the model is that it does not provide an explanation for the avalanche behaviour. The approach is based on a mean-first-passage time model [75] which assumes that the energy barrier (associated with the first transforming domain) changes monotonically with the driving field H. The barrier $E_{\mathrm{b}}(H)$ is infinite for $H > H_{\mathrm{h}}$ and vanishes for $H \leq H_{\mathrm{l}}$. Only within this interval $H_{\mathrm{h}} - H_{\mathrm{l}}$ thermal fluctuations can play a role in determining the onset of the transition. Therefore, the transition onset field H_{t} (or transition temperature) is a random variable that must be averaged over different equivalent experimental realizations. From the dependence of the average transition field and its standard deviation on the driving field rate, the fields H_{h} and H_{l} can be estimated.

Within the preceding framework, the ideal *athermal* case corresponds to the limit in which the interval $H_{\mathrm{h}} - H_{\mathrm{l}} \to 0$ not only for the first transforming domain but also for all the subsequent barriers to be overcome. This is equivalent to the assumption that $\tau_{\mathrm{th}} \to \infty$. In this case the detailed response of the order parameter $m(H)$ is time independent and its derivative must satisfy:

$$\frac{\mathrm{d}m}{\mathrm{d}t} = \frac{\mathrm{d}m}{\mathrm{d}H}\,\dot{H}\,. \tag{3.1}$$

Thus, although $\mathrm{d}m/\mathrm{d}t$ may exhibit a dependence on the driving rate, the product $\dot{H}^{-1}\mathrm{d}m/\mathrm{d}t$ must be rate independent. This scaling behaviour can be used to test the validity of the *athermal* hypothesis of a given transition.

Figure 3.12 shows an example of the scaling behaviour corresponding to a first order MT in a Cu–Zn–Al alloy. The dynamics is monitored by detecting the acoustic emission (AE) generated during the transition.

3.3.3 Avalanche Dynamics

As mentioned above, avalanches are typically detected in a broad range of energy, size and time scales. This supported the idea of the existence of criticality in such systems. Experiments for the detection of avalanches are usually

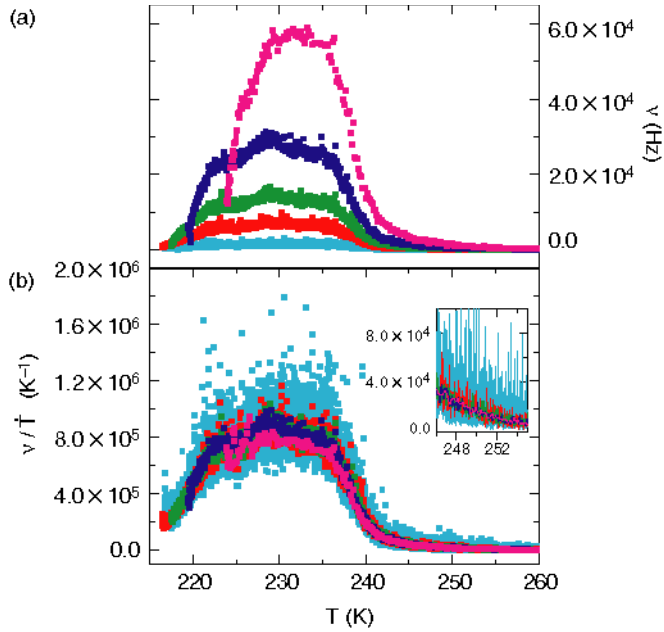

Fig. 3.12. (**a**) Number of AE signals per unit time (ν) as a function of temperature recorded during continuous cooling runs for a Cu–Zn–Al sample at different rates from $\dot{T} = 0.5\,\mathrm{K/min}^{-1}$ (*upper curve*) to $5\,\mathrm{K/min}^{-1}$ (*lower curve*). (**b**) Scaled AE as a function of temperature. Inset shows an enlarged view of the tail region

performed on systems which exhibit a strong *athermal* character. In this case, avalanches only occur when the system is driven by the control field. If the field is kept constant no response is observed. However, in some cases avalanches have been detected at constant field and temperature as a function of time. In these cases, the systems are sufficiently close to the athermal limit so that avalanches can still be discriminated by an experimental threshold, although thermal fluctuations cannot be ruled out. An example is presented in Fig. 3.13 (isothermal transformation in Cu–Al–Ni). This discussion suggests that, in practice, the *athermal* character of a system depends not only on its intrinsic features but also on the resolution of the experimental technique being used and the range of driving rates that are experimentally accessible. The experimental analysis of the avalanche properties has been performed by means of several techniques which enable its study at different scales. These include AE for the detection of the elastic waves associated with the avalanches in MT, Barkhausen noise recordings in magnetic systems, calorimetry, or even direct imaging methods that allow an analysis of the spatial scales of the avalanches. The statistical distributions of avalanche size, duration, energy, etc. are commonly described in terms of the following probability distribution with two free parameters,

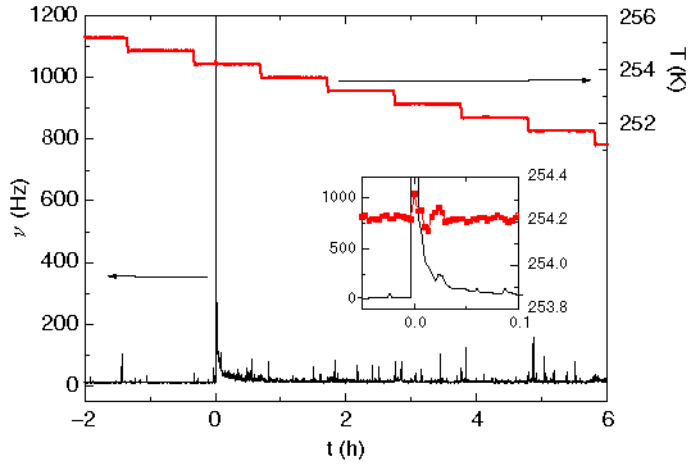

Fig. 3.13. Number of AE signals per unit time (ν) as a function of time for MT of a Cu–Al–Ni sample recorded during stepwise cooling. Inset shows a detailed view of AE recorded isothermally

$$p(Z) = \frac{\mathrm{e}^{-\lambda Z} Z^{-x}}{\int_{Z_{\min}}^{Z_{\max}} \mathrm{e}^{-\lambda Z} Z^{-x} \mathrm{d}Z} \,, \tag{3.2}$$

where $Z_{\min}$ and $Z_{\max}$ are the minimum and maximum experimentally detectable values of the magnitude Z, x is a characteristic power-law exponent and λ determines the exponential correction to the power-law behaviour. When $|\lambda|$ is much smaller than $Z_{\max}^{-1}$, the exponential correction can be neglected and the system is assumed to exhibit critical behaviour. When this is not the case, for $\lambda > 0$ the system is called subcritical while for $\lambda < 0$ it is called supercritical. Figure 3.14 shows an example of the distribution of the amplitudes of AE avalanches during the MT in a Ni–Mn–Ga alloy. It has been shown that the distribution of avalanches in structural [76] and magnetostructural [77] transitions exhibits a dependence on cycling. The first transition after proper annealing of the sample at high enough temperature usually exhibits a clearly non-critical distribution of avalanches (supercritical or subcritical). The effect of a subsequent cycling is to modify the value of $|\lambda|$ until a stable critical distribution is reached with well-defined values of the exponents. In MT this has been related to the increase of the density of dislocations which in turn results in an increase of favourable nucleation centers for the transition.

For Barkhausen noise in magnetic systems and AE in MT, different universality classes have been proposed that are characterized by sets of critical exponents. Nevertheless, dependences on temperature [78] and driving rate [79, 80] have also been reported. Thus, whether the exponents are really universal or not is still a question under debate.

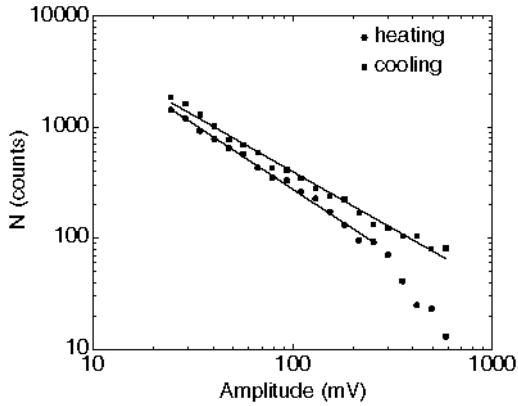

Fig. 3.14. Distribution of AE avalanches during MT in a Ni–Mn–Ga alloy. *Lines* are fits to the distribution (3.2)

3.3.4 Modelling Avalanches

The prototypical model for understanding avalanche behaviour in first-order athermal phase transitions is the Random Field Ising Model with $T = 0$ metastable dynamics [4]. This is a lattice model with spin variables S_i (which can represent domains or small regions of the material) localized on each lattice site and coupled ferromagnetically. Quenched Gaussian random fields with zero mean and standard deviation σ are defined on each site. They represent the effect of compositional and morphological disorder. The model is subjected to an external field. When the system is driven by very high values of the field H, the saturated state with all $S_i = +1$ evolves following a deterministic dynamics consisting of a local energy relaxation of single spins. Once a spin flips, this may trigger the flip of neighbouring spins and initiate an avalanche. During avalanches the driving field is kept constant until a new metastable situation is reached. This kinetics, which has also been called adiabatic, conveniently mimics athermal dynamics in real systems and corresponds to a situation of rate independent hysteresis in which τ_{av} is much smaller than τ_{dr} and τ_{th}.

By numerical simulations one obtains hysteresis loops consisting of a sequence of avalanches joining metastable states. These avalanches are in general microscopic which means that in the thermodynamic limit, the associated jumps involve the transformation of a vanishingly small fraction of the system. Interestingly, the loops exhibit a transition from being smooth when $\sigma > \sigma_{\mathrm{c}}$ to showing a ferromagnetic macroscopic discontinuity when $\sigma < \sigma_{\mathrm{c}}$. At σ_{c} the distribution of avalanches is critical and can be characterized by a well defined exponent.

Other similar models including random bonds, random anisotropy, vacancies, etc. have also been studied. They all display similar behaviour and it

has been shown that the critical exponents exhibit a high degree of universality [81].

These models reveal that, indeed, the existence of disorder is one of the key ingredients in the scenario described in the previous sections. Nevertheless, we note that they do not take into account the existence of long-range interactions arising from compatibility conditions which are essential to understand the formation of multidomain structures. Moreover, one may speculate that long-range forces are also responsible for the observed *learning* process during cycling in which the system seeks an optimal path connecting the high and low-symmetry phases which avoid high energy barriers. After the learning period, a stationary state for which the transition is reproducible from cycle to cycle should be reached. This state should be determined by a compromise between the increase of energy associated with the increase of disorder and the corresponding reduction of metastability (which supposes a reduction of dissipated energy). The tendency of the distribution of avalanches to become critical after a certain number of cycles supports that learning is induced by long-range interactions.

Recently, a more realistic approach to modelling avalanches in MT has been undertaken by Ananthakrishna and collaborators [82]. They proposed a model based on a free energy functional which includes an effective long-range term that describes the transformation induced strain–strain interaction and an inhomogeneous stress field (Gaussian distributed) adequate to mimic the nucleation of martensitic domains in the vicinity of defect sites. Dissipation is accounted for by means of a Rayleigh dissipative functional. While elastic compatibility is, for the sake of simplicity, not properly taken into account, the model has the ability of reproducing most of the dynamical signatures typical of MT in shape memory alloys including the athermal character. The model generates dynamical disorder during the transformation which occurs through energy bursts which in turn are identified with AE signals. These bursts are correlated with the growth and shrinkage of martensitic plates. In agreement with the experiments, they obtained that size and duration of AE bursts follow power-law statistics with exponents comparable to those reported for Cu-based alloys. An interesting result of the model relates the evolution of the martensitic morphology with thermal cycling during a certain training period [83]. After this initial number of cycles the model exhibits repetitive bursts of energy under successive cycles. This cycling evolution, which is in agreement with cycling experiments [76], is shown to be mediated through strain–strain long-range interactions. The authors concluded that during the training period the long-range term has a tendency to smooth out higher energy barriers in the free energy landscape which induces a transformation pathway along a unique set of low energy metastable configurations.

3.4 Conclusion

A vast majority of functional materials invariably have some form of disorder which crucially affects their properties. In particular, disorder extends the region of the first-order transition. Disorder typically has a distribution sketched in Fig. 3.1. The central part of the distribution impacts the kinetics of the transition such as the athermal nature and avalanche behaviour of AE in MT. In contrast, the tails of the distribution are responsible for pretransitional effects, including prescursor modulations, taking advantage of the premonitory softening behaviour. We illustrated these points in both purely elastic shape memory alloys (Ni–Al, NiTi, Cu–Al–Ni, Cu–Zn–Al and Cu–Al–Be) and magnetoelastic alloys (Ni–Mn–Ga, Co–Ni–Ga). The coupling of structure to magnetism enhances the softening of the anomalous phonon below the Curie point and may also lead to a magnetoelastic tweed. In some alloys (e.g. Co–Ni–Al) a purely magnetic modulation (i.e. magnetic tweed) can be present above the Curie temperature. Thus, the notion of tweed appears to be very generic and the tweed can exist in such diverse materials as ferroelectrics, CMR manganites and high-temperature superconductors. We pointed out the common ingredients in these materials that are responsible for tweed. These materials are sensitive to local symmetry breaking perturbations (i.e. disorder). Therefore, various tweed patterns are stabilized by anisotropic long-range interactions which may arise from elastic compatibility constraints and from the surface of the crystal. We emphasized the athermal nature of the transition in some of these materials and discussed the main characteristics including complex free energy landscapes due to the presence of quenched disorder and the dependence of hysteresis as well as avalanche behaviour on the driving rate (of an external field). We also outlined a simple model for understanding the avalanches. This chapter represents an attempt to unify some disorder related concepts in ferroic materials but clearly many questions remain open in this field.

Acknowledgements

We are grateful to the members of our group, Xavier Illa, Jordi Marcos, Francisco-José Pérez-Reche, Marcel Porta and Carlos Triguero, who actively participated in obtaining some of the results presented in this chapter. We also thank our colleagues M. Acet (Duisburg University), M. Morin (INSA – Lyon), M. Stipcich (IFIMAT – Tandil) and C. Stassis and J. Zarestky (Ames Laboratory) for valuable discussions. This work was supported by Spanish CICYT (MAT2001-3251), Catalan DURSI (2001SGR00066) and in part by the US Department of Energy.

References

1. H.B. Callen: Thermodynamics and an Introduction to Thermostatics, 2nd edn. (John Wiley & Sons, New York, 1985), pp. 215–244
2. A.J. Millis: Solid State Commun. **126**, 3 (2003)
3. J. Imry, M. Wortis: Phys. Rev. B **19**, 3580 (1979)
4. J.P. Sethna, K. Dahmen, S. Kartha, J.A. Krumhansl, B.W. Roberts, J.D. Shore: Phys. Rev. Lett. **70**, 3347 (1993)
5. S. Kartha, J.A. Krumhansl, J.P. Sethna, L.K. Wickham: Phys. Rev. B **52**, 803 (1995); and references therein
6. S.R. Shenoy, T. Lookman, A. Saxena, A.R. Bishop: Phys. Rev. B **60**, R12537 (1999); T. Lookman, S.R. Shenoy, K.Ø. Rasmussen, A. Saxena, A.R. Bishop: Phys. Rev. B **67**, 024114 (2003)
7. F.J. Pérez-Reche, E. Vives, L. Mañosa, A. Planes: Phys. Rev. Lett. **87**, 195701 (2001)
8. R.J. McQueeney, Y. Petrov, T. Egami, G. Shirane, Y. Endoh: Phys. Rev. Lett. **82**, 628 (1999)
9. G. Shirane, Y. Yamada: Phys. Rev. **177**, 858 (1969)
10. D. Louca, T. Egami, E.L. Brosha, H. Röder, A.R. Bishop: Phys. Rev. B **56**, R8475 (1997)
11. W. Reichardt, M. Braden: Physica B **263–264**, 416 (1999)
12. A. Planes, L. Mañosa: Solid State Phys. **88**, 159 (2001); and references therein
13. Z. Jincang, L. Lihua, D. Cheng, L. Jianqi, C. Hong, L. Xigui, C. Guosheng: Phys. Rev. B **65**, 54513 (2002)
14. J.M. Tranquada, B.J. Sternlieb, J.D. Axe, Y. Nakamura, S. Uchida: Nature **375**, 561 (1995)
15. X. Meng, K.Z. Baba-Kishi, G.K.H. Pang, H.L. Chang, C.L. Choy, H.S. Luo: Phil. Mag. Lett. **84**, 191 (2004)
16. L. Tanner: Phil. Mag. **14**, 111 (1966)
17. S.M. Shapiro, J.Z. Larese, Y. Noda, S.C. Moss, L.E. Tanner: Phys. Rev. Lett. **57**, 3199 (1986)
18. N. Mathur, P. Littlewood: Nature Mater. **3**, 207 (2004)
19. C. Zener: Phys. Rev. **71**, 846 (1947)
20. J. Friedel: J. Phys. (Paris) Lett. **35**, L59 (1974)
21. W. Petry: J. Phys. IV **5**, C2 (1995)
22. G. Mazzolai, A. Biscarini, B. Coluzzi, F.M. Mazzolai, A.R. Ross, T.A. Lograsso: Mater. Sci. Eng. A **370**, 497 (2004)
23. L. Mañosa, M. Jurado, A. Planes, J. Zarestky, T. Lograsso, C. Stassis: Phys. Rev. B **49**, 9969 (1994)
24. T. Davenport, L. Zhou, J. Trivisono: Phys. Rev. B **59**, 3421 (1999)
25. G.L. Zhao, B.N. Harmon: Phys. Rev. B **45**, 2818 (1992); Phys. Rev. B **48**, 2031 (1993)
26. S.M. Shapiro, B.X. Yang, Y. Noda, L.E. Tanner, D. Schryvers: Phys. Rev. B **44**, 9301 (1991)
27. L. Mañosa, J. Zarestky, T. Lograsso, D.W. Delaney, C. Stassis: Phys. Rev. B **48**, 15708 (1993)
28. P.-A. Lingård, O.G. Mouritsen: Phys. Rev. Lett. **57**, 2458 (1986); Y.-Y. Ye, Y. Chen, K.-M. Ho, B.N. Harmon, P.-A. Lindgård: Phys. Rev. Lett. **58**, 1769 (1987)

29. B.E. Warren: X-Ray Diffraction (Dover Publications, New York 1990) p. 174
30. I.M. Robertson, C.M. Wayman: Phil. Mag. **48**, 421 (1983); Phil. Mag. **48**, 443 (1983); Phil. Mag. **48**, 629 (1983)
31. S. Muto, S. Takeda, R. Oshima: J. Appl. Phys. **27**, L1387 (1988)
32. L.E. Tanner, A.R. Pelton, R. Gronsky: J. Phys. **12**, C4 (1982)
33. G. Van Tendeloo, M. Chandrasekaran, F.C. Lovey: Proceedings of the International Conference on Martensitic Transformations (The Japan Institute of Metals, Sendai, 1986), p. 868
34. V.A. Chernenko, C. Seguí, E. Cesari, J. Pons, V.V. Kokorin: Phys. Rev. B **57**, 2659 (1998)
35. H. Seto, Y. Noda, Y. Yamada: J. Phys. Soc. **59**, 978 (1990)
36. E. Cesari, V.A. Chernenko, V.V. Kokorin, J. Pons, C. Seguí: Acta Mater. **45**, 999 (1997)
37. R. Kainuma, H. Nakano, K. Ishida: Metall. Mater. Trans. **27A**, 4153 (1996)
38. This is a quite general characteristic in Cu-based shape memory alloys. See for instance [12] for a discussion
39. G. Fritsch, V.V. Kokorin, A. Kempf: J. Phys.: Condens. Matter **6**, L107 (1994)
40. A. Zheludev, S.M. Shapiro, P. Wochner, M. Schwartz, M. Wall, L.E. Tanner: J. Phys. IV **5**, C8 (1995)
41. K. Tsuchiya, A. Tsutsumi, H. Nakayama, S. Ishida, H. Ohtsuka, M. Umemoto: J. Phys. IV **112**, 907 (2003)
42. S.M. Shapiro, B.X. Yang, G. Shirane, Y. Noda, L.E. Tanner: Phys. Rev. Lett. **62**, 1298 (1989)
43. K. Ullakko, J.K. Huang, C. Kantner, R.C. O'Handley, V.V. Kokorin: Appl. Phys. Lett. **69**, 1966 (1996)
44. L. Mañosa, A. Planes, J. Zarestky, T. Lograsso, D.L. Schlagel, C. Stassis: Phys. Rev. B **64**, 24305 (2001)
45. U. Stuhr, P. Vorderwisch, V.V. Kokorin: J. Phys.: Condens. Matter **12**, 7541 (2000)
46. U. Stuhr, P. Vorderwisch, V.V. Kokorin, P.A. Lindgård: Phys. Rev. B **56**, 14360 (1997)
47. M. Stipcich, L. Mañosa, A. Planes, M. Morin, J. Zarestky, T. Lograsso, C. Stassis: Phys. Rev. B **70**, 054115 (2004)
48. A. Gonzàlez-Comas, E. Obradó, L. Mañosa, A. Planes, V.A. Chernenko, B.J. Hattink, A. Labarta: Phys. Rev. B **60**, 7085 (1999)
49. A. Zheludev, S.M. Shapiro, P. Wochner, L.E. Tanner: Phys. Rev. B **54**, 15045 (1996)
50. T. Castán, E. Vives, P.A. Lindgård: Phys. Rev. B **60**, 7071 (1999)
51. L. Mañosa, A. Gonzàlez-Comas, E. Obradó, A. Planes, V.A. Chernenko, V.V. Kokorin, E. Cesari: Phys. Rev. B **55**, 11068 (1997)
52. A. Planes, E. Obradó, A. Gonzàlez-Comas, L. Mañosa: Phys. Rev. Lett. **79**, 3926 (1997)
53. T. Castán, A. Planes, A. Saxena: Phys. Rev. B **67**, 134113 (2003)
54. V.K. Wadhawan. Introduction to Ferroic Materials (Gordon & Breach, UK, 2000)
55. R.D. Gomez. Experimental Methods in the Physical Sciences. Ed. by M. De Graef, Y. Zhu, Vol. 36 (2001), p. 69
56. M. De Graef. Experimental Methods in the Physical Sciences. Ed. by M. De Graef, Y. Zhu, Vol. 36 (2001), p. 27

57. Y. Murakami, D. Shindo, K. Oikawa, R. Kainuma, K. Ishida: Acta Mater. **50**, 2173 (2002)
58. A. Saxena, T. Castán, A. Planes, M. Porta, Y. Kishi, T.A. Lograsso, D. Viehland, M. Wuttig, M. De Graef: Phys. Rev. Lett. **92**, 197203 (2004)
59. Z. Xu, M.C. Kim, J.F. Li, D. Viehland: Phil. Mag. A **74**, 395 (1996)
60. S. Kartha, T. Castán, J.A. Krumhansl, J.P. Sethna: Phys. Rev. Lett. **67**, 3630 (1991)
61. H.S. Park, Y. Murakami, D. Shindo, V.A. Chernenko, T. Kanomata: Appl. Phys. Lett. **83**, 3752 (2003)
62. M. De Graef, Y. Kishi, Y. Zhu, M. Wuttig: J. Phys. IV (Fr.) **112**, 993 (2003)
63. Y. Kishi, M. De Graef, C. Craciunescu, T.A. Lograsso, D.A. Neumann, M. Wutting: J. Phys. IV (Fr.) **112**, 1021 (2003)
64. O. Tikhomirov, H. Jiang, J. Levy: Phys. Rev. Lett. **89**, 147601 (2002)
65. L. Yiping, A. Murthy, G.C. Hadjipanayis, H. Wan: Phys. Rev. B **54**, 3033 (1996)
66. S. Sergeenkov, M. Ausloos: Phys. Rev. B **52**, 3614 (1995)
67. M.M. Reyhani, P.G. McCornick: Scr. Metall. **21**, 549 (1987)
68. J.P. Sethna, K.A. Dahmen, C.R. Myers: Nature **410**, 242 (2001)
69. W. Cao, J.A. Krumhansl, R.J. Gooding: Phys. Rev. B **41**, 11319 (1990); M. Rao, S. Sengupta: Phys. Rev. Lett. **78**, 2168 (1997)
70. A. Planes, F.J. Pérez-Reche, E. Vives, L. Mañosa: Scr. Mater. **50**, 181 (2004)
71. G. Bertotti: Hysteresis in Magnetism (Academic Press, San Diego, 1998)
72. V. Hardy, S. Majumdar, S.J. Crowe, M.R. Lees, D.M. Paul, L. Hervé, A. Maignan, S. Hébert, C. Martin, C. Yaicle, M. Hervieu, B. Raveau: Phys. Rev. B **69**, 20407(R) (2004)
73. E. Dagotto, J. Burgy, A. Moreo: Solid State Commun. **126**, 9 (2003)
74. K.H. Ahn, T. Lookman, A.R. Bishop: Nature **428**, 401 (2004)
75. M.C. Mahato, S.R. Shenoy: J. Stat. Phys. **73**, 123 (1993)
76. F.J. Pérez-Reche, M. Stipcich, E. Vives, L. Mañosa, A. Planes, M. Morin: Phys. Rev. B **69**, 064101 (2004)
77. F. Casanova, A. Labarta, X. Batlle, E. Vives, J. Marcos, L. Mañosa, A. Planes, Eur. Phys. J. B **40**, 427 (2004)
78. E. Puppin: J. Phys.: Condens. Matter **16**, 1183 (2004)
79. G. Bertotti, G. Durin, A. Magni: J. Appl. Phys. **75**, 5490 (1994)
80. F. Pérez-Reche, B. Tadić, L. Mañosa, A. Planes, E. Vives: Phys. Rev. Lett. **93**, 195701 (2004)
81. K.A. Dahmen, J.P. Sethna: Phys. Rev. B **53**, 14874 (1996)
82. R. Ahluwalia, G. Ananthakrishna: Phys. Rev. Lett. **86**, 4076 (2001)
83. S. Sreekala, G. Ananthakrshna: Phys. Rev. Lett. **90**, 135501 (2003)

4

Huge Magnetoresistance in Association with Strong Magnetoelastic Effects

L. Morellon and M.R. Ibarra

There exists a broad phenomenology in solid state physics in which the interplay of interactions of different nature may be changed and controlled by external parameters such as temperature, magnetic field, and hydrostatic/chemical pressure. In some cases, this results in the modification of a delicate energetic balance in the system and, as a consequence, a phase transition or transformation can occur. In this review, we report significant magnetoresistance associated with strong magnetoelastic effects, as observed in intermetallic and magnetic oxide compounds.

4.1 Introduction

Functional materials with a strong coupling between structural, magnetic, and electronic degrees of freedom are of prime interest nowadays because many different physical properties of both fundamental and applied interest, such as the magnetocaloric effect, magnetostriction, and magnetoresistance [1–5], are maximized. All the relevant phenomenology, which usually takes place in the vicinity of phase transitions, typically of first order, occurs in these systems upon changing external thermodynamic parameters, e.g., magnetic field, temperature, or hydrostatic pressure. For a general review on the recent advances and future directions in magnetic materials, the excellent review by Jiles [6] is recommended. In this contribution we focus on systems where an applied magnetic field brings about simultaneously a strong change in both the length of the sample (magnetostriction) and in the electrical resistivity (magnetoresistance). We present relevant examples of different materials exhibiting this distinct feature and the physical scenarios underlying the observed phenomenology will be described and discussed. Briefly, the most outstanding prototypes are systems undergoing one or more of the following phase transitions as a function of temperature:

- Magnetic–crystallographic transformations
- Moment instabilities and spin fluctuations
- Metal–insulator transitions
- Charge/orbital instabilities.

4.2 Magnetic–Crystallographic Transformations

4.2.1 $Gd_5(Si_xGe_{1-x})_4$

$Gd_5(Si_xGe_{1-x})_4$ is a unique family of intermetallic materials where many interesting properties and intriguing behavior have been recently discovered [7]. The unprecedented giant magnetocaloric effect [8–10], strong magnetoelastic effects [11, 12], and giant magnetoresistance [13–15] can be highlighted as the most relevant. This phenomenology has been associated with an intrinsically layered crystallographic structure combined with a magnetic–martensitic first-order phase transformation [16]. The coupled magnetic–crystallographic transition can be induced reversibly by the change of external parameters such as temperature, magnetic field, or applied pressure, and therefore, these alloys are attractive for their potential applications in magnetic refrigeration and/or as magnetic sensors and actuators [17].

Three extended solid solution regions exist in the temperature–composition (T–x) phase diagram [18,19]: the Si-rich solid solution, $0.575 \leq x \leq 1$, has the orthorhombic Gd_5Si_4-type structure [O(I)]; the intermediate phase $0.4 < x \leq 0.503$ has a room temperature monoclinic (M) structure; and the Ge-rich region, $0 < x \leq 0.3$ crystallizes in the Gd_5Ge_4-type orthorhombic structure [O(II)]. All three structures are composed of identical two-dimensional (2D) subnanometer-thick layers (slabs) interconnected via partially covalent interslab X–X bonds (X = Si, Ge). In the O(I) structure, all the slabs are interconnected by X–X bonds; half of these bonds are broken in the M structure and none remain in the O(II) structure. The magnetic–crystallographic transition involves breaking/reforming specific covalent X–X bonds [16] and the low-temperature ground state for all compositions $0 < x \leq 1$ is always ferromagnetic (FM) with all the slabs being interconnected, i.e., with the O(I) structure. The M structure is always paramagnetic (PM) whereas the O(II) can support either PM or antiferromagnetism (AFM) [12, 19]. The magnetic behavior of the $R_5(Si_xGe_{1-x})_4$ compounds can be understood qualitatively in terms of competition between intralayer (within the 2D slabs, conventional indirect $4f$–$4f$ RKKY) and interlayer exchange interactions (between slabs, direct Gd–Si/Ge–Gd superexchange propagated via the X–X bonds) [7, 20].

As an example we selected a Ge-rich alloy, $Gd_5(Si_{0.1}Ge_{0.9})_4$. This compound shows upon cooling a second-order transition to the AFM state at $T_N = 127\,K$ without changing the room-temperature O(II) structure, followed by a first-order magnetostructural transition O(II)[AFM] $\rightarrow$ O(I)[FM] at $T_C = 81\,K$. As seen in Fig. 4.1 the low-temperature O(I)[FM] state has a lower resistivity, $\Delta\rho/\rho \approx 50\%$, and a larger length, $\Delta l/l \approx 0.16\%$ (along the particular direction represented in Fig. 4.1, a decrease as large as 1.6% being expected along the a direction [12]). Applying a magnetic field at $T > T_C$ induces a first-order transition into the O(I)[FM] state (Fig. 4.2) and, therefore, large magnetovolume and giant magnetoresistance effects [14] are expected as can be clearly seen in Fig. 4.3 at selected temperatures.

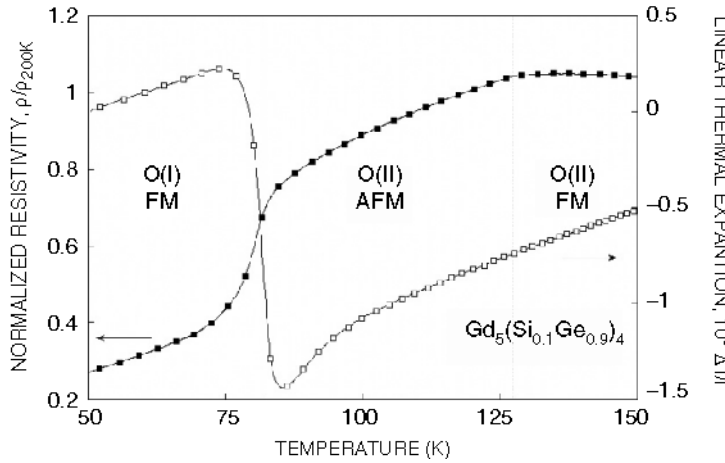

Fig. 4.1. Zero-field electrical resistivity (ρ) and linear thermal expansion ($\Delta l/l$) of $Gd_5(Si_{0.1}Ge_{0.9})_4$ as a function of (increasing) temperature. The ρ values have been normalized to the 200 K value ($\rho/\rho_{200\,\mathrm{K}}$). The different crystallographic and magnetic phases are indicated

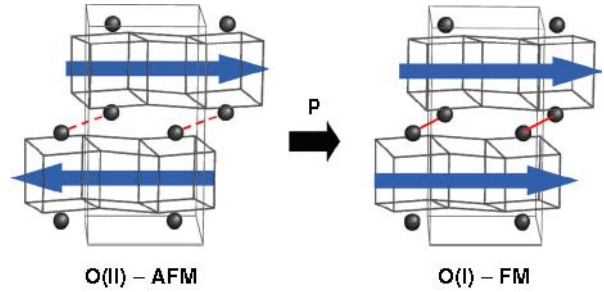

Fig. 4.2. Schematic representation of the crystallographic and magnetic structures of $Gd_5(Si_{0.1}Ge_{0.9})_4$ in the (a, b) plane at $T < T_N$. Only the X = Si, Ge atoms participating in the X–X covalent-like bonds are depicted as *solid spheres*. A *solid line* linking the X atoms represents a formed bond [O(I)] whereas a *dashed line* is used for a broken one [O(II)]. *Solid arrows* are used to illustrate the change in the magnetic coupling as a function of magnetic field

4.2.2 MnAs

Another well-known example of a system with a magnetostructural transition is MnAs. This alloy is ferromagnetic at room temperature and exhibits a first-order loss of magnetic ordering during heating at $T_C \approx 310$ K, accompanied by a volume contraction of about 2% [21, 22]. This magnetic–crystallographic transformation involves a distortion from the FM high-symmetry hexagonal

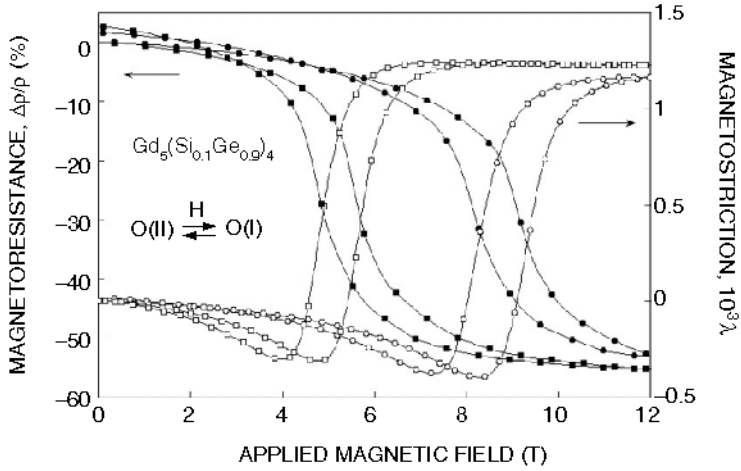

Fig. 4.3. Magnetoresistance $\Delta\rho/\rho$ (*block symbols*) and magnetostriction λ (*open symbols*) isotherms as a function of the applied magnetic field at selected temperatures of $T = 100\,\mathrm{K}$ (*squares*) and $110\,\mathrm{K}$ (*circles*)

NiAs-type $B8_1$ phase (space group $P6_3/mmc$) into the lower symmetry PM orthorhombic MnP-type B31 phase (space group $Pnma$) [23]. At higher temperatures, $T_D \approx 394\,\mathrm{K}$, MnAs undergoes an additional second-order displacive transition back to the NiAs-type structure.

The detailed magnetic phase diagram of MnAs was first established by Zieba et al. [24] and revised more recently by Chernenko et al. [25]. Magnetostriction values of 0.66% (linear contraction) were reported at the field-induced PM(B31) $\rightarrow$ FM($B8_1$) transition in good agreement with the values determined from thermal expansion in zero field, see Fig. 4.4. Assuming isotropic behavior, the maximum volume magnetostriction is approximately equal to 2.1% at 310 K, nearly three times larger than the value associated to the AFM–FM transition in FeRh, see Sect. 4.3 and [26].

Recent neutron diffraction data in an applied field [27] give a direct microscopic evidence that the crystallographic transformation involves breaking and reforming metal–metal bonds. Coexistence and growth of the FM phase at the expense of the PM B31 phase as the magnetic field increases is observed, which is possible since the B31 phase is derived from the $B8_1$ phase by a cooperative displacement of pairs of $[1, -1, 0]$ rows toward one another to form stronger Mn–Mn bonds. These also create shorter Mn–As bonds, which raise the antibonding states that σ-bond to the As atoms and trigger the transition to a low-spin state [28]. The field-induced phase transition is accompanied by an enhanced magnetoresistance response of about 17% at 310 K, see Fig. 4.5, in a similar fashion to that of the colossal magnetoresistance (CMR) Mn perovskites, as will be discussed later.

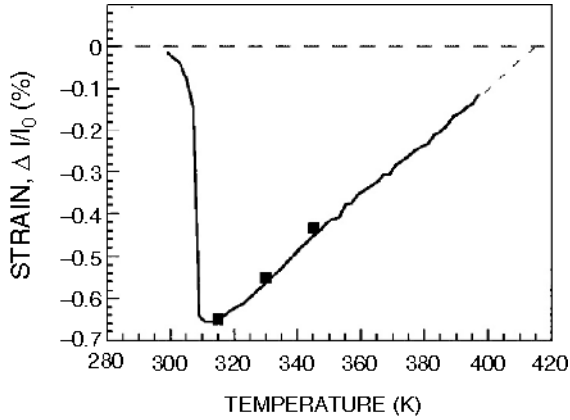

Fig. 4.4. Linear thermal expansion as a function of temperature. The data points were measured in magnetic fields [25]

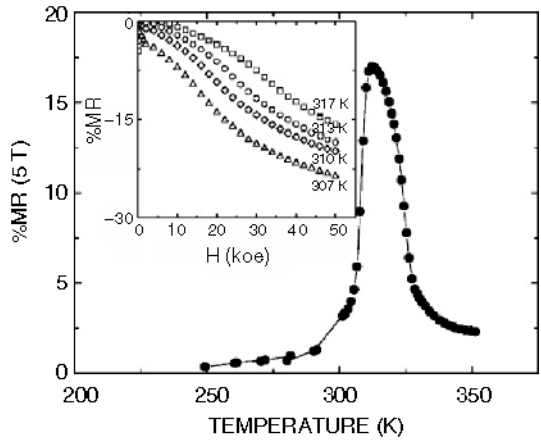

Fig. 4.5. Magnetoresistance ratio MR $= \{[\rho(0) - \rho(5\,\mathrm{T})]\,/\rho(0)\} \times 100$ versus temperature of MnAs. Inset: MR versus H [27]

4.3 Moment Instabilities and Spin Fluctuations

4.3.1 FeRh

It is well known that in the ordered CsCl crystallographic structure of $Fe_{0.5}Rh_{0.5}$ a PM–FM phase transition occurs at $T_C \approx 650\,K$, within the FM phase a peculiar FM–AFM phase transition takes place at a temperature $T_{F-AF} \approx 350\,K$ [29]. Simultaneously, at this transition a 0.9% volume contraction occurs without change in the crystallographic structure together with a large drop in the electrical resistivity [30]. This singular transition

strongly depends on the concentration, and it is only present in a very narrow concentration range of 5% around $x = 0.5$ in the binary $Fe_{1-x}Rh_x$ phase diagram [31]. Neutron diffraction experiments [32] performed in the AF phase showed that only the iron atoms carry a relatively large local magnetic moment $\mu_{Fe} \approx 3.2\,\mu_B$ with no magnetic moment on the rhodium sites. In the FM phase, the iron moment remains with the same value, however, a local magnetic moment appears on the rhodium sites $\mu_{Rh} \approx 0.9\,\mu_B$. First-principles total-energy band-structure calculations [33] predicted an equilibrium type-II AF magnetic ordering [antiferromagnetic coupling between successive layers of (111) iron layers] with no magnetic moment on the Rh sites. A metastable FM state is also predicted to exist with a larger unit cell volume than in the AF ground state. The FM state is very close in energy to the low-volume AF state and can be reached either thermally or by applying a magnetic field, as seen in magnetization measurements [26].

Thermal expansion measurements reveal that the stoichiometric FeRh alloy is an interesting system in which both Invar and anti-Invar effects are present in different range of temperatures [34]. The Invar-like behavior is observed at and below T_C and is mainly attributed to transverse fluctuations of the local magnetic moments, which remain practically constant through and below the transition within the FM phase. The anti-Invar behavior is observed at T_{F-AF} and is associated with the collapse of the local μ_{Rh}, as a consequence of the longitudinal spin fluctuations at low temperatures.

Huge field-induced volume magnetostriction (the anisotropic magnetostriction is negligible) has been observed in this alloy above room temperature, $\omega = (8.2 \pm 0.2) \times 10^{-3}$ [34]. As shown in Fig. 4.6, this value is reached above a certain critical field, above which it remains constant. The value observed for the field-induced volume magnetostriction is comparable to that found

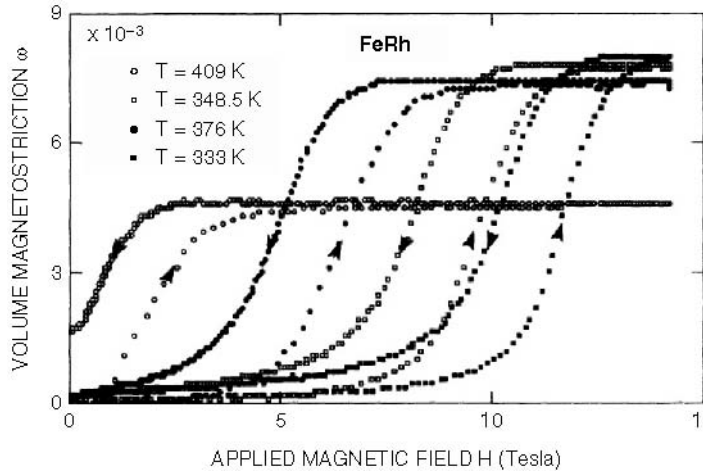

Fig. 4.6. Isotherms of the volume magnetostriction ω for FeRh as function of the applied magnetic field (the *arrows* indicate the direction of the field variation) [34]

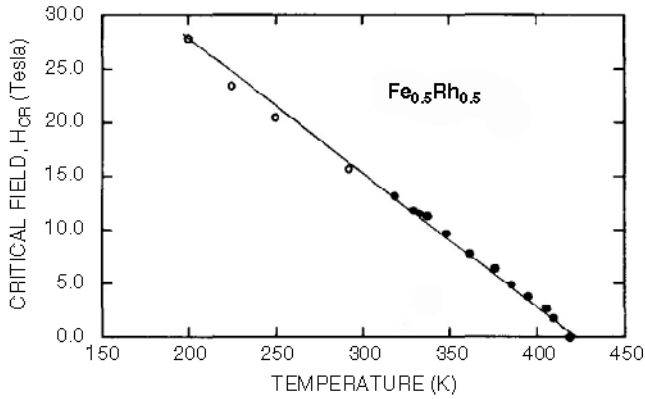

Fig. 4.7. Thermal dependence of the critical field obtained from magnetostriction (*filled circle*) [34] and magnetoresistance (*open circle*) measurements [35]

in thermal expansion measurements and, therefore, the effect of the field is that of inducing a transition from the low-volume AF to the high-volume FM state through a first-order magnetic phase transition at a certain critical field. This gives experimental support to the theoretically predicted existence of a metastable ferromagnetic high-volume state in which Rh has a local magnetic moment.

In addition, a large magnetoresistance ratio, $\Delta\rho/\rho \cong -50\%$ has been found [35] at the field-induced transition in good agreement with that observed in zero field at the transition temperature. In Fig. 4.7 the temperature–magnetic field phase diagram as determined from both magnetoresistance and magnetostriction experiments is displayed, clearly demonstrating that both effects are coupled, and confirming earlier theoretical predictions [36] that proposed FeRh should behave as a natural multilayer system.

4.3.2 $Hf_{1-x}Ta_xFe_2$

The $Hf_{1-x}Ta_xFe_{2-y}$ intermetallic compounds crystallize in the hexagonal $MgZn_2$-type structure (C-14 Laves phase, space group $P6_3/mmc$) with one Mg site ($4f$) and two sites for Zn ($2a$ and $6h$). $HfFe_2$ is a ferromagnet with an order temperature $T_C \approx 600\,K$ [37], and $TaFe_2$ is a paramagnet [38]. The magnetic phase diagram of the $Hf_{1-x}Ta_xFe_2$ series was reported by Nishihara and Yamaguchi [39–41], a first-order AFM–FM transition with decreasing temperature within the concentration range $0.1 < x < 0.3$ being detected. In the FM state, the Fe ions in both sites carry a local magnetic moment of $\approx 1\,\mu_B$, whereas in the AFM state only the ions at the $6h$ site have a local magnetic moment of $\approx 0.7\,\mu_B$, with no magnetic moment being detected at the $2a$ sites. The fundamental question on whether the $2a$ Fe moment is identically zero, i.e., a nonlocal moment, or there is a local paramagnetic moment which vanishes on time averaging due to fast fluctuations within the experimental

characteristic time has been answered in a recent contribution by means of Mössbauer spectroscopy in an applied magnetic field [42]. The H–T phase diagram can be explained qualitatively in the framework of the Moriya and Usami theory for an itinerant electron system in which ferro- and antiferromagnetism coexist [43].

The thermally induced AFM–FM transition is accompanied by a large volume jump of $\Delta V/V \approx 1.2\%$ [40] and a resistivity anomaly of $\Delta\rho/\rho \approx 25\%$ ($x = 0.2$) [44]. The FM state can be reached from the AFM state by application of an external magnetic field and, therefore, strong magnetostriction and magnetoresistance effects are expected and indeed found experimentally [44–46]. In Fig. 4.8 the volume magnetostriction ω isotherms for $Hf_{0.83}Ta_{0.17}Fe_{1.98}$ at selected temperatures are shown (the anisotropic magnetostriction is negligible). A huge value $\omega \approx 0.7\%$ close to room temperature is found. This value coincides with the zero-field thermal expansion, thus demonstrating this transition can be understood on the basis of a first-order transition from a low-volume low-spin state (AFM) to a high-volume high-spin state (FM), i.e., Invar behavior according to Moruzzi [47], and is attributed to the variation of the local moment of Fe at both sites of the crystallographic structure.

The associated magnetoresistance effect in a $Hf_{0.845}Ta_{0.155}Fe_2$ at various temperatures is displayed in Fig. 4.9. The observed giant magnetoresistance has been attributed to changes in the conduction electron scattering caused by the metamagnetic transition.

4.3.3 $La(Fe_xAl_{1-x})_{13}$

The $La(Fe_xAl_{1-x})_{13}$ alloys crystallize in the cubic $NaZn_{13}$-type structure in the composition range between $x = 0.46$ and $x = 0.92$. Such a dense structure

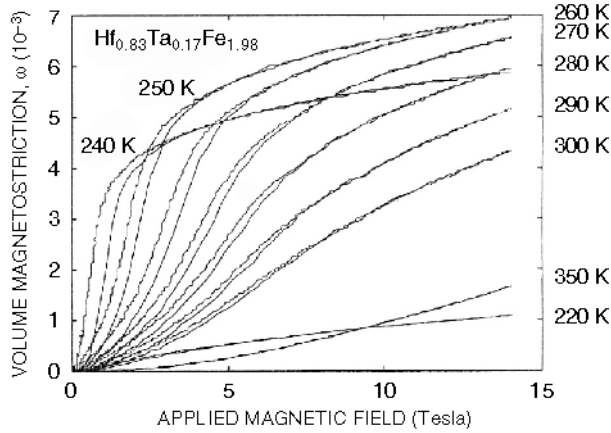

Fig. 4.8. Volume magnetostriction isotherms ω for $Hf_{0.83}Ta_{0.17}Fe_{1.98}$ at some selected temperatures [46]

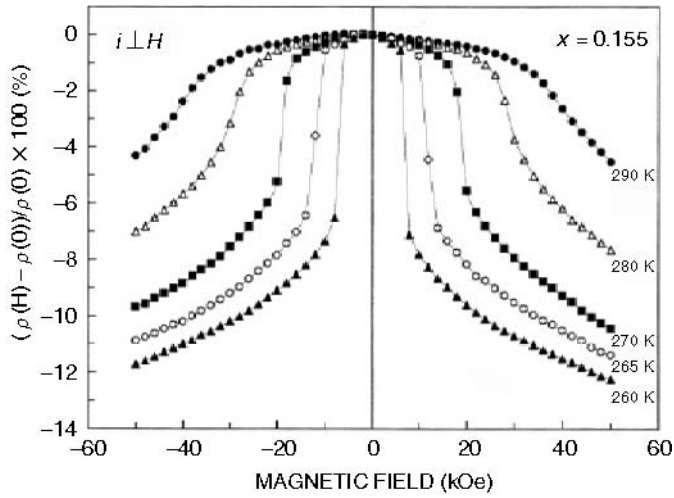

Fig. 4.9. Magnetoresistance measured for $Hf_{0.845}Ta_{0.155}Fe_2$ at various temperatures [45]

similar to fcc-Fe support different magnetic states due to the itinerancy of the 3d electrons, whose correlations bring about the complicated behavior of spin fluctuations [43]. The FM and AFM states are stabilized in the concentration range $0.60 \leq x \leq 0.86$ and $0.87 \leq x \leq 0.92$, respectively [48]. The FM and AFM states are very close in energy, and the AFM–FM metamagnetic transition takes place by application of magnetic field and pressure [48–50]. In addition, a temperature-induced first-order transition has been found in a narrow concentration range $0.860 < x < 0.869$ [51].

As an example, the magnetoresistance and volume magnetostriction of the antiferromagnetic alloys $x = 0.88$ and $x = 0.89$, respectively, are depicted in Fig. 4.10. The magnetoresistance amounts to about 17% in a field of 4.76 T at low temperatures for $x = 0.88$. For $x = 0.89$, the volume magnetostriction at 4.2 K and above the spin-flip transition is huge, $\omega = 1\%$. The irreversibility at low fields seen in Fig. 4.10 (right) is due to the appearance of visible cracks in the sample. More information on the antiferromagnetic structure of these alloys can be found elsewhere [52].

4.4 Metal–Insulator Transitions

The compounds that we describe are the mixed valent manganites, with formula $R_{1-x}A_xMnO_3$ where R^{3+} is a rare-earth ion and A^{2+} is an alkali earth. In the extreme compounds, $RMnO_3$ and $AMnO_3$, the manganese ions are either Mn^{3+} (d^4) or Mn^{4+} (d^3). These compounds have crystallographic structures derived from the ideal cubic perovskite, the manganese ion occupying the center of oxygen octahedra. The crystal-electric-field splitting created by

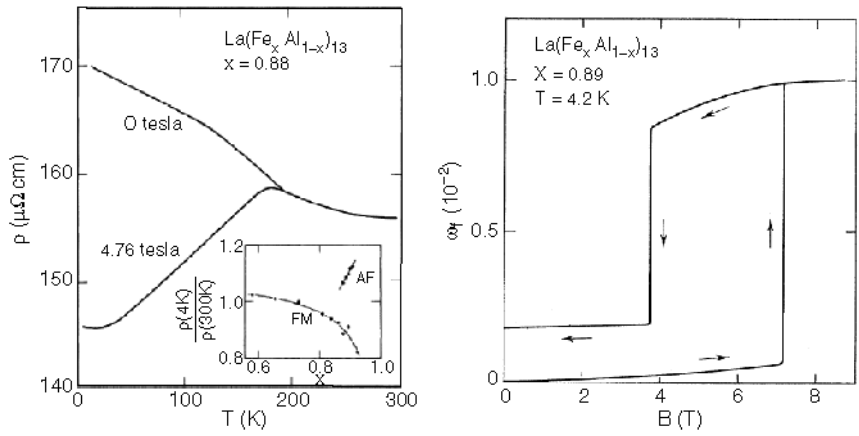

Fig. 4.10. Temperature dependence of the electrical resistivity ρ for an antiferromagnetic $x = 0.88$ alloy in zero field and in an applied magnetic field of 4.76 T greater than the critical field of the AFM–FM transition (*left*). Forced volume magnetostriction isotherm at 4.2 K for an AFM alloy $x = 0.89$ (*right*) [48]

the negative ligands imposes the symmetry of the magnetic electrons: $t_{2g}{}^3e_g{}^1$ in the case of Mn^{3+} and $t_{2g}{}^3$ in the case of Mn^{4+}. The magnetic interactions are governed by the superexchange antiferromagnetic interaction through the π-oxygen orbital $t_{2g}(Mn)$–$2p_\pi(O)$–$t_{2g}(Mn)$. As a result, these compounds are antiferromagnets at low temperature. Substitution of R^{3+} by A^{2+} has a strong influence on the magnetic, structural, and magnetotransport properties of these compounds, leading to complex phase diagrams. The main effect is the creation of holes with e_g symmetry. These electronic states are strongly hybridised with the σ oxygen orbitals in such a way that e_g holes can easily hop from one Mn^{3+} ion to other Mn^{3+} with the only condition that the first Hund rule should not be violated (high spin state). Within this scheme the hole transfer is conditioned to the existence of e_g occupied states with the same spin polarisation, i.e., the electronic transfer is favored under ferromagnetic alignment of the t_{2g} spin ($S = 3/2$) cores. This corresponds to the double exchange interaction in which electron hopping over a ferromagnetic background gives rise to a very high conductivity. Then, ferromagnetism in these compounds is usually associated with a metallic behavior. The formalism to describe this interaction was proposed by Zener [53] and current models involve the use of ferromagnetic Kondo Hamiltonian to explain the relevant phenomena, see for instance the recent review article by Moreo et al. [54].

In general, the lack of long-range magnetic order or the existence of antiferromagnetic long-range order originated from the superexchange interaction are incompatible with the electron mobility, and the system is an insulator. Therefore, we can find very interesting systems in which the conduction electrons are fully polarized and show a high itinerancy under ferromagnetic

alignment of the magnetic moments ("Half-metallic ferromagnets"). Because the hopping probability between neighboring Mn atoms is modulated by the alignment of the core t_{2g} magnetic moments, large magnetoresistance can be expected. The optimum hole doping concentration is around $x = 1/3$, and for concentrations larger than $x = 0.5$, long-range ferromagnetic order is not present.

In the paramagnetic phase a tendency toward localization takes place due to the electron–phonon interaction, which is quite relevant in these compounds as was demonstrated by the strong isotopic effect [55]. The interplay of the above mentioned interactions gives rise to a rich phenomenology reviewed in [56–58].

4.4.1 Colossal Magnetoresistance (CMR) and Huge Volume Effects

In this section we concentrate on the relevant magnetovolume effect discovered in the mixed-valent manganites. The measurements were performed on polycrystals by using the strain-gauge technique at low temperature and the push-rod method at temperatures higher than room temperature. These measurements compared quite well with the results obtained from neutron diffraction experiments. In Fig. 4.11 we show the thermal dependence of the resistivity and the thermal expansion for $La_{0.6}Y_{0.7}Ca_{0.33}MnO_3$. In the paramagnetic phase ($T \geq T_C = 160\,K$) the resistivity has a semiconductor-like behavior. In this phase the compound is paramagnetic and insulator (PMI). Below T_C the system is ferromagnetic and the resistivity sharply decreases by four orders of magnitude. This is a consequence of the double exchange interaction, which favors the electronic itinerancy. In this phase we found ferromagnetic and metallic resistivity (FMM). The observed dramatic effect on

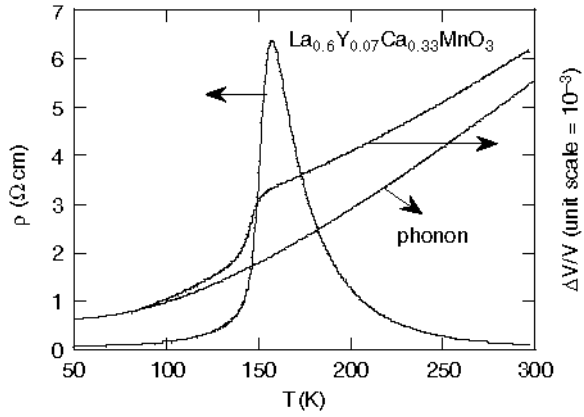

Fig. 4.11. Thermal expansion and resistivity in $La_{0.6}Y_{0.07}Ca_{0.33}MnO_3$. An anomalous contribution over the phonon expansion above T_C is observed. At this temperature, a sharp decrease in the resistivity takes place (metal–insulator transition)

the resistivity also has a strong influence on the thermal expansion, which is manifested by a sharp decrease in the sample volume as one crosses from the PMI to the FMM phase [59] (the thermal expansion is isotropic). The Grüneisen fit of the thermal expansion curve using a Debye temperature $\theta_D = 500\,K$ gives the results shown in Fig. 4.11, in which the thermal expansion in the FMM phase follows the phonon lattice behavior. However, in the PMI phase an extra anomalous contribution was found, being necessary to increase the temperature up to three times T_C in order to recover the phonon behavior.

Other interesting compound with the same hole concentration is the mixed valent manganite $Pr_{0.7}Ca_{0.3}MnO_3$ [60]. The resistivity shows an insulating behavior even at low temperatures, which is a direct consequence of the absence of ferromagnetic order, and the thermal expansion results do not show any sharp anomaly, as observed in the former La–Ca compounds. Only a small bump at $T_{CO} = 210\,K$ is observed, which is associated with the establishment of a charge ordering state. However, the thermal expansion does not follow the Grüneisen behavior. The extra volume contribution at low temperature is associated with the existence of an insulator antiferromagnetic state at low temperature below $T_N = 150\,K$.

From these results one can easily conclude the existence of an extra volume contribution associated with the insulator state. The source of this volume anomaly was associated with a polaronic effect [59]. When an electron moves on an ionic background with an average lifetime shorter than $10^{-15}\,s$ (characteristic time associated with a 3d metal bandwidth) the wave function is characterized by a Bloch function. However, if the electron is near the ionic core for a period of $\approx 10^{-12}\,s$, a polarization of the lattice is possible. The electric field created by the electron will attract the positive ions and push away the negative ions. The resultant electric field decreases because of the increase of the dielectric constant, due to the combined effect of polarization and ionic displacement. If the electron tries to move, it will feel a force that tends to restore it back to the original position. The result is the formation of a potential well originated by the electrostatic and elastic energy. The entity formed by the charge + distortion is called lattice polaron. Depending on the temperature range this polaron can move in the lattice, either by thermal activation overcoming the potential barrier or by tunneling forming a narrow polaronic band with a bandwidth given by the Heisenberg's uncertainty relationship ($\Delta\omega\Delta\tau = \hbar$). Recent NMR spin echo experiments [61] revealed that the average lifetime of these entities is $\Delta\tau_p > 10^{-5}\,s$.

The extra contribution on the thermal expansion observed in the insulator regime is a consequence of this lattice polaron formation. The comparison of these results with small angle neutron scattering (SANS) gave evidence for the magnetic nature of the polaron responsible for the anomalous volume effect. One observes in a SANS experiment a magnetic contribution of ferromagnetic clusters with magnetic correlation length of the order 10–30 Å [62]. The SANS intensity is related to the number of dispersion centers with short-

range ferromagnetic correlations. By comparison with the thermal expansion anomaly, one can demonstrate how the volume anomaly associated with the localized charges or polarons has a magnetic origin. The magnetic correlation length diverges as T_C is approached.

This conclusion supported by SANS experiments can also be extracted from magnetostriction measurements. The magnetic polaron is the combination of a lattice polaron plus ferromagnetic clusters. This is a logical situation within the framework of the double exchange in mixed valent manganites. If the charge (electron or hole) is localized on a Mn ion, a probability of charge transfer to the next neighbor exists and this implies a parallel alignment or the Mn moments, i.e., the electronic hopping between surrounding Mn ions gives rise to the formation of a magnetic polaron with an average lifetime at a determined ionic site $\Delta\tau_p \geq 10^{-5}$ s, as determined from NMR experiments [61]. The same experiment also allowed to determine that the hopping time for the electron within the polaron is less than 10^{-9} which is the characteristic time given by the Larmor frequency for the indistinguishable Mn^{3+}–Mn^{4+} resonance line.

4.4.2 Magnetostriction and Magnetoresistance in the Paramagnetic Phase

The magnetostriction measured in paramagnetic phase in mixed valent manganites with CMR is rather anomalous [59] with values, field and thermal dependence never observed before in a disordered magnetic phase. The Callen & Callen theory [63] using the one and two ion correlation functions predicts that the volume (ω) and anisotropic magnetostriction (λ_t) in paramagnetic phase are proportional to the square of the applied magnetic field ($\omega = \lambda_{\parallel} + 2\lambda_{\perp} \approx H^2$ and $\lambda_t = \lambda_{\parallel} - \lambda_{\perp} \approx H^2$) for localized magnetic moment systems. That is what is observed in many rare-earth intermetallics. The use of the crystal-electric-field theory allows using perturbation techniques to obtain information about the quadrupolar interaction in intermetallics [64]. This theory also predicts a quadratic dependence of parastriction with field. Usually the parastriction is very small and anisotropic in magnetic crystalline materials with well localized magnetic moments.

We found in mixed valent manganites a very unusual behavior: the parastriction is huge, corresponds to a volume effect, and does not have a quadratic dependence with the field for temperaztures between $T_C < T < 1.8T_C$. In Fig. 4.12a we show the magnetostriction measured in the paramagnetic phase of $La_{0.6}Y_{0.07}Ca_{0.33}MnO_3$ and, in Fig. 4.12b, we show the comparison with the anomalous contribution to the thermal expansion. The anisotropic magnetostriction was found to be negligible ($\lambda_{\parallel} \approx \lambda_{\perp}$). In this compound the long-range magnetic order is destroyed at $T_C = 150$ K as determined from the thermal dependence of the intensity of the neutron diffraction peaks. We can observe the large value of ω at fields larger than 2 T and a field dependence

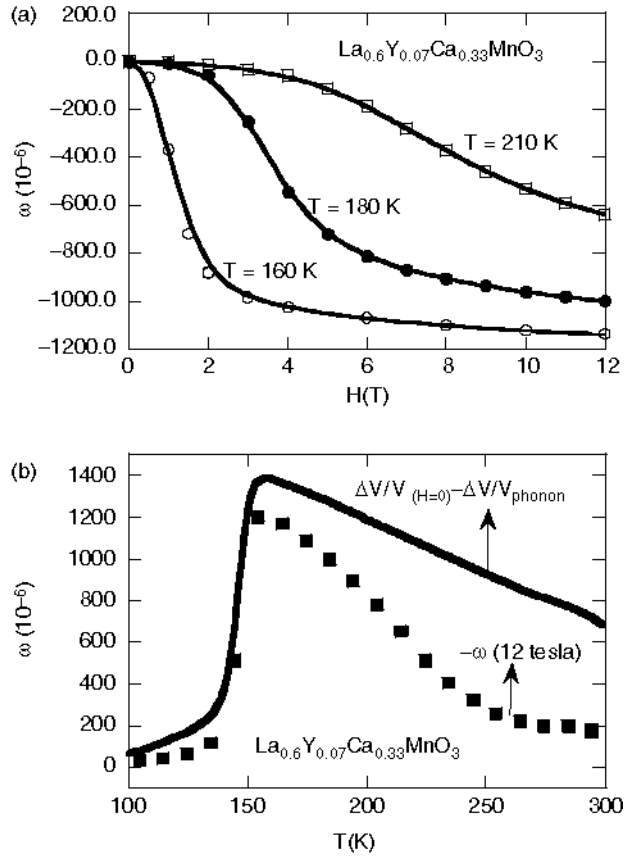

Fig. 4.12. Magnetostriction in the paramagnetic phase. (**a**) Volume magnetostriction isotherms. (**b**) Comparison of the extra contribution to the volume thermal expansion to the volume magnetostriction at 12 T. The lack of correspondence at temperatures well above T_C is due to the lack of saturation of $\lambda_t(H)$

uncharacteristic of a paramagnet. This is, to our knowledge, the largest magnetostriction ever measured in a paramagnet, making this compound attractive not only from the point of view of the relevant magnetoresistance behavior, but also from the spectacular magnetostriction effect. Moreover, the tight relation between the magnetostriction and magnetoresistance offers a unique opportunity to get an insight into the relevant mechanisms operational in these compounds. The comparison of the anomalous spontaneous and high field value of magnetostriction shows that the field effect is the suppression of the volume anomaly in the thermal expansion. If we reconsider the previous argument, the observed magnetostriction in the paramagnetic phase should have its origin in the destruction of magnetic polarons under field, i.e., in the delocalization under field of the trapped charges. This argument would explain the sharp decrease of the resistivity under field (CMR). In addition

to magnetostriction measurements, a microscopic study by means of SANS supported this assumption [62].

From the previous considerations we can describe the paramagnetic state of the CMR mixed valent manganite La–Ca as an insulating state in which localized charges give rise to an extra contribution to the spontaneous ω. These localized charges carry a ferromagnetic polarized cloud with a correlation length $\xi \approx 12\,\text{Å}$. Under applied magnetic field ξ increases and the magnetic polarons percolate, inducing a ferromagnetic conducting state. Then, the huge magnetostriction observed in the paramagnetic phase originates from an insulator–metal transition, which is related to a percolative transition [62] from a high to a low volume state. We should call the attention of the readers to the peculiar and new behavior described here. First, the existence of well-defined nanometric ferromagnetic electronic cloud with an average life time larger than $10^{-5}\,\text{s}$. This constitutes a kind of dynamic phase segregation known as magnetic polarons. They are responsible for the CMR and parastriction effects in manganites. Second, the magnetic polarons are of different nature than those proposed by Kasuya [65] and Nagaev [66] which are based on an impurity effect which does not give rise to magnetovolume effects.

4.4.3 Magnetostriction in Inhomogeneous Electronic Systems: Static Phase Segregation

In Sect. 4.4.2 we underlined the relevance of dynamic phase segregation, in the form of magnetic polarons, on the magnetostriction in mixed valent manganites. In this section, we deal with a new phenomenology also found in these magnetic oxides. We show how magnetostriction experiments were essential to predict the existence of static phase separation, subsequently confirmed by other microscopic techniques. Nowadays, the existence of inhomogeneous states in different series of mixed valent manganites is well established [54]. The situation can be complex considering different doping level on the e_g band as a result of x variation in compounds $La_{1-x}M_xMnO_3$ where M is an alkaline earth. In order to illustrate the magnetostriction effect when this phenomenon takes place, we selected a fixed hole concentration Mn^{4+} of 0.33, i.e., $La_{2/3}Ca_{1/3}MnO_3$.

This compound is ferromagnetic below $T_C = 260\,\text{K}$ and shows at this temperature a first-order transition [67] from the insulator state with formation of magnetic polarons to the metallic state, as we already described for $La_{0.6}Y_{0.07}Ca_{1/3}MnO_3$. The substitution of ≈10% of La by Tb has a strong effect on the ordering temperature, decreasing to $T_C = 150\,\text{K}$, but all the phenomenology is similar to that found in the sample with Y described previously. This is a general trend in manganites: the substitution of La^{3+} by another rare-earth ion as Tb^{3+}, keeping the same hole-doped concentration, produces a decrease of the ferromagnetic double exchange interaction strength. This is a result of the narrowing of the electronic e_g bandwidth driven by the reduction of the Mn–O–Mn bond angle as a consequence of the smaller ionic radii of Tb^{3+} ions [68,69]. At $x > 0.25$ the compounds are not long-range magnetically

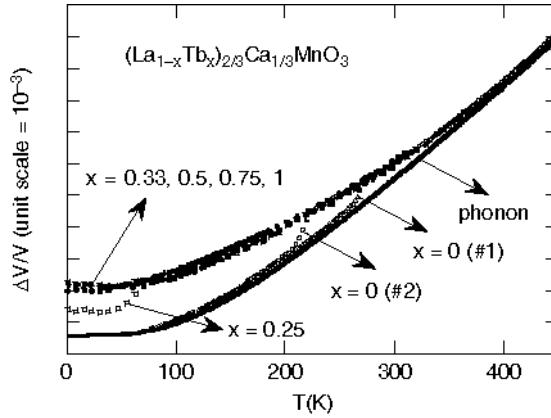

Fig. 4.13. Volume thermal expansion for different compounds of the series La–Tb. Notice the low temperature behavior. The extra contribution to the thermal expansion persists for the insulating compounds. The metallic state follows the Grüneisen calculated phonon thermal expansion. The compound $x = 0.25$ remains in an intermediate state, which is an indication of the existence of an inhomogeneous state with static phase segregation (coexistence of FMM and PMI)

ordered and a spin glass state (disordered ferromagnetic clusters of $\xi \approx 20$ Å) is found in the region close to $x = 0.25$. At this particular concentration, long-range ferromagnetic ordered regions coexist with paramagnetic regions. First experimental evidence of phase segregation in this compound was obtained from the thermal expansion measurements. In Fig. 4.13 we show the thermal expansion results for $x = 0.25$ and other compounds of the series. At larger Tb doping level ($x > 0.25$) the systems are insulators at low temperatures and show similar behavior (i.e., high volume insulator state). However, for low Tb doping, $x < 0.25$, there exists a sharp anomaly associated with the volume reduction at T_C, consequence of the insulator–metal transition as explained before. Unlike the two former systems, the considered compound $x = 0.25$ displays an intermediate volume state at low temperature. This state was considered as a result of an inhomogeneous para–ferromagnetic transition at $T_C \approx 80$ K [70].

The isothermal volume magnetostriction curves (not displayed here) do not saturate, which is interpreted as an indication of the stability of the inhomogeneous state even at 12 T. We can explain these results considering the establishment of microferromagnetic metallic regions below $T_C \approx 80$ K coexisting with a paramagnetic insulator even at very low temperature. Under field, the volume fraction of the ferromagnetic region increases with field, and consequently reducing the overall volume of the sample. These conclusions, directly obtained from magnetostriction measurements, were further confirmed by resistivity and SANS experiments. In Fig. 4.14 we show the temperature dependence of magnitudes of both quantities. We can observe a drop in the

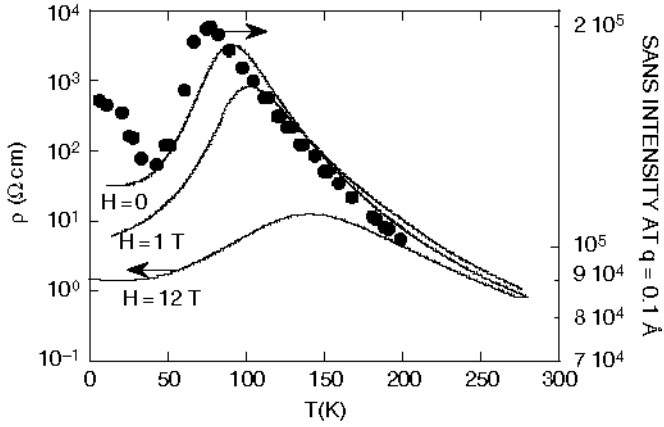

Fig. 4.14. Comparison of the resistivity with the SANS intensity at $q = 0.1\,\text{Å}$ in $x = 0.25$. The field effect on the resistivity is also shown

resistivity at T_C but the remnant low temperature resistivity is rather high ($\rho \approx 50\,\Omega\,\text{cm}$). However, under applied field it decreases in two orders of magnitude. The final confirmation of the existence of an inhomogeneous state is the thermal dependence of SANS intensity. The enhancement of the SANS intensity as temperature decreases is the result of magnetic polaron formation as explained before. The sharp decrease of this magnitude at T_C is an indication of formation of large clusters. These clusters are large enough to give a magnetic coherent contribution to the Bragg neutron diffraction intensity, as demonstrated in powder neutron diffraction experiments [70] ($\xi > 500\,\text{Å}$). This contribution is far from the magnetic signal expected from the establishment of long-range ferromagnetic order. Once more, the remanent SANS contribution at low temperatures can be attributed to the existence of short-range ferromagnetic clusters.

4.5 Charge/Orbital Instabilities

Charge ordering (CO) is a well-known phenomenon in magnetic oxides. The archetypical example is the magnetite Fe_3O_4. In this compound Verwey [71] proposed the long-range ordering of the Fe^{2+} and Fe^{3+} ions at the octahedral oxygen site of the spinel structure. This implies an extra charge periodicity which has been used as an example of Wigner crystal formation. This is a good example of strongly correlated states, i.e., the electrons in the real space try to keep away from each other as much as possible. The ground state is consequently insulating. Nevertheless, the exact nature and pattern of CO state in magnetite is a matter of discussion [72]. In mixed

valent manganites the existence of CO has extensively been found in many compounds and is associated with the existence of orbital ordering. The static situation originates from the strong Coulomb repulsion. However, the ordered charges have e_g symmetry with an anisotropic charge density on the ionic sites: $3z^2 - r^2$, $x^2 - y^2$ (Jahn–Teller degeneracy), this implies a new degree of freedom (pseudospin space) [73,74]. Of course, the space symmetry breaking of the pseudospin would make independent the charge and the orbital ordering. Nevertheless this situation is not observed in mixed valent manganites. The order of the charges alone would give rise only to an isotropic distortion of the unit cell. In spite of it, a strong anisotropic tetragonal distortion of the unit cell (without changing the symmetry) is found. A nice example is the compound $La_{0.35}Ca_{0.65}MnO_3$ where superlattice electron diffraction spots indicated the long-range charge order [75] below $T_{CO} = 270\,K$. In addition, lattice distortions were detected by neutron diffraction experiments [76] suggesting the existence of an orbital ordering. The magnetic ordering is not always related to the existence of charge/orbital ordering. For instance, in this compound the long-range antiferromagnetic state occurs at $T_N \approx 140\,K$, well below T_{CO} [77].

Spin disorder or antiferromagnetism brings about charge localization. However, ferromagnetism causes delocalization through the double exchange mechanism. In this case the kinetic energy avoids the formation of the Wigner crystal. Transitions between charge ordering insulator and ferromagnetic-metallic states can occur either spontaneously or under an applied field, when these two "quantum phases" have nearly degenerate minima in the free energy.

We focus our attention on $Pr_{0.7}Ca_{0.3}MnO_3$. The crystallographic structure is orthorhombic, *Pbnm* space group. At $T_{CO} \approx 210\,K$ a transition to a charge ordering state takes place. Below this temperature the compound is an insulator down to 4 K. Nevertheless, a first-order insulator–metal transition can be induced by the application of a magnetic field. Below $T_N \approx 150\,K$ this compound orders antiferromagnetically in a CE-type structure. Below ≈100 K a canting of the magnetic moment was proposed giving rise to a ferromagnetic component [78]. A great effort was dedicated to establish the deep connection between magnetic and transport properties in this compound. Our effort was oriented toward the study of the lattice effects, with the aim of getting an insight into the underlying spin–charge–lattice coupling.

In Fig. 4.15a we show the thermal expansion results on $Pr_{0.7}Ca_{0.3}MnO_3$ under applied magnetic field of 0, 6 and 12 T. A comparison of the experimental results and the calculated lattice contribution (using a $\theta_D = 500\,K$) allows us to distinguish three different temperature ranges. Below ≈400 K there exists an extra contribution, as observed in the La–Ca compound, which we associated with the charge localization of small polarons. At $T_{CO} \approx 210\,K$ we observe a smooth anomaly which coincides with the temperature at which the charge ordering was observed in neutron diffraction experiments [78]. We proposed [60] at this temperature a transition from an incoherent small polaron regime above T_{CO} to a coherent regime in which a charge ordered lattice is

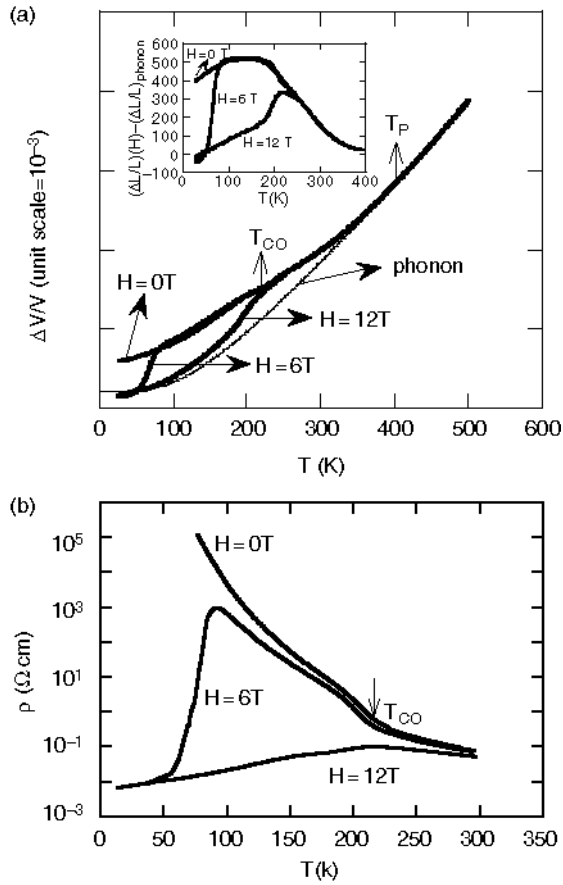

Fig. 4.15. Linear thermal expansion (**a**) and resistivity (**b**) at different field values of $Pr_{0.7}Ca_{0.3}MnO_3$. Inset in (**a**) is the extra anharmonicity associated with the insulator state

formed. We would like to underline the lack of volume effect (isotropic distortion) at this transition, yet the lattice is strongly distorted (large anisotropic change in the lattice parameters). Under an applied magnetic field of 6 T at ≈80 K a change in the volume is observed (≈0.14%). At 12 T the field induced transition is shifted up to 210 K. It apparently seems that at this field value, the charge ordering is completely suppressed in the whole temperature range. These results can be understood considering that the volume distortion associated with the charge localization (due to an extra anharmonic contribution) disappears as the charge is released. When that happens, the thermal expansion recovers the Grüneisen thermal dependence (phonon contribution). This is the situation of the metallic state in $La_{2/3}Ca_{1/3}MnO_3$. To make this effect more clear the extra anharmonicity is displayed in the inset of Fig. 4.15a.

In this compound, as happens in the reported La–Ca compounds, a close correlation of the volume with the resistivity exists. As can be observed in Fig. 4.15b, the spontaneous behavior is characterized by a semiconductor-like dependence of the resistivity with a smooth anomaly at 210 K. Under a field of 6 T an insulator–metal transition takes place at ≈80 K and at 12 T the charge ordered state is not reached, in good agreement with thermal expansion measurements.

The analysis of the magnetostriction and magnetoresistance allows an additional piece of information to be obtained. Two different behaviors were found above and below T_{CO} as can be observed in Fig. 4.16a, b, respectively. The volume magnetostriction above T_{CO} shows a continuous increase of volume with field and no hysteresis is observed. This behavior is similar to the already reported one for the La–Ca compound with the same carrier concen-

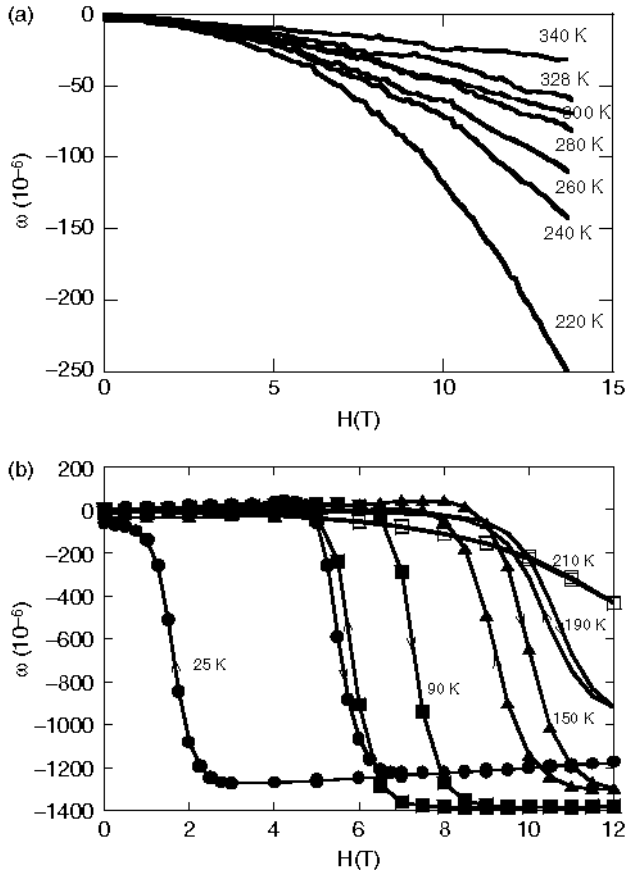

Fig. 4.16. Volume magnetostriction isotherms above (**a**) and below (**b**) the charge ordering transition

tration. Thus, we associate this magnetostriction with the progressive delocalization of the carriers. The small value of this magnetostriction and the lack of saturation may be related to a weak magnetic character of the polaron. Fields higher than 14 T would be necesary in order to completely release the charge. The behaviour below T_{CO} is completely different. Below 150 K the volume magnetostriction isotherms show a clear saturation with a very large hysteresis. This constitutes an indication of the complete destruction of the charge ordered state with the field, and also the first-order nature for the insulator–metal transition. The change in volume at the field-induced transition has the same value as the spontaneous extra volume contribution and opposite sign. A comparison of Fig. 4.17a, b shows the close relation between the magnetoelastic and magnetotransport properties in this compound.

All the reported results on this compound reveal the different nature of the interplaying interactions in mixed valence manganites. Above T_{CO} the Weiss temperature is positive [79] and the presence of lattice polarons with a weak magnetic character supports the presence of short-range ferromagnetic

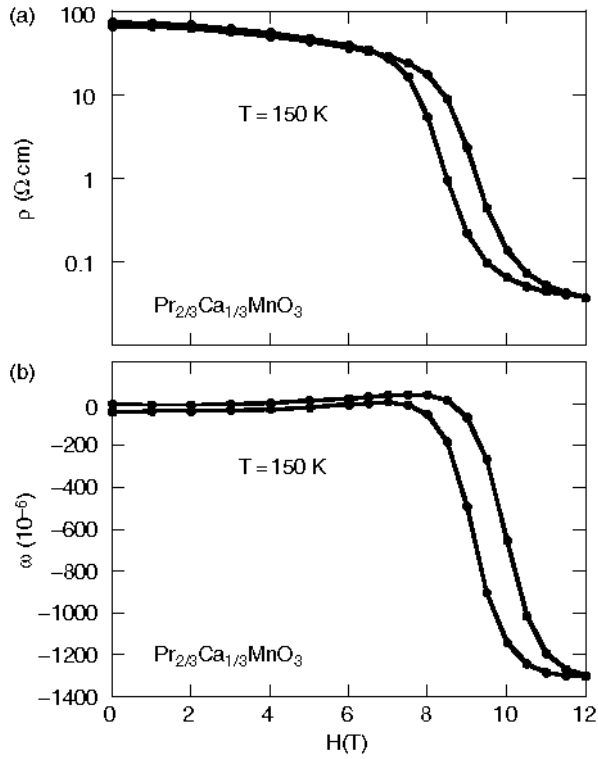

Fig. 4.17. Comparison of the close correlation between magnetostriction and resistivity in $Pr_{0.7}Ca_{0.3}MnO_3$

correlations of double exchange origin. The existence of lattice polarons is an indication of the strong electron–phonon interaction. Below T_{CO} the progressive localization of the carrier favors the ordering of the charges, probably by the long-range coulomb interaction. Below T_N the compound orders antiferromagnetically due to the superexchange interaction. Then, it is not surprising to find a large field effect, given the different ground states available which are almost degenerate in energy.

It is also worth mentioning some recent magnetovolume effects found in compounds in which the long-range charge/orbital ordering is not achieved, but the existence of short-range orbital order can lead to large magnetovolume effects when the system is close to an orbital instability, due to the above mentioned competition between ferrometallic and charge/orbital order insulator. This situation is realised in the series $Sm_{1-x}Sr_xMnO_3$. This compound has para-insulator to ferromagnetic-metallic transition below $T_C = 120\,K$. At this transition a sharp decrease of the resistivity in more than three orders of magnitude was found and also large field induced strains [80]. To get an insight on the mechanisms underlying this behavior [81] we performed thermal expansion and magnetostriction measurements. The results can be explained in a similar way as in the former $La_{2/3}Ca_{1/3}MnO_3$ compound described previously. The extra contribution to the thermal expansion was associated with the existence of magnetic polarons above T_C. In these compounds, however, short-range orbital order has been observed from the analysis of the X-ray resonant scattering around the 220 Bragg reflection [74]. The extra contribution to the volume thermal expansion nicely scales with the intensity of the diffuse X-ray scattering, in a similar fashion to the scaling of the extra contribution to the thermal expansion above T_c in $La_{2/3}Ca_{1/3}MnO_3$ with the SANS intensity. This short-range orbital ordering may be also associated with the formation of a ferromagnetic cloud and consequently with magnetic polarons. SANS experiments confirmed the coexistence of both kinds of short-range ordered regions [82]. With all the experimental evidence a polaronic behavior (Janh–Teller or orbital polarons) seems to be responsible for the localization of carriers which gives rise to the spontaneous magnetoelastic effects.

4.6 Conclusion

In this short review, we selected a number of different archetypal compounds in which magnetoresistance and magnetostriction effects are intimately related. In general, the underlying mechanism is the electron itinerancy in magnetic oxides and, the change of the electronic structure due to a structural transformation or the modification of the magnetic moment due to a change of the longitudinal fluctuations. In spite of the vast phenomenology, a complete and unified theoretical description of the experiments is still lacking. The aim of this review has been to show that magnetostriction can provide relevant information on physical processes in solids and how the volume or anisotropic

magnetostriction are at the base of magnetic or orbital instabilities which drastically influence the electrical transport properties.

Acknowledgments

Most of the reported work is based on experiments performed in our group. The authors would like to thank P.A. Algarabel, C. Marquina, J.M. De Teresa, C. Ritter, and Z. Arnold.

References

1. V.K. Pecharsky, K.A. Gschneidner Jr.: J. Magn. Magn. Mater. **200**, 44 (1999)
2. A.M. Tishin: Magnetocaloric effect in the vicinity of phase transitions. In: Handbook of Magnetic Materials, ed. by K.H.J. Buschow. Vol. 12 (Elsevier, Amsterdam, 1999), pp. 395–524
3. A. Del Moral, P.A. Algarabel, J.I. Arnaudas, L. Benito, M. Ciria, C. de la Fuente, B. García-Landa, M.R. Ibarra, C. Marquina, L. Morellon, J.M. De Teresa: J. Magn. Magn. Mater. **242–245**, 788 (2002)
4. A. Barthélémy, A. Fert, J.P. Contour, M. Bowen, V. Cros, J.M. De Teresa, A. Hamzic, J.C. Faini, J.M. George, J. Grollier, F. Montaigne, F. Pailloux, F. Petroff, C. Vouille: J. Magn. Magn. Mater. **242–245**, 68 (2002)
5. V. Sechovsky, L. Havela, H. Nakotte, E. Bruck: IEEE Trans. Magn. **32**, 4687 (1996)
6. D.C. Jiles: Acta Mater. **51**, 5907 (2003)
7. V.K. Pecharsky, K.A. Gschneidner Jr.: Adv. Mater. **13**, 683 (2001)
8. V.K. Pecharsky, K.A. Gschneidner Jr.: Phys. Rev. Lett. **78**, 4494 (1997)
9. V.K. Pecharsky, K.A. Gschneidner Jr.: Appl. Phys. Lett. **70**, 3299 (1997)
10. V.K. Pecharsky, K.A. Gschneidner Jr.: J. Magn. Magn. Mater. **167**, L179 (1997)
11. L. Morellon, P.A. Algarabel, M.R. Ibarra, J. Blasco, B. García-Landa, Z. Arnold, F. Albertini: Phys. Rev. B **58**, R14 721 (1998)
12. L. Morellon, J. Blasco, P.A. Algarabel, M.R. Ibarra: Phys. Rev. B **62**, 1022 (2000)
13. L. Morellon, J. Stankiewicz, B. García-Landa, P.A. Algarabel, M.R. Ibarra: Appl. Phys. Lett. **73**, 3462 (1998)
14. L. Morellon, P.A. Algarabel, C. Magen, M.R. Ibarra: J. Magn. Magn. Mater. **237**, 119 (2001)
15. E.M. Levin, V.K. Pecharsky, K.A. Gschneidner Jr.: Phys. Rev. B **60**, 7993 (1999)
16. W. Choe, V.K. Pecharsky, A.O. Pecharsky, K.A. Gschneidner Jr., V.G. Young Jr., G.J. Miller: Phys. Rev. Lett. **84**, 4617 (2000)
17. D.C. Jiles, C.C.H. Lo: Sens. Actuators A **106**, 3 (2003)
18. V.K. Pecharsky, K.A. Gschneidner Jr.: J. Alloys Compd. **260**, 98 (1997)
19. A.O. Pecharsky, K.A. Gschneidner Jr., V.K. Pecharsky, C.E. Schindler: J. Alloys Compd. **338**, 126 (2002)
20. E.M. Levin, V.K. Pecharsky, K.A. Gschneidner Jr.: Phys. Rev. B **62**, R14 625 (2000)
21. B.T.M. Willis, H.P. Rooksby: Proc. Phys. Soc. Lond. Sect. B **67**, 290 (1954)

22. C.P. Bean, D.S. Rodbell: Phys. Rev. **126**, 104 (1962)
23. R.H. Wilson, J.S. Kasper: Acta Crystallogr. **17**, 95 (1964)
24. A. Zieba, Y. Shapira, S. Foner: Phys. Lett. **91A**, 243 (1982)
25. V.A. Chernenko, L. Wee, P.G. McCormick, R. Street: J. Appl. Phys. **85**, 7833 (1999)
26. J.B. McKinnon, D. Melville, E.W. Lee: J. Phys. C **1**, S46 (1962)
27. J. Mira, F. Rivadulla, J. Rivas, A. Fondado, T. Guidi, R. Caciuffo, F. Carsughi, P.G. Radaelli, J.B. Goodenough: Phys. Rev. Lett. **90**, 097 203/1 (2003)
28. J.B. Goodenough, J.A. Kafalas: Phys. Rev. B **157**, 389 (1967)
29. M. Fallot, R. Hocart: Rev. Sci. **77**, 498 (1939)
30. J.S. Kouvel, C.C. Hartelius: J. Appl. Phys. **33**, 1343 (1962)
31. G. Shirane, C.W. Chen, P.A. Flinn: Phys. Rev. **131**, 183 (1963)
32. G. Shirane, C.W. Chen, P.A. Flinn, R. Nathans: J. Appl. Phys. **34**, 1044 (1963)
33. V.L. Moruzzi, P.M. Marcus: Phys. Rev. B **46**, 2864 (1992)
34. M.R. Ibarra, P.A. Algarabel: Phys. Rev. B **50**, 4196 (1994)
35. P.A. Algarabel, M.R. Ibarra, C. Marquina, A. del Moral, J. Galibert, M. Iqbal, S. Askenazy: Appl. Phys. Lett. **66**, 3062 (1995)
36. V.L. Moruzzi, P.M. Marcus: Phys. Rev. B **46**, 14 198 (1992)
37. T. Nakamichi, K. Kai, Y. Aoki, K. Ikeda, M. Yamamoto: J. Phys. Soc. Jpn **29**, 794 (1970)
38. K. Kai, T. Nakamichi, M. Yamamoto: J. Phys. Soc. Jpn **29**, 1094 (1970)
39. Y. Nishihara, Y. Yamaguchi: J. Phys. Soc. Jpn **51**, 1333 (1982)
40. Y. Nishihara, Y. Yamaguchi: J. Phys. Soc. Jpn **52**, 3630 (1983)
41. Y. Nishihara, Y. Yamaguchi: J. Magn. Magn. Mater. **31–34**, 77 (1983)
42. H.R. Rechenberg, L. Morellon, P.A. Algarabel, M.R. Ibarra: Phys. Ref. B **71**, 104412 (2005)
43. T. Moriya, K. Usami: Solid State Commun. **23**, 935 (1977)
44. H.G.M. Duijn, E. Brück, A.A. Menovsky, K.H.J. Buschow, F.R. de Boer, R. Coehoorn, M. Winkelmann, K. Siemensmeyer: J. Appl. Phys. **81**, 4218 (1997)
45. Y. Nagata, T. Hagii, S. Yashiro, H. Samata, S. Abe: J. Magn. Magn. Mater. **292**, 11(1999)
46. L. Morellon, P.A. Algarabel, M.R. Ibarra, Z. Arnold, J. Kamarad: J. Appl. Phys. **80**, 6911 (1996)
47. V.L. Moruzzi: Phys. Rev. B **41**, 6939 (1990)
48. T.T.M. Palstra, G.J. Nieuwenhuys, J.A. Mydosh, K.H.J. Buschow: Phys. Rev. B **31**, 4622 (1985)
49. K. Irisawa, A. Fujita, H. Mitamura, T. Goto, K. Fukamichi: J. Alloys Compd. **327**, 17 (2001)
50. K. Irisawa, A. Fujita, H. Mitamura, T. Goto, K. Fukamichi: J. Alloys Compd. **329**, 42 (2001)
51. K. Irisawa, A. Fujita, K. Fukamichi: J. Alloys Compd. **305**, 17 (2000)
52. R.B. Helmholdt, T.T.M. Palstra, G.J. Nieuwenhuys, J.A. Mydosh, A.M. van der Kraan, K.H.J. Buschow: Phys. Rev. B **34**, 169 (1986)
53. C. Zener: Phys. Rev. **82**, 403 (1951)
54. A. Moreo, S. Yunoki, E. Dagotto: Science **283**, 2034 (1999)
55. G.M. Zhao, K. Conder, H. Keller, K.A. Muller: Nature **381**, 676 (1996)
56. C.N.R. Rao, B. Raveau: Colossal Magnetoresistance charge ordering and related properties of manganese oxides (World Scientific, Singapore, 1998)
57. J.M.D. Coey, M. Viret, S. von Molnar: Adv. Phys. **48**, 167 (1999)

58. Y. Tokura: Colossal Magnetoresistive Oxides (Gordon and Breach, New York, 2000)
59. M.R. Ibarra, P.A. Algarabel, C. Marquina, J. Blasco, J. García: Phys. Rev. Lett. **75**, 3541 (1995)
60. J.M. De Teresa, M.R. Ibarra, C. Marquina, P.A. Algarabel, S. Oseroff: Phys. Rev. B **54**, R12 689 (1996)
61. C. Kapusta, P.C. Riedi, W. Kocemba, G.J. Tomka, M.R. Ibarra, J.M. De Teresa, M. Viret, J.M.D. Coey: J. Phys.: Condens. Matter **11**, 4079 (1999)
62. J.M. De Teresa, M.R. Ibarra, P.A. Algarabel, C. Ritter, C. Marquina, J. Blasco, J. García, A. del Moral, Z. Arnold: Nature **386**, 256 (1997)
63. E.R. Callen, H.B. Callen: Phys. Rev. **139**, A455 (1965); E.R. Callen, H.B. Callen: Phys. Rev. **129**, 578 (1963)
64. P. Morin, D. Schmitt: Quadrupolar interactions and magnetoelastic effects in rare-earth intermetallic compounds. In: Ferromagnetic Materials, ed. by K.H.J. Buschow, E.P. Wohlfarth. Vol. 5 (Elsevier, Amsterdam, 1990), pp. 1–132
65. T. Kasuya, A. Yanase: Rev. Mod. Phys. **40**, 684 (1968)
66. E.L. Nagaev: Physi. Status Solidi b **65**, 11 (1974); E.L. Nagaev: J. Magn. Magn. Mater. **110**, 39 (1992)
67. J.M. De Teresa, M.R. Ibarra, J. Blasco, J. García, C. Marquina, P.A. Algarabel, Z. Arnold, K. Kamenev, C. Ritter, R. Von Helmolt: Phys. Rev. B **54**, 1187 (1996)
68. J. Fontcuberta, B. Martínez, A. Seffar, S. Piñol, J.L. García-Muñoz, X. Obradors: Phys. Rev. Lett. **76**, 1122 (1996)
69. J.M. De Teresa, M.R. Ibarra, C. Marquina, P.A. Algarabel, J. Blasco, J. García, A. Del Moral: Phys. Rev. Lett. **76**, 3392 (1996)
70. J.M. De Teresa, C. Ritter, M.R. Ibarra, P.A. Algarabel, J.L. García-Muñoz, J. Blasco, J. García, C. Marquina: Phys. Rev. B **56**, 3317 (1997)
71. E.J.W. Verwey, P.W. Haayman: Physica **8**, 979 (1941)
72. J. García, G. Subías, M.G. Proietti, H. Renevier, Y. Joly, J.L. Hodeau, J. Blasco, M.C. Sánchez, J.F. Bérar: Phys. Rev. Lett. **85**, 578 (2000)
73. K.I. Kugel, D.I. Khomskii: Usp. Fiz. Nauk **136**, 621 (1982) [Sov. Phys. Uspekhi **25**, 231 (1982)]
74. Y. Tokura, N. Nagaosa: Science **288**, 462 (2000)
75. C.H. Chen, S.W. Cheong: Phys. Rev. Lett. **76**, 4042 (1996)
76. M.R. Ibarra, J.M. De Teresa, J. Blasco, P.A. Algarabel, C. Marquina, J. García, J. Stankiewicz, C. Ritter: Phys. Rev. B **56**, 8252 (1997)
77. H. Kuwahara, Y. Tokura: First-order insulator–metal transitions in perovskite manganites with charge-ordering instability. In: Colossal Magnetoresistance Charge Ordering and Related Properties of Manganese Oxides, ed. by C.N.R. Rao, B. Raveau (World Scientific, Singapore, 1998), pp. 217–239
78. H. Yoshizawa, H. Kawano, Y. Tomioka, Y. Tokura: Phys. Rev. B **52**, 13145 (1995)
79. M.R. Lees, J. Barratt, G. Balakrishnan, D.M.K. Paul, M. Yethiraj: Phys. Rev. B **52**, 14303 (1995)
80. Y. Tomioka, H. Kuwahara, A. Asamitsu, M. Kasai, Y. Tokura: Appl. Phys. Lett. **70**, 3609 (1997)
81. C. Marquina, M.R. Ibarra, A.I. Abramovich, A.V. Michurin, L.I. Koroleva: J. Magn. Magn. Mater. **226**, 999 (2000)
82. J.M. De Teresa, M.R. Ibarra, P. Algarabel, B. García-Landa, C. Marquina, C. Ritter, A. Maignan, C. Martin, B. Raveau, A. Kurbakov, V. Trounov: Phys. Rev. B **65**, 100403 (2002)

5

Interplay of Spin, Charge, and Lattice in CMR Manganites and HTSC Cuprates

T. Egami

5.1 Introduction

In the field of electronics technology oxides have been primarily used only as insulators, such as native SiO_2, or as magnetic materials, for instance ferric oxides as recording media and recording heads. For semiconductors doped silicon has been used almost exclusively, and simple metals, such as aluminum, copper and gold, have been used for contacts and connectors. This practice, however, could change dramatically in the next decade or so. Firstly, high-temperature superconductivity (HTSC) was discovered in the cuprates by Bednorz and Müller [1]. This was a major surprise, since majority of oxides are insulators or poor conductors. Then the so-called colossal magnetoresistivity (CMR) was observed in some manganites [2]. These discoveries could be harbingers for oxides to become mainstream electronic materials in the future.

These functional oxides are not simple oxides such as SiO_2 or Al_2O_3, but are complex oxides composed of many elements including transition metals, and usually have a complex lattice structure. Not only is the lattice structure complex but also the physical interactions in these solids are complex, involving spin, charge, orbital, and lattice degrees of freedom. The remarkable properties of these complex oxides originate from the interplay, i.e., competition and collaboration, among these multiple degrees of freedom. Such a state of strongly interacting forces was rarely encountered in the history of the condensed matter research, where most phenomena were explained in terms of the linear response to small perturbation. Understanding of these competing forces requires the use of a multitude of novel experimental techniques and new theoretical approaches, usually involving extensive numerical simulations.

A major difficulty often faced in studying these intertwined multiple degrees of freedom is that complexity of the phenomena often conceals the true order parameter. In particular, disorder in the system tends to have much more profound effects than in simple systems, leading to localization of the effects and destroying the long-range order. Thus the conventional experimental

and theoretical approaches that rely on the long-range order are frequently ineffective, and we need *local* approaches to separate intertwined forces. In this chapter we describe how the pulsed neutron atomic pair-density function (PDF) approach has facilitated understanding of the mechanism of the ionic size effect on the CMR manganites and the spin–charge stripes in the cuprates, and how PDF measurements and inelastic pulsed neutron scattering measurements of phonons revealed involvement of phonons in the HTSC phenomenon.

5.2 Stability of Polaronic Phase in the CMR Manganites

5.2.1 Colossal Magnetoresistivity

Certain transition metal oxides such as manganites $A_{1-x}A'_xMnO_3$, where A is a trivalent ion (rare earths) and A′ is a divalent ion (alkali earth or Bi and Pb), undergo a phase transition from a paramagnetic or antiferromagnetic insulator to a ferromagnetic metal. Near the point of the metal–insulator transition (MIT), an applied magnetic field can induce the ferromagnetic transition and thus can greatly change the resistivity. This effect, called CMR [2], was extensively studied during the last ten years as a representative case of unusual properties of complex oxides fueled by the possibility of application. The basic properties of the oxides involved have been known for a long time, going back to the pioneering study by Jonker and Van Santen [3]. Initially the MIT in the manganites was considered to be caused purely by the magnetic interaction; metallic conduction is possible only in the ferromagnetic state, while in the paramagnetic state spin scattering causes high resistivity and creates spin polarons. This simple view was first questioned by Millis et al. [4] who advocated the need for considering other interactions to confine and localize charge carriers as polarons, most likely the lattice contribution involving the Jahn–Teller (JT) effect, to fully explain the experimental results.

The lattice contribution to polarons was soon experimentally confirmed by various local probes [5–8]. For instance a Mn^{3+} ion in insulating $LaMnO_3$ has four *d*-electrons in the $t_{2g}{}^3$-$e_g{}^1$ high-spin configuration. Because of the singly occupied e_g level this ion is JT active, and the MnO_6 octahedron becomes elongated along one axis. In this case there are two Mn–O bond lengths, four short (∼1.95 Å) and two long (∼2.1 Å) within the MnO_6 octahedron. On the other hand a Mn^{4+} ion has no e_g electron, so that the MnO_6 octahedron retains cubic symmetry and all the six Mn–O neighbor distances are the same. If doped holes in $La_{1-x}Ca_xMnO_3$ are localized to form polarons they affect the lattice structure by locally reducing the JT distortion. But unless polarons form a long-range order such changes in the local JT distortion cannot be easily detected by the standard diffraction methods. On the other hand the local structural probes, such as the atomic PDF analysis of neutron diffraction or the extended X-ray absorption fine structure (EXAFS) method, convincingly

demonstrated that the local JT distortion exists at some Mn sites but not at others. The Mn sites without or reduced JT distortion must coincide with the sites with localized holes.

5.2.2 Pulsed Neutron PDF Method

The structure of a crystal is defined by its symmetry, lattice parameters, and atomic positions within the unit cell, all of which can be determined by measuring the position and the intensity of the Bragg diffraction peaks. Thus usually structure determination implies the analysis of the Bragg peaks in the diffraction pattern. However, real crystals are never perfect and contain lattice defects. In complex systems such as the CMR oxides electron–lattice interaction causes local changes in the lattice structure and destroys translational symmetry, but such local changes are not directly reflected in the crystal structure. These short-range deviations from the perfect lattice structure produce diffuse scattering [9]. If the diffuse scattering forms a broad peak, the position of the peak indicates the periodicity of the superstructure and the width gives the information on the structural correlation length. But in order to determine the actual deviations, for instance in terms of atomic displacements, many diffuse scattering peaks have to be studied and analyzed. While such studies are possible and useful information has been obtained [10], a simpler and more reliable approach is to use the PDF analysis.

In the PDF analysis the powder diffraction intensities are determined with neutrons and X-rays with relatively high energies up to a large momentum transfer, Q ($=4\pi \sin\theta/\lambda$, θ is the diffraction angle and λ is the wavelength of the scattering probe), and the results are Fourier-transformed to obtain the atom–atom correlation function after correction for absorption and other factors [11]. The pair-density function, $\rho(r)$, is defined by

$$\rho(r) = \rho_0\, g(r) = \frac{1}{4\pi N r^2} \sum_{i,j} \delta(r - r_{ij})\,, \tag{5.1}$$

where r_{ij} is the distance between atoms i and j, ρ_0 is the number density of atoms, and N is the number of atoms in the system. It is customary to call $g(r)$ the pair-distribution function, and $4\pi r^2 \rho_0 g(r)$ the radial-distribution function (RDF). They are obtained from the diffraction data by

$$\rho(r) = \rho_0 + \frac{1}{2\pi^2 r} \int_0^\infty [S(Q) - 1] \sin(Qr)\, Q \,\mathrm{d}Q\,, \tag{5.2}$$

where $S(Q)$ is the normalized structure function determined by powder diffraction measurement.

In powder diffraction measurement *all* the diffuse scattering intensities are measured in addition to the Bragg peaks, while in the case of direct

Fig. 5.1. The Neutron Powder Diffractometer (NPDF) of the Lujan Center, Los Alamos National Laboratory, during the upgrading work supported by the National Science Foundation DMR00-76488. A large backscattering detector frame for position-sensitive ^{3}He detectors is seen with a technician inside

measurement of diffuse scattering from a single crystal usually only a few peaks are chosen for measurement, since the diffuse scattering intensities are usually weak and the measurement is time consuming. Thus the PDF represents full atomic correlation, not compromised by shortcuts in the experiment. This is an important point, since it is so easy to miss critical information by not studying all the diffuse intensities. Even though the angular information is lost by powder averaging the PDF method is a valuable tool that should be used first in evaluating the local disorder.

The PDF method has long been used almost exclusively for the study of short-range order in liquids and glasses, but the advent of modern radiation sources, such as pulsed neutron sources and synchrotron radiation sources, which deliver short wavelength probes, made it possible to apply this technique on crystalline solids with strong disorder [11]. Also by the use of high Q-resolution spectrometer, such as the Neutron Powder Diffractometer (NPDF) of the Lujan Center, Los Alamos National Laboratory (Fig. 5.1), it is now possible to determine the PDF up to 200 or 300 Å as shown in Fig. 5.2, thereby seamlessly connecting the short-range structural analysis with the conventional analysis of the long-range order [12, 13]. This method has been quite effective in characterizing the local structure of CMR manganites and related oxides, and facilitating understanding of their physical properties in terms of their local structure [11, 14].

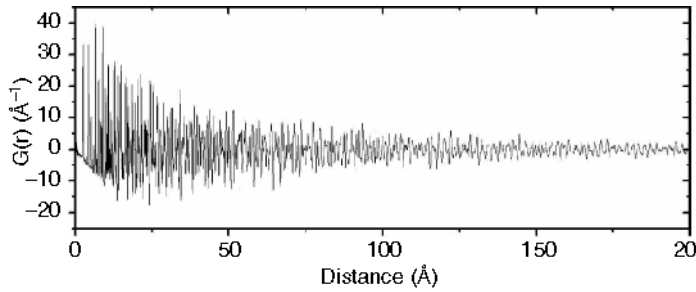

Fig. 5.2. The pair-density function (PDF) of crystalline Ni powder at $T = 10\,\mathrm{K}$ obtained by the NPDF [13]

5.2.3 Polaron Stability

While the polaron formation is central to the phenomenon of MIT in the manganites, it soon became recognized that the highly collective nature of the ground state is necessary to explain the high response to the magnetic field by the CMR manganites. In the insulating phase charges are not only confined in the polaronic state, but also form a charge-ordered state. CMR is achieved in the mesoscopic mixed phase state of charge-ordered insulator and metal [15]. Note that charge ordering and polaron formation are actually very closely related phenomena, since the charge-ordered state is simply the crystallized state of polarons (polaron lattice), rather than the charge-density waves (CDW) state driven by the Fermi surface instability. The competing forces that determine the stability of polarons, thus MIT, are the following:

1. Forces to localize charges; electron–phonon (e–p) interaction and spin correlation
2. Forces to delocalize charges; electron kinetic energy and lattice elasticity

In classical mechanics a localized static body has a lower kinetic energy, but in quantum mechanics localization results in strong local variation in the wavefunction, and thus in a higher kinetic energy. Thus electron kinetic energy prefers charge delocalization. The balance between the two forces could be expressed by the renormalized e–p coupling constant,

$$\lambda = \frac{g^2}{Kt\langle\cos\frac{\theta}{2}\rangle}\,, \tag{5.3}$$

where K is the relevant elastic constant, g is the bare e–p coupling parameter, t is the hopping integral in the tight-binding approximation and θ is the angle made by neighboring spins [16, 17]. If λ exceeds a critical value charges will be localized as polarons in the charge-ordered state.

The value of λ varies with composition, and even when the charge density is the same, it depends on the ionic size of the A-site ions, $\langle r_\mathrm{A}\rangle$ [18]. When the

value of $\langle r_A \rangle$ is large, the system is a stable ferromagnetic metal for $x < 0.5$, and when it is small it is an insulator. At the crossover state the solid is precariously balanced and the CMR behavior is observed. Therefore understanding this ionic size effect is crucial in understanding the forces that cause the CMR effect. It is generally considered that the balance is affected through the change in t, thus the electronic bandwidth [18, 19]. A large A-site ion expands the lattice and makes the Mn–O–Mn bond straight, while a small A-site ion contracts the lattice and makes the Mn–O–Mn bond buckled. In the buckled Mn–O–Mn bond the p–d overlap is reduced and the value of t is reduced accordingly. While this explanation sounds reasonable, a closer look reveals a fault in this explanation. Actually the change in the buckling angle of the Mn–O–Mn bond due to the ionic size change is rather small, and the expected change in t is too small to explain the observed drastic effect [20,21]. It is true that the manganites with small A-site ions have a narrow band, but that is a consequence of charge localization, and not the cause, because polaron formation renormalizes the electron bandwidth as shown by Holstein [22].

The true story is a bit more complex and involves the elastic field around a polaron [23, 24]. A lattice polaron is formed by displacements of neighboring ions that trap the charge carrier. In the case of the manganites these displacements are related to the JT distortion. The polaron site should have no JT distortion and has six short Mn–O bonds, while the insulating sites outside are JT distorted and have four short bonds and two long bonds as for Mn^{3+}. Thus the fraction of the sites without the JT distortion can be deduced by comparing the density of short Mn–O bonds and that of long Mn–O bonds. They can be determined by the PDF analysis. As shown in Fig. 5.3 Mn–O bonds are seen as split peaks in the neutron PDF. The peaks are negative since the neutron scattering length of Mn is negative. By evaluating the areas of these peaks the number ratio of long and short Mn–O bonds can be obtained, and the fraction of the sites with or without the local JT distortion can be calculated from the ratio. Figure 5.4 shows the fraction of the sites without the JT distortion as a function of the A-site ionic size, $\langle r_A \rangle$, evaluated by the pulsed neutron PDF study for $A_{0.7}A'_{0.3}MnO_3$ [24]. By dividing the density of sites without the local JT distortion by the charge density ($x = 0.3$) it is possible to evaluate the size of the polaron. Figure 5.4 shows that when the ionic size is small polarons occupy a single site, and as the ionic size is increased the polaron expands, and finally practically all the sites lose local JT distortion and the system becomes a homogeneous metal.

If the value of $\langle r_A \rangle$ is large and the Mn–O–Mn bond is straight this local lattice contraction associated with the loss of local JT distortion produces a long-range strain field around it as shown in Fig. 5.5a. But if the Mn–O–Mn bond is sufficiently buckled when $\langle r_A \rangle$ is small, the local lattice contraction is accommodated by the unbuckling of the bond as in Fig. 5.5b. In other words transverse phonons can screen the local strains. The effect of the long-range strain field on the polaron formation energy was evaluated using the

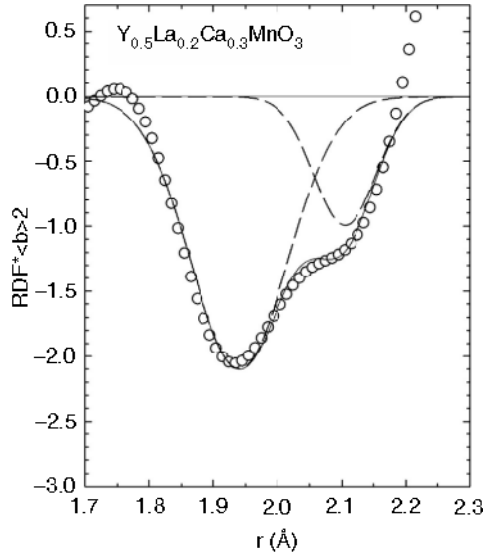

Fig. 5.3. The RDF of $Y_{0.5}La_{0.2}Ca_{0.3}MnO_3$ in the range of r from 1.7 to 2.3 Å, showing the peak for the Mn–O bonds, determined by pulsed neutron diffraction [23]. Here the RDF $= 4\pi r^2 \rho(r)$, where $\rho(r)$ is the PDF and $\langle b \rangle$ is the composition average of the neutron scattering length. The Mn–O peak can be fit by two sub-peaks corresponding to short and long Mn–O bonds

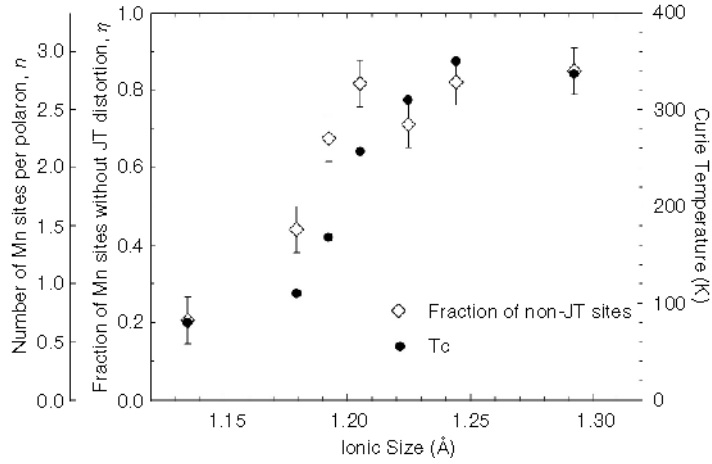

Fig. 5.4. The fraction of the Mn sites without the local Jahn–Teller distortion in $A_{0.7}A'_{0.3}MnO_3$ with various A and A′ ions, as a function of the average ionic size, $\langle r_A \rangle$, determined by the PDF analysis of the pulsed neutron diffraction data [24]. It gives the size of the polaron when divided by the charge density in terms of the number of Mn sites involved

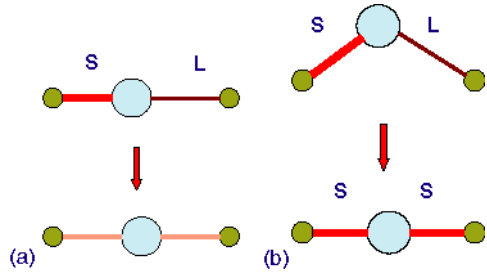

Fig. 5.5. The mechanism of local accommodation of polaronic strain. When the Mn–O–Mn bond is straight, loss of local Jahn–Teller distortion reduces the long (L) Mn–O bond to a short (S) one and creates a long-range stress field (**a**). However, when the Mn–O–Mn bond is sufficiently buckled, unbuckling locally accommodates the polaronic strain, and the long-range stress field will not be created (**b**) [23]

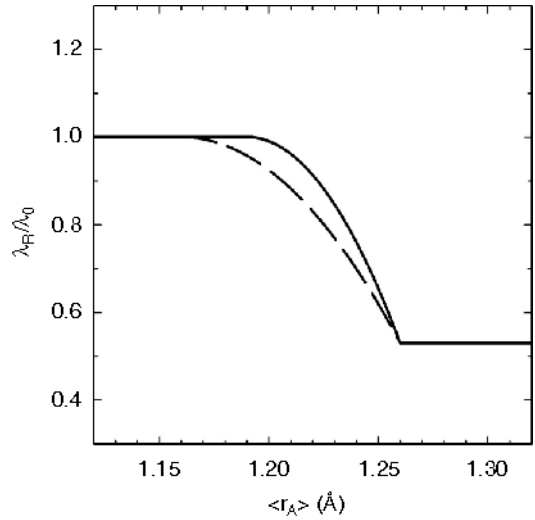

Fig. 5.6. The effective electron–lattice coupling parameter normalized to the single-site value without the long-range stress field. The effect of the long-range stress field is to reduce the effective coupling parameter, since the energy to create a polaron is increased. The dashed line is for a slightly different choice of critical parameters [23]

continuum approximation by Eshelby [23]. It was found that the presence or absence of the long-range strain field changes the effective coupling constant λ by nearly a factor of 2, as shown in Fig. 5.6 [23]. In other words what changes with the A-site ionic size is not the value of t, but the effective value of K. This example shows that the details of the local atomic structure can have profound effects on the properties of complex oxides by affecting the balance among the competing forces.

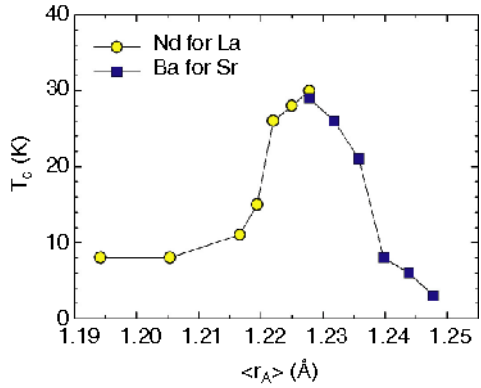

Fig. 5.7. Dependence of the superconductive transition temperature, T_C, on the ionic size of the site for La/Nd and Sr/Ba due to the formation of the stripe state [23, 26, 27]

5.3 Stability of Spin–Charge Stripes in the Cuprates

In some cuprate compounds doped charges are localized in the spin–charge stripes composed of charged stripes and antiferromagnetic stripes [25]. The stability of the stripes also depends on the ionic size as well as charge density [25], and the size effect can be explained by the same mechanism just discussed for the CMR manganites [23]. For example, in the system $(La,Nd)_{1.88}(Sr,Ba)_{0.12}CuO_4$ with the hole density $x \simeq 1/8$ the superconducting critical temperature, T_C, depends strongly on the ionic size as shown in Fig. 5.7, and the stripes are observed when T_C is suppressed, suggesting that the stripes and superconductivity compete against each other [26, 27].

Doped holes enter the hybridized $Cu(d_{x^2-y^2})$–$O(p_x)$ anti-bonding σ-orbital, thus when holes are localized they reduce the local Cu–O bond distance. Indeed the Cu–O distance in the averaged lattice structure changes from 1.903 Å in La_2CuO_4 [28] to 1.889 Å in $La_{1.85}Sr_{0.15}CuO_4$ [29] and 1.882 Å in $La_{1.8}Sr_{0.2}CuO_4$ [30], all at 10 K, indicating contraction of about 0.1 Å for each hole. Since the linear hole density in the stripe is 50%, if all the holes are in the single row of oxygen or copper the Cu–O bond will contract by 0.05 Å. Figure 5.7 shows that the optimum state is achieved for $\langle r_A \rangle = 1.237$ Å, and when $\langle r_A \rangle$ is reduced by 0.07 Å the stripe structure becomes stable. This change in the La/Nd–O distance corresponds to the change in the Cu–O distance of 0.05 Å, exactly the amount expected. Thus if this much of a change in the Cu–O distance can be accommodated by the unbuckling of the Cu–O–Cu bond, the stripe state can be stabilized. If the Cu–O–Cu bond is nearly straight and the contraction of the Cu–O bond creates a long-range stress field, the cost of the elastic energy to create the stripe state suppresses the stripes and superconductivity remains alive. When a large Ba ion ($r_A = 1.47$ Å [31])

is added instead of Sr, it expands the Cu–O–Cu bond locally, allowing it to become bifurcated and stabilizing the stripes. This analysis demonstrates that the same strain accommodation mechanism explains both the CMR phenomenon in the manganites and the stability of the stripes in the cuprates.

5.4 Electron–Phonon Coupling and Mechanism of Superconductivity in the Cuprates

5.4.1 Local Lattice Distortion and Inhomogeneous Electronic States

For a long time the majority opinion on the microscopic mechanism of HTSC in the cuprates has been that it is a purely electronic phenomenon, probably described by the t–J Hamiltonian, and the lattice has no role [32]. However, recent evidences [33–35] are seriously beginning to challenge this long-held opinion by the majority. Indeed a large number of studies indicate that the lattice of the cuprates has local distortion, which changes near the superconducting transition temperature, T_{C}, or the pseudo-gap temperature, T_{PG} [36,37]. It is even possible that the lattice plays a crucial role in the HTSC phenomenon.

Local structural probes suggest that below a certain temperature the local environment of Copper ion appears to show two distinct configurations, possibly corresponding to fully doped and strongly underdoped states [38,39]. The appearance of these two components is consistent with the presence of spin–charge stripe structure, but the evidence for the existence of such a structure is weak. The earlier discussion on the stripes suggests that unless the ionic size is favorable strong charge localization into the stripe structure is not likely to take place. It is more likely that weaker localization into some nanoscale domains with different charge densities is taking place. Indeed beautiful scanning tunneling microscopy–scanning tunneling spectroscopy (STM–STS) observations [34,35] revealed the presence of such nano-scale electronic inhomogeneity. While there are still some controversies regarding the STM results on the effect of surface, it is now generally accepted that in the cuprates the presence of electronic inhomogeneity does not interfere with superconductivity for some mysterious reason. However, not everybody agrees that the electronic inhomogeneity is necessary for superconductivity to occur. An experiment that would give an answer to this point will have an enormous impact.

5.4.2 Electron–Phonon Coupling in the Cuprates

The observation of local lattice distortion associated with electronic inhomogeneity obviously implies coupling of the lattice with the electrons, but it could merely be a consequence of electronic inhomogeneity, rather than the cause. On the other hand more direct evidence of strong e–p coupling was found in the angle-resolved photoemission spectroscopy (ARPES) study [33].

It is particularly important that the ARPES result showed that the e–p coupling is strong only for a particular branch of the phonons, the Cu–O bond-stretching longitudinal optical (LO) modes toward the zone-boundary half-breathing mode (Fig. 5.8) that shows strong softening with doping and anomalous temperature dependence [40–44]. Inelastic neutron scattering study of the phonons in $YBa_2Cu_3O_{6.95}$ has shown that a shift in the spectral intensity of scattering occurs with temperature [44]. In the energy range related to the Cu–O bond-stretching LO modes intensities are transferred from the range around 62 meV to the range around 53 meV as temperature is reduced. To illustrate this change the inelastic neutron scattering intensity was measured at various temperatures at $\boldsymbol{Q} = (3.25, 0, 0)$ in the units of reciprocal lattice vectors, or $\boldsymbol{q} = (\pi/2, 0, 0)$ in the phonon vector in the units of inverse lattice parameter. Figure 5.9 shows the difference in the average intensity from 51 to 55 meV, I(1), and from 56 to 68 meV, I(2), as a function of temperature [44]. The change occurs below about 90 K, close to $T_C = T_{PG}$ (=93 K). For $YBa_2Cu_3O_{6.95}$ ($T_C = 60$ K) a similar change starts around 150 K ($\simeq T_{PG}$), so that the change must be related to the pseudo-gap temperature, rather than T_C.

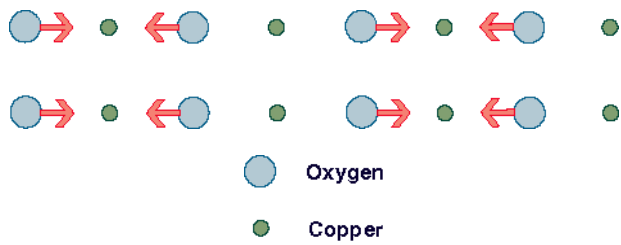

Fig. 5.8. In plane Cu–O half-breathing mode at $\boldsymbol{q} = (\pi, 0)$

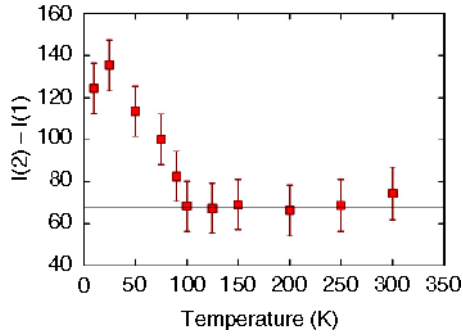

Fig. 5.9. Difference in the average inelastic neutron scattering intensity from a single crystal of $YBa_2Cu_3O_{6.95}$ at $\boldsymbol{Q} = (3.25, 0, 0)$, from 51 to 55 meV, I(2), and from 56 to 68 meV, I(1), as a function of temperature [44]. T_C is 93 K for this sample

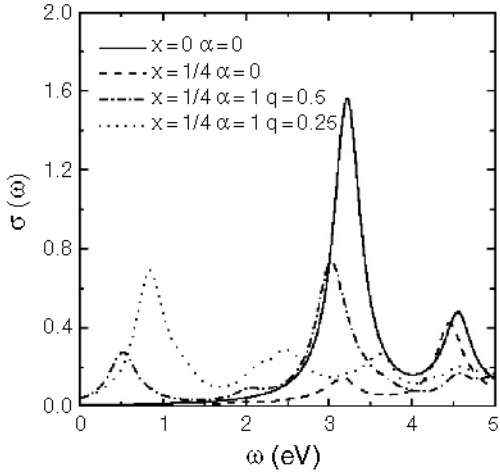

Fig. 5.10. Optical conductivity of the Cu–O chain with and without doping ($x = 0, 0.25$) and with and without e–p coupling ($\alpha = 0, 1$) for the phonon with $q = 0.25$ and 0.5, calculated for a one-dimensional Hubbard model [48]. Note that the effect of phonon is found up to a large energy range

Such a strong e–p coupling of the Cu–O bond-stretching mode was theoretically predicted [45,46]. In simple metals the lattice vibration can be described in terms of the deformation potential, which is almost totally screened by free electrons, except for the Friedel oscillation. In the cuprates the screening length is longer than the interatomic distances because of low charge density, and Cu and O maintain their ionicity. Thus the d-orbitals of Cu and the p-orbitals of O move with the nuclei, so that the change in the interatomic distance between Cu and O due to lattice vibrations changes the p–d overlap. This changes the hopping integral, t, between Cu and O, in the mechanism known as the Su–Schrieffer–Heeger (SSH) coupling [47]. For simple metals the effect of phonons is limited to the electrons close to the Fermi level within the phonon frequency $\omega_{\rm ph}$. However, in the cuprates the effect extends up to many eVs away from the Fermi level, since the whole band structure is modified by the phonons. Consequently the optical conductivity is modified up to high energy scale as shown in Fig. 5.10 as calculated with the Hubbard model with the SSH coupling [48]. It was found that the optical conductivity is modified up to a large energy scale by superconductive transition and this was argued to be the evidence for an electronic mechanism [49–51]. However, this result suggests that the change in the optical conductivity with the onset of superconductivity is perfectly consistent with the phonon mechanism.

It is interesting to note that in ferroelectric oxides, such as $BaTiO_3$, this SSH coupling produces electronic polarization as large as the ionic polarization [52, 53]. In the ionic state Ti^{4+} and O^{2-} have d^0 and p^6 orbital occupation, but upon forming a covalent bond they hybridize to form a p–d orbital. Ti–O

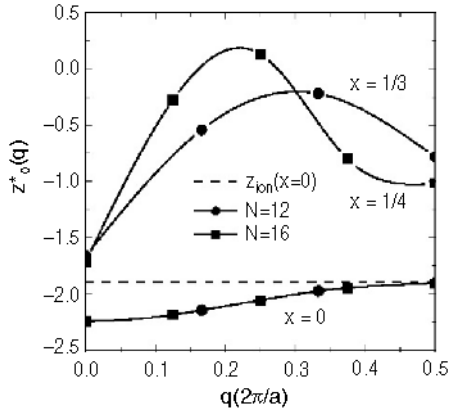

Fig. 5.11. The q dependence of the effective charge of oxygen in the 1-d Hubbard model due to the LO phonon mode, calculated for the ring of $N = 12$ sites with doping level $x = 0, 1/3$ and for $N = 16$ with $x = 0, 1/4$. The dashed line indicates the ionic value (static charge) [48]

bond-stretching phonons modify this p–d overlap, thus t between Ti and O. If the Ti–O distance is reduced the p–d overlap will increase, and electron will be transferred from O to Ti. The current due to the charge transfer produces the electronic polarization [52, 53]. In the doped cuprates, on the other hand, reducing the distance between Cu and O results in the transfer of holes, rather than electrons, and the resulting electronic polarization has an opposite sense as the ionic polarization as shown in Fig. 5.11 [48]. It is noted that for the titanates the electronic polarization is maximum at $q = 0$, resulting in uniform ferroelectric polarization, but in the doped cuprates it is large at a finite wavevector q, roughly corresponding to $2k_{\mathrm{F}}$, where k_{F} is the Fermi momentum. The maximum electronic polarization is as large as the ionic polarization, just as in the case of the titanates. This explains the strong e–p coupling of the Cu–O bond-stretching mode for $q > 0$. Moreover, the phonon-induced charge transfer is spin polarized due to the strong electron correlation effect, and therefore the phonon strongly modifies the spin excitation energies and spin correlations [48]. This extra spin–phonon coupling may justify calling the e–p coupling in this system unconventional.

5.4.3 Vibronic Mechanism of High Temperature Superconductivity

The earlier discussions above demonstrate the unconventional nature of the e–p coupling for the Cu–O bond-stretching mode in the cuprates, but would it be strong enough to explain the high temperature superconductivity? Within

the framework of the Bardeen Cooper and Schrieffer (BCS) mechanism [54] the answer is almost certainly negative. The charge carrier density is low, and the e–p coupling estimated from the ARPES data [33] is not strong enough to explain the value of T_C over 100 K. However, if phonons were to contribute to the HTSC, it is not likely to be through the conventional BCS mechanism. The BCS theory assumes the Fermi level of electrons to be far larger than the phonon energy, and thus the Fermi velocity is much greater than the sound velocity, and the Migdal theorem [55] applies. However, the carriers that show a large superconducting gap are around the $(\pi, 0)$ point, which is a saddle point and has a zero velocity. Furthermore the strong electronic spatial inhomogeneity observed by the STM–STS suggests that the BCS picture of fast electrons interacting with the phonon once may not be appropriate.

The possible importance of spatial inhomogeneity was first suggested by Gor'kov [56], and was extensively discussed by Phillips [57–59] and by Bianconi [38, 60]. The idea is that inhomogeneity results in charge confinement that produces jumps in electron dispersion and a high density of states (DOS) at the Fermi level (shape resonance). Phillips further speculated that the resultant superconductivity is highly inhomogeneous, and has filamental character, which seems to be true for underdoped samples.

While these arguments assume a conventional e–p coupling with Fermi liquid, it is possible that the e–p coupling is unconventional and nonadiabatic. As a result of confinement the group velocity of electrons is further reduced. If it is comparable to the sound velocity the Migdal theorem is no longer valid, and we have to consider a resonant, nonadiabatic vibronic coupling in real space [61, 62]. Superconductivity due to real space pairs was proposed by Schafroth [63]. Due to mathematical difficulties his theory could not be advanced as much as the BCS theory at that time, but with modern computers it may now be possible to go beyond what has been done nearly a half century ago. Here we briefly sketch the idea of vibronic pairing that could explain the HTSC phenomenon.

Coupling of the wave packet of the half-breathing phonon to the electron wave packets, made of regions in k space around four reciprocal lattice points equivalent to the $(\pi, 0)$ point, could lead to formation of phonon-induced vibronic two-hole bound states with each hole in two different sublattices, thereby reducing the repulsive Coulomb energy and gaining the exchange energy [64]. Strong vibronic coupling of such a bound state can result in large values of T_C [62]. The spatial extent of such a bound state is determined by the area of the flat band in the k space near the $(\pi, 0)$ point, and would form domains of 20–30 Å in size, in agreement with the STM observation. Such a bound state could be the origin of the electronic inhomogeneity. In between the bound states hole-poor regions will develop antiferromagnetic spin correlations, which can create a pseudo-gap. Since the bound state can be formed stably only when the Fermi surface is close to the saddle point of electron dispersion, forming a bridge around the $(\pi, 0)$ point. In strongly underdoped systems small Fermi surfaces are formed around the (π, π) points

and the energy at the $(\pi, 0)$ point is low, which makes the bound state unstable. In the overdoped state a large Fermi surface is formed and the energy at the $(\pi, 0)$ point is high, again making the bound state unstable. Thus the phonon-induced vibronic bound state can be formed only in the intermediate hole densities when the Fermi level is close to the saddle point, explaining why T_C forms a dome as a function of doping [64]. While this scenario needs further development and experimental and theoretical verification, it appears to explain so many properties of this complex system, and is worth pursuing further.

5.5 Conclusions

It is clear that the complex interplay of spin, charge, orbital, and lattice degrees of freedom is the underlying mechanism that produces remarkable properties such as HTSC and CMR in transition metal oxides. In trying to disentangle this intertwined state of multiple variables we have to deal with all these factors together on the same footing. Such an approach, however, marks strong departure from the past practice, where we usually start from the state well defined by a dominant interaction, and take into account of less dominant forces by perturbation. In some cases we can start from the balanced state defined by the mean-field approximation and correct for the deviations. However, collective effects of multiple degrees of freedom can render the mean-field approximation invalid, particularly in the close vicinity of the critical point. A novel approach, which appears to be more effective in this new world of complexity, is the local approach, both in experiment and theory.

As examples of local approach we discussed two subjects, the polaron stability in the CMR manganites and the vibronic mechanism of high temperature superconductivity. The latter is a mere speculation at this moment, and further research is warranted to test this scenario. When we succeed in constructing a full theory of the vibronic mechanism it could form a new platform for the science of strongly interacting complex systems. The research in this field is important and exciting even for this reason alone.

Acknowledgments

The author acknowledges his collaborators, in particular, D. Louca, P. Piekarz, M. Tachiki, J.-H. Chung, R.J. McQueeney, M. Arai, M. Yethiraj, H.A. Mook, C. Frost, S. Tajima and Y. Endoh for their contributions, and K.A. Müller, J.B. Goodenough, L. Gor'kov, J.C. Phillips, P.W. Anderson, A. Bussmann-Holder, N. Nagaosa, M. Khomoto, Z.-X. Shen, A. Lanzara, D. Mihailovic, E. Weger, J.J. Tu, E.W. Plummer, A.R. Bishop, and P. Dai for valuable insights, discussions, and comments. This work was supported by the National Science Foundation through DMR01-02565.

References

1. J.G. Bednorz, K.A. Müller: Z. Phys. B **64**, 189 (1986)
2. S. Jin, T.H. Tiefel, M. McCormack, R.A. Fastnacht, R. Ramesh, L.H. Chen: Science **264**, 413 (1994)
3. G.H. Jonker, J.H. Van Santen: Physica **16**, 337 (1959); J.H. Van Santen, G.H. Jonker: Physica **16**, 599 (1950)
4. A.J. Millis, P.B. Littlewood, B.I. Shraiman: Phys. Rev. Lett. **74**, 5144 (1995)
5. S.J.L. Billinge, R.G. DiFrancesco, G.H. Kwei, J.J. Neumeier, J.D. Thompson: Phys. Rev. Lett. **77**, 715 (1996)
6. C.H. Booth, F. Bridges, G.J. Snyder, T.H. Geballe: Phys. Rev. B **54**, R15606 (1996)
7. D. Louca, T. Egami, E.L. Brosha, H. Röder, A.R. Bishop: Phys. Rev. B **56**, R8475 (1997)
8. D. Louca, T. Egami: Phys. Rev. B **59**, 6193 (1999)
9. L. Vasiliu-Doloc, S. Rosenkranz, R. Osborn, S.K. Sinha, J.W. Lynn, J. Mesot, O.H. Seeck, A.J. Fedro, J.F. Mitchell: Phys. Rev. Lett. **83**, 4393 (1999)
10. B.J. Campbell, S.K. Sinha, R. Osborn, S. Rosenkranz, L. Vasiliu-Doloc, J.F. Mitchell, Z. Islam, O.H. Seeck, J.W. Lynn: Phys. Rev. B **67**, 020409 (2003)
11. T. Egami, S.J.L. Billinge: Underneath the Bragg Peaks: Structural Analysis of Complex Materials (Pergamon, Oxford, 2003)
12. T. Proffen, T. Egami, S.J.L. Billinge, A.K. Cheetham, D. Louca, J.B. Parise: Appl. Phys. A **74**, S163 (2002)
13. T. Egami: Z. Kristallogr. **219**, 122 (2004)
14. T. Egami, in: Structure and Bonding, ed. by J.B. Goodenough, Vol. 98 (Springer, Berlin Heidelberg New York, 2001), p. 115
15. E. Dagotto, T. Hotta, A. Moreo: Phys. Rep. **344**, 1 (2001)
16. H. Röder, J. Zang, A.R. Bishop: Phys. Rev. Lett. **76**, 1356 (1996)
17. A.J. Millis, B.I. Shraiman, R. Mueller: Phys. Rev. Lett. **77**, 175 (1996)
18. H.Y. Hwang, S.W. Cheong, P.G. Radaelli, M. Marezio, B. Batlogg: Phys. Rev. Lett. **75**, 914 (1995)
19. A.P. Ramirez: J. Phys.: Condens. Matter **9**, 8171 (1997)
20. P.G. Radaelli, M. Marezio, H.Y. Hwang, S.W. Cheong, B. Batlogg: Phys. Rev. B **54**, 8992 (1996)
21. J.A. Fernandez-Baca, P. Dai, H.Y. Hwang, C. Kloc, S.W. Cheong: Phys. Rev. Lett. **80**, 4012 (1998)
22. T. Holstein: Ann. Phys. (Paris) **8**, 325 (1959)
23. T. Egami, D. Louca: Phys. Rev. B **65**, 094422 (2002)
24. D. Louca, T. Egami, W. Dmowski, J.F. Mitchell: Phys. Rev. B **64**, R180403 (2001)
25. J.M. Tranquada, B.J. Sternlieb, J.D. Axe, Y. Nakamura, S. Uchida: Nature (London) **375**, 561 (1995)
26. M.K. Crawford, R.L. Harlow, E.M. McCarron, W.E. Farneth, J.D. Axe, H. Chou, Q. Huang: Phys. Rev. B **44**, 7749 (1991)
27. Y. Maeno, N. Kakei, Y. Tanaka, T. Tomita, F. Nakamura, T. Fujita, in: Lattice Effects in High-T_C Superconductors, ed. by Y. Bar-Yam, T. Egami, J.M. de Leon, A.R. Bishop (World Scientific, Singapore, 1992), p. 542
28. J.D. Jorgensen, B. Dabrowski, S. Pei, D.G. Hinks, L. Soderholm, B. Morosin, J.E. Schirber, E.L. Venturini, D.S. Ginley: Phys. Rev. B **38**, 11337 (1988)

29. R.J. Cava, A. Santoro, D.W. Johnson, W.W. Rhodes: Phys. Rev. B **35**, 6716 (1987)
30. P.G. Radaelli, D.G. Hinks, A.W. Mitchell, B.A. Hunter, J.L. Wagner, B. Dabrowski, K.G. Vandervoort, H.K. Viswanathan, J.D. Jorgensen: Phys. Rev. B **49**, 4163 (1994)
31. R.D. Shannon: Acta. Crystallogr. A **32**, 751 (1976)
32. P.W. Anderson: The Theory of Superconductivity in the High-T_C Cuprates (Princeton University Press, Princeton, 1997)
33. A. Lanzara, P.V. Bogdanov, X.J. Zhou, S.A. Kellar, D.L. Feng, E.D. Lu, T. Yoshida, H. Eisaki, A. Fujimori, K. Kishio, J.I. Shimoyama, T. Noda, S. Uchida, Z. Hussain, Z.X. Shen: Nature (London) **412**, 510 (2001)
34. S.H. Pan, J.P. O'Neal, R.L. Badzey, C. Chamon, H. Ding, J.R. Engelbrecht, Z. Wang, H. Eisaki, S. Uchida, A.K. Gupta, K.W. Ng, E.W. Hudson, K.M. Lang, J.C. Davis: Nature (London) **413**, 282 (2001)
35. K.M. Lang, V. Madhavan, J.E. Hoffman, E.W. Hudson, H. Eisaki, S. Uchida, J.C. Davis: Nature (London) **415**, 412 (2002)
36. T. Egami, S.J.L. Billinge, in: Physical Properties of High Temperature Superconductors V, ed. by D. Ginsberg (World Scientific, Singapore, 1996), p. 265
37. N.L. Saini, H. Oyanagi, T. Ito, V. Scagnoli, M. Filippi, S. Agrestini, G. Campi, K. Oka, A. Bianconi: Eur. Phys. J. B **75**, 36 (2003)
38. A. Bianconi, N.L. Saini, A. Lanzara, M. Missori, T. Rossetti, H. Oyanagi, H. Yamaguchi, K. Oka, T. Ito: Phys. Rev. Lett. **76**, 3412 (1996)
39. E.S. Bozin, G.H. Kwei, H. Takagi, S.J.L. Billinge: Phys. Rev. Lett. **84**, 5856 (2000)
40. L. Pintschovius, N. Pyka, W. Reichardt, A.Y. Rumiantsev, N.L. Mitrofanov, A.S. Ivanov, G. Collin, P. Bourges: Physica C **185–189**, 156 (1991)
41. L. Pintchovius, W. Reichardt, in: Physical Properties of High Temperature Superconductors IV, ed. by D. Ginsberg (World Scientific, Singapore, 1994), p. 295
42. R.J. McQueeney, Y. Petrov, T. Egami, M. Yethiraj, G. Shirane, Y. Endoh: Phys. Rev. Lett. **82**, 628 (1999)
43. T. Egami, J.H. Chung, R.J. McQueeney, M. Yethiraj, H.A. Mook, C. Frost, Y. Petrov, F. Dogan, Y. Inamura, M. Arai, S. Tajima, Y. Endoh: Physica B **62**, 316 (2002)
44. J.H. Chung, T. Egami, R.J. McQueeney, M. Yethiraj, M. Arai, T. Yokoo, Y. Petrov, H.A. Mook, Y. Endoh, S. Tajima, C. Frost, F. Dogan: Phys. Rev. B **67**, 014517 (2003)
45. S. Ishihara, T. Egami, M. Tachiki: Phys. Rev. B **55**, 3163 (1997)
46. Y. Petrov, T. Egami: Phys. Rev. B **58**, 9485 (1998)
47. W.P. Su, J.R. Schrieffer, A.J. Heeger: Phys. Rev. Lett. **42**, 1698 (1979)
48. P. Piekarz, T. Egami: Phys. Rev. B **72**, 054530 (2005)
49. D.N. Basov, E.J. Singley, S.V. Dordevic: Phys. Rev. B **65**, 054516 (2002)
50. H.J.A. Molegraaf, C. Presura, D. van der Marel, P.H. Kes, M. Li: Science **295**, 2239 (2002)
51. A.F. Santander-Syro, R.P.S.M. Lobo, N. Bontemps, Z. Konstantinovic, Z.Z. Li, H. Raffy: Eur. Phys. Lett. **62**, 568 (2003)
52. R.D. King-Smith, D. Vanderbilt: Phys. Rev. B **47**, 1651 (1993)
53. R. Resta: Rev. Mod. Phys. **66**, 899 (1994)
54. J.R. Schrieffer: Theory of Superconductivity (Benjamin, New York, 1964)
55. A.B. Migdal: Sov. Phys. JETP **1**, 996 (1958)

56. L.P. Gor'kov, A.V. Sokol: JETP Lett. **46**, 420 (1987)
57. J.C. Phillips: Phys. Rev. B **41**, 8968 (1990)
58. J.C. Phillips: Phys. Rev. Lett. **88**, 216401 (2002)
59. J.C. Phillips, A. Saxena, A.R. Bishop: Rep. Prog. Phys. **66**, 2111 (2003)
60. A. Bianconi: Int. J. Mod. Phys. B **14**, 3289 (2000)
61. J.B. Goodenough, J. Zhou: Phys. Rev. B **42**, 4276 (1990)
62. M. Tachiki, M. Machida, T. Egami: Phys. Rev. B **67**, 174506 (2003)
63. M.R. Schafroth: Phys. Rev. **111**, 1958 (72)
64. T. Egami: J. Phys. Chem. Solids, in press

6

Neutron Scattering Studies of Anomalous Phonon Behavior in Functional Materials

S.M. Shapiro

6.1 Introduction

Functional materials can be defined as those materials with crucial materials properties that are primarily the output arising from the electrical, magnetic, or mechanical responses to changes in the environment, such as temperature, stress, electrical or magnetic fields. These materials differ from what are called structural materials, which are utilized for their strength and other mechanical properties. In most cases the strong response of the useful functional materials arises from the proximity of operating conditions to a phase transition in these materials, such as metal–insulator (MI) transitions, the onset of ferroelectricity, ferromagnetism, superconductivity or structural transitions such as martensitic phase transitions in shape-memory alloys. These phase transitions, together with their associated functional responses are known to be highly sensitive to the presence of impurities, alloying additions, crystalline defects and their state of organization, i.e., to the atomic scale structures, nanostructures and microstructures.

In this chapter the focus will be on the magnetic and structural properties of several functional materials with particular emphasis on characterizing their properties by inelastic neutron scattering. We shall consider the strong interaction between the lattice and the electronic or magnetic properties of the material as revealed by studying the lattice dynamics of the system. First there will be a brief description of the neutron scattering technique and what is measured followed by a discussion of the types of phonon anomalies occurring as a result of electron–phonon coupling. Examples from the literature will be given of these interactions observed in the giant or colossal magnetoresistance materials and high temperature superconductors. The chapter will conclude with a discussion of the anomalous phonon behavior observed in magnetic shape memory alloys.

6.2 Neutron Scattering

Neutrons are an ideal probe for studying the lattice and spin dynamics of solids [1]. The wavelength of the neutron is comparable to the inter-atomic spacing in solids, (1–2 Å) and the energies of the neutrons are comparable to lattice energies (∼50 meV). The energy resolution needed in an experiment to measure excitations is on the order of 10%, which is readily achievable in a triple axis spectrometer. With the new generation of synchrotron X-ray sources, inelastic X-ray scattering is demonstrating that it, too, can measure dispersion curves in solids [2]. Since the incident energy of the photons is in the keV regime, an energy resolution of 10^{-6} is needed to probe the lattice dynamics. Nevertheless, the flux is so great with synchrotron X-ray sources that it is now feasible to do such high-resolution experiments. The advantage with X-rays is that small samples can be studied along with thin films. However, for magnetic scattering the coupling of neutrons is more direct and still the preferred method.

In an X-ray or neutron experiment an incident beam with a well defined energy (E_i) and momentum ($\boldsymbol{k}_\mathrm{i}$) prepared by a monochromator crystal strikes the sample. The particles are scattered by the sample and their energy analyzed by an analyzer crystal. The rules of momentum and energy conservation govern the entire process:

$$\boldsymbol{Q} = \boldsymbol{\tau} + \boldsymbol{q} = \boldsymbol{k}_\mathrm{i} - \boldsymbol{k}_\mathrm{f} \,, \tag{6.1}$$

$$\hbar\omega = E_\mathrm{i} - E_\mathrm{f} \,, \tag{6.2}$$

$\boldsymbol{Q}$ and $\hbar\omega$ are the momentum and energy, respectively, transferred to the material and they are inferred by measuring differences between the incident and final neutron wavevectors ($\boldsymbol{k}_\mathrm{i}$, $\boldsymbol{k}_\mathrm{f}$) and energies ($E_\mathrm{i}$, E_f). $\boldsymbol{\tau}$ is a reciprocal lattice vector and $\boldsymbol{q}$ is the momentum measured within a Brillouin zone. The neutron also has a spin and this is important in measuring the magnetic properties of a material including the magnetic structure and spin wave excitations.

In studying lattice vibrations the neutron couples to the atomic displacements through a neutron–nuclear interaction. The intensity of the scattered neutrons is proportional to the scattering function $S(\boldsymbol{Q},\omega)$, which can be written as

$$S(\boldsymbol{Q},\omega) = [n(\omega+1)]\ \chi''(\boldsymbol{Q},\omega) \,, \tag{6.3}$$

where $[n(\omega)+1]$ is the Bose–Einstein distribution function and for high temperatures where $kT \gg \hbar\omega$, $n(\omega)+1$ is approximated by $kT/\hbar\omega$. $\chi''(\boldsymbol{Q},\omega)$ is the imaginary part of the dynamical susceptibility and for the case where neutron scattering from the lattice creates or destroys a single phonon one has

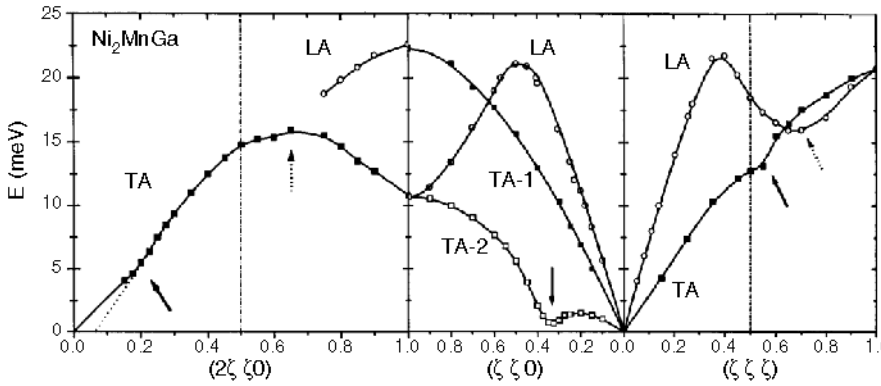

Fig. 6.1. Phonon dispersion curve of Ni_2MnGa measured at room temperature. Data from [3]

$$\chi''(\boldsymbol{Q},\omega) = \frac{1}{2}\frac{(2\pi)^3}{\nu_0}\sum_{\boldsymbol{\tau},\boldsymbol{q}}\delta(\boldsymbol{Q}-\boldsymbol{q}-\boldsymbol{\tau}) \times \sum_s \frac{1}{\omega_{\boldsymbol{q}s}} F(\boldsymbol{Q})^2[\delta(\omega-\omega_{\boldsymbol{q}s})-\delta(\omega+\omega_{\boldsymbol{q}s})] \ , \tag{6.4}$$

$F(\boldsymbol{Q})$ is the dynamical structure factor given by

$$F(\boldsymbol{Q}) = \sum_j \frac{b_j}{\sqrt{m_j}}\,(\boldsymbol{Q}\cdot\boldsymbol{\xi}_{j,s})\,\mathrm{e}^{\mathrm{i}(\boldsymbol{Q}\cdot\boldsymbol{d}_j)}\mathrm{e}^{-W_j} \ . \tag{6.5}$$

Here, b_j is the neutron scattering length for atom j with mass m_j. $\boldsymbol{\xi}_{j,s}$ is the eigenvector of atom j of the s phonon branch with frequency ω_s and e^{-W_j} is the Debye–Waller factor. By measuring the intensity of a phonon in different Brillouin zones with the same $\boldsymbol{q}$, one can in principle determine the atomic displacements $\boldsymbol{\xi}_{j,s}$. Equation (6.5) is used to separate out the transverse from longitudinal modes due to the dot product. With a triple axis instrument it is straightforward to keep $\boldsymbol{q}$ constant and vary ω during an experiment. Doing this for several $\boldsymbol{q}$ with different $\boldsymbol{\tau}$ a dispersion curve can be measured. Figure 6.1 shows the phonon dispersion curve measured for the ferromagnetic shape memory alloy Ni_2MnGa [3], which will be discussed in more detail later.

The most obvious feature is the very low energy of the TA_2 mode propagating along the $[\zeta\zeta 0]$ direction and the strong dip around $\zeta = 1/3$. The arrows indicate anomalies that are most likely due to strong electron–phonon coupling at particular wavevectors predicted by the Fermi surface.

6.3 Phonon Anomalies

A lattice dynamical theory involves calculating the eignevalues of a dynamical matrix, which is proportional to the interatomic force constants [4]. A simple

Born–von Kármán model is usually a good starting point. This essentially is a fit of a dispersion curve to a number of Fourier components. For a nearly harmonic solid, the acoustic dispersion curves are sinusoidal and there are only a few Fourier components needed which are proportional to near or next-near neighbor force constants. If there are anomalies as shown in Fig. 6.1, more terms are needed in the Fourier analysis and the simple Fourier expansion is no longer adequate and more sophisticated methods are needed.

In this section we shall consider here two types of phonon anomalies: (1) Kohn anomalies which are directly related to the Fermi surface and very often are subtle features or kinks in a dispersion curve; and (2) soft mode anomalies that are considered as precursor to a phase transformation and show large temperature or pressure dependence of the phonon energies at a particular wavevector.

6.3.1 Kohn Anomalies

Kohn anomalies are a direct consequence of electron–phonon coupling. We can describe the dynamical matrix as a sum of two terms [5]

$$\mathsf{D} = \mathsf{D}_{\mathrm{SR}} + \mathsf{D}_{\mathrm{LR}} \,. \tag{6.6}$$

D_{SR} are the short range mostly harmonic terms that can be described by a Born–von Kármán analysis. In a metal D_{LR} are longer range terms such as electron–phonon interactions. Many authors calculated the electron–phonon coupling for metals, but the approach of Varma and Weber [6] is generally used. This term is related to the generalized electronic susceptibility and is a negative quantity, which would reduce the eigenvalues of D and thus cause a reduction in the phonon frequency

$$\mathsf{D}_{\mathrm{LR}} \approx -\sum_{\boldsymbol{k},\mu,\nu} \frac{f_{\boldsymbol{k},\mu}(1-f_{\boldsymbol{k}+\boldsymbol{q},\nu})}{\varepsilon_{\boldsymbol{k}+\boldsymbol{q},\nu}-\varepsilon_{\boldsymbol{k},\mu}}\, \mathsf{M}_{\boldsymbol{k},\mu;\boldsymbol{k}+\boldsymbol{q},\nu}\, \mathsf{M}_{\boldsymbol{k}+\boldsymbol{q},\nu;\boldsymbol{k},\mu} \,. \tag{6.7}$$

Here, f is the Fermi function and $\varepsilon_{\boldsymbol{k},\mu}$ are energies of the μth electronic band with momentum $\boldsymbol{k}$. It can be seen that if there is a wavevector spanning the Fermi surface the denominator will be small and D_{LR} can be large enough to cause a reduction in the phonon energy. The quantities, M, are the complicated matrix elements giving the strength of the electron–phonon coupling. Both quantities, the electronic structure and the matrix elements, are amenable to calculation and determine the strength of the observed anomalies.

Figure 6.2 demonstrates the validity of the calculations [7]. The data points were measured by inelastic neutron scattering after the calculations of Zhao and Harmon [8], who predicted anomalies in the binary alloy, $Ni_{50}Al_{50}$ at the positions of the arrows. As it can be seen they are in close agreement with the experimental results, which were obtained after the predictions were made.

Not only were the positions of the anomalies well predicted, but their strengths as well. It is stronger along the [ζζζ] direction than the [ζ00] direction. The crosses in Fig. 6.2 are from earlier measurements on this material [9].

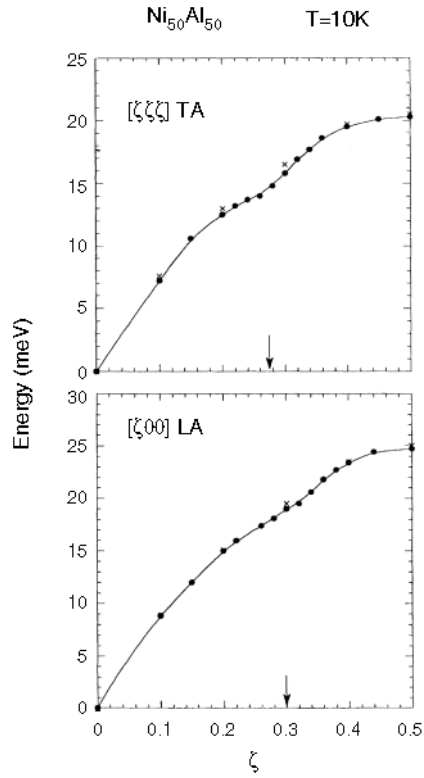

Fig. 6.2. The measured phonon dispersion curve of the [$\zeta\zeta\zeta$]–TA (*top*) and the [ζ00]–LA (*bottom*) branch in the $Ni_{50}Al_{50}$ alloy. The arrows indicated the predicted q-values of the anomaly by Zhao and Harmon [8]. Data from [7]

These authors measured the dispersion curve at well-separated q-values and were not able to confirm the anomalies predicted later. It shows the importance of having sufficient number of data points to accurately determine the shape of the dispersion curve.

6.3.2 Soft Modes

Soft modes in structural phase transitions are another example of phonon anomalies, but that are more dramatic than the small features of Kohn anomalies. The soft mode theory of structural phase transitions was first proposed by Anderson [10] and Cochran [11] to describe the phase transition occurring in ferroelectrics. In this theory there is a particular lattice vibration whose displacements are those that are needed to transform the system from its high temperature-high symmetry phase to its lower symmetry-low temperature ground state. The restoring forces for this mode get weaker and weaker as the transition is approached and the frequency tends to zero. Looking at

the dynamical matrix of (6.6) the short-range forces can be viewed as harmonic forces which are temperature independent. They can be parametized as $\mathsf{D}_{\mathrm{SR}} = -KT_{\mathrm{c}}$. The longer ranged anharmonic forces are proportional to temperature: $\mathsf{D}_{\mathrm{LR}} = KT$. The eigenvalue of the dynamical matrix is proportional to the square of the mode energy, $\hbar\omega$

$$(\hbar\omega)^2 = K(T - T_{\mathrm{c}})\,. \tag{6.8}$$

This shows that the phonon energy would go to zero at the critical temperature, T_{c}. The crystal becomes unstable at this temperature and transforms into its low temperature structure.

The soft mode theory of phase transitions has been demonstrated in many systems [12]. The prototypical one is $SrTiO_3$, which undergoes an antiferroelectric transition [13] near 100 K. The soft mode is a zone boundary phonon and the temperature dependence is shown in Fig. 6.3. The bottom portion shows the energy of the zone boundary mode measured at the $(1/2, 1/2, 1/2)$

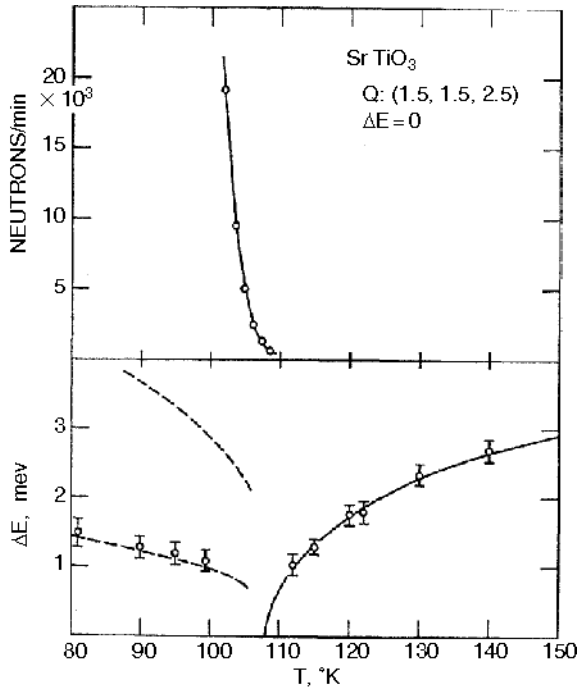

Fig. 6.3. The temperature dependence of the soft mode measured at the $(1/2, 1/2, 1/2)$ zone boundary (*bottom*) and the intensity of the elastic scattering at this position (*top*), which becomes a new Bragg peak in the low temperature phase. Data from [13]

R-point of the Brillouin zone. The solid line is a fit to (6.8) with $T_c = 108\,\mathrm{K}$. The upper portion shows the intensity of the elastic scattering as a function of temperature and reveals a new Bragg peak appearing below the transition temperature corresponding to a lowering of the symmetry.

6.4 Phonon Anomalies in the Manganites

The ferromagnetic perovskites of the type $La_{1-x}Me_xMnO_3$ (Me=Ca or Sr) are under intense study due to the important discovery of their giant magnetoresistance for certain regions of doping [14]. In these regions the ground state is ferromagnetic and at temperatures above the Curie temperature they become insulating. The magnetic ordering can partly be explained by the double exchange mechanism. However, to explain the temperature dependent behavior of the resistivity requires a strong electron–phonon interaction arising from the Jahn–Teller splitting of the Mn^{3+} d-band e_g levels. The structural and magnetic phase diagrams are complex and exhibit regions where charge ordering of the Mn^{3+} and Mn^{4+} occurs. The exciting physics in these systems lies in the coupling between the spin, the charge, the electrons, the lattice, and orbital degrees of freedom – all the fundamental entities in solid state physics.

Below we review one of the experiments on this system where inelastic neutron scattering experiments have shed light on the interaction between the spins and the lattice. The lattice vibrations associated with the Jahn–Teller distortions involve the atomic motions of the MnO_6 octahedra and should show anomalous behavior as the temperature is reduced below the MI phase transition. Zhang et al. [15] studied this in detail in $La_{0.7}Ca_{0.3}MnO3$ above and below the ferro-to-paramagnetic transition temperature, $T_c \sim 240\,\mathrm{K}$, which coincides with the MI transition. Figure 6.4 shows the dispersion curve of the optic modes along the $[\zeta 00]$ direction measured at 10 K. The interesting mode is the highest energy mode with energy $\hbar\omega_3 \sim 71\,\mathrm{meV}$ at $\zeta = 0$. This is the in plane MnO_3 bond stretching mode, which is the Jahn–Teller mode. Calculations and measurements in the undoped materials show that this upper mode is essentially dispersionless or should bend upwards as ζ increases. Instead, the mode bends downward with a negative dispersion. This anomalous effect is related to the charge ordering that occurs at the MI phase transition.

Figure 6.5 shows the temperature dependence of this mode. It exhibits anomalous damping and a decrease of intensity throughout the Brillouin zone with increasing temperature. It is argued that this anomalous behavior is due to the decoherence effects of the local dynamic phase fluctuations associated with short-range polaron or charge/orbital orderings when the system approaches T_c.

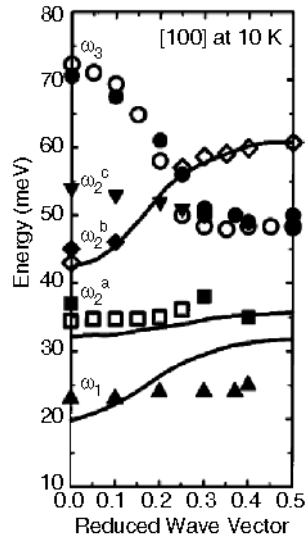

Fig. 6.4. Measured optical phonon dispersion curves in $La_{0.7}Ca_{0.3}MnO_3$ at 10 K. The *open circles* were measured in the Sr doped material. The *solid lines* are the results calculated by a screened shell model under cubic symmetry. Data from [15]

6.5 Phonon Anomalies in High Temperature Superconductors

Since the discovery of high temperature superconductors nearly 20 years ago, the basic mechanism behind the electron pairing leading to the superconductivity remains unexplained [16]. All of the cuprates have interesting magnetic properties that change dramatically with doping. Therefore, it is thought that magnetism plays an important role in the coupling mechanisms that lead to the high T_c. Up until recently electron–phonon coupling was thought to play a minor role in establishing the high superconducting transition temperatures. The discovery of stripes [17] in the cuprates – the separation of spin and charge – has given more impetus to the study of phonon anomalies in these compounds. It is unclear whether the appearance of stripes helps or hinders the onset of superconductivity. Studies of phonon behavior can help elucidate the role of charge ordering in superconductivity because phonons with a displacement pattern closely related to the charge stripe wavevector should have anomalously low energies analogous to what has been observed as precursor phenomenon to charge-density wave order in low-dimensional metals [18]. The phonon most likely connected to stripes is the highest frequency phonon, a longitudinal optic branch involving Cu–O stretching vibrations.

A study of the phonon anomalies in the high temperature superconductor YBCO ($YBa_2Cu_3O_{6.6}$) with $T_c \sim 60$ K was performed by Pintschovius

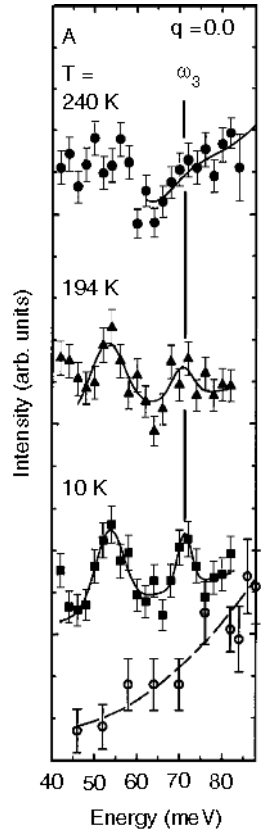

Fig. 6.5. Temperature dependence of energy scans at the Brillouin zone center in $La_{0.7}Ca_{0.3}MnO_3$. ω_3 is the Mn–O bond stretching Jahn–Teller mode. Data from [15]

et al. [19]. They chose this material because incommensurate magnetic fluctuations are well documented and the wavevector of any phonon anomalies would be twice the wavevector of the magnetic fluctuations if the anomaly is related to the stripes. The structure of this crystal is orthorhombic and the crystal is twinned in the $(0, 0, 1)$ plane. It is difficult, therefore, to separate the modes propagating along the $[\zeta 00]$ and $[0\zeta 0]$ directions, but Pintschovius et al. [19] were able to do so. Figure 6.6a shows the calculated dispersion curves of the Δ_1 longitudinal optic modes calculated from an interaction potential model. The red and blue color corresponds to modes propagating along the $[\zeta 00]$ and $[0\zeta 0]$ directions, respectively. The phonons propagating along $[\zeta 00]$ have a slightly higher energy because of the smaller Cu–O distance. The upper branches between 65 and 75 meV are the Cu–O stretching vibrations. In Fig. 6.6b the measured phonon dispersion curves with the same color representation are shown. The most anomalous feature is the rapid drop of the frequencies for the high-energy phonons propagating along the $[0\zeta 0]$ direction at about halfway to the zone boundary at $\zeta \sim 0.25$.

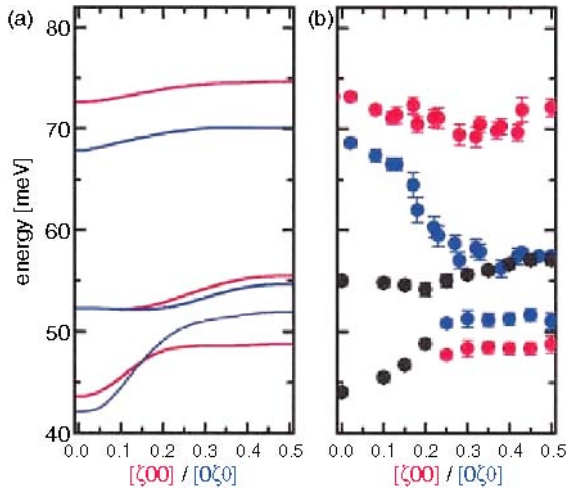

Fig. 6.6. Dispersion curves of the high energy longitudinal phonons in $YBCO_{0.66}$. (**a**) Calculated curves from an interaction potential mode. The *red* (*blue*) *curve* corresponds to the [ζ00] ([0ζ0]) direction. (**b**) Measured dispersion curves. *Red* (*blue*) correspond to the [ζ00] ([0ζ0]) direction. The *black symbols* denote phonon peaks where the assignment could not be resolved. From [19]

If one studies the displacement pattern associated with this phonon it is seen that it is readily compatible with dynamic charge stripe formation with a period of about 4 times the b lattice parameter. However, there are some inconsistencies when compared to the magnetic data, which suggests that the modulation is along the a direction and the above phonon measurements imply that the charge modulation is along the b direction. This was discussed in a later paper where the phonons in an optimally doped $YBCO_{6.95}$ sample were studied [20]. In this experiment they studied the dispersion and the temperature dependence of Δ_4 phonons. These phonons also involve Cu–O stretching, but they differ from the Δ_1 symmetry in that the elongations in the Cu–O bi-layer are out of phase for Δ_4 and in phase for Δ_1. The behavior of the two are similar, but the interactions of the Δ_1 modes with c-axis polarized branches leads to complications in the measurements. These latest results provide more convincing arguments that the phonon anomalies in the Cu–O stretching mode indicate a dynamic one-dimensional charge density modulation with the Cu–O planes.

6.6 Ferromagnetic Shape Memory Alloys

Most shape memory materials are tuned by varying the temperature. However, there is a growing list of shape memory alloys that, in addition to the

Martensitic transformation exhibit ferromagnetic ordering. The major interest in these materials arises from the possibility of tuning the strain and the shape memory transition by applying a magnetic field, rather than temperature. This opens up a new domain for actuator applications since changing a magnetic field is a quicker operation than changing temperature. In Ferromagnetic Shape Memory Alloys (FSMA), the Curie temperature (T_C) is weakly dependent on composition and the Martensitic temperature (T_M) is strongly dependent upon the composition. T_M can therefore be tuned to be higher or lower than T_C. The fundamental excitations in the spin system are magnons and those of the lattice are the phonons. Since these collective excitations are proportional to the couplings between the individual spins (magnons) and atoms (phonons) a study of them is important to understanding the fundamental mechanism of the transformations and the coupling between the spin and the lattice. Precursor effects such as critical scattering and softening of magnon energies are well known in magnetic transitions, but not ubiquitous in the Martensitic transformations. A study of the temperature dependence of the magnons and phonons is therefore important in delineating the precursor phenomena and the interaction of the magnetic and structural properties.

6.6.1 Iron-Based Alloys

The coupling of the structural and magnetic properties in iron-based alloys has been known for many decades. Invar alloys have the interesting and technologically very important property of having zero or slightly negative thermal expansion over a very wide temperature range [21]. This useful property has been exploited in the construction of high precision mechanical instruments, but is not fully explained. It disappears above the Curie temperature so is related to the magnetic ordering. Most theories are based upon the volume instabilities of the magnetic moments that give rise to a magneto-elastic coupling that will offset the normal lattice expansion. Understanding the temperature dependent behavior of the phonons will shed light on this coupling.

$Fe_{65}Ni_{35}$ is the canonical invar alloy but other Fe-alloys, such as Fe–Pt and Fe–Pd exhibit similar invar properties. All of these show a change in phonon dispersion as the system orders ferromagnetically. Figure 6.7 shows the dispersion curve [22] of the [$\zeta\zeta 0$] TA_2 phonon branch for several invar alloys along with bcc Fe. At temperatures above the Curie temperature the dispersion follows the normal linear acoustic behavior for small ζ-values. For temperatures below the Curie temperature an anomalous curvature in the dispersion over nearly the entire Brillouin zone develops. A more detailed picture is shown for $Fe_{72}Pd_{28}$ in Fig. 6.8 [23]. At 676 K, which is higher than the Curie temperature $T_C \sim 575$ K, the dispersion shows the usual linear behavior. Below T_C it develops a concave behavior, which increases as the temperature is lowered. This is demonstrated in Fig. 6.9 where the ratio of the phonon energies measured below T_C to that above T_C is plotted for several ζ-values as a function of temperature. For all ζ, the softening starts at T_C and is

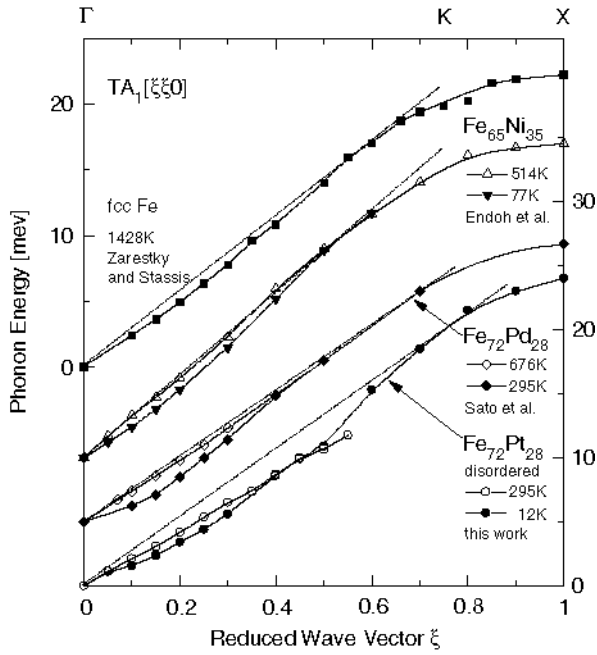

Fig. 6.7. [ζζ0]-TA_2 dispersion curves for several Fe-based alloys and bcc Fe. Data from [22]

largest for the smaller ζ. This behavior is also observed in the other alloys shown in Fig. 6.7 and demonstrates the coupling between the magnetic ordering and the phonon behavior. A measure of the phonon linewidth also shows an increase with decreasing temperature starting at the Curie temperature as shown in Fig. 6.10. This broadening was confined only to the [110] TA_2 branch which exhibits the softening. The other branches measured along symmetry directions exhibit normal behavior.

6.6.2 Heusler-Based Alloys

Ni_2MnGa

This material has generated a tremendous amount of interest over the past 10 years largely due to the coexistence of a shape memory Martensitic transition with ferromagnetic ordering and the possibility of inducing a large strain by application of a magnetic field. Recently it was shown that a 10% strain can be induced by application of a magnetic field at room temperature [24]. This is an enormous amount; much larger than piezoelectric induced strain. The symmetry of the high temperature phase of this material is cubic with the fcc Heusler-$L2_1$ structure (Fm3m) with Curie temperature near 380 K, which

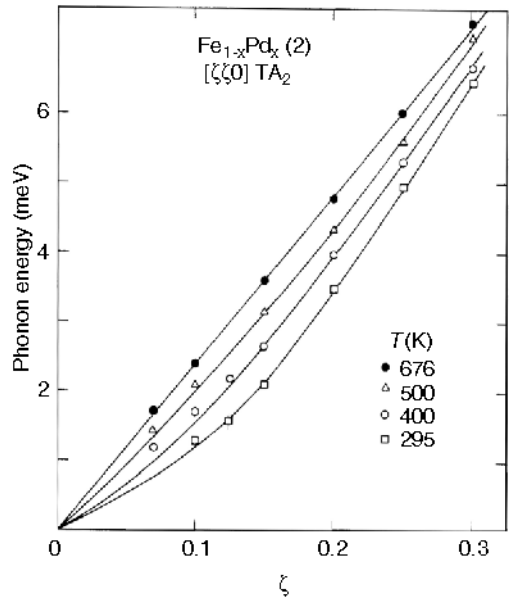

Fig. 6.8. Temperature dependence of the $[\zeta\zeta 0]$-TA_2 branch for $Fe_{72}Pd_{28}$. Data from [23]

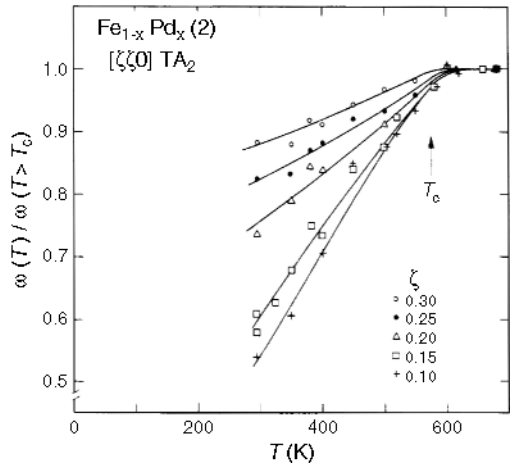

Fig. 6.9. Temperature dependence of the $[\zeta\zeta 0]$-TA_2 phonons for $Fe_{72}Pd_{28}$, normalized by the phonon energy above T_C. Data from [23]

varies little with composition. The Martensitic transformation temperature varies drastically with composition and the low symmetry phase is either orthorhombic or tetragonal, depending upon the composition. Figure 6.11 shows the phase diagram of Ni_2MnGa constructed from published reports [25]. The quantity α is a weighted composition of Mn and Ga, which is easily converted

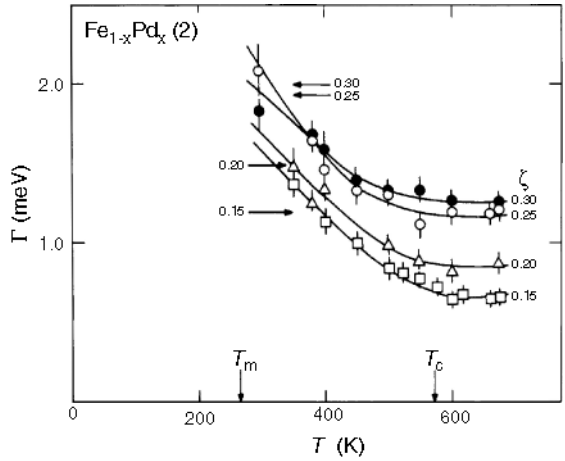

Fig. 6.10. Temperature dependence of the phonon linewidth of the $[\zeta\zeta 0]$-TA_2 branch for $Fe_{72}Pd_{28}$. Data from [23]

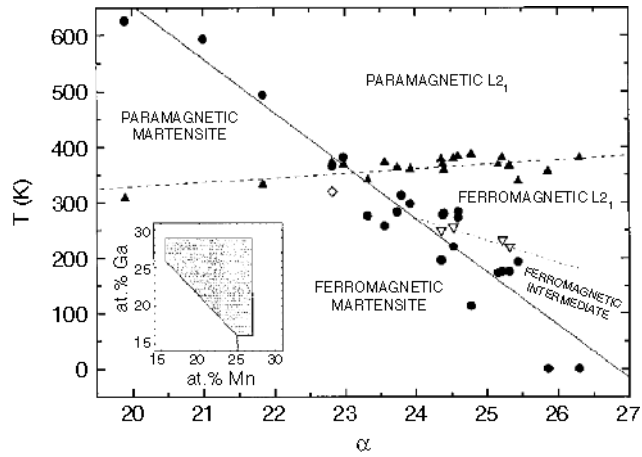

Fig. 6.11. Phase diagram of Ni_2MnGa from [25]. The *filled circles* and *filled triangles* are the Martensitic and Curie temperatures, respectively. The *open triangles* represent the transition to the intermediate modulated phase. The hatched region in the inset represents the composition range from which the data have been taken

to the electron per atom ratio. For $\alpha = 25$ the composition is stoichiometric and $e/a = 7.5$. The solid circles show the variation of the Martensitic transformation temperature and the solid triangles represent the Curie temperature, which is nearly independent of composition, whereas the Martensitic temperature varies dramatically with composition. The open triangles delineate a phase transformation into an intermediate modulated cubic phase, which exists just prior to the transformation to the Martensitic phase.

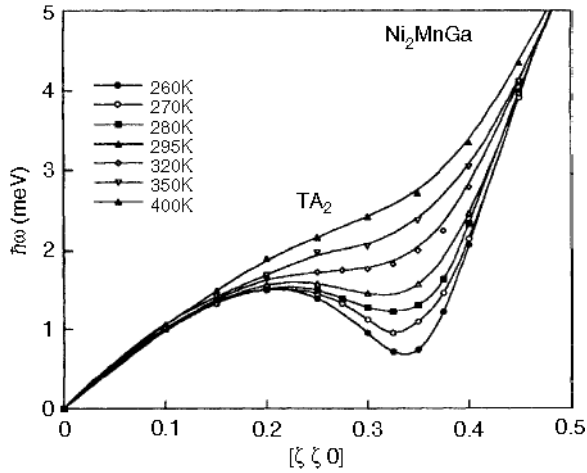

Fig. 6.12. Temperature dependence of anomalous TA_2 branch in Ni_2MnGa. Data from [26]

The phonon dispersion curve for Ni_2MnGa is shown in Fig. 6.1. The obvious anomaly is the $[\zeta\zeta 0]$-TA_2 mode. A more detailed temperature study of the low energy portion of this branch is shown in Fig. 6.12 [26]. At the highest temperature, 400 K, which is above the Curie temperature, the dispersion branch shows a small wiggle. Since the anomaly is still present about the Curie temperature this suggests that the coupling between the magnetic and lattice properties is small. As the temperature is lowered towards the Martensitic temperature, $T_M \sim 220$ K, a distinct minimum develops at $\zeta_0 = 0.33$. The energy of the mode never goes to zero and reaches a minimum at $T_I = 260$ K, 40 K above T_M and then begins to increase again, still within the cubic phase. This suggests that another phase develops between T_I and T_M and coexists with the parent phase. This is the ferromagnetic intermediate phase shown in the phase diagram of Fig. 6.11.

The elastic scans along the $[\zeta\zeta 0]$ transverse direction are shown in Fig. 6.13. At elevated temperature a small diffuse bump is observed at $\zeta_0 = 0.33$, the same wavevector as the anomaly seen in the dispersion curve. As T decreases the intensity grows as the frequency decreases. Around 260 K there is a strong increase in the intensity and it becomes narrower and Bragg-like, indicating that an ordered modulation of the cubic phase sets in. This temperature is the same as the minimum of the dispersion curve. This type of elastic scattering associated with a phonon softening is ubiquitous in many structural transformations and is related to defects of the lattice [27]. The phonon softening is usually viewed as a precursor to the low temperature phase. It is worth noting that in the Martensitic phase, there is a modulation of the lattice [28] with a wave vector $\zeta_0 \sim 0.43$, which is quite different from 0.33. Thus the phonon

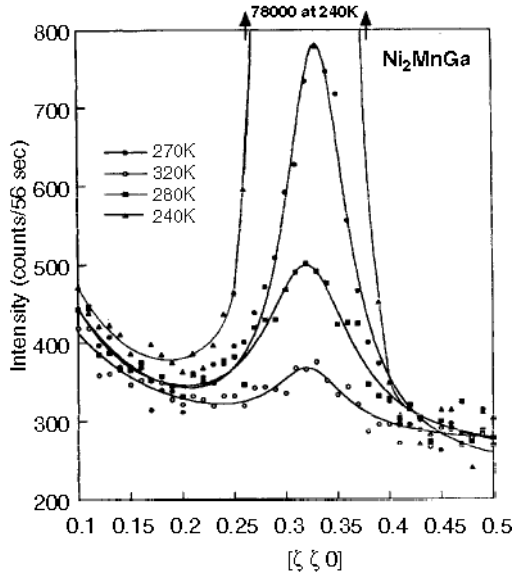

Fig. 6.13. Temperature dependence of the elastic scattering along the [ζζ0] transverse direction. Data from [26]

softening should not necessarily be viewed as a precursor to the Martensitic phase, but more appropriately a precursor to the intermediate phase.

Since the phonon dispersion curve did not become linear above the Curie temperature it was suggestive that the coupling to the magnetization is weak and there was little effect of the magnetic ordering on the phonon behavior. This is not strictly correct. When the square of the phonon frequency measured at $\zeta_0 \sim 0.33$ is plotted as a function of temperature a change of slope occurs at the magnetic ordering temperature [28] as seen in Fig. 6.14.

What is the origin of the phonon softening and modulation observed at the wavevector $\zeta = 0.33$? Self-consistent first principles calculations of the electron energy spectrum, density of electronic states, and the generalized susceptibility and of various Fermi surface cross sections have been carried out by several groups. One group [29] concluded that Fermi surface nesting could not be the driving force of the phonon softening because the calculation showed that the nesting wavevector in the ferromagnetic phase of Ni_2MnGa is $\zeta_0 = 0.42$, which is substantially larger than the experimental value of $\zeta_0 = 0.33$ as shown above. This was reconciled by a later study [30] where the changes in the Fermi surface upon magnetic order were calculated. Since the phonon softening persists down to T_M, which is well above zero, the magnetization is not fully saturated. Lee et al. [30] showed that the nesting vector does, indeed, depend upon the magnetization. They found that the Fermi surface nesting is optimized at 80% of full magnetization and the nesting vector is $\zeta_0 = 1/3$, the same wavevector as the observed phonon softening. However,

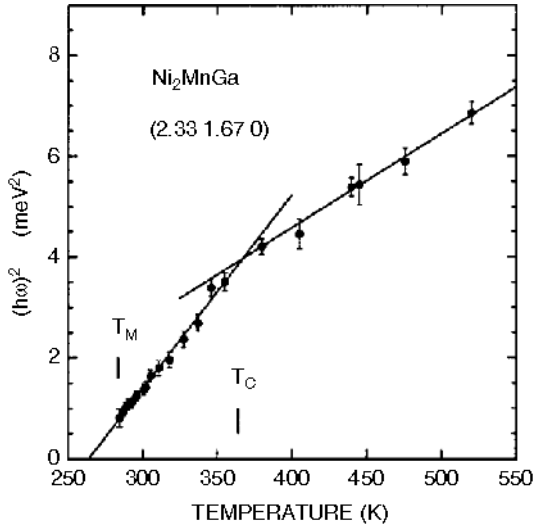

Fig. 6.14. Square of phonon energy of [ζζ0]-TA_2 mode, $\zeta = 0.33$ vs. temperature for $Ni_{2.06}Mn_{0.94}Ga$. The Curie temperature for this alloy is $T_C = 364\,K$ and $T_M = 284\,K$. Data from [28]

these calculations would suggest that the nesting vector and therefore the wavevector of the anomaly and its associated diffuse elastic peak should be temperature dependent, which it is not. The 80% magnetization level occurs close to the temperature region near where the premartensitic transition occurs. At lower temperatures in the Martensite phase, the magnetism is near saturation and the nesting vector has shifted to $\zeta_0 = 0.42$, consistent with the observations [31]. Studies of single domain samples of Ni_2MnGa in the tetragonal Martensite phase show that the lattice modulation is at $\zeta_0 = 0.42$, which corresponds to the weakly temperature dependent phonon anomaly of the [ζζ0] TA_2 phonons [31].

Co_2NiGa

This compound was recently discovered [32] and is isomorphic to Ni_2MnGa, although much less is known about the material. For example, in the Ni-compound, most of the magnetization is localized on the Mn sites, with a small moment (10%) on the nickel sites. The magnetic properties for the Co compound are unknown. It orders around 380 K and the Martensitic transformation temperature is near room temperature. The stoichiometery can be varied and a complete phase diagram has not been mapped out. The variation of the transition temperature with e/a ratio [33] is nearly identical to Ni_2MnGa. A single crystal of Co_2NiGa was grown with composition $Co_{1.92}Ni_{0.88}Ga_{1.2}$ with a T_M on cooling near ∼280 K. The phonon dispersion curve and the elastic scattering along the [ζζ0]-TA2 direction were measured

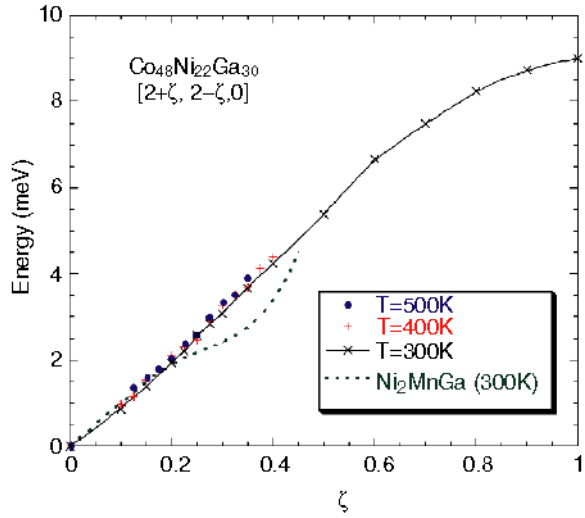

Fig. 6.15. The [ζζ0]-TA_2 phonon branch measured in $Co_{1.92}Ni_{0.88}Ga_{1.2}$ at several temperatures within the cubic phase. The *dashed line* shows the same branch measured in Ni_2MnGa. Data from [34]

in the Austenite phase at several temperatures [34] and is shown in Fig. 6.15. There is no anomaly in the dispersion curve nor is there any temperature dependence. The elastic scans revealed no diffuse peaks and thus no modulation. Therefore, no intermediate phase exists between the Austenite and the cubic phase.

The absence of any anomaly and diffuse scattering in $Co_{1.92}Ni_{88}Ga_{1.2}$ is surprising since it is so similar to Ni_2MnGa in terms of structural and magnetic properties. On the other hand, the absence of the intermediate phase and no phonon softening implies that the phonon softening observed in Ni_2MnGa is more likely a precursor to the intermediate phase rather than the Martensite phase. This argument can be extended to the phonon softening observed in other shape memory alloy systems and raises the question of whether phonon anomalies are precursors to the Martensitic transformation or to the pre-martensitic phase.

6.7 Summary

The technologically important functional materials exhibit phase transitions that are driven by a coupling of fundamental quantities, such as electron phonon coupling or a coupling of two different degrees of freedom such as magnetic spins or atomic displacements. It was demonstrated in this chapter that by inelastic neutron scattering studies of the lattice dynamics, a great deal of information about the coupling can be learned. These measurements, coupled to the theory, can lead to an understanding of the driving mechanism

of the transitions. Examples from studies of a diverse group of materials ranging from high T_c compounds, the manganites and magnetic shape memory alloys show anomalies in various relevant phonon branches.

Acknowledgments

I would like to acknowledge the collaborations with an excellent group of scientists: P. Vorderwisch (Hahn Meitner Institute), A. Zheludev (ORNL), Jason Gardner (BNL/NIST), Guongyong Gu (BNL). Particular thanks go to my colleagues at Ames Laboratory, T. Lograsso and D. Schlagel who grew the excellent crystals for the neutron studies. Work at Brookhaven is supported by the Office of Science, U.S. Department of Energy, under Contract No. DE-AC02-98CH10886.

References

1. G. Shirane, S.M. Shapiro, J.M. Tranquada: Neutron Scattering with a Triple-Axis Spectrometer-Basic Techniques (Cambridge University Press, 2002)
2. J. Wong, M. Krisch, D.L. Farber, F. Occelli, A.J. Schwartz, T.C. Chiang, M. Wall, C. Boro, R. Xu: Science **301**, 1078 (2003)
3. A. Zheludev, S.M. Shapiro, P. Wochner, L.E. Tanner: Phys. Rev. B **54**, 15 045 (1996)
4. M. Born, K. Huang: Dynamical Theory of Crystal Lattices (Oxford University Press, 1954)
5. C.M. Varma, W. Weber: Phys. Rev. Lett. **39**, 1094 (1977)
6. C.M. Varma, W. Weber: Phys. Rev. B **19**, 6142 (1979)
7. H. Chou, S.M. Shapiro: Phys. Rev. B **48**, 16 088 (1993)
8. G.L. Zhao, B.N. Harmon: Phys. Rev. B **45**, 2818 (1992)
9. M. Mostoller, R.M. Nicklow, D.M. Zehner, S. Lui, J.M. Mundenar, E.W. Plummer: Phys. Rev. B **40**, 2856 (1989)
10. P.W. Anderson: Qualitative considerations on the statistics of the phase transition in batio$_3$-type ferroelectrics. In: Fizika Dielekrikov, ed. by G.I. Skanavi (Academia Nuak, Moscow, USSR, 1960) pp. 290–295
11. W. Cochran: Adv. Phys. **9**, 387 (1960)
12. A.D. Bruce, R.A. Cowley: Structural Phase Transitions (Taylor & Francis, London, 1981)
13. G. Shirane, Y. Yamada: Phys. Rev. **177**, 858 (1969)
14. A.M. Goldman: Science **274**, 1630 (1996)
15. J. Zhang, P. Dai, J.A. Fernandez-Baca, E.W. Plummer, Y. Tomioka, Y. Tokura: Phys. Rev. Lett. **86**, 3823 (2001)
16. P.W. Anderson: The Theory of Superconductiviy in High-T_c Cuprates (Princeton University Press, 1997)
17. J.M. Tranquada, B.J. Sternlieb, J.D. Axe, Y. Nakamura, S. Uchida: Nature **375**, 561 (1995)
18. D.E. Moncton, J.D. Axe, F.J. DiSalvo: Phys. Rev. B **16**, 801 (1977)
19. L. Pintschovius, W. Reichardt, M. Kläser, T. Wolf, H. v. Löhneysen: Phys. Rev. Lett. **89**, 037 001-1 (2002)

20. L. Pintschovius, D. Reznik, W. Reichardt, Y. Endoh, H. Hiraka, J.M. Tranquada, H. Uchiyama, T. Masui, S. Tajima: cond/mat 0308357 (unpublished); Phys. Rev. B **69**, 214506-1 (2004)
21. E.F. Wassermann: The Invar and anti-Invar Effect: finally understood after 100 years? In: The Invar Effect: Centennial Symposium, ed. by J. Wittenauer (Minerals Metals & Materials Society, 1997) p. 51
22. J. Kästner, W. Petry, S.M. Shapiro, A. Zheludev, J. Neuhaus, T. Roessel, E.F. Wassermann, H. Bach: Eur. Phys. J. B **10**, 641 (1999)
23. M. Sato, B.H. Grier, S.M. Shapiro, H. Miyajima: J. Phys. F: Met. Phys. **12**, 2117 (1982)
24. A. Sozinov, A.A. Likhachev, N. Lanska, K. Ullakko, V.K. Lindroos: J. Phys. IV France **112**, 955 (2003)
25. A. Gonzàlez-Comas, E. Obradó, L. Mañosa, A. Planes, V.A. Chernenko, B.J. Hattink, A. Labarta: Phys. Rev. B **69**, 7085 (1999)
26. A. Zheludev, S.M. Shapiro, P. Wochner, L.E. Tanner: Phys. Rev. B **51**, 11 310 (1995)
27. J.B. Hastings, S.M. Shapiro, B.C. Frazer: Phys. Rev. Lett. **40**, 237 (1978)
28. U. Stuhr, P. Vorderwisch, V.V. Kokorin, P.A. Lindgård: Phys. Rev. B **56**, 14 360 (1997)
29. O.I. Velikokhatnyi, I.I. Naumov: Physics of the Solid State **41**, 617 (1999)
30. Y. Lee, J. Rhee, B.N. Harmon: Phys. Rev. B **66**, 054 424-1 (2002)
31. P. Vorderwisch et al. (unpublished)
32. M. Wuttig, J. Li, C. Craciunescu: Scripta Mater. **44**, 2393 (2001)
33. C. Craciunescu, Y. Kishi, T.A. Lograsso, M. Wuttig: Scripta Mater. **47**, 285 (2002)
34. S.M. Shapiro et al. (unpublished)

7

The Structures and Transformation Mechanism in the Ferromagnetic Shape Memory Alloy Ni_2MnGa

P.J. Brown, T. Kanomata, and M. Matsumoto, K.-U. Neumann, and K.R.A. Ziebeck

7.1 Introduction

The phenomenon of coupled magnetic and structural phase transitions is very rare in condensed matter physics. Such systems can exhibit many interesting properties including giant magneto-caloric, magneto-resistance and magneto-striction, and consequently have great technological potential. Of particular interest are materials that can be formed at one temperature T_F, then cooled to a lower temperature T_{M} and plastically deformed and on heating to T_F regain their original shape. In recovering their shape the alloys can produce a displacement or a force, or a combination of the two. Such behaviour is known as the shape memory effect and usually takes place by change of temperature or by applied stress. However for many applications such as for actuators the transformation is not sufficiently rapid. Poor energy conversion also limits the applicability of many shape memory alloys. Therefore considerable effort has been made to find a magnetic system in which the phase transition can be controlled by a magnetic field at constant temperature. Numerous materials have been studied but the Ni–Mn–Ga system has proved the most encouraging [1]. Since Ni_2MnGa orders ferromagnetically below $T_{\mathrm{C}} = 365\,\mathrm{K}$ the possibility of producing giant field induced strains which are an order of magnitude larger than those observed in rare-earth transition metal alloys has stimulated a large number of investigations aimed at applications [2, 3]. The origin of the shape memory effect in Ni_2MnGa is the thermo-elastic phase change from the cubic $L2_1$ Heusler structure to a phase of lower symmetry which takes place at $T_m \cong 200\,\mathrm{K}$ on cooling [4]. Different transformation temperatures and structures [5, 6] have been reported for the low temperature phase. The variations are probably due to non-stoichiometry or stress.

7.2 The Crystal Structure of the Cubic Austenite Phase

Intermetallic compounds formed at the stoichiometric composition X_2YZ and with the cubic $L2_1$ structure as shown in Fig. 7.1 are usually classified as

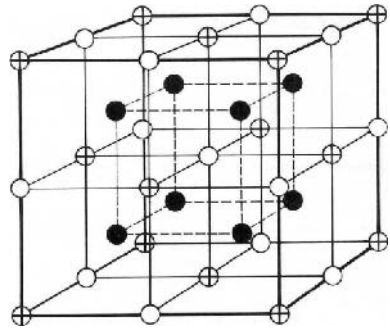

Site	A	B	C	D
$L2_1$	Mn	Ni	Ga	Ni
B2	Mn/Ga	Ni	Mn/Ga	Ni

Fig. 7.1. The Heusler $L2_1$ and B2 structures

Heusler alloys. The X and Y constituents are normally transition metals and Z a group B element. Initial interest focussed on the ferromagnetic properties of Cu_2MnAl [7] at a time when the antiferromagnetic properties of manganese were not known. Subsequently a large number of Heusler alloys have been discovered with a wide range of physical properties [8]. Particular interest has focussed on X_2MnZ compounds in which the magnetic moment is confined to the manganese atoms. Since the Mn atoms are separated by $a/\sqrt{2}$ with $a \sim 6\,\text{Å}$, direct overlap of the 3d functions is negligible. Consequently these compounds provide good model systems for studying localised magnetic behaviour in metallic systems. Galvanomagnetic measurements indicate that the transport properties are due only to the s and p electrons. Extensive measurements have shown that the physical properties are sensitive to the degree of stoichiometry and the degree of atomic order. However in many studies these parameters have not been established and therefore it is impossible to correlate results from different investigations.

Experiments on Ni–Mn–Ga alloys show that stoichiometry strongly influences the transition temperature T_M but that the change in Curie temperature is less pronounced. Furthermore, although a wide range of heat treatments is used to make the alloys, a detailed structural analysis is seldom carried out and hence the degree of atomic order remains uncertain. It is frequently assumed that the austentite phase has the $L2_1$ structure, but sometimes this is just inferred from the lattice parameter or from observation of fundamental reflections which are order independent. Thus there are very few examples where the correlation between changes in physical properties and the crystallographic structure, which is essential for a complete understanding of shape memory, have been made. Since the atomic numbers of Ni, Mn and Ga (28, 25 and 31) are close it is difficult to obtain a reliable estimate of the atomic order from

X-ray powder diffraction measurements. Neutron diffraction which probes the bulk structure (10^{-2} m), enables a quantitative structural refinement to be obtained from powder data particularly if the profile refinement technique [9] is employed. The nuclear coherent scattering amplitudes of 1.03, −0.373 and 0.723 [10^{-12} cm] for Ni, Mn and Ga respectively are significantly different making neutron diffraction particularly appropriate for these materials.

The Heusler unit cell shown in Fig. 7.1 is comprised of four interpenetrating fcc lattices A, B, C and D with origins at (000), $(\frac{1}{4}\frac{1}{4}\frac{1}{4})$, $(\frac{1}{2}\frac{1}{2}\frac{1}{2})$ and $(\frac{3}{4}\frac{3}{4}\frac{3}{4})$. Bragg reflections are permitted when the Miller indices are unmixed which gives rise to three types of structure factors:

- h, k, l all odd

$$F(111) = 4[(f_A - f_C) + i(f_B - f_D)]\,; \tag{7.1}$$

- h, k, l all even and $h + k + l = 4n + 2$

$$F(200) = 4|f_A - f_B + f_C - f_D|\,; \tag{7.2}$$

- h, k, l all even and $h + k + l = 4n$

$$F(220) = 4|f_A + f_B + f_C + f_D|\,; \tag{7.3}$$

where f_A, f_B, f_C and f_D are the average scattering factors of the atoms in the respective sublattices. The reflections for which $h + k + l = 4n$ are the order independent principal reflections.

If the alloys are ordered in the $L2_1$ structure the structure factors become

$$F(111) = 4|f_A - f_C|\,, \tag{7.4}$$

$$F(200) = 4|f_A + f_C - 2f_{B/D}|\,, \tag{7.5}$$

$$F(220) = 4|f_A + f_C + 2f_{B/D}|\,. \tag{7.6}$$

A comparison between the square of the structure factors of Ni_2MnGa for both X-rays and neutrons in Table 7.1 shows that the latter technique is more appropriate for structural analysis. Possible types of atomic disorder and models describing disorder have been extensively discussed [9]. Although there is an infinite number of ways in which the atoms XYZ can be distributed over the lattices ABCD there are several types of preferential disorder which frequently occur in Heusler alloys. B2 disorder implies the interchange of atoms

Table 7.1. X-ray and neutron structure factors of Ni_2MnGa in the $L2_1$ structure

	$F^2(111)$	$F^2(200)$	$F^2(220)$
X-ray (10^{-24} cm^2)	45.74	0	15937.0
Neutron (10^{-24} cm^2)	19.22	46.79	92.93

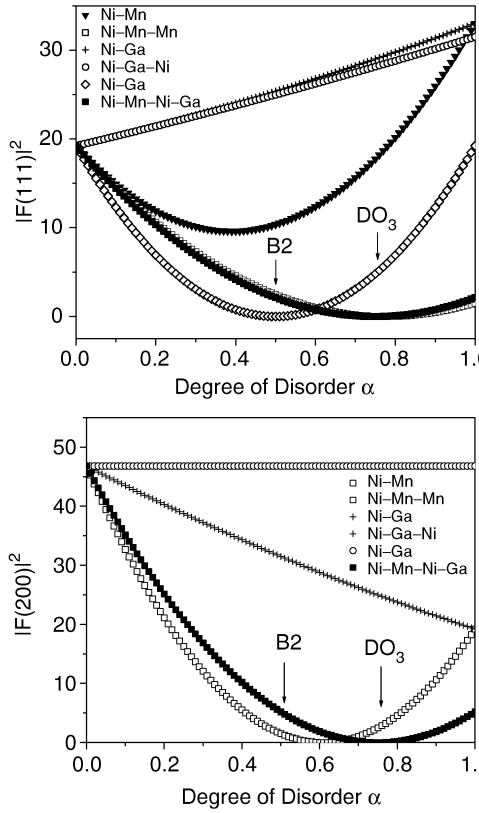

Fig. 7.2. The effect of preferential disorder on the neutron structure factors of Ni_2MnGa

on the A and C lattices which can lead to a substantial change in properties since the atomic separation between some pairs of Mn atoms is reduced to $a/2$. The effects of preferential disorder on the structure factors can be characterised using a single parameter α defined as the fraction of either Y or Z atoms not on their 'correct' sites. The effects of the various types of disorder on the squares of the structure factors and hence Bragg intensities for neutron scattering are shown in Fig. 7.2.

7.3 Bulk Magnetic Properties

Between 200 K and the Curie temperature 370 K the thermal variation of the magnetisation of stoichiometric Ni_2MnGa follows that expected for an isotropic ferromagnet. The structural phase transition at 200 K introduces a preferred axis of magnetisation (c axis) which in low fields (<1 T) produces an abrupt decrease in the magnetisation measured on polycrystalline samples as shown in Fig. 7.3. However the field dependence of magnetisation below

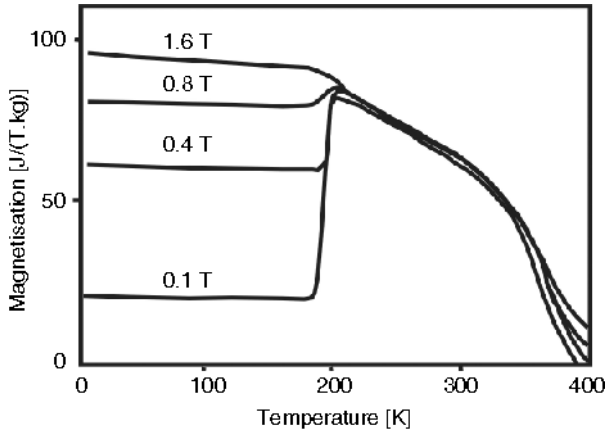

Fig. 7.3. The thermal dependence of the magnetisation of stoichiometric Ni_2MnGa measured in different applied fields

Table 7.2. A summary of the bulk magnetic properties of stoichiometric Ni_2MnGa

μ_{00} (μ_B)	T_C (K)	Θ (K)	P_{eff}/Mn (μ_B)	μ_p/Mn (μ_B)	μ_p/μ_{00}
4.17	376	378	4.75	3.85	0.89

Table 7.3. A summary of the structural parameters of stoichiometric Ni_2MnGa

a_{295} (Å)	V_{295} (Å^3)	T_M (K)	$a_{4.2}$ (Å)	$c_{4.2}$ (Å)	c/a	$V_{4.2}$ (Å^3)
5.825	198	202	5.92	5.566	0.94	195

T_M suggests that the magneto-crystalline anisotropy is small [10]. Measurements on a single crystal with one variant (crystallographic domain) gives the anisotropy for the $\langle 100 \rangle$ hard axis as $\sim$3.9 J/kg [11]. Thus for fields above $\sim$1 T it is possible to approach saturation and determine the spontaneous magnetisation from standard Arrott plots. A summary of the magnetic properties is given in Table 7.2. From these measurements it is clear that the magnetic moment essentially remains constant through the structural phase transition. This is in contrast to the Laves phase compound YMn_2 and the metal insulator system V_2O_3 in which a collapse of the transition metal moment destroys long range magnetic order producing a structural phase transition involving $\sim$5% change in cell volume [12]. The neutron diffraction measurements on Ni_2MnGa, above and below T_M, summarised in Table 7.3, show that there is negligible volume change. Further evidence that the amplitude of the manganese moment remains fixed is provided by the Curie–Weiss susceptibility observed above the Curie temperature. The Curie constant yields a paramagnetic moment $\mu_p = 2S = 3.85\,\mu_B$ close to the ground state value. This feature is common to all X_2MnZ compounds in which the bulk of the moment is on the Mn atoms [8].

7.4 Spin Dynamics

Inelastic neutron scattering experiments [13] in the cubic ferromagnetic phase of Ni_2MnGa give the spin wave stiffness of 108 meV Å^2. This is the only study yet reported of the spin dynamics in the ferromagnetic phase. However insight into what might be expected can be obtained from results obtained on isostructural compounds [8]. The spin wave dispersion in Ni_2MnSn, which has a similar moment distribution and Curie temperature, has been measured at 50 K in three principal symmetry directions out to the zone boundaries [14]. Local moment systems in which the spectrum of quantum (single particle) fluctuations is well separated from the thermal region are expected to support spin waves throughout the Brillouin zone. Evidence that this situation prevails is provided by the spin wave energy at the zone boundary ∼40 meV (∼450 K) which is comparable to the Curie temperature 360 K. The dispersion was analysed using a Heisenberg model including exchange constants out to the 8th nearest neighbour. Both positive and negative exchange constants were obtained as expected for an indirect RKKY exchange mechanism. The exchange constants derived yield a paramagnetic Curie temperature $k_B\Theta_P = \frac{2}{3}S(S+1)\sum_i z_i\ J_i = 337\,\mathrm{K}$ which is close to 344 K, the value observed from susceptibility measurements. A similar analysis leads to a ground state spin wave stiffness constant $D(0) = \frac{1}{3}S\sum_i J_i\,\xi_i^2\,a^2$ of 154 meV Å. Renormalisation of the spin wave stiffness constant in these systems is observed to be stronger than expected on the basis of spin wave scattering alone. The value is consistent with that observed for Ni_2MnGa in the cubic phase. These measurements and others on Heusler alloys [8] suggest that the response in Ni_2MnGa will be similar and of a local nature.

7.5 Paramagnetic Response

The local nature of the magnetic interactions is also expected to characterise the paramagnetic phase. Although no experimental data are yet available for Ni_2MnGa, support for this conjecture is provided by the Curie–Weiss susceptibility and paramagnetic neutron scattering experiments on the isostructural compound Pd_2MnSn. The temperature dependence of the susceptibilities of X_2MnZ alloys [8] and in particular of both Ni_2MnGa and Pd_2MnSn show that the amplitude of the Mn moment remains constant and persists into the paramagnetic phase. For Pd_2MnSn polarised neutron scattering experiments [15] show that the paramagnetic phase is characterised by directionally disordered local moments of fixed magnitude. Since relativistic effects are unimportant and spin is conserved the observed scattering extrapolates to the cross section at $Q = 0$ given by the uniform susceptibility χ, i.e. the $\omega = 0$ susceptibility. The spin–spin correlation function $\langle \boldsymbol{S_q} \cdot \boldsymbol{S_{-q}} \rangle$ at $Q = 0$ is given by $\sum_j \langle \boldsymbol{S}_i \cdot \boldsymbol{S}_j \rangle = 3k_B\,\chi\,T$ which is related to the partial differential cross section

by $\frac{d\sigma}{d\Omega} = \sum_j \frac{2}{3}\langle \boldsymbol{S}_i \cdot \boldsymbol{S}_j \rangle (r_o\gamma)^2 f^2$, where $(r_o\gamma) = 0.54 \times 10^{-13}$ cm and f is the form factor which is unity at $Q = 0$.

The magnetic correlation function

$$S(\boldsymbol{q},\omega) = \int_{-\infty}^{\infty} \mathrm{d}t\, \mathrm{e}^{-\mathrm{i}\omega t} \sum_{i,j} \mathrm{e}^{\mathrm{i}\boldsymbol{q}(\boldsymbol{R}_i - \boldsymbol{R}_j)} \langle \boldsymbol{S}_i(t) \cdot \boldsymbol{S}_j(0) \rangle \tag{7.7}$$

is related to the imaginary part of the dynamic susceptibility

$$S(\boldsymbol{q},\omega) = \frac{1}{1 - \mathrm{e}^{-\frac{\hbar\omega}{kT}}}\, \chi''(\boldsymbol{q},\omega)\,. \tag{7.8}$$

For a system of local magnetic moments a sum rule for the scattering can then be defined

$$\sum_{\boldsymbol{q}} \int_{-\infty}^{\infty} \mathrm{d}\omega\, S(\boldsymbol{q},\omega) = \int_{-\infty}^{\infty} \mathrm{d}\omega \sum_{\boldsymbol{q}} \int_{-\infty}^{\infty} \mathrm{d}t\, \mathrm{e}^{-\mathrm{i}\omega t} \sum_{i,j} \mathrm{e}^{\mathrm{i}\boldsymbol{q}(\boldsymbol{R}_i - \boldsymbol{R}_j)} \langle \boldsymbol{S}_i(t) \cdot \boldsymbol{S}_j(0) \rangle \tag{7.9}$$

which yields

$$N\langle S^2 \rangle = NS(S+1)\,. \tag{7.10}$$

Typically the sum rule is obtained by integrating the scattering up to some finite energy, which for a system with an ordered ground state is usually the maximum spin wave energy $\sim k\,T_\mathrm{C}$. By integrating the response over the same range in q and ω as in the ground state the sum rule was conserved. In the paramagnetic phase the response is diffusive centred on $\omega = 0$ with a width $\Delta\omega$ that increases from zero at $q = 0$ to the maximum value $\sim k\,T_\mathrm{C}$ at the zone boundary. The scattering function can be described by a double Lorentzian appropriate for diffusive behaviour [16]

$$S(\boldsymbol{q},\omega) \propto T \left[\frac{1}{(\kappa_1^2 + q^2)}\right] \left[\frac{\Lambda_1\, q^2}{(\Lambda_1\, q^2)^2 + \omega^2}\right]\,, \tag{7.11}$$

where κ_1 is the inverse correlation length and Λ_1 characterises the line width.

7.6 Inelastic Neutron Scattering

The dispersion of acoustic phonons in the cubic austenite phase of Ni_2MnGa has been determined using inelastic neutron scattering and a single crystal with $T_\mathrm{M} \sim 220\,\mathrm{K}$ [17]. The measurements show a pronounced softening of the TA_2 phonon propagating in the [110] direction at a wave vector $q \sim 0.33$. This softening begins above the Curie temperature in the paramagnetic phase and becomes more pronounced but not complete as the temperature is lowered. A maximum softening was observed at $\sim$260 K below which temperature a pre-martensitic phase, characterised by a $\left[\frac{1}{3}\frac{1}{3}0\right]$ propagation vector, is established down to T_M. The lack of complete softening often observed in structural

phase transitions has been attributed to a coupling of the phonon modes with lattice strains [18]. The thermal variation of the $q = 0.325$ mode is shown in Fig. 7.4. From this figure it may be seen that the mode reaches a minimum frequency close to 260 K but below this temperature the frequency begins to increase. Above 260 K the square of the phonon energy has a linear dependence on temperature as expected for a soft mode. Extrapolation of the straight line fit yields a transition temperature $T_0 \sim 250$ K which is somewhat lower than the transition temperature for the sample. This has led to the conjecture that an additional phase occurs between 250 and 220 K, possibly of an incommensurate nature which would give rise to tweed behaviour [19]. However neutron diffraction measurements show that pre-martensitic phase with the $\left[\frac{1}{3}\frac{1}{3}0\right]$ modulation extends down to the martensitic phase transition [20].

Precursor phenomena are not expected for first order phase transitions but they can occur in second order transformations. Their presence prior to some martensitic phase transitions has been explained assuming anharmonic coupling between a TA_2 phonon mode and the long wavelength shear mode associated with $c' = \frac{1}{2}(c_{11} - c_{12})$. The shear constants c_{44} and c' [21–23] both show a pronounced dip at the onset of the pre-martensitic phase with that of c' being substantially larger at ∼60%. Consequently the elastic anisotropy c_{44}/c' increases significantly at this temperature. Below the transition c' increases thus reducing c_{44}/c' to a value smaller than that observed in related Cu–Ni–Al and Cu–Zn–Al compounds undergoing a structural phase transition [24].

The neutron elastic scattering in the martensitic phase of the crystal, used to establish the soft mode behaviour, has also been investigated [25]. The five fold modulation along the [ξξ0] direction which had been proposed [5] on the basis of X-ray measurements could not be observed. However, new Bragg peaks were found in scans along [ξξ0], the peak at $\xi = 0.43$ being the most

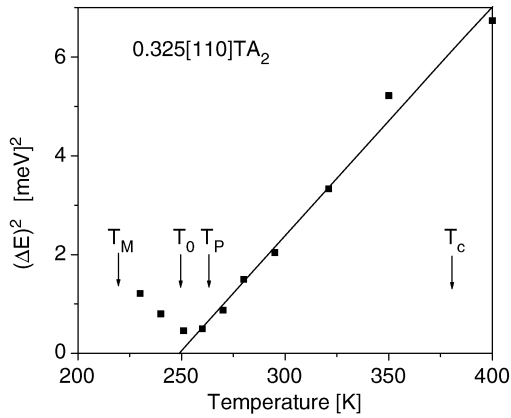

Fig. 7.4. The temperature dependence of the soft mode behaviour of the TA_2[110] phonon with $q = 0.325$. T_M, T_P and T_0 are the martensitic, pre-martensitic and extrapolated transition temperatures

intense. This value corresponds to $\xi = 3/7$ and is consistent with the recently proposed [20] seven fold modulated structure for the martensitic phase. A calculation of the structure factors for the proposed model shows that the majority of the satellites are weak but the strongest reflection is $\left[\frac{3}{7}\frac{3}{7}0\right]$. More recent inelastic measurements have identified a partial softening of the TA mode at this wave vector [26].

7.7 Neutron Diffraction

High resolution powder and single crystal measurements have enabled the phase diagram and structures of stoichiometric Ni_2MnGa to be established [20]. The low absorption cross section and the difference in the coherent nuclear scattering amplitudes of the three elements make neutron scattering the appropriate technique.

When annealed at 800°C and then quenched, Ni_2MnGa has the $L2_1$ structure. This was confirmed by neutron powder diffraction measurements in the paramagnetic phase at 400 K. The lattice parameter was determined to be 5.8636 Å. At 300 K the compound still has the $L2_1$ structure as shown in Fig. 7.5 but is ferromagnetic with a moment of $2.4\,\mu_B$ located on the Mn

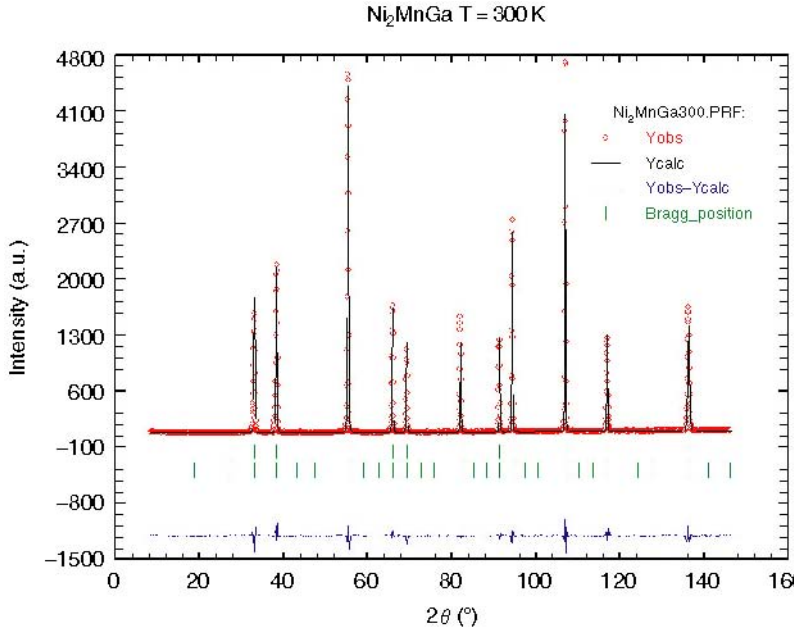

Fig. 7.5. The observed and calculated neutron diffraction patterns of stoichiometric Ni_2MnGa in the ferromagnetic phase at 300 K, together with the difference pattern

Table 7.4. Parameters of the cubic $L2_1$ structure of stoichiometric Ni_2MnGa determined from profile refinement of neutron powder diffraction patterns at 300 and 400 K

Cubic Heusler L21 structure, space group $Fm\bar{3}m$								
Mn	4a	000	Ga	4b	$\frac{1}{2}\frac{1}{2}\frac{1}{2}$	Ni	8c	$\frac{1}{4}\frac{1}{4}\frac{1}{4}$
				300 K			400 K	
a (Å)				5.8229(2)			5.8636(2)	
				Ferromagnetic			Paramagnetic	
Mn moment (μ_B)				2.4(2)			–	
Mn occupancy				1			1	
Ga occupancy				1			1	
Ni occupancy				1			1	
χ^2				4.9			4.7	

atoms in excellent agreement with the value obtained from magnetisation measurements. A refinement carried out in which the Ni atoms were allowed to carry a moment did not improve the goodness of fit as indicated by a chi-squared test. The results of the refinement are given in Table 7.4. However polarised neutron measurements indicate that the nickel atoms carry a small moment [27].

7.8 Pre-Martenstic Phase

At 220 K there was a slight change to the powder diffraction pattern. The main fcc peaks remained essentially unchanged but in addition a number of smaller peaks were observed. The position of the smaller peaks could be accounted for using the reported three fold modulation of the lattice in the pre-martensitic phase [16]. However a detailed investigation of the pre-martensitic phase was undertaken using neutron single crystal diffraction.

At room temperature, the reflections observed in single crystal measurements were just those characteristic of the cubic Heusler $L2_1$ structure. On cooling from 300 K additional reflections became apparent around 255 K which could be indexed as $\boldsymbol{g} \pm \boldsymbol{\tau}$, where $\boldsymbol{g}$ is a reciprocal lattice vector of the fcc lattice and $\boldsymbol{\tau} = \frac{1}{3}, -\frac{1}{3}, 0$. The six domains which give the six armed star of $\boldsymbol{\tau}$ correspond to three different possible orientations of c_{orth} $[001]_{\text{cubic}}$, $[010]_{\text{cubic}}$ and $[100]_{\text{cubic}}$ for each of which a_{orth} can have two different orientations. The six domains occurring around the $(-2\,-2\,0)$ reflection are shown in the neutron Laue pattern presented in Fig. 7.6 [28]. A q scan along $h\ -h\ 0$ from -1.45 $-2.55\ \ 0$ to $-2.55\ -1.45\ \ 0$ carried out at 215 K is shown in Fig. 7.7.

The data are plotted on a log scale to enable comparison of the satellite reflections with the fundamental $-2-2\ \ 0$ peak. The satellites arising from the $\frac{1}{3}\frac{1}{3}0$ modulated pre-martensitic phase persisted down to ∼200 K at which

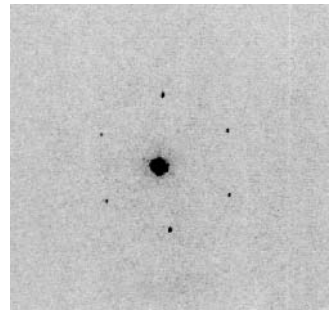

Fig. 7.6. A neutron Laue photograph in the premartensitic phase of Ni_2MnGa showing the fundamental $-2\,-2\,0$ reflection and the $\frac{1}{3}\,\frac{1}{3}0$ satellite reflections

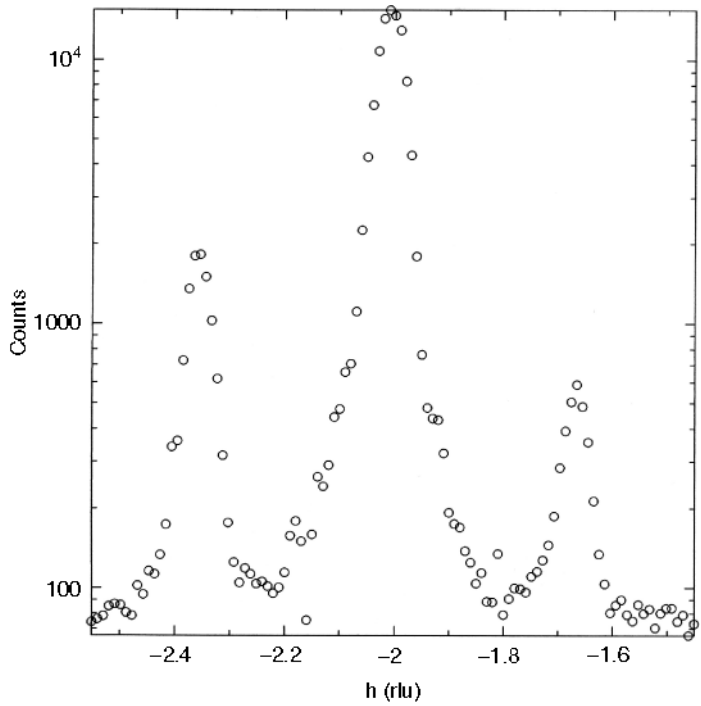

Fig. 7.7. q scan along $h\bar{h}0$ through the $\bar{2}\bar{2}0$ reflection at 215 K

temperature the crystal transformed to the martensitic phase. Other than the fundamental fcc and satellite reflections no further Bragg peaks were observed in this temperature range. This was also confirmed at 220 K using high resolution neutron powder diffraction. The thermal evolution of the integrated intensity of three reflections $-4\,-4\,4$; $-4+\frac{1}{3}$, $-4-\frac{1}{3}$, 4 and $-4+\frac{1}{3}$, -4, $4+\frac{1}{3}$ are shown in Fig. 7.8. The integrated intensities of the satellite peaks

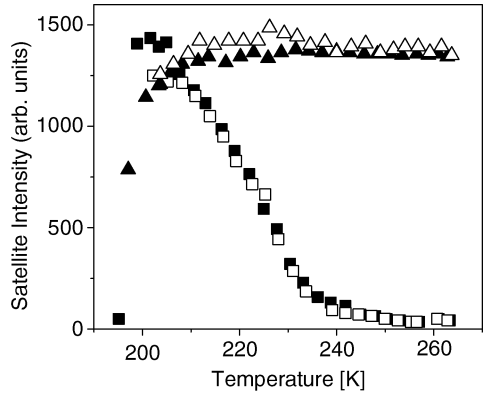

Fig. 7.8. The temperature dependence of the fundamental $4\bar{4}0$ reflection (*triangles*) and the $(-3.66, -4.33, 4)$ satellite reflection (*squares*) in the premartensitic phase of stoichiometric Ni_2MnGa. The *open* symbols are for zero field and the *filled* ones for $B = 0.5\,\mathrm{T}$

generated using all members of the star from all accessible reciprocal lattice vectors in the positive quadrant of reciprocal space were measured at 230 and 215 K. The measured reflections were assigned to their respective domains and the domain populations estimated from reflections measured in more than one domain. The populations were used to scale and average all the measurements to obtain a set of integrated intensities for the satellite reflections scaled to the whole crystal volume. The atomic positions refined for a modulated structure which has space group Pnnm are given in Table 7.5. The orthorhombic

Table 7.5. Structural parameters for the pre-martensitic and martensitic phases refined in space group Pnnm. Only the values given as decimal fractions were refined

			230 K			215 K			20 K		
Atomic positions			x	y	z	x	y	z	x	y	z
2Mn1	2a	000									
4Mn2			0.013	$\frac{1}{3}$	0	0.02189	$\frac{1}{3}$	0	0.041	$\frac{1}{7}$	0
4Mn3	4g	$xy0$							-0.070	$\frac{2}{7}$	0
4Mn4									0.072	$\frac{3}{7}$	0
2Ga1	2b	$00\frac{1}{2}$									
4Ga2			0.015	$\frac{1}{3}$	$\frac{1}{2}$	0.0051	$\frac{1}{3}$	$\frac{1}{2}$	0.009	$\frac{1}{7}$	$\frac{1}{2}$
4Ga3	4g	$xy0$							0.026	$\frac{2}{7}$	$\frac{1}{2}$
4Ga4									0.062	$\frac{3}{7}$	$\frac{1}{2}$
4Ni1	4f	$\frac{1}{2}0z$			$\frac{1}{4}$			$\frac{1}{4}$			$\frac{1}{4}$
8Ni2			0.4930	$\frac{1}{3}$	$\frac{1}{4}$	0.4870	$\frac{1}{3}$	$\frac{1}{4}$	0.476	$\frac{1}{7}$	$\frac{1}{4}$
									0.549	$\frac{2}{7}$	$\frac{1}{4}$
									0.433	$\frac{3}{7}$	$\frac{1}{4}$
Manganese moment (μ_B)			3.05						3.07		
χ^2			10			9			9		

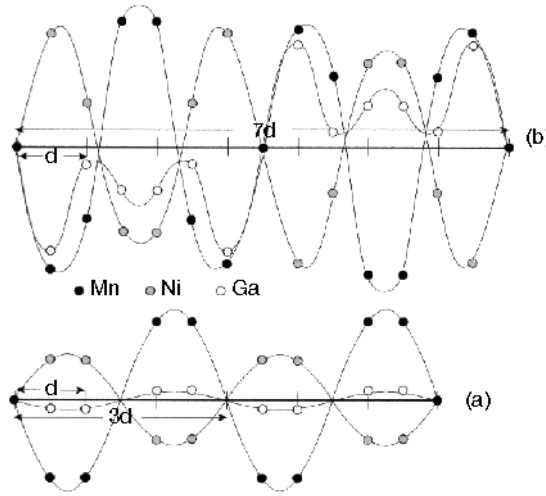

Fig. 7.9. Displacements parallel to a_{orth} of atoms in successive (010) planes of (**a**) the pre-martensitic phase at 215 K and (**b**) the martensitic phase at 20 K. The displacements are represented on an arbitrary scale. For clarity that in (**a**) is twice that in (**b**). d is the lattice spacing of the cubic cell in the $\langle 110 \rangle$ direction $a_{\mathrm{cubic}}/\sqrt{2}$

super-cell which accounts for all the observed reflections has $a_{\mathrm{ortho}} = a_{\mathrm{cub}}/\sqrt{2}$, $b_{\mathrm{ortho}} = 3a_{\mathrm{cub}}/\sqrt{2}$ and $c_{\mathrm{ortho}} = a_{\mathrm{cub}}$; with $a_{\mathrm{ortho}} \parallel [110]_{\mathrm{cub}}$, $b_{\mathrm{ortho}} \parallel [1\bar{1}0]_{\mathrm{cub}}$ and $c_{\mathrm{ortho}} \parallel [001]_{\mathrm{cub}}$. In this structure successive (110) planes of atoms are displaced with respect to one another in the [110] direction by an amount which is modulated with a period of three lattice spacings in the [110]. The displacement along a_{ortho} of the sublattices of Mn, Ni and Ga atoms in planes parallel to $(010)_{\mathrm{ortho}}$ are plotted against their positions on the b_{ortho} axis in Fig. 7.9. It may be seen that the modulations of the Mn and Ni sublattices are out of phase and so the structural distortion is more nearly equivalent to a compression wave in the $(010)_{\mathrm{ortho}}$ planes, propagating in the $[100]_{\mathrm{ortho}}$ direction, than it is to a simple displacement of the planes. There is some evidence for reflections with $h = 0$ that the structure may relax in other directions as well but the data were not sufficient to permit the associated y or z displacements to be determined.

7.8.1 Field Dependence

The effect of a magnetic field on the pre-martensitic phase and the possibility of domain switching has also been investigated [29]. After cooling from the cubic phase to 219 K the relative populations of the 6 different domains of the $\frac{1}{3}\frac{1}{3}0$ modulated pre-martensitic phase were found to be essentially equal. The equality was found not to be altered by the application of a field of 2 T applied parallel to [001]. The 2 T field increased the mean satellite intensity by a small amount, consistent with the alignment of the magnetisation parallel

to [001]. In a further experiment the crystal was cooled into the martensitic phase at 165 K and a field of 2 T was applied along [001] and then removed. This treatment completely suppressed all twins with c-axes perpendicular to [001]. Hence the domain population of the martensitic phase was substantially modified. The crystal with this configuration was then warmed to 219 K and the relative populations of the pre-martensitic domains determined. Again all 6 domains were found to be essentially equally populated; they do not follow the distribution of domains in the martensitic phase.

7.9 The Martensitic Phase

Below 200 K the powder diffraction pattern is considerably more complicated as may be seen from the pattern obtained at 20 K and shown in Fig. 7.10. Apart from the improved resolution the diffraction pattern is similar to that originally reported [4]. Some of the original fcc peaks split, the weak peaks observed at 220 K disappear and new peaks emerge. The number and position of the Bragg peaks remained essentially unchanged down to 4 K the lowest temperature at which measurements were made. The splitting of the Bragg peaks is consistent with the loss of cubic symmetry whilst the appearance of new peaks suggests that the translational symmetry is also altered.

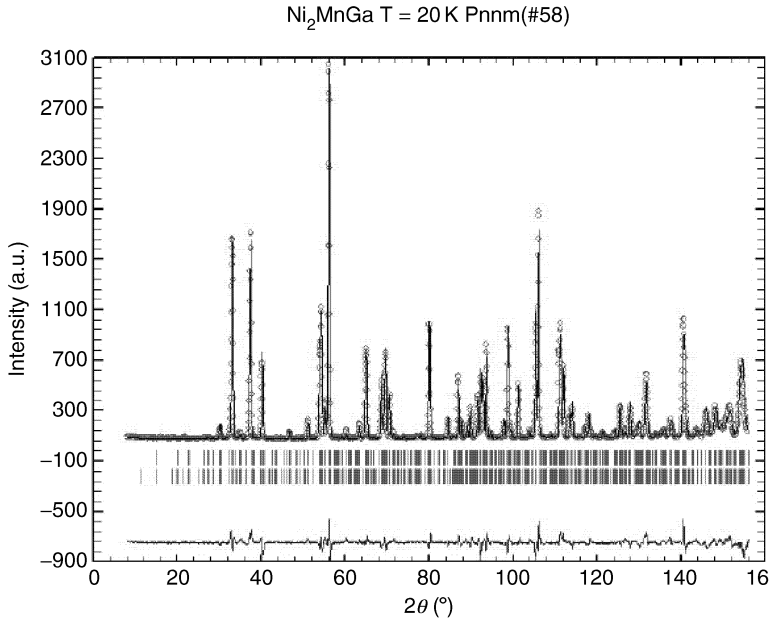

Fig. 7.10. The observed and calculated neutron diffraction patterns of ferromagnetic Ni_2MnGa in the transformed phase at 20 K, together with the difference pattern

An initial refinement was carried out based on the previous report [4] that the low temperature phase was tetragonal. A bct tetragonal cell was employed with space group I4/mma and lattice parameters $a = b = a_t/\sqrt{2} = 4.187\,\text{Å}$ and $c = c_t = 5.566\,\text{Å}$. However this model only accounted for some of the strong peaks. The possibility that the material had not fully transformed and that there remained a residual cubic component was also considered. However the cubic pattern could not account for the extraneous intense peaks. Closer inspection of the intense Bragg peaks which above T_m were of the form $(h + k + l) = 2n$ suggested that they split into three at the transformation suggesting orthorhombic symmetry and the loss of the four fold axis. Based on this observation a new refinement was carried out using the space group Imma. This structure accounted for the splitting of the intense peaks but was unable to account for the additional weaker ones.

Having established the nature of the transformation, the possible modifications to the orthorhombic cell which could account for the additional peaks were considered. Based on X-ray measurements a five fold modulation of the low temperature bct phase has been proposed [5]. Dependent on stoichiometry or residual stress other periodicities have also been suggested [4, 29]. However none of these structures accounted for the 'additional' peaks observed in the neutron powder diffraction pattern. However a structure similar to that of the precursor phase but with a seven fold increase in the length of the b axis was able to account for all of the observed reflections. Using the new super-cell with lattice parameters $a = 4.2152$, $b = 29.3016$ and $c = 5.5570\,\text{Å}$, and space group Pnnm a refinement accounted for all of the observed peaks and did not generate any additional ones. It may be seen that the degree of orthorhombic distortion $(a - b/7)$ is relatively small; its observation is only made possible by the high resolution of the diffractometer. The results of the refinement in which the atomic positions were permitted to vary consistent with the space group Pnnm are given in Table 7.5. In addition the manganese atoms were allowed to carry a ferromagnetic moment. As for the refinement at higher temperatures the moment was confined to the manganese atoms with an additional constraint that the four manganese atoms had the same moment. The moment was found to lie along the c axis. Displacements parallel to a_{ortho} of the atoms in successive planes parallel to $(010)_{\text{ortho}}$ are plotted in Fig. 7.9. Comparison with the results obtained for the pre-martensitic phase shows that although the unit cells of the phases are quite distinct the modulation of the martensitic phase is far from sinusoidal and its dominant frequency is not very different from the pre-martensitic phase. In both phases the displacements of the Mn and Ni sublattices are out of phase.

7.10 Structural and Magnetic Phase Diagram

These high resolution neutron powder and single crystal diffraction experiments on stoichiometric samples of Ni_2MnGa with $T_M = 200\,\text{K}$ have enabled

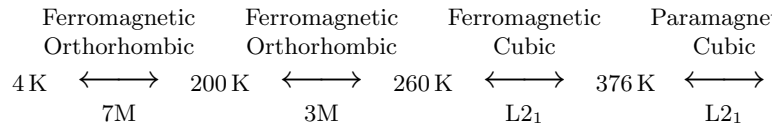

Fig. 7.11. The sequence of structural and magnetic phase transitions in stoichiometric Ni_2MnGa

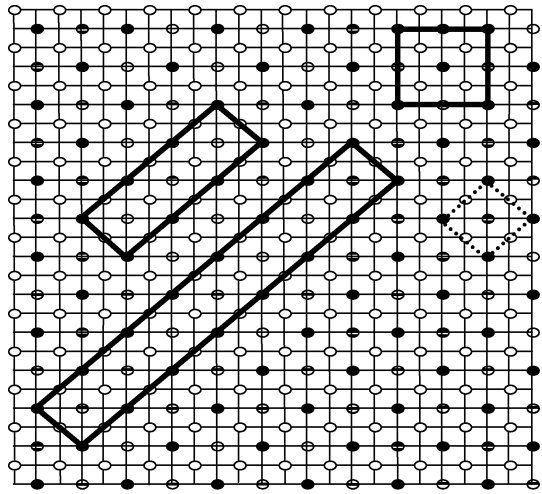

Fig. 7.12. Projection on the (001) plane of the ideal $L2_1$ Heusler structure, showing the $L2_1$ cell, the body centred tetragonal cell and the two orthorhombic super-cells. All the cells have the same c axis

the sequence of structural phase transitions shown in Fig. 7.11 to be established. The relationships between the unit cells of the three structurally different phases is illustrated in Fig. 7.12. The super-structures found for the two low temperature phases are derived from the cubic Heusler structure by a periodic displacement of the atoms in successive (110) planes along the $[1-10]$ direction. This leads to an orthorhombic unit cell with space group Pnnm with $a_{\text{ortho}} \parallel [1{-}10]_{\text{cubic}}$, $b_{\text{ortho}} \parallel [110]_{\text{cubic}}$ and $c_{\text{ortho}} \parallel [001]$, and $a_{\text{ortho}} = a_{\text{cubic}}/\sqrt{2}$, $b_{\text{ortho}} = n\, a_{\text{cubic}}/\sqrt{2}$ and $c_{\text{ortho}} = a_{\text{cubic}}$, where n is the periodicity of the displacement. The periodicities were found not to change on the application of magnetic fields up to 2 T or stress up to 560 MPa. The change from three to seven fold modulation occurs abruptly at T_m without any intermediate step. A seven fold modulation has been reported [30,31] for shape memory alloys in the series $Nixal_{1-x}$ with $0.6 \leq x \leq 0.65$. In the higher temperature phase the materials have the CsCl structure which is closely related to the Heusler structure through B2 disorder. On the basis of Landau analysis [32] it has been proposed that the modulation arises again from the anharmonic coupling of a Σ_4 phonon with the elastic constant c'.

7.11 Mechanism

The martensitic phase transition in Ni_2MnGa, fundamental to its shape memory behaviour, can be described by two successive 110 type shears leading to 36 possible different orientations for the axes of the pseudo-tetragonal martensitic phase. Identification of the tetragonal domains is facilitated by the relatively large c/a ratio $\sim$0.94. However it is still necessary to determine the distribution and orientation of the domains which has been made possible by the use of multidetectors available on the diffractometers at the ILL in Grenoble. Neutron diffraction is an appropriate tool since the tetragonal distortion is well within the instrumental resolution and the low absorption allows the whole of relatively large samples ($\sim$50 mm^3) to be studied.

Diffraction experiments have been carried out on annealed and on prestressed crystals and also on crystals subject to in situ stress and applied magnetic field [29]. Scans through the position of the fundamental reflections were made at small temperature intervals in the range 220 to 174 K both heating and cooling. The contour plot in Fig. 7.13 shows the evolution of the 400 and 040 reflections from an annealed sample above during and below the transition. At temperatures above 206 K all the samples were found to resume their original form giving, for each reflection, in each thermal cycle, a single well

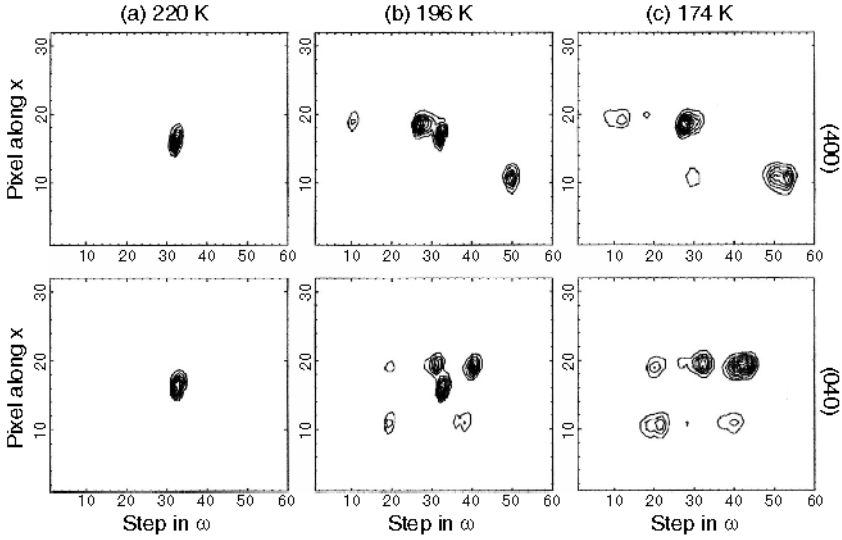

Fig. 7.13. Contour plots of the counts summed over the vertical pixels of the detector from 7 to 25 as a function of the scattering angle (*vertical axis*) and the scan step (*horizontal axis*) for scans through the 040 and 400 reflections of an annealed crystal. Higher values of x correspond to smaller scattering angles. At 220 K (**a**) the sample is in the cubic phase, at 196 K (**b**) it is transforming and at 174 K (**c**) it is in the pseudo-tetragonal phase

defined diffraction peak in a constant position no matter how many different peaks were present in the martensitic phase. The number and orientation of the martensitic twins observed in the transformed phase is different for each sample and evolves during thermal cycling. The number of twins observed is always many fewer than allowed by symmetry. The positions of peaks in the scans enable the orientation relationships of the martensitic twins relative to the cubic crystal to be determined. These were found to be consistent with the transformation proceeding by two successive shears on {110} planes in $\langle 1-10\rangle$ directions. There are two ways in which such shears can lead to a pseudo-tetragonal cell ($c/a < 1$).

A general shear stress, such as those expected to occur in martensitic transformations, can be described by a shear displacement $\boldsymbol{\tau}$ in a plane $\boldsymbol{k}$; $\boldsymbol{\tau}$ must lie in the plane so $\boldsymbol{\tau} \cdot \boldsymbol{k} = 0$. The displacement of a point with radius vector $\boldsymbol{r}$ due to stress is

$$\boldsymbol{\delta} = (\boldsymbol{r} \cdot \boldsymbol{k})\boldsymbol{\tau} \,, \tag{7.12}$$

and the matrix M describing the transformation of the unit cell $\boldsymbol{r'} = \mathsf{M}\,\boldsymbol{r}$ is given by

$$M_{ij} = \delta(ij) + \tau_i k_j \,. \tag{7.13}$$

For two successive shears $\boldsymbol{\tau}$ on $\boldsymbol{k}$ and $\boldsymbol{\sigma}$ on $\boldsymbol{q}$, small enough for the products of the displacements to be negligible, the matrix, written out in full, becomes

$$\mathsf{M} = \begin{pmatrix} 1+\tau_1 k_1 + \sigma_1 q_1 & \tau_1 k_2 + \sigma_1 q_2 & \tau_1 k_3 + \sigma_1 q_3 \\ \tau_2 k_1 + \sigma_2 q_1 & 1+\tau_2 k_2 + \sigma_2 q_2 & \tau_2 k_3 + \sigma_2 q_3 \\ \tau_3 k_1 + \sigma_3 q_1 & \tau_3 k_2 + \sigma_3 q_2 & 1+\tau_3 k_3 + \sigma_3 q_3 \end{pmatrix} . \tag{7.14}$$

The matrix represents an orthogonal transformation if

$$\begin{aligned} \tau_1 k_2 + \tau_2 k_1 &= -\sigma_1 q_2 - \sigma_2 q_1 \,, \\ \tau_2 k_3 + \tau_3 k_2 &= -\sigma_2 q_3 - \sigma_3 q_2 \,, \\ \tau_3 k_1 + \tau_1 k_3 &= -\sigma_3 q_1 - \sigma_1 q_3 \,, \end{aligned} \tag{7.15}$$

and in this case the volume of the transformed cell, given by

$$V' = V(1 + \tau_1 k_1 + \sigma_1 q_1 + \tau_2 k_2 + \sigma_2 q_2 + \tau_3 k_3 + \sigma_3 q_3) \tag{7.16}$$

is unchanged because of the orthogonality between $\boldsymbol{\tau}$ and $\boldsymbol{k}$, and $\boldsymbol{\sigma}$ and $\boldsymbol{q}$.

7.12 Martensitic Twinning in Ni_2MnGa

In Ni_2MnGa the shears occur on 110 planes in the $\langle -110\rangle$ directions. Taking $\boldsymbol{k}$, $\boldsymbol{\tau}$ as (011), $[0{-}\tau\tau]$ and $\boldsymbol{q}$, $\boldsymbol{\sigma}$ as $(101), [\sigma 0{-}\sigma]$; the transformation matrix becomes

$$\mathsf{M} = \begin{pmatrix} 1+\sigma & 0 & \sigma \\ 0 & 1-\tau & -\tau \\ -\sigma & -\tau & 1+\tau-\sigma \end{pmatrix} . \tag{7.17}$$

For the pseudo-tetragonal shears in Ni_2MnGa $c/a < 1$, so either $\tau = -\sigma$ and the c axis of the pseudo-tetragonal cell is parallel to the cubic [001] direction, or $\tau = 2\sigma$ and the c axis is parallel to [010]. The two possibilities are given by

$$\mathsf{M}_{1xy} = \begin{pmatrix} 1+\sigma & 0 & \sigma \\ 0 & 1+\sigma & \sigma \\ -\sigma & -\sigma & 1-2\sigma \end{pmatrix}, \quad \mathsf{M}_{2xy} = \begin{pmatrix} 1+\sigma & 0 & \sigma \\ 0 & 1-2\sigma & -2\sigma \\ -\sigma & 2\sigma & 1+\sigma \end{pmatrix}. \quad (7.18)$$

The first index in the subscript indicates whether it arises from equal shears (type 1) or if the second shear is twice the first (type 2). The second and third indices identify the axes perpendicular to the two shears, for type 2 twins the second index corresponds to the longer displacement.

$$\mathsf{M}_{2zy} = \begin{pmatrix} 1+\sigma & -\sigma & -2\sigma \\ \sigma & 1+\sigma & 0 \\ -2\sigma & 0 & 1-2\sigma \end{pmatrix}, \quad \mathsf{M}_{2zx} = \begin{pmatrix} 1+\sigma & \sigma & 0 \\ -\sigma & 1+\sigma & 2\sigma \\ 0 & -2\sigma & 1-2\sigma \end{pmatrix}. \quad (7.19)$$

The three matrices, M_{1xy}, M_{2zy} and M_{2zx} have identical diagonal components but are distinguished by off diagonal terms which describe the orientation of tetragonal axes with respect to the cubic ones; for example the component M_{23} gives the rotation of the y and z axes about x. In all three matrices one of the three pairs of off diagonal elements is zero and this may be used to identify the shears, giving rise to different domains in the transformed crystal. For the type 1 domains it is the tetragonal c axis about which there is no rotation, whereas for type 2 domains it is one of the other a axes. The shear displacement $\sigma = 2(a-c)/3(a+c)$. For type 1 shears the mean rotation about the three axes is $2\sigma/3$ whereas for type 2 it is σ.

The two shears giving rise to type 1 matrices are equivalent: there are 12 different ways in which pairs of 110 planes inclined at 120° to one another may be chosen, leading to 12 differently oriented type 1 twin domains. Each type 1 twin shares one a axis with another twin and the other a axis with a third. For type 2 matrices the two shears are distinct, so there are 24 differently oriented type 2 twin domains. Each type 2 twin shares its c axis with one other member of the set and one of its a axis with a third.

The effects of applying a uniaxial stress and magnetic field above and below T_M were studied in a thermal cycling experiment similar to that described previously. Figure 7.14 shows the effect of a very small uniaxial stress on the twin populations. The domains whose c axes are parallel to the stress are favoured, while those with perpendicular c axes, disappear. A very similar behaviour is observed on applying a magnetic field; 0.03 T was sufficient to convert all twins whose c axes were perpendicular to the field direction to ones with parallel c axes. These results suggest that magneto-strictive strain rather than magneto-crystalline anisotropy is responsible for the change in domains brought about by applying a magnetic field. The domains can change identity by simple reversal of the unfavourable shears. For example a [010] domain formed by type 1 shears on 101 and 011 will change to an [001]

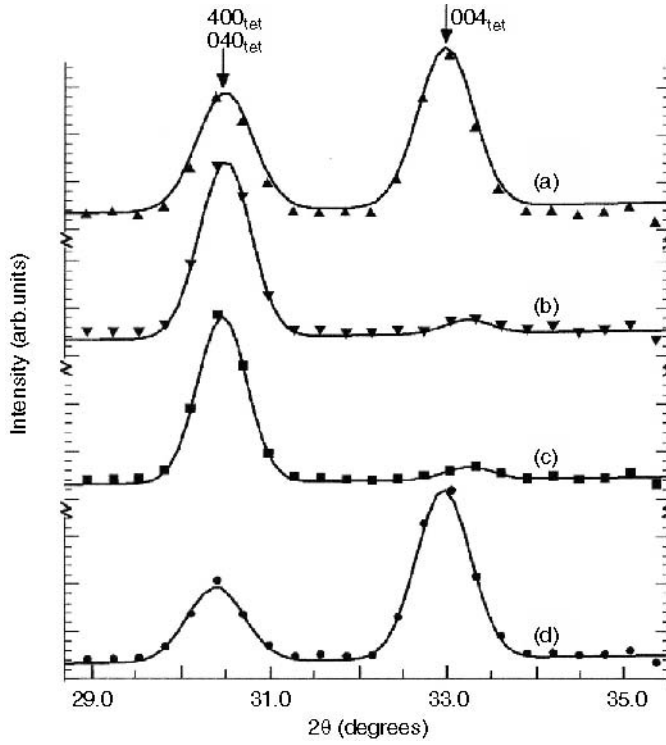

Fig. 7.14. Intensity recorded at 172 K in scans through the position of the cubic 400 reflection plotted against the scattering angle (2θ). (**a**) After cooling with no applied stress, (**b**) is (**a**) with 30 MPa applied at 172 K ∥ [001]; (**c**) is (**b**) with the 30 MPa stress removed, and (**d**) is after heating to 250 K and recooling with no stress applied. The higher angle peak in the scans is due to domains with the pseudo-tetragonal c axis parallel to [100]; they are suppressed by the stress

domain of type 2 if the shear on 011 is reversed and doubled. Similarly a [100] domain of type 2 formed by shears on 110 and 101 can be converted to a type 1 [001] domain by reversing and halving the shear on 101. The temperatures and fields at which different types of domain were found to switch are reported in Table 7.6. Type 1 domains were found to occur with twice the frequency of type 2 amongst both the annealed and the stressed samples. Using this classification, the mean rotations for the types of domain were calculated. These gave $\sigma = 0.019(3)$ for the type 1 domains and $\sigma = 0.14(2)$, $2\sigma = 0.24(2)$ for type 2 domains. The values calculated from the lattice parameters is $\sigma = 0.02$. The rotations are roughly in accord with the model for the type 1 domains but are significantly smaller than expected for the type 2 domains. Using the position of the superstructure reflections below T_{M} the orientations of the long orthorhombic axis with respect to the rotation matrices were determined. For all type 1 domains for which data were available

Table 7.6. The temperature and fields at which domain switching occurs in the martensitic phase of Ni_2MnGa with initial twin configurations

			Dominant twins	
Temperature (K)	Field (T)	Constant	Before	After
174	0.2	T	$2xy$	$1xy$
159	0.25	H	$1yz$ $(2yz)$	$2zx$
164	0.25	T	$1xz$	$1xy$
179	0.3	T	$1yz$ $1xz$	$1xy$
174	<0.5	T	$1xz$ $1yz$	$2zy$ $1xy$
176.5	4.5	H	$2yz$ $2xz$	$2zx$

this axis was found to be parallel to the bisector of the normals to the two slip planes involved. For type 2 domains the long y axis was either parallel or perpendicular to the slip plane on which the smaller of the two shears occur.

7.13 Non Stoichiometric Samples

The influence of stoichiometry on the magnetic and structural properties of Ni–Mn–Ga alloys have been investigated by several groups [33–35]. Discussion here will focus on the $Ni_{2+x}Mn_{1-x}Ga$ series in which only the amounts of Ni and Mn are varied. X-ray and resistivity measurements [33] have been used to study the effects of stoichiometry on the transition temperature T_M and the Curie temperature T_C. The resulting phase diagram presented in Fig. 7.15 shows that T_M increases with x, while T_C slowly decreases with the two temperatures coinciding at $\sim$325 K for $x = 0.19$.

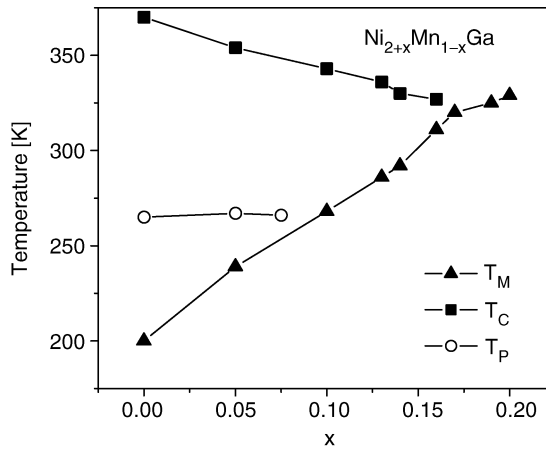

Fig. 7.15. Magnetic phase diagram of $Ni_{2+x}Mn_{1-x}Ga$

In addition to optimising the transition temperatures the mechanical properties are also improved. They are more ductile so that the manufacture of devices becomes feasible. The electronic structure calculations on $Ni_{2.17}Mn_{0.83}Ga$ predict that the martensitic phase can have tetragonal, orthorhombic or a monoclinic structure, with the latter being the most probable [36]. The choice of the monoclinic structure arises from differences in kinetic energy to which the excess nickel atoms make an important contribution. It is predicted that the excess nickel atoms preferentially occupy the manganese sites and that the magnetic moments in the monoclinic structure are smaller by about $0.3\,\mu_B$ than in the parent cubic structure. The crystallographic structure of $Ni_{2.19}Mn_{0.81}Ga$ has been investigated by neutron diffraction [37,38] using a triple axis spectrometer and a sample in which the structural phase transition and Curie temperature coincide at 350 K. This temperature is higher than that reported by [39] for an alloy of the same composition. In the paramagnetic phase the compound was reported to have the Heusler structure with the excess nickel atoms occupying the deficit Mn sites. On cooling, the martensitic phase was found to contain two phases with different structures, although details of the refinement, in particular the atomic positions were not given. At 297 K one phase is reported to have an orthorhombic modification of the Heusler structure with lattice parameters 6.092, 5.751 and 5.483 Å, and the other a monoclinic structure with parameters of 4.246, 5.463 and 12.678 Å, and $\beta = 99.2°$ [38]. At 350 K 30% of the sample was found to be in the cubic parent phase and 70% in the transformed martensitic phase. Analysis of the high angle data for which the magnetic Bragg component was negligible revealed that the percentage of cubic phase was reduced to 15% by application of a field of 5 T. On removal of the field the volume of the cubic phase only returned to 22%. This observation suggests that the phase transition in $Ni_{2.19}Mn_{0.81}Ga$ can be controlled isothermally by the application of a field. Subsequent neutron powder diffraction measurements on $Ni_{2.17}Mn_{0.83}Ga$ confirm that the crystallographic structure is field dependent in the vicinity of T_M [40]. The choice of composition was dictated by the temperature range of the cryomagnet available at the ILL. High resolution diffraction experiments on both $Ni_{2.19}Mn_{0.81}Ga$ and $Ni_{2.17}Mn_{0.83}Ga$ show that the sequence of phase transitions is the same for both compounds although the transition temperatures were slightly higher for the Ni rich compound. The measurements also show that the thermal evolution of the phase transition is more complex than previously reported. Although the sequence of transitions has been established the structures of the phases have not been completely determined. Above 310 K $Ni_{2.17}Mn_{0.83}Ga$ has the $L2_1$ structure with lattice parameter $a = 5.79$ Å in which the excess Ni atoms occupy the vacant manganese sites. In the refinement it was assumed that the moment is confined to the Mn atoms. A small moment $\sim 0.2\,\mu_B$ may be associated with the Ni atoms but polarised single crystal measurements are required to confirm this. At low temperatures, in the ground state, the compound has a tetragonal structure with cell parameters $a = b = 3.87$, $c = 6.47$ Å and space

group I4/mmm. Although the a and b axes change by ∼5.5% and the c axis by almost 12% there is negligible change in atomic volume. The large change in cell parameters and the relatively high transition temperature $T_M = 301\,K$ make the compound a promising candidate for applications. However below ∼305 K an intermediate phase appears and for a significant temperature interval this phase coexists with the cubic and tetragonal structures. By ∼250 K the tetragonal phase dominates with only small remnants of the Bragg peaks of the intermediate structure remaining. The complexity of the transition is reflected in the strong hysteresis in the transport properties [41]. An orthorhombic unit cell based on that proposed by Inoue et al. [38] enabled all of the strong peaks of the intermediate phase to be indexed. Although the structure determination is not yet complete it is clear that unlike stoichiometric Ni_2MnGa the martensitic phase of the non-stoichiometric material is not a simple modulation of the cubic parent structure.

7.14 Electron Concentration

Fermi surface nesting and strong electron–phonon coupling have been shown to give rise to phonon softening in systems undergoing a martensitic phase transition [42]. The generalised susceptibility and the Fermi surface geometry of Ni_2MnGa have been computed in both the ferromagnetic ($T = 0$) and paramagnetic phases [43]. In the ferromagnetic phase a nesting wave vector was found at $[0.43, 0.43, 0]$. Subsequently the peak in the generalised susceptibility was calculated as a function of magnetisation [44]. Using a moment of 80% of the ground state value, which is appropriate for the pre-martensitic phase, the nesting wave vector was estimated to be $\left[\frac{1}{3}\,\frac{1}{3}0\right]$. These wave vectors are consistent with the features observed in inelastic neutron scattering and diffraction measurements. The importance of Fermi surface nesting on the structural and magnetic properties of chromium and its dilute alloys [45] is well established. In these alloys the magnitude of the nesting wave vector depends on whether the solute is electron rich or poor with respect to chromium. Thus if Fermi surface nesting drives the phase transition in Ni_2MnGa this transition will also be sensitive to changes in electron concentration.

Both the phase stability and magnetic properties of Heusler alloys, particularly those based on X_2MnZ, are known to depend on the electron concentration. This has been shown most forcibly in the Pd_2MnIn system by changing In for Sn and Sb [46]. By making these substitutions, new magnetic phases are introduced with only half as much Sb as Sn required to produce the same effect. Although some models have assumed that the electron concentration is only affected by the Z atom while the X atoms just change the lattice parameter, a similar magnetic phase diagram has been observed in $Pd_{2-x}Ag_xMnIn$ [47]. Recent measurements on $Ni_{2-x}Cu_xMnGa$ [48] and $Ni_2MnGa_{1-x}Sn_x$ [49] show that the structural phase transition is progressively suppressed with increasing x. The magnetisation of $Ni_2MnGa_{0.95}Sn_{0.05}$

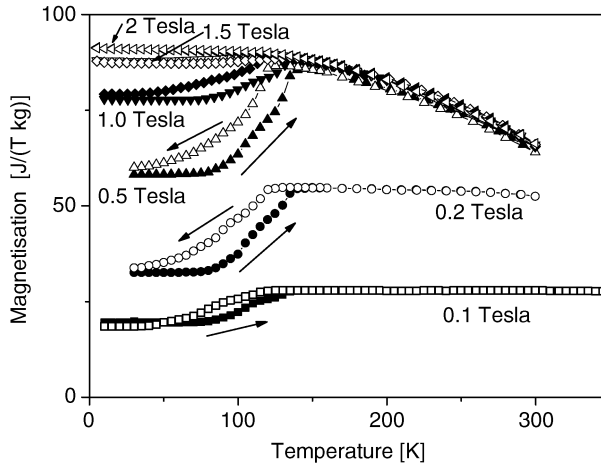

Fig. 7.16. The magnetisation of $Ni_2MnGa_{0.95}Sn_{0.05}$ measured in different external fields as indicated in the figure. The measurement were made while both heating and cooling as indicated by the arrows

is shown in Fig. 7.16. The reduction in magnetisation at low temperatures is similar to that observed in Ni_2MnGa as a result of the martensitic transition which suggests that in $Ni_2MnGa_{0.95}Sn_{0.05}$ T_M is reduced to ∼150 K. Since Sn is located to the right of Ga in the periodic table its substitution for Ga adds electrons to the band raising the chemical potential. Consequently a change in nesting wave vector should also be observed. Recent neutron powder diffraction measurements [50] carried out on the alloy at 5 K suggest some change to the structure of the transformed phase compared to that observed in the parent compound.

The influence of atomic order on the magnetic properties of X_2MnZ is well established [8]. Stoichiometric Ni_2MnGa is reported to melt at 1382 K [51] and on cooling undergoes a $B2 \rightarrow L2_1$ phase transition at 1071 K [52]. Magnetisation and resistivity measurements on a sample quenched from 1000°C indicate that the phase transition occurs at $T_M \sim 103$ K, substantially lower than the value reported for samples quenched from 800°C. A small reduction in the ferromagnetic moment was also observed although the Curie temperature remained largely unaffected. The electronic Sommerfeld coefficient obtained from heat capacity measurements although enhanced is smaller than that observed for the 800°C quenched sample [10]. The results are consistent with band structure calculations [53] and the electronic changes brought about by atomic disorder.

7.15 Polarised Neutron Scattering

Electronic structure calculations for Ni_2MnGa show a peak in the density of states (DOS) at the Fermi level [53]. On the basis of these calculations it was

Table 7.7. Least squares fit to the magnetic structure factors of Ni_2MnGa at 230 and 100 K. The first line gives the results for a model in which the magnetisation is only associated with atoms on the A and B/D sites. The results in the second line are for a model in which a moment is also allowed on the C sites

Site	$T = 230$ K				$T = 100$ K		
	A(Mn)	C(Ga)	B/D(Ni)		A(Mn)	C(Ga)	B/D(Ni)
Moment (μ_B)	2.3	0	0.22		2.84	0	0.38
χ^2		142				32	
Moment (μ_B)	2.27	−0.12	0.19		2.82	−0.08	0.36
χ^2		20				13	
Moment (μ_B)	2.29	−0.11	0.20		2.80	−0.06	0.358
e_g (%)	51.0		58	$x^2 - y^2$ (%)	23		15.0
				$3z^2 - r^2$ (%)	20		48.0
t_{2g} (%)	49.0		42	xy (%)	13		27.0
				$zx \pm zy$(%)	44		9.0
χ^2		20				9	

argued that it is the redistribution of electrons around the Fermi level which drives the phase transition. The reduction in symmetry is able to lift the degeneracy of electron bands at the Fermi level causing the peak in the DOS to split. Combined with the energy required for creating the lattice distortion the resulting shift in the energy bands and the resulting re-population of these bands lowers the free energy of the whole system making such a transformation energetically favourable. A polarised neutron diffraction measurement [27] of the unpaired spin distribution has revealed a change in symmetry at the phase transition. A summary of the results is given in Table 7.7. In the cubic phase the unpaired electrons have overall e_g symmetry. In the transformed phase there is a transfer of moment from the Mn xy (t_{2g}) to the Ni $3z^2 - r^2$ (e_g) orbitals. Although the experimental moments differ in detail from those expected from band structure calculations, the change in symmetry of the magnetisation distribution is consistent with a band Jahn–Teller origin for the phase transition.

7.16 Conclusion

The bulk magnetic properties of Ni_2MnGa are similar to those of other Heusler alloys in which the moment is confined to the Mn atoms. Consequently the magnetic response is also expected to be of a local nature characteristic for moments of fixed amplitude. Both magnetisation and neutron diffraction measurements show that the structural phase transition responsible for shape memory behaviour is not driven by a collapse of the manganese moment. Polarised neutron diffraction measurements show that at T_M there is a redistribution of electrons between 3d sub-bands of different symmetries, as

expected for a band Jahn–Teller mechanism. Further support for this electronic origin for the transition is provided by the dependence of T_M on atomic order and electron concentration.

A combination of powder and single crystal neutron diffraction measurements has enabled the sequence of structural phase transitions in stoichiometric Ni_2MnGa to be established. For the first time the atomic positions in the three phases have been determined. The modulated structures of the pre-martensitic and martensitic phases are consistent with the soft mode behaviour of the TA_2 phonon observed in the two phases. Structural models based on X-ray and electron diffraction measurements, and in particular a five fold modulation do not account for the neutron diffraction pattern below T_M. The neutron measurements show that the three fold modulation observed in the pre-martensitic phase becomes a seven fold modulation below the phase transition. Both modulations take place in the [110] direction of the cubic parent phase. Similar measurements on non-stoichiometric samples show that the phase diagram is significantly altered.

The single crystal measurements undertaken in a magnetic field or under applied stress provide detailed insight into the mesoscopic origin of the shape memory effect. A very small amount of stress applied in the martensitic phase introduces an inelastic response in the martensitic domain population. It is proposed that such stress induced twinning substitutes for normal slip by movement of dislocations, in the plastic deformation process. The martensitic twin domains transform into one another; those whose c axes are parallel to the axis of stress being favoured. However the only domains which can form are those which bear fixed relationships to the parent cubic crystal and these relationships are determined by the orientation of the {110} planes on which the shears occurred in the martensitic transformation. When the reverse shears occur on warming, they all lead to the original cubic crystal orientation. A polycrystalline sample in the martensitic phase would consist of a large number of different martensitic twin domains each of which would have formed part of a parent cubic crystallite with a certain orientation. Deformation in the martensitic phase has the same effect within each crystallite as applying stress to the single crystal; the crystallite deforms plastically by stress induced twinning, which switches the c axis of unfavourably oriented domains. However all twins formed from a single cubic crystallite always transform back into the original orientation regardless of how their population may have been changed in the martensitic phase. Hence the original shape is restored.

References

1. Proceedings of SMART (Sendai, Japan, 2000)
2. R.C. O'Handley: J. Appl. Phys. **83**, 3263 (1998)
3. S.J. Murray, M. Farinelli, C. Kantner, J.K. Haung, S.M. Allen, R.C. O'Handley: J. Appl. Phys. **83**, 7297 (1998)

4. P.J. Webster, K.R.A. Ziebeck, S.L. Town, M.S. Peak: Phil. Mag. B **49**, 295 (1984)
5. V.V. Martynov, V.V. Kokorin: J. Phys. III. France **2**, 739 (1992)
6. V.A. Chernenko, A. Amengual, E. Cesari, V.V. Kokorin, I.K. Zasimchuk: J. de Phys. IV **5**, C2 (1995)
7. F. Heusler: Verh. Dtsch. Phys. Ges. **5**, 219 (1903)
8. P.J. Webster, R.K.A. Ziebeck: Heusler Alloys. In: Landolt Börnstein Neue Series, ed. by O. Madelung, Vol. 19 (Springer, Berlin Heidelberg, 1988) p. 75
9. J. Rodriguez-Carvajal: `FullProf` version 3.3, Laboratoire Leon Brillouin (1997)
10. M. Kreissl, K.U. Neumann, T. Stephens, K.R.A. Ziebeck: J. Phys.: Condens. Matter **15**, 3831 (2003)
11. R. Tickle, R.D. James: J. Mag. Mag. Mater. **195**, 627 (1999)
12. J.W. Taylor, T.J. Smith, K.H. Andersen, H. Capellmann, R.K. Kremer, A. Simon, O. Schärpf, K.U. Neumann, K.R.A. Ziebeck: Euro. Phys. Journal B **12**, 199 (1999)
13. U. Stuhr, P. Vorderwisch: BENSC experimental report. 43 (1995)
14. Y. Noda, Y. Ishikawa: J. Phys. Soc. Japan **40**, 690 (1976)
15. K.R.A. Ziebeck, P.J. Webster, P.J. Brown, J.A.C. Bland: J. Mag. Mag. Mater. **24**, 258 (1981)
16. G. Shirane, Y.J. Uemura, J.P. Wicksted, Y. Endoh, Y. Ishikawa: Phys. Rev. B **31**, 1227 (1985)
17. A. Zheludev, S.M. Shapiro, P. Wochner, A. Schwartz, M. Wall, L.E. Tanner: Phys. Rev. B **51**, 11 310 (1995)
18. J.A. Krumhansl, R.J. Goodings: Phys. Rev. B **39**, 3047 (1989)
19. T. Castán, A. Planes, A. Saxena: Phys. Rev. B **67**, 134 113 (2003)
20. P.J. Brown, J. Crangle, T. Kanomata, M. Matsumoto, B. Ouladdiaf, K.U. Neumann, K.R.A. Ziebeck: J. Phys.: Condens. Matter **14**, 10 159 (2002)
21. L. Mañosa, A. Gonzàlez-Comas, E. Obradó, A. Planes, V.A. Chernenko, V.V. Kokorin, E. Cesari: Phys. Rev. B **55**, 11 068 (1997)
22. J. Worgull, E. Petti, J. Trivisonno: Phys. Rev. B **54**, 15 695 (1996)
23. A. Gonzàlez-Comas, E. Obradó, L. Mañosa, A. Planes, V.A. Chernenko: Phys. Rev. B **60**, 7085 (1999)
24. M. Ahlers: Phil. Mag. A **82**, 1093 (2002)
25. A. Zheludev, S.M. Shapiro, P. Wochner, L.E. Tanner: Phys. Rev. B **54**, 5045 (1996)
26. S.M. Shapiro: Neutron Scattering Studies of Anomalous Phonon Behavior in Functional Materials. In: Workshop on the Interplay of Magnetism and Structure in Functional Materials (Benasque, 2004)
27. P.J. Brown, A.Y. Bargawi, J. Crangle, K.U. Neumann, K.R.A. Ziebeck: J. Phys.: Condens. Matter **11**, 4715 (1999)
28. P.J. Brown, K.U. Neumann, C. Wilkinson, K.R.A. Ziebeck: (2003), work in progress
29. P.J. Brown, B. Dennis, J. Crangle, T. Kanomata, M. Matsumoto, K.U. Neumann, L.M. Justham, K.R.A. Ziebeck: J. Phys.: Condens. Matter **16**, 65 (2004)
30. S.M. Shapiro, B.X. Yang, Y. Noda, L.E. Tanner, D. Schryvers: Phys. Rev. B **44**, 9301 (1991)
31. Y. Yamada, Y. Noda, K. Fuchizaki: Phys. Rev. B **42**, 10 405 (1990)
32. R.J. Goodings, J.A. Krumhansl: Phys. Rev. B **39**, 1535 (1989)

33. V.V. Khovailo, T. Takagi, A.D. Bozhko, M. Matsumoto, V.G. Shavrov: J. Phys.: Condens. Matter **13**, 9655 (2001)
34. V.V. Khovailo, T. Takagi, J. Tani, R.Z. Levitin, A.A. Cherechukin, M. Matsumoto, R. Note: Phys. Rev. B **65**, 092 410 (2002)
35. N. Glavatska, G. Mogylny, I. Glavatskiy, V. Gavriljuk: Scripta Materialia **46**, 605 (2002)
36. S. Ishida, M. Furugen, S. Asano: Int. J. Appl. Eletrom. **12**, 41 (2000)
37. K. Inoue, K. Enami, M. Igawa, K. Inoue, Y. Yamaguchi, K. Ohoyama: In: Proc. Int. Conf. Solid–Solid Phase Transformations, ed. by M. Koiwa, K. Otsuka, T. Miyazaki (The Japan Institute of Metals, 1999) pp. 1120–1123
38. K. Inoue, K. Enami, Y. Yamaguchi, K. Ohoyama, Y. Morii, Y. Matsuoka, K. Inoue: J. Phys. Soc. Japan **69**, 3485 (2000)
39. A.N. Vasil'ev, A.D. Bozhko, V.V. Khovailo, I.E. Dikshtein, V.G. Shavrov, V.D. Buchelnikov, M. Matsumoto, S. Suzuki, T. Takagi, J. Tani: Phys. Rev. B **59**, 1113 (1999)
40. K. Fröhlich: MPhil. Thesis, Loughborough University, (2004)
41. V.V. Khovailo, V. Novosad, T. Takagi, D.A. Fillipov, R.Z. Levitin, A.N. Vasil'ev: Phys. Rev. B **70**, 174413 (2004)
42. G.L. Zhao, B.N. Harmon: Phys. Rev. B **45**, 2818 (1992)
43. O.I. Velikokhatny, I.I. Naumov: Phys. Solid State **41**, 617 (1999)
44. Y. Lee, J.K. Rhee, B.N. Harmon: Phys. Rev. B **66**, 054 424 (2002)
45. E. Fawcett: Rev. Modern Physics **60**, 209 (1988)
46. P.J. Webster, M.R.I. Ramadan: J. Mag. Mag. Mater. **5**, 51 (1977); **13**, 301 (1979)
47. P.J. Webster, K.R.A. Ziebeck, R.M. Mankikar: J. Mag. Mag. Mater. **54–57**, 1355 (1986)
48. T. Kanomata, T. Nozawa, D. Kikuchi, H.M. Nishihara, K. Koyama, K. Watanabe, in: Proc. INABIO (Sendai, 2004)
49. P. Anders: MPhil. Thesis, Loughborough University (2003)
50. J. Rasch: MPhil. Thesis, Loughborough University (2004)
51. R.W. Overholser, M. Wuttig, D.A. Neumann: Scr. Mater. **40**, 1095 (1999)
52. V.V. Khovailo, T. Takagi, A.N. Vasilev, H. Miki, M. Matsumoto, R. Kainuma: Phys. Status Solidi A **183**, R1 (2001)
53. S. Fujii, S. Ishida, S. Asano: J. Phys. Soc. Japan **58**, 3657 (1987)

8

Imaging Techniques in Magnetoelastic Materials

S.P. Venkateswaran and M. De Graef

8.1 Introduction

One of the main characteristics distinguishing magnetoelastic materials from other materials is the presence of magnetic domains in addition to the more conventional microstructural features, such as twin boundaries, planar defects, dislocations, and so on. In this chapter, we will briefly review the imaging of these magnetic domains and domain walls by means of Lorentz transmission electron microscopy (LTEM). Lorentz microscopy occupies a special place among the methods for domain characterization in the sense that it is possible to obtain direct quantitative information about critical parameters, such as the domain wall width, which play an important role in the overall magnetic behavior of the material. In addition, LTEM enables a direct study of the interactions between magnetic domain walls and structural features, such as twin boundaries and defects. Other characterization techniques for magnetic domain structures will not be covered in detail, since there are many good review articles or textbooks available for them (e.g., [1, 2]).

In this chapter, we will first describe the Lorentz microscopy method from the classical physics point of view, followed by a quantum mechanical description in terms of the phase of the electron wave traveling through the sample. Then, we introduce a phase reconstruction method, based on the transport-of-intensity equation, which permits determination of the total phase shift of the electron wave. In the second half of the chapter, we will apply the method to selected magnetoelastic compounds, in particular Ni_2MnGa and Co_2NiGa. One of the most important observations is the presence of *magnetoelastic tweed* in the austenitic state of Co_2NiGa.

8.2 Lorentz Image Formation Theory

8.2.1 Classical Description

A high energy electron moving with velocity $\boldsymbol{v}$ through a region of space (in this case, a thin foil of thickness t, Fig. 8.1a) containing a (static) magnetic

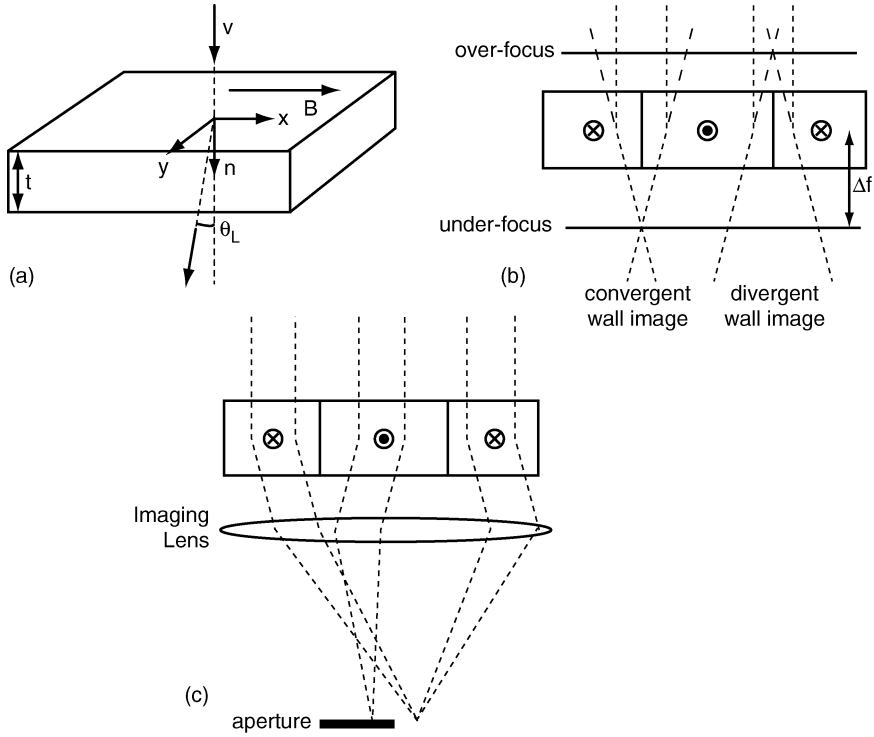

Fig. 8.1. (**a**) Illustration of a high energy electron traveling through a foil with a permanent magnetic induction; electron trajectories for the Fresnel (out-of-focus) imaging mode (**b**), and the Foucault mode (**c**)

induction $\boldsymbol{B}$, experiences a Lorentz force $\boldsymbol{F}_{\mathrm{L}}$ given by

$$\boldsymbol{F}_{\mathrm{L}} = -|e|(\boldsymbol{v} \times \boldsymbol{B}) \,. \tag{8.1}$$

If we decompose $\boldsymbol{B}$ into a component B_z along the beam direction $\boldsymbol{n}$ and a component $B_\perp$ in the plane normal to $\boldsymbol{n}$, then one can readily show [3] that the electron will be deflected by an angle θ_{L}, given by

$$\theta_{\mathrm{L}} = \frac{e\,\lambda}{h}\, B_\perp t \equiv C\, B_\perp\, t \tag{8.2}$$

with λ the electron wavelength; e and h have their usual meaning. The prefactor C depends on the electron microscope accelerating voltage, and is typically about $0.5\,\mu\mathrm{rad\,nm^{-1}\,T^{-1}}$. In other words, for a 100 nm thick foil with a saturation induction of 1 T, the deflection angle is 60.6 µrad for a 200 kV electron. This angle is about two orders of magnitude smaller than the typical Bragg angle for electron diffraction, indicating that all magnetic information is confined close to the transmitted electron beam.

Lorentz microscopy observations of magnetic domains in a material require that this material is placed in a field-free region of the microscope, instead of the typical 2 T field of the objective lens. This can be achieved by turning off the main objective lens and using a weaker lens placed below the sample, or, alternatively, one can shield the specimen area from the magnetic field. In many situations, the total attainable magnification is severely reduced, so that additional magnification (for instance, through a postcolumn imaging energy filter [4]) may be required.

There are two standard imaging methods in Lorentz microscopy. The first is known as the *Fresnel mode* (or *out-of-focus mode*). In this mode, the main objective lens of the microscope is focused on a plane slightly above or below the sample, producing an out-of-focus image (Fig. 8.1b). Electrons which travel near a magnetic domain wall, indicated by the vertical lines, will be deflected in opposite directions, and in the out-of-focus image an increase/decrease of intensity will be observed. An intensity increase is known as a *convergent wall image* and a decrease corresponds to a *divergent wall image*. A reversal of focus from under-focus to over-focus also reverses the image contrast. While the Fresnel image delineates the location of magnetic domain walls, it is an out-of-focus image and, therefore, slightly blurred. For materials with a low saturation induction, a significant microscope defocus may be required to create the Fresnel images, and there may also be a magnification change associated with the defocus.

The second observation mode is known as the Foucault mode. In this mode, the image is always in-focus, and a circular aperture in the back focal plane of the main imaging lens is used to eliminate certain electrons from the beam (Fig. 8.1c). Magnetic domains which deflected electrons into the blocked section of the beam will remain dark in the image, whereas other domains will be bright. The Foucault image mode therefore produces contrast between entire magnetic domains. Given the small deflection angles, it is difficult to reproducibly position the aperture. In the present chapter, we will only make use of the Fresnel imaging method.

It is also possible to send a fine electron probe through the thin foil, and record the deflections of this probe as the beam is scanned across the sample. This technique is known as Differential Phase Contrast microscopy, and is described in detail in the literature [5].

8.2.2 Quantum Mechanical Description

The quantum mechanical description of electron scattering from a magnetic thin foil is based on the Aharonov–Bohm relation [6], which states that the wave function of an electron traveling with velocity v through a region of space with an electrostatic potential $V(\boldsymbol{r})$ and a magnetic vector potential $\boldsymbol{A}(\boldsymbol{r})$ acquires a phase shift φ, equal to

$$\varphi = \varphi_{\mathrm{e}} + \varphi_{\mathrm{m}} = \sigma \int_L V(\boldsymbol{r})\,\mathrm{d}z - \frac{e}{\hbar}\int_L \boldsymbol{A}(\boldsymbol{r})\cdot\mathrm{d}\boldsymbol{r}\,, \tag{8.3}$$

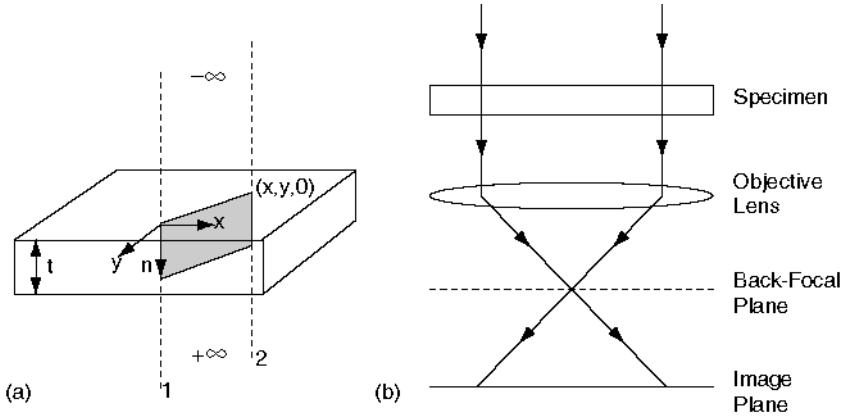

Fig. 8.2. (**a**) Illustration of the electron trajectories used for the quantum mechanical description of Lorentz deflection. (**b**) schematic of the specimen and the objective lens back focal plane and image plane

where L represents the electron trajectory and $\sigma = 2\pi\gamma m_0 e\lambda/h^2$ is the interaction constant ($\gamma = (1 - v^2/c^2)^{-1/2}$ is the relativistic parameter, m_0 is the rest mass of the electron, and c denotes the speed of light). The prefactor of the magnetic term is $0.00151927\,\mathrm{T}^{-1}\,\mathrm{nm}^{-1}$. Usually, one works with the phase difference between two trajectories, as shown in Fig. 8.2a. It is straightforward to show that the phase of electron 2 with respect to electron 1 is given by

$$\varphi_\mathrm{m} = \pi \frac{\Phi_\mathrm{m}}{\Phi_0}\,, \tag{8.4}$$

where Φ_m is the flux between the two trajectories and Φ_0 is the flux quantum $h/2e$.

If the incident electron wave is described by a plane wave with wave vector $\boldsymbol{k}$, with inverse length $2\pi/\lambda$, then the exit wave (i.e., the wave function at the exit plane of the thin foil) is given by a modulated plane wave (modulated both in phase and amplitude):

$$\psi(\boldsymbol{r}) = \sqrt{I(\boldsymbol{r}_\perp)}\,\mathrm{e}^{\mathrm{i}\varphi(\boldsymbol{r}_\perp)}\,\mathrm{e}^{\mathrm{i}\boldsymbol{k}\cdot\boldsymbol{r}}\,. \tag{8.5}$$

The vector $\boldsymbol{r}_\perp$ is a vector in a plane normal to the beam direction and $I(\boldsymbol{r})$ is the intensity.

This wave then travels down the microscope column and is affected by the magnetic lenses (primarily the objective mini-lens or the special Lorentz lens). The action of a magnetic lens is conveniently described by a point spread function $T(\boldsymbol{r})$ in direct space, or a microscope transfer function $T(\boldsymbol{q})$ in reciprocal or Fourier space. One can show that the lens produces a Fourier transform of the wave function in its back focal plane (bfp); a second Fourier transform then produces an amplitude in the image plane (ip) (see Fig. 8.2b).

Mathematically, this is described as

$$\psi_{\mathrm{bfp}}(\boldsymbol{q}) = \mathcal{F}[\psi(\boldsymbol{r})]\, T(\boldsymbol{q})\,; \tag{8.6}$$

$$\psi_{\mathrm{ip}}(\boldsymbol{r}) = \mathcal{F}^{-1}[\mathcal{F}[\psi(\boldsymbol{r})]\, T(\boldsymbol{q})] = \psi(\boldsymbol{r}) \otimes T(\boldsymbol{r})\,. \tag{8.7}$$

$\mathcal{F}[\cdots]$ represents the Fourier transform operator and $\otimes$ is the convolution operator. The image intensity is then simply the modulus-squared of the last expression.

The microscope transfer function consists of three components (for the so-called *linear imaging model*):

$$T(\boldsymbol{q}) = a(|\boldsymbol{q} - \boldsymbol{q}_0|)\, \mathrm{e}^{\mathrm{i}\chi(\boldsymbol{q})}\, \mathrm{e}^{-g(\boldsymbol{q})}\,. \tag{8.8}$$

In this relation, we have

- $a(|\boldsymbol{q} - \boldsymbol{q}_0|)$: the *aperture function*, which represents a circular aperture (1 inside and 0 outside the aperture hole). The vector $\boldsymbol{q}_0$ represents the center location, so that Foucault images can also be considered;
- $\mathrm{e}^{\mathrm{i}\chi(\boldsymbol{q})}$: the *phase contrast function*, which contains all lens aberrations, including spherical aberration, astigmatism, and defocus, which produce a phase shift;
- $\mathrm{e}^{-g(\boldsymbol{q})}$: the *attenuation* or *damping function*, which contains all microscope instabilities (accelerating voltage, lens currents, etc.) and also the *beam divergence*, which can be taken as a measure of the beam coherence.

For Lorentz microscopy, one can employ a Taylor expansion of both exponential functions, since the deflection angles, and, therefore, the length of the relevant $\boldsymbol{q}$-vectors, are small. The aperture function is chosen so that all Bragg-scattered electrons are removed, and the attenuation function contains only the beam divergence contribution. The resulting Lorentz transfer function can then be written explicitly as

$$\mathcal{T}_{\mathrm{L}}(\boldsymbol{q}) = a(\boldsymbol{q} - \boldsymbol{q}_0)\, \mathrm{e}^{z_2 q^2}\, \mathrm{e}^{z_4 q^4} \tag{8.9}$$

with

$$z_2 = -\left(\pi\theta_{\mathrm{c}}\Delta f\right)^2 + \mathrm{i}\pi\lambda\Delta f\,;$$

$$z_4 = -\frac{\left(\pi\lambda\Delta\right)^2}{2}\,.$$

In these equations, we have the following symbols: θ_{c} (beam divergence angle), Δf (microscope defocus), and Δ (defocus spread). For Lorentz microscopy, all other aberrations, including spherical aberration, can be ignored.

8.2.3 Phase Reconstruction

Keeping only terms of order q^2 in (8.9), we can compute the intensity in the image plane, by an inverse Fourier transform. Taking the modulus squared, we obtain the following expression:

$$I(\boldsymbol{r},\Delta f) = I(\boldsymbol{r},0) - \frac{\lambda\Delta f}{2\pi}\nabla\cdot(I(\boldsymbol{r},0)\nabla\varphi) + \frac{(\theta_{\mathrm{c}}\Delta f)^2}{2\ln 2}\left[\sqrt{I(\boldsymbol{r},0)}\,\nabla^2\sqrt{I(\boldsymbol{r},0)} - I(\boldsymbol{r},0)(\nabla\varphi)^2\right] .$$

In this equation, the intensity in the image plane for a defocus Δf is represented by $I(\boldsymbol{r},\Delta f)$; in particular, the in-focus image is represented by $I(\boldsymbol{r},0)$. If we ignore the beam divergence term, and we assume that there is no contrast in the in-focus image, then we find

$$I(\boldsymbol{r},\Delta f) = 1 - \frac{\lambda\Delta f}{2\pi}\nabla^2\varphi\,. \tag{8.10}$$

In other words, the image intensity is only different from 1 when the lens is defocused, and then only where the Laplacian of the phase is nonzero, i.e., at the magnetic domain walls. This relation expresses the origin of Fresnel domain wall contrast. Changing the sign of the defocus changes the contrast of the domain wall image.

Subtracting the expression for $I(\boldsymbol{r},-\Delta f)$ from $I(\boldsymbol{r},\Delta f)$, and rearranging terms we have

$$-\frac{2\pi}{\lambda}\frac{I(\boldsymbol{r},\Delta f) - I(\boldsymbol{r},-\Delta f)}{2\Delta f} = \nabla\cdot(I(\boldsymbol{r},0)\nabla\phi)\ . \tag{8.11}$$

In the limit of vanishingly small defocus, the left-hand side becomes a derivative and we arrive at the so-called *Transport-of-Intensity Equation* (TIE)[1] [7–10]

$$\nabla\cdot(I(\boldsymbol{r},0)\nabla\phi) = -\frac{2\pi}{\lambda}\frac{\partial I(\boldsymbol{r},0)}{\partial z}\ . \tag{8.12}$$

There are various methods to solve this equation. The most straightforward is by means of Fourier transforms, as described in detail in [10, 11]. The formal solution is given by

$$\phi(\boldsymbol{r},0) = -\frac{2\pi}{\lambda}\nabla^{-2}\left\{\nabla\cdot\left[\frac{1}{I(\boldsymbol{r},0)}\nabla\left(\nabla^{-2}\left[\frac{\partial I(\boldsymbol{r},0)}{\partial z}\right]\right)\right]\right\}\ . \tag{8.13}$$

The operator ∇^{-2} is the inverse Laplacian operator, which can be defined in terms of Fourier transforms as

$$\nabla^{-2}[f(\boldsymbol{r})] = -\frac{1}{4\pi^2}\mathcal{F}^{-1}\left[\frac{\mathcal{F}[f(\boldsymbol{r})]}{|\mathbf{q}|^2}\right]. \tag{8.14}$$

As an example, consider the series of images in Fig. 8.3. Figure 8.3a is a 1024×1024 gray-scale image of the red spot on Jupiter and is taken to be the amplitude of the exit wave function. For the phase we select an image

[1]The name of this equation was first coined by Teague [7], who showed that this formalism could be applied to phase retrieval.

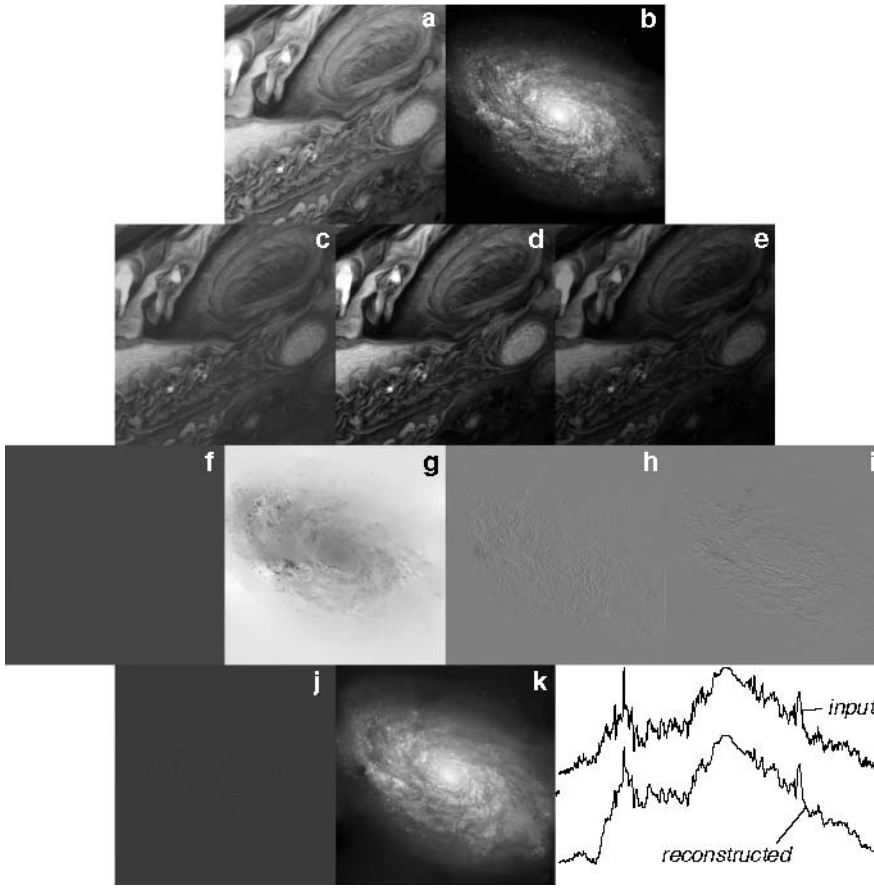

Fig. 8.3. Illustration of the phase reconstruction algorithm, using a "wave function" which consists of (**a**) Jupiter's red spot (amplitude) and (**b**) the NGC4414 spiral galaxy (phase). (**c**–**e**) Represent a through-focus series computed for a 200 kV TEM and (**f**–**k**) are the intermediate steps of the algorithm (see text for more details). A linear profile across the center of the input and reconstructed phases are also shown

of the NGC4414 spiral galaxy (shown in Fig. 8.3b).[2] A small constant was added to the amplitude image to ensure that its minimum intensity is strictly larger than zero. From these two images we compute a through-focus series using (8.7). The in-focus image is simply given by the square of the amplitude image. The defocus value used for the series of images shown in Fig. 8.3c–e is $\Delta f = 1\,\text{nm}$, with a wavelength of $\lambda = 0.002508\,\text{nm}$ (for 200 kV electrons), and a pixel size of $1 \times 1\,\text{nm}$. Next, we use the computed through-focus series to reconstruct the phase of the exit wave. Figure 8.3f shows the longitudinal

[2]Both images are in the public domain and were taken from `http://nix.nasa.gov/`.

derivative $\partial I/\partial z$ as the difference between the over-focus and under-focus images. It is clear that this difference image contains mostly phase information. The result of the inverse Laplacian operating on image (f) is shown in (g). Then we take the gradient of (g) and divide both components by the in-focus image. The resulting components are shown in (h) and (i). The divergence operator combines (h) and (i) into (j), and a final inverse Laplacian results in the reconstructed phase shown in (k). It can be shown [8] that this reconstruction is unique. Since the inverse Laplacian is a low-pass filter operation, there are fewer small details in the reconstructed phase compared to the input phase. The overall phase variations are reconstructed with sufficient accuracy, as seen from the line scan comparison on the bottom row: the top profile represents the intensity variations along a horizontal line through the center of the input image. The bottom profile is the reconstructed intensity; the reconstructed profile appears smoother than the input profile, but contains all significant phase variations.

8.3 Applications of LTEM to Ferromagnetic Shape Memory Alloys

After this somewhat lengthy introduction about the experimental methods we now turn our attention to the application of phase reconstruction methods to ferromagnetic shape memory alloys, which form a special class of magnetoelastic materials. We will focus on the Ni_2MnGa and Co_2NiGa systems in both the austenitic and martensitic states. Around the stoichiometric composition, both alloy systems have the cubic Heusler structure (space group $Fm\bar{3}m$, although it is sometimes more convenient to describe the unit cell as consisting of $2 \times 2 \times 2$ "body-centered cubic" cells) [12, 13]. In the austenitic state, the magnetocrystalline anisotropy is very small [14], so that the magnetization vector orientation, nominally along the $\langle 111 \rangle$ directions, is dominated by the demagnetization energetics. As a consequence, the magnetic domain configurations in the austenitic Ni_2MnGa composition range are strongly affected by the sample shape, in particular for the thin foils used for LTEM. In the martensitic state, the tetragonal crystal structure has a significantly larger magnetocrystalline anisotropy, so that the magnetization is aligned along the tetragonal axis [001]. This orientation is not very sensitive to the sample shape, so that the magnetic domain configurations in thin foils are likely similar to those in the bulk. In the following subsections, we will describe representative magnetic domain configurations for both alloy systems, in both austenitic and martensitic states.

Observations on Ni_2MnGa were performed on a [001]-oriented stoichiometric single crystal thin foil, and on off-stoichiometry polycrystalline foils, which were electrolytically thinned. We prepared the Co–Ni–Ga alloys used for this work as described in [15]. Thin foils for TEM observations were prepared using mechanical thinning followed by argon ion milling. In this chapter,

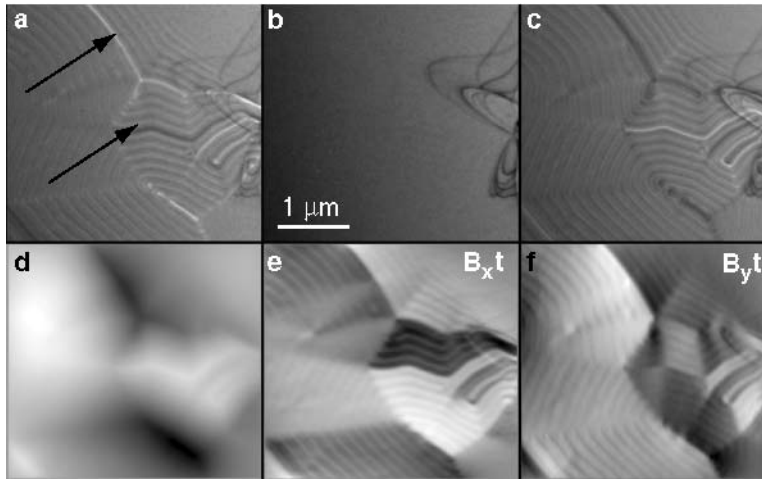

Fig. 8.4. (**a**–**c**) Four hundred kilo volt through-focus series of a relatively featureless region in a [001] oriented Ni_2MnGa foil; (**d**) reconstructed phase, and (**e**–**f**) are the components of the projected in-plane magnetic induction

we report on the nominal compositions $Ni_{50}Mn_{29}Ga_{21}$ and $Ni_{48}Mn_{22}Ga_{30}$. Lorentz observations were carried out on a JEOL 4000EX atomic resolution TEM operated at 400 kV and equipped with a Gatan Imaging Filter which enables zero-loss filtered Lorentz work at magnifications of 60,000× at the CCD camera. A 300 kV JEOL 3000F was used at the Brookhaven National Laboratory for energy filtered in situ cooling observations in Lorentz mode.

8.3.1 Ni_2MnGa, Austenitic State

Figure 8.4 shows a through-focus series (a–c) of a domain wall configuration in a stoichiometric Ni_2MnGa single crystal foil, oriented with the [001] direction close to the electron beam. The center image (b) is the in-focus image and shows very little contrast, apart from some bend contours.[3] In the underfocus (a) and over-focus (c) images, two types of contrast are observed: high contrast lines [arrowed in (a)], corresponding to 180° domain walls, and lower contrast fringe-like lines. A reconstructed phase is shown in (d), along with the components of the gradient of the phase in (e) and (f). For a foil of uniform thickness, with weak demagnetization field, one can show that these gradient components are proportional to the in-plane components of the magnetic induction, multiplied by the foil thickness. From these images, we find that

[3]Bend contours arise when the thin foil is slightly bent or warped, and locally the Bragg condition for a particular set of planes is satisfied, giving rise to dark curved lines.

the striations, which have a periodicity of about 100 nm, correspond to domain walls between regions with [111]-type magnetization directions. When the magnetization oscillates between the [111] and [11$\bar{1}$] directions, i.e., the vertical component oscillates in the upward and downward directions, domain walls of the 71° and 109° type are formed. This type of oscillatory behavior reduces the demagnetization field and hence the magnetostatic energy with respect to a large domain with a single [111] magnetization direction (recall that the foil normal is [001], so that the magnetization always has an out-of-plane component).

Another example of this oscillatory behavior is shown in Fig. 8.5. The arrows indicate the locations of dislocations in the foil. The figure shows the magnitude of the in-plane magnetization component multiplied by the foil thickness, $t\sqrt{B_x^2 + B_y^2}$. The nearly circular domain configuration is due to pinning by the dislocations, and the domain walls are of the 71° and 109° type. The contrast is brighter at the domain walls, indicating that the in-plane component of the magnetic induction is larger, consistent with the interpretation of the previous paragraph. In the thinnest portions of the sample foil, the domain wall character changes, and one finds mostly cross-tie walls. This observation is potentially important for thin film applications of these materials.

Occasionally, the 180° domain walls show a diamond-like feature, as illustrated in the through-focus series in Fig. 8.6a–c. The reconstructed in-plane induction components are shown in (d) and (e). This can be interpreted as a short segment of 180° which is orthogonal to the main domain wall, and separated from the other magnetic domains by means of 90° domain walls. Model phase computations confirm that the observed domain configuration is

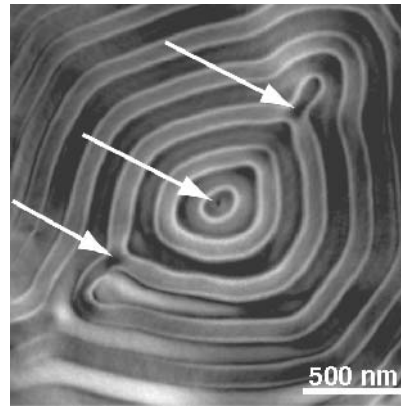

Fig. 8.5. Nearly circular domain wall configuration in a stoichiometric single crystal foil of Ni_2MnGa. *Arrows* indicate dislocations which pin the domain walls. The image intensity is proportional to $t\sqrt{B_x^2 + B_y^2}$ and was computed from the reconstructed phase (not shown)

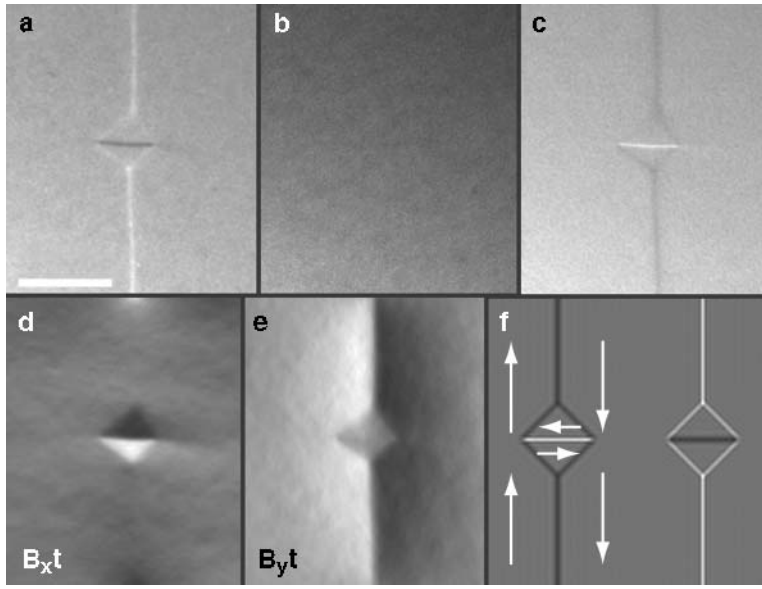

Fig. 8.6. Diamond-like domain wall configuration observed on a 180° domain wall in a [001]-oriented single crystal foil of stoichiometric Ni_2MnGa

consistent with the configuration illustrated in (f), which shows the simulated over-focus and under-focus images.

While all observations in the preceding paragraphs were carried out on a single crystal foil, oriented with [001] along or close to the beam direction, observations on polycrystalline foils reveal that for an arbitrary foil orientation the magnetization pattern consists of wavy domain boundaries, as shown in the through-focus series of Fig. 8.7. The composition of this alloy is

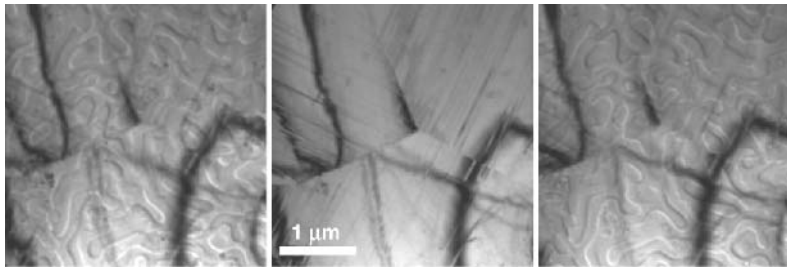

Fig. 8.7. Through-focus series of a triple junction of grain boundaries in a polycrystalline $Ni_{50}Mn_{29}Ga_{21}$ foil. The straight lines in each grain are planar stacking faults

$Ni_{50}Mn_{29}Ga_{21}$. Wavy domain walls are present in all three grains. The domain walls do not appear to be hindered by the presence of the grain boundaries.

8.3.2 Ni_2MnGa, Martensitic State

Observations in the martensitic state of the stoichiometric Ni_2MnGa thin foil were carried out using an in situ liquid nitrogen cooling stage at the Brookhaven National Laboratory's 300 kV field emission TEM. Lorentz images were recorded during cooling from room temperature to about 90 K. Representative Fresnel under-focus images are shown in Fig. 8.8a–c. In (a), the transformation has just started, and the domain walls begin to break up into smaller domain wall segments. It is possible that the strain associated with the advancing martensite plates causes the large initial domains to become unstable and break up into smaller, oval-shaped domains. In (b), several martensite plates have crossed the field of view, and the small domains are located inside neighboring martensite variants. The domain walls rotate and become aligned with the variant boundaries, as can be seen in the upper region of (b). Finally, when the transformation is complete, all martensite plate boundaries coincide with magnetic domain walls, as can be seen from the dark and bright fringe contrast at each of the twin boundaries. Due to excessive sample motion during the transformation, it was nearly impossible to record through-focus series for phase reconstruction. The fine-scale mottled contrast in all images is due to "dirt" being deposited on the cold sample inside the microscope vacuum.

Room temperature observations in $Ni_{50}Mn_{29}Ga_{21}$, with the transformation temperature $T_M \approx 320$ K, are shown in Fig. 8.9. At room temperature, due to chemical inhomogeneity of the sample, some regions are still in the austenite phase, while others have already transformed into martensite. The central in-focus image in Fig. 8.9 shows several martensite plates entering an austenite grain. The out-of-focus images show the typical wavy domain walls of the austenitic state, whereas in the martensitic state, the domain walls are straight, because of the larger magnetocrystalline anisotropy. Note also that

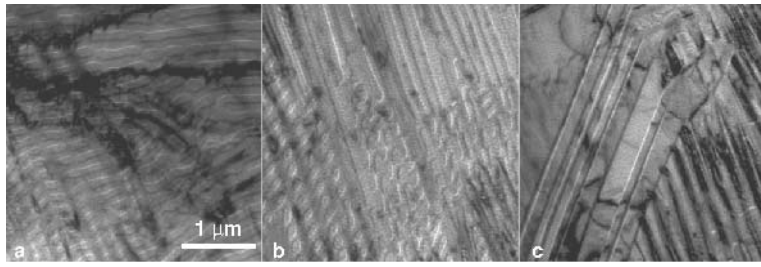

Fig. 8.8. In situ cooling observations of a stoichiometric Ni_2MnGa thin foil. From (**a**) to (**c**) the martensitic transformation progresses by first breaking up the long magnetic domains, then the martensite plates grow across the field of view, and finally all martensite plate boundaries coincide with magnetic domain walls

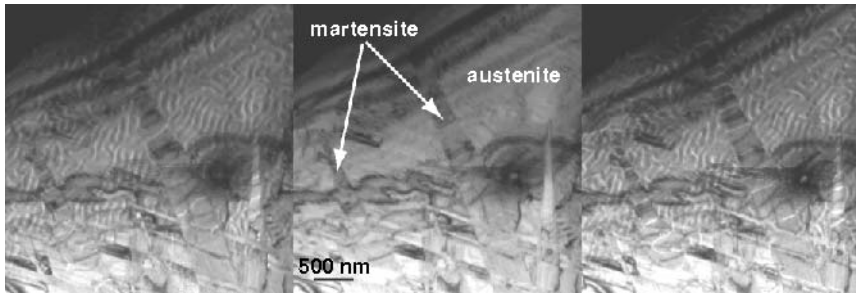

Fig. 8.9. Through-focus series in a two-phase $Ni_{50}Mn_{29}Ga_{21}$ thin foil. The austenite grain, with wavy domain walls, contains several martensite plates (*arrowed*)

the domain walls across the martensite needles are still attached to the domains in the neighboring austenite. The continuity of the domain walls across the phase boundaries is a topic of ongoing investigation.

8.3.3 Co_2NiGa, Austenitic State

Lorentz TEM observations were carried out on a $Co_{50}Ni_{29}Ga_{21}$ alloy that was quenched from 1200 K. This alloy was chosen so that the structural transformation, T_M, and Curie temperatures, T_C, were located below and above room temperature, respectively, i.e., $T_M \simeq 148$ K and $T_C \simeq 393$ K, as determined by elastic spectroscopy and vibrating sample magnetometry. Figure 8.10 shows a bright-field image of the (400) bend contour of this alloy, taken at room temperature near the [110] zone axis orientation. The image reveals ferroelastic or structural domains. Tweed-like contrast can be seen, with a characteristic length scale of about 10 nm. In this image, the cross-hatched tweed patterns are clearly evident on both sides of the bend contour. In electron diffraction patterns (inset in Fig. 8.10), diffuse streaks along the ⟨110⟩-type directions were observed, typical for tweed modulated structures.

Figure 8.11 shows a through-focus series of Fresnel Lorentz images for this alloy. Image (c) is the in-focus image and it shows tweed contrast near the central bend contour. The under-focus (a) and over-focus (b) images show strong striations of a length scale similar to that of the tweed striations. Since these striations are only visible in the out-of-focus images, they must be ascribed to magnetic modulations. This is further shown in Fig. 8.11d, which is the difference between images (a) and (b). It was shown in Sect. 8.2 that this difference image is proportional to the Laplacian of the magnetic component of the phase of the electron wave, which indicates a magnetic origin for the striations. The coincident elastic and magnetic modulations have a wavelength in the range of 50–100 nm.

While tweed-like striations, such as the ones shown in Fig. 8.10, have been observed in many systems that undergo martensitic transformations, the appearance of tweed contrast in Lorentz images is relatively uncommon.

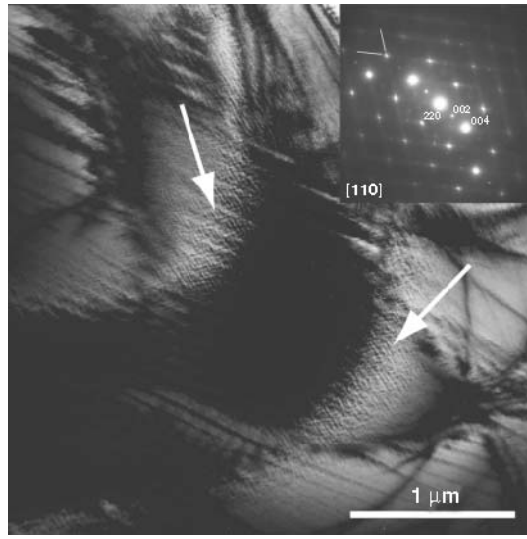

Fig. 8.10. Bright field image and corresponding electron diffraction pattern for the near [110] zone axis orientation of $Co_{48}Ni_{22}Ga_{30}$). The tweed contrast near the (004) bend contour is consistent with the appearance of diffuse streaks along apparent [112] directions (indicated by *solid white lines* in the diffraction pattern). B2 superlattice reflections are clearly present (micrographs taken on a Philips CM20 operated at 200 kV)

Two types of tweed contrast have been observed in Lorentz mode: (a) analogous to structural tweed, *magnetic tweed* is diffraction contrast present in TEM observations, corresponding to modulations in the *magnetization* (instead of strain) above the *Curie temperature* T_C (instead of the structural transition temperature T_M); (b) *magnetoelastic tweed* contrast is due to the coupling of strain to magnetization in the temperature range above T_M (and possibly also above the Curie temperature). Magnetic tweed has likely been observed above the Curie temperature in $Co_{38}Ni_{33}Al_{29}$ alloys [15, 16]. For a detailed analysis of magnetic and magnetoelastic tweed we refer to the recent paper by Saxena et al. [17].

8.3.4 Co_2NiGa, Martensitic State

Figure 8.12 shows a series of twins in the martensitic state of the $Co_{48}Ni_{22}Ga_{30}$ alloy. This alloy has a martensitic transformation temperature at room temperature (about 296 K). The in-focus image (top center) shows finely spaced twin boundaries, with an average twin width of around 200 nm. The out-of-focus images reveal that most of the twin boundaries coincide with magnetic domain walls. However, the domain walls occasionally traverse the twin domains, giving rise to a stepped appearance, as is clearly visible in the reconstructed phase map and its gradient components (bottom row). A detailed

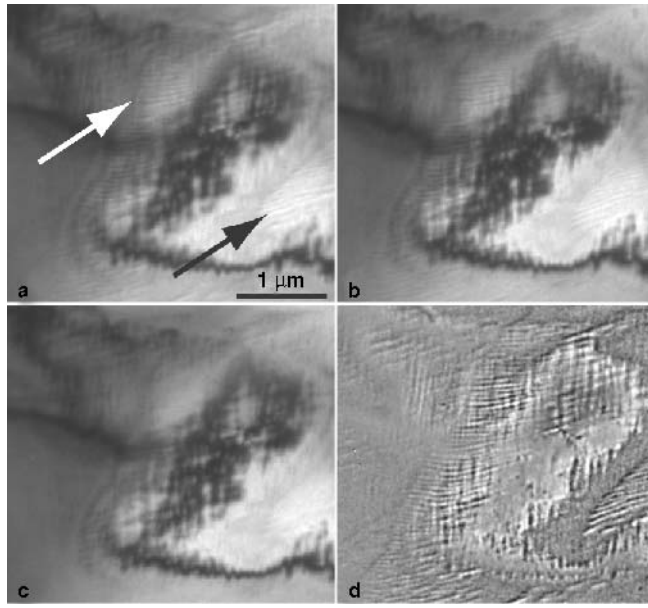

Fig. 8.11. Zero-loss under-focus (**a**) and over-focus (**b**) images (Fresnel imaging mode, 400 kV) of a region near a bend contour. The in-focus image (**c**) shows tweed contrast, and the out-of-focus images reveal the presence of an additional modulated structure (*arrowed*) which is magnetic in nature. (**d**) shows the difference between (**a**) and (**b**), and is proportional to the Laplacian of the phase of the electron wave. Contrast variations in (**d**) are indicative of magnetic contrast

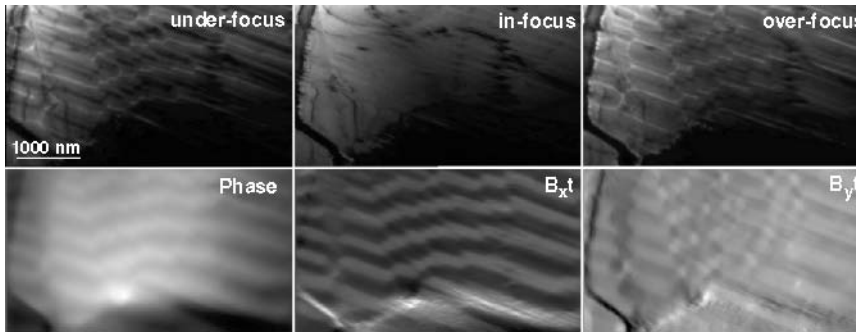

Fig. 8.12. Through-focus series of martensite twin boundaries in a $Co_{48}Ni_{22}Ga_{30}$ alloy, along with reconstructed phase and phase gradient components

analysis of these images also shows that not every twin boundary coincides with a magnetic domain wall.

A more detailed study of magnetoelastic tweed and the domain structure of the martensitic state in the Co–Ni–Ga system is currently underway. In order to determine the interactions between domain walls and twin boundaries, an

in situ magnetic field sample holder is being designed, so that the behavior of the domains can be studied in real time under an applied magnetic field.

8.4 Summary

In this chapter, we have reviewed the application of LTEM methods to the study of the magnetic microstructure of ferromagnetic shape memory alloys. After a brief overview of the image formation theory, including the beam deflection due to the Lorentz force, we have introduced the concept of the TIE, which can be used to reconstruct the phase shift of the electron beam. This phase shift contains all the information on the magnetic microstructure.

The phase reconstruction method was then applied to the austenitic and martensitic states of Ni_2MnGa and Co_2NiGa alloys, both stoichiometric single crystals and nonstoichiometric polycrystals. In the austenitic state, Ni_2MnGa exhibits wavy magnetic domain boundaries, consistent with the low magnetocrystalline anisotropy. Upon cooling, the martensite plates form, and the magnetic domain structure adapts itself to the now strongly uniaxial magnetization state. In alloys with a room temperature M_S, the wavy domain walls of the austenite continue across individual martensite plates.

In the Co_2NiGa system, we have presented evidence for the presence of magnetoelastic tweed contrast in the austenitic state, due to the coupling of strain to magnetization. In the martensitic state, magnetic domain boundaries coincide with martensite variant boundaries, but often complex interactions are observed in which domain walls cross groups of martensite plates. The interactions between structural interfaces and magnetic domain walls is the topic of ongoing research.

Acknowledgments

The authors gratefully acknowledge financial support from the US Department of Energy, Basic Energy Science, contract number DE-FG02-01ER45893 and the US National Science Foundation, Grant number DMR-0095586.

References

1. E. Völkl, L.F. Allard, D.C. Joy (Eds.): Introduction to Electron Holography (Kluwer/Plenum, Dodrecht/New York, 1999)
2. M. De Graef, Y. Zhu (Eds.): Magnetic Microscopy and its Applications to Magnetic Materials, Vol. 36 (Academic, New York, 2000)
3. M. De Graef: Lorentz microscopy: Theoretical basis and image simulations. In: Magnetic Microscopy and its Applications to Magnetic Materials. Ed. by M. De Graef, Y. Zhu (Academic, New York, 2000), Vol. 36 of Experimental Methods in the Physical Sciences

4. J. Dooley, M. De Graef: Micron **28**, 371 (1997)
5. J.N. Chapman, G.R. Morrison: J. Magn. Magn. Mater. **35**, 254 (1983)
6. Y. Aharonov, D. Bohm: Phys. Rev. **115**, 485 (1959)
7. M.R. Teague: J. Opt. Soc. Am. **73**, 1434 (1983)
8. T.E. Gureyev, A. Roberts, K.A. Nugent: J. Opt. Soc. Am. A **12**, 1942 (1995)
9. T. Gureyev, K. Nugent: J. Opt. Soc. Am. A **13**, 1670 (1996)
10. D. Paganin, K.A. Nugent: Phys. Rev. Lett. **80**, 2586 (1998)
11. M. De Graef: Introduction to Conventional Transmission Electron Microscopy (Cambridge University Press, Cambridge, 2003)
12. J. Soltys: Acta Phys. Pol. A **46**, 383 (1974)
13. M. Wuttig, J. Li, C. Craciunescu: Script. Mater. **44**, 2393 (2001)
14. Q. Pan, R.D. James: J. Appl. Phys. **87**, 4702 (2000)
15. Y. Kishi, M. De Graef, C. Cracionescu, T.A. Lograsso, D.A. Neumann, M. Wuttig: J. Phys. IV **112**, 993 (2003)
16. Y. Murakami, D. Shindo, K. Oikawa, R. Kainuma, K. Ishida: Acta Mater. **50**, 2173 (2002)
17. A. Saxena, T. Castán, A. Planes, M. Porta, Y. Kishi, T.A. Lograsso, D. Viehland, M. Wuttig, M. De Graef: Phys. Rev. Lett. **92**, 197203 (2004)

9

A Way to Search for Multiferroic Materials with "Unlikely" Combinations of Physical Properties

R.D. James and Z. Zhang

9.1 Introduction

The ideas presented in this chapter begin with the observation by physicists (Hill [1, 2] and Hill and Rabe [3]), probing new phenomena through the use of first principles studies, that the simultaneous occurrence of ferromagnetism and ferroelectricity is unlikely. While these studies do not usually consider the possibility of a phase transformation, there is a lot of indirect evidence that, if the lattice parameters are allowed to change a little, then one might have coexistence of "incompatible properties" like ferromagnetism and ferroelectricity. Thus, one could try the following: seek a reversible first-order phase transformation, necessarily also involving a distortion, from, say, ferroelectric to ferromagnetic phases. If it were highly reversible, there would be the interesting possibility of controlling the volume fraction of phases with fields or stress. The key point is reversibility.

This chapter is an exploration of these ideas. To use these ideas as the basis for the search for new materials there are two major questions that need to be addressed:

1. Why are electromagnetic properties of crystalline materials so sensitive to the precise values of the lattice parameters of the crystal, and how does one understand the dependence?
2. What governs the reversibility of phase transformations?

Here we offer a few thoughts on (1) and a deeper analysis of (2).

Even big first-order phase changes can be highly reversible (liquid water to ice, some shape memory materials), and we argue here that in solids it is the nature of the shape change that is critical. We suggest, based on a close examination of measured hysteresis loops in various martensitic systems, that an idea based on "good fitting of the phases" governs reversibility, and we quantify this idea. The idea lends itself to alloy development and we present work in this direction.

9.2 Single Phase Multiferroics

A prototype for this idea is the search for materials that are both ferromagnetic and ferroelectric. All previous work on the search for materials that are simultaneously ferroelectric and ferromagnetic has been done on single phase materials, or on dual phase materials in which the phases are fixed and may only interact through elasticity. Recently there has been renewed interest in the physics community with the development of methods of density functional theory (DFT) that treat spin accurately. This work is nicely summarized by Hill [1, 2]. The materials that have been discovered, either experimentally or from DFT studies, are mostly of the family $BiXO_3$, the example $BiMnO_3$ having apparently been discovered by DFT. Hill [2] explains why single phase ferroelectric plus ferromagnetic materials are so rare. Briefly, the ferromagnetism is commonly associated with filled $3d$ orbitals, while ferroelectricity, at least in perovskites, is nearly always caused by displacement of the cation which is favored by vacant d orbitals. $BiMnO_3$ just happens to have the "accident" of strongly directional d orbitals that are vacant in just the right directions to promote a ferroelectric displacement. Hill concludes, "Therefore, we should in fact *never* expect the coexistence of ferroelectricity and ferromagnetism."

These studies leave open the possibility of simultaneous ferroelectricity and ferromagnetism in nonperovskite crystal structures. A natural starting place for such studies would be rare earth materials, that utilize unpaired $4f$ electrons. But ferroelectricity is rare in these systems.

Turning these ideas around, if one simply alloys a ferromagnetic oxide with a ferroelectric oxide[1] then one should expect a phase transition. Of course, the phase transformation could be diffusional, and there might be a substantial degradation of e.g., the ferromagnetic properties, as the ferroelectric compound is added.

9.3 Basic Idea

In a nutshell, our idea is that materials with properties that are considered "unlikely" or "impossible" in single phase may become possible in multiphase materials. This is particularly true for certain unlikely combinations of interesting electromagnetic properties. In recent years, based on first principles studies referenced earlier, it has become clear that electromagnetic properties like ferromagnetism, ferroelectricity, and linear (dielectric tensor) and nonlinear optical properties are extremely sensitive to the precise values of the lattice parameters of the material. In a first-order phase transformation involving *a change of lattice parameters* – and therefore a local change of shape – there is

[1]There was substantial empirical work of this type in the former Soviet Union in the late 1950s and early 1960s, also unpublished work from Phillips Lab, involving the replacement of the cation of ferroelectric perovskites by magnetic cations.

the possibility of coexistent phases with completely different properties. If the phase transition is highly reversible, the relative volume fraction of the two phases can be readily changed.

To exhibit this behavior, a material must simultaneously satisfy several conditions (1) the system must have a phase boundary between two distinct phases; (2) it must be possible to induce a transformation from one phase to another by a reasonable applied field or stresses; (3) the kinetics of transformation should be sufficiently fast (i.e., diffusional processes and reordering should be avoided); and (4) the transformation must be highly reversible. Items (2) and (3) suggest the use of martensitic phase transformations which are diffusionless and which also, because of the distortion, can take advantage of the lattice parameter sensitivity of properties. We discuss item (4) in detail later.

9.4 Lattice Parameter Sensitivity

An important piece of insight gained from the first principles' calculations is that the conditions for simultaneous ferromagnetism and ferroelectricity are often highly dependent on the lattice parameters of the material: change the lattice parameters a little and the existence of ferroelectricity/ferromagnetism can change drastically. The issue is well known in the first principles study of ferroelectrics: as Cohen explains in a recent review [4], "Properties of ferroelectrics are extremely sensitive to volume (pressure), which can cause problems since small errors in volume... can result in large errors in computed ferroelectric properties." In fact, it is not that uncommon for workers to adjust lattice parameters to unphysical or nonequilibrium values so as to get ferroelectric properties right.

This sensitivity is also well known in ferromagnetic materials. The oft stated "reason" for ferromagnetism in Heusler alloys like Ni_2MnGa is that the Heusler structure "expands the lattice" by putting the Mn atoms far apart. Similarly, the magnetic properties of strong magnets are improved by diffusing nitrogen into the lattice [5]. The latter is thought not to be due to important band structure interactions involving N but to a small average expansion of the lattice parameter. More recent examples show that this expansion can be affected in $BiFeO_3$ by using epitaxial lattice mismatch to expand the lattice; this has led [6] to the single phase ferroelectric/ferromagnetic with apparently the strongest single-phase polarization/magnetization.

A specific example that does involve a martensitic phase transformation is the ferromagnetic shape memory alloy Ni_2MnGa. This alloy undergoes a diffusionless cubic to tetragonal transformation at $-10°C$ (composition $Ni_{51.3}Mn_{24.0}Ga_{24.7}$) with less than 3°C hysteresis, and having a distortion matrix

$$\mathbf{U}_1 = \begin{pmatrix} 0.952 & 0 & 0 \\ 0 & 1.013 & 0 \\ 0 & 0 & 1.013 \end{pmatrix}, \tag{9.1}$$

i.e., $\mathbf{U}_1$ represents the linear transformation (in the cubic basis) that maps the austenite lattice to the martensite lattice. In transforming from austenite to martensite the saturation magnetization increases about 25%, and the magnetic anisotropy undergoes a dramatic change: austenite is almost perfectly isotropic and saturates at about 600 Oe, while martensite saturates at about 1,000 Oe on the (easy) c-axis and at 12,000 Oe on the (hard) a-axis [7].

What are the origins of this sensitivity to changes of lattice parameters? In general terms sensitivity can arise from various sources, e.g., large mismatch in dimensionless material constants, percolation. In the present case our feeling is that it arises from bifurcation. That is, it seems that the appearance of properties like ferroelectricity and ferromagnetism can be viewed as bifurcations, in which the bifurcation parameters are the lattice parameters. If such bifurcations are of the usual "pitchfork" type, then the implied infinite slope of the bifurcation curve at the bifurcation point implies sensitivity to changes of lattice parameters. Very often, in areas ranging from the structural mechanics of shells to the Jahn–Teller effect [8], bifurcation is associated with broken symmetry. Fortunately, bifurcation theory (with symmetry) can be quantitative, and it is expected that such analyses could guide the implementation of the present idea.

9.5 What Makes Big First Order Phase Transformations Reversible?

For the discussion of the reversibility of martensitic phase transformations we will use the sizes of hysteresis loops as a measure of reversibility. This provides one measure of reversibility, but other measures are also important, e.g., the number of times one can go back and forth through the transformation without unacceptable damage to the material measured via degradation of some physical property. In plasticity, the area inside the initial hysteresis loop correlates in many cases with fatigue life and the simplest theories of plasticity take the "cold work" as proportional to this area. Similar ideas are believed to hold for transformations and the little available data supports this [9]. We will concentrate on shape memory alloys, which already show good reversibility.

The most widely accepted explanations of hysteresis in structural phase transformations arise from two sources (a) pinning of interfaces by defects and (b) thermal activation. A close examination of the experimental data does not, however, seem to support either of these ideas.

Consider, for example, the revealing measurements of hysteresis of Otsuka, Sakamoto, and Shimizu [10] on Cu–14.0Al–4.2Ni (mass%). This alloy is interesting in that it has fully reversible transformations cubic $\rightarrow$ orthorhombic ($\beta_1 \rightarrow \gamma_1'$), cubic $\rightarrow$ monoclinic ($\beta_1 \rightarrow \beta_1'$, $\beta_1 \rightarrow \beta_1''$), as well as intermartensite transitions, also including an α_1' phase. These are all considered highly reversible, but there are dramatic differences in the sizes of the hysteresis

loops. In particular, the $\beta_1 \rightarrow \beta_1'$ transformation has incredibly small hysteresis relative to the others. But this data of Otsuka et al. were all measured *on the same specimen*. Thus, each of these transformations sees the same sea of underlying defects in the material. If "pinning" was the explanation for these dramatic differences in the size of the hysteresis, then it would somehow have to involve the *interaction* of the phase transformation with the defect. But if one looks at all the fundamental measured transformation data for $\beta_1 \rightarrow \beta_1'$ vs. say $\beta_1 \rightarrow \gamma_1'$, e.g., transformation strain, latent heat, elastic moduli of phases, one does not see major differences. In fact, $\beta_1 \rightarrow \beta_1'$ has a bigger transformation strain matrix by any reasonable measure than $\beta_1 \rightarrow \gamma_1'$.

Thermal activation (e.g., transition state theory) also does not seem to be relevant. In fact, the data of Otsuka et al. [10] shows that the hysteresis for the $\beta_1 \rightarrow \beta_1'$ is bigger at higher temperatures, in contradiction to the predictions of theories based on thermal activation.

In the CuZnAl system there are very similar observations, even though the parent phase here has essentially DO_3 ordering. A $\beta_1 \rightarrow \beta_1'$ transformation $Cu_{68}Zn_{15}Al_{17}$ has dramatically smaller hysteresis than the other transformations in this system.

It is also instructive to look at the widely studied NiTiCu system. Certain of these alloys are used in orthodontic applications precisely because of their low hysteresis. Alloys of NiTiCu with 10–20 at. % Cu have the lowest known hysteresis in this system. A tabulation of the width of the hysteresis during stress-induced transformation by Miyazaki and Otsuka [11] is summarized in Table 9.1.

We believe that a completely different idea explains, at least qualitatively, these observations. To explain the idea, in Table 9.2 we write the distortion matrices of the very low hysteresis alloys mentioned earlier (these are obtained from the measured lattice parameters of both phases by formulas given in [12]). For the purpose of comparison, those of NiTi and the cubic to orthorhombic $\beta_1 \rightarrow \gamma_1'$ transformation in $Cu_{69}Al_{27.5}Ni_{3.5}$ are also listed.

Notice first that determinants of all of these matrices are close to 1. Since distortion matrices deform unstressed austenite to unstressed martensite, the determinant measures the volume ratio of martensite to austenite,

Table 9.1. Width of the stress hysteresis in NiTiCu alloys according to Miyazaki and Otsuka [11]

Alloy	Width of the hysteresis (MPa)
$Ti_{41.5}Ni_{48.5}Cu_{10.0}$	400
$Ti_{45.5}Ni_{49.5}Cu_{5.0}$	300
$Ti_{44.5}Ni_{50.5}Cu_{5.0}$	200
$Ti_{44.5}Ni_{45.5}Cu_{10.0}$	100
$Ti_{45.5}Ni_{44.5}Cu_{10.0}$	100
$Ti_{50.0}Ni_{40.0}Cu_{10.0}$	100

Table 9.2. Distortion matrices for various transformations with their eigenvalues and determinant

Alloy	Distortion matrix	Eigenvalues	Determinant
$Ni_{50}Ti_{50}$	$\begin{pmatrix} 1.0243 & 0.05803 & -0.04266 \\ 0.05803 & 1.0243 & -0.04266 \\ -0.04266 & -0.04266 & 0.9563 \end{pmatrix}$	1.1066 **0.9663** 0.9321	0.9966
$\mathbf{Ni_{40.5}Ti_{49.5}Cu_{10.0}}$	$\begin{pmatrix} 1.0260 & -0.02740 & 0 \\ -0.02740 & 1.0260 & 0 \\ 0 & 0 & 0.9508 \end{pmatrix}$	1.0534 **0.9986** 0.9508	1.0002
$Cu_{69}Al_{27.5}Ni_{3.5}$ $(\beta_1 \to \gamma_1')$	$\begin{pmatrix} 1.0424 & 0.0194 & 0 \\ 0.0194 & 1.0424 & 0 \\ 0 & 0 & 0.9178 \end{pmatrix}$	1.0618 **1.0230** 0.9178	0.9969
$\mathbf{Cu_{69}Al_{27.5}Ni_{3.5}}$ $(\beta_1 \to \beta_1')$	$\begin{pmatrix} 1.0716 & 0.0516 & 0 \\ 0.0516 & 1.0311 & 0 \\ 0 & 0 & 0.9127 \end{pmatrix}$	1.1067 **0.9959** 0.9127	1.0060
$\mathbf{Cu_{68}Zn_{15}Al_{17}}$ $(\beta_1 \to \beta_1')$	$\begin{pmatrix} 1.087 & 0.0250 & 0 \\ 0.0250 & 1.010 & 0 \\ 0 & 0 & 0.9093 \end{pmatrix}$	1.0944 **1.0026** 0.9093	0.9977

The alloys shown in bold have the lowest hysteresis in their respective systems; middle eigenvalues are also shown in bold

so a determinant of 1 means no volume change. It is well understood that this condition is important for reversibility, especially in polycrystals: if there is a volume change then an island of martensite growing in austenite would generate stress and vice versa. This would happen both ways through the transformation, and therefore any (total) free energy decreasing path between phases would necessarily be part of a hysteretic loop. According to a result of Bhattacharya [13], in a material with cubic austenite, $\det = 1$ is also *sufficient* that there be a microstructure of martensite filling an interior region, with no long range stresses, that satisfies the boundary conditions imposed by the surrounding austenite. However, all the determinants listed in Table 9.2 apparently must be sufficiently close to 1 to minimize this effect on hysteresis, as there does not seem to be a correlation with the low hysteresis cases.[2]

However, there is a striking correlation between the low hysteresis alloys and the condition $\lambda_2 = 1$, where $\lambda_1 \leq \lambda_2 \leq \lambda_3$ are the ordered eigenvalues of the distortion matrix. From Table 9.2 one can see that $|\lambda_2 - 1|$ is an order of magnitude smaller in the low hysteresis alloys than in the others.

[2]Though we should add that these were measurements of hysteresis in stress-induced transformation, and also the measurements on the copper based alloys were done on single crystals. While there is typically a correlation between stress-induced and temperature-induced hysteresis, the full explanation for the relevance of the special conditions could be more subtle.

The condition $\lambda_2 = 1$ is relevant to issues of compatibility [14]. This condition is necessary and sufficient that the austenite be exactly compatible with the martensite (without fine twinning). Mathematically, given a symmetric distortion matrix $\mathbf{U}_1$, the condition $\lambda_2 = 1$ is necessary and sufficient that there exist a rotation matrix $\mathbf{R}$ and a pair of vectors $\mathbf{a}, \mathbf{n}$ such that

$$\mathbf{R}\mathbf{U}_1 - \mathbf{I} = \mathbf{a} \otimes \mathbf{n}. \tag{9.2}$$

In fact, if $\lambda_2 = 1$, there are precisely two solutions $(\mathbf{R}_1, \mathbf{a}_1 \otimes \mathbf{n}_1)$ and $(\mathbf{R}_2, \mathbf{a}_2 \otimes \mathbf{n}_2)$ of (9.2) and these can be written down explicitly [12, 14]. This contrasts sharply with the typical case $\lambda_2 \neq 1$. In that case the typical microstructure at transition is shown in Fig. 9.1.

As is well known in the theory of martensite, the microstructure of Fig. 9.1 is governed by the crystallographic theory of martensite. For our later purposes we will need to describe a few of the results of that theory. First, we need to display the full set distortion matrices corresponding to the martensite. There is a theory for constructing these [15] based on symmetry and the Ericksen–Pitteri neighborhood, but we will just present the final results, shown below in the cases relevant to this chapter.

1. Cubic to tetragonal:

$$\mathbf{U}_1 = \begin{pmatrix} \beta & 0 & 0 \\ 0 & \alpha & 0 \\ 0 & 0 & \alpha \end{pmatrix}, \quad \mathbf{U}_2 = \begin{pmatrix} \alpha & 0 & 0 \\ 0 & \beta & 0 \\ 0 & 0 & \alpha \end{pmatrix}, \quad \mathbf{U}_3 = \begin{pmatrix} \alpha & 0 & 0 \\ 0 & \alpha & 0 \\ 0 & 0 & \beta \end{pmatrix}. \tag{9.3}$$

2. Cubic to orthorhombic:

$$\mathbf{U}_1 = \begin{pmatrix} \alpha & \delta & 0 \\ \delta & \alpha & 0 \\ 0 & 0 & \beta \end{pmatrix}, \quad \mathbf{U}_2 = \begin{pmatrix} \alpha & 0 & \delta \\ 0 & \beta & 0 \\ \delta & 0 & \alpha \end{pmatrix}, \quad \mathbf{U}_3 = \begin{pmatrix} \beta & 0 & 0 \\ 0 & \alpha & \delta \\ 0 & \delta & \alpha \end{pmatrix},$$

$$\mathbf{U}_4 = \begin{pmatrix} \alpha & -\delta & 0 \\ -\delta & \alpha & 0 \\ 0 & 0 & \beta \end{pmatrix}, \quad \mathbf{U}_5 = \begin{pmatrix} \alpha & 0 & -\delta \\ 0 & \beta & 0 \\ -\delta & 0 & \alpha \end{pmatrix}, \quad \mathbf{U}_6 = \begin{pmatrix} \beta & 0 & 0 \\ 0 & \alpha & -\delta \\ 0 & -\delta & \alpha \end{pmatrix}.$$

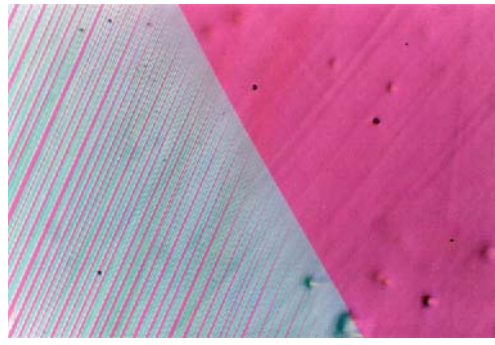

Fig. 9.1. Austenite/martensite interface in the $\beta_1 \to \gamma_1'$ transformation of $Cu_{69}Al_{27.5}Ni_{3.5}$. (Picture courtesy: C. Chu)

3. Cubic to monoclinic
   (a) $\langle 110 \rangle$ polarized:

$$\mathbf{U}_1 = \begin{pmatrix} \sigma & \tau & \rho \\ \tau & \sigma & \rho \\ \rho & \rho & \xi \end{pmatrix}, \quad \mathbf{U}_2 = \begin{pmatrix} \sigma & \rho & \tau \\ \rho & \xi & \rho \\ \tau & \rho & \sigma \end{pmatrix}, \quad \mathbf{U}_3 = \begin{pmatrix} \xi & \rho & \rho \\ \rho & \sigma & \tau \\ \rho & \tau & \sigma \end{pmatrix},$$

$$\mathbf{U}_4 = \begin{pmatrix} \sigma & -\tau & -\rho \\ -\tau & \sigma & \rho \\ -\rho & \rho & \xi \end{pmatrix}, \quad \mathbf{U}_5 = \begin{pmatrix} \sigma & -\rho & -\tau \\ -\rho & \xi & \rho \\ -\tau & \rho & \sigma \end{pmatrix}, \quad \mathbf{U}_6 = \begin{pmatrix} \xi & -\rho & -\rho \\ -\rho & \sigma & \tau \\ -\rho & \tau & \sigma \end{pmatrix},$$

$$\mathbf{U}_7 = \begin{pmatrix} \sigma & -\tau & \rho \\ -\tau & \sigma & -\rho \\ \rho & -\rho & \xi \end{pmatrix}, \quad \mathbf{U}_8 = \begin{pmatrix} \sigma & -\rho & \tau \\ -\rho & \xi & -\rho \\ \tau & -\rho & \sigma \end{pmatrix}, \quad \mathbf{U}_9 = \begin{pmatrix} \xi & -\rho & \rho \\ -\rho & \sigma & -\tau \\ \rho & -\tau & \sigma \end{pmatrix},$$

$$\mathbf{U}_{10} = \begin{pmatrix} \sigma & \tau & -\rho \\ \tau & \sigma & -\rho \\ -\rho & -\rho & \xi \end{pmatrix}, \quad \mathbf{U}_{11} = \begin{pmatrix} \sigma & \rho & -\tau \\ \rho & \xi & -\rho \\ -\tau & -\rho & \sigma \end{pmatrix}, \quad \mathbf{U}_{12} = \begin{pmatrix} \xi & \rho & -\rho \\ \rho & \sigma & -\tau \\ -\rho & -\tau & \sigma \end{pmatrix}.$$

   (b) $\langle 100 \rangle$ polarized:

$$\mathbf{U}_1 = \begin{pmatrix} \rho & \sigma & 0 \\ \sigma & \tau & 0 \\ 0 & 0 & \beta \end{pmatrix}, \quad \mathbf{U}_2 = \begin{pmatrix} \tau & 0 & \sigma \\ 0 & \beta & 0 \\ \sigma & 0 & \rho \end{pmatrix}, \quad \mathbf{U}_3 = \begin{pmatrix} \beta & 0 & 0 \\ 0 & \rho & \sigma \\ 0 & \sigma & \tau \end{pmatrix},$$

$$\mathbf{U}_4 = \begin{pmatrix} \tau & \sigma & 0 \\ \sigma & \rho & 0 \\ 0 & 0 & \beta \end{pmatrix}, \quad \mathbf{U}_5 = \begin{pmatrix} \rho & 0 & \sigma \\ 0 & \beta & 0 \\ \sigma & 0 & \tau \end{pmatrix}, \quad \mathbf{U}_6 = \begin{pmatrix} \beta & 0 & 0 \\ 0 & \tau & \sigma \\ 0 & \sigma & \rho \end{pmatrix},$$

$$\mathbf{U}_7 = \begin{pmatrix} \rho & -\sigma & 0 \\ -\sigma & \tau & 0 \\ 0 & 0 & \beta \end{pmatrix}, \quad \mathbf{U}_8 = \begin{pmatrix} \tau & 0 & -\sigma \\ 0 & \beta & 0 \\ -\sigma & 0 & \rho \end{pmatrix}, \quad \mathbf{U}_9 = \begin{pmatrix} \beta & 0 & 0 \\ 0 & \rho & -\sigma \\ 0 & -\sigma & \tau \end{pmatrix},$$

$$\mathbf{U}_{10} = \begin{pmatrix} \tau & -\sigma & 0 \\ -\sigma & \rho & 0 \\ 0 & 0 & \beta \end{pmatrix}, \quad \mathbf{U}_{11} = \begin{pmatrix} \rho & 0 & -\sigma \\ 0 & \beta & 0 \\ -\sigma & 0 & \tau \end{pmatrix}, \quad \mathbf{U}_{12} = \begin{pmatrix} \beta & 0 & 0 \\ 0 & \tau & -\sigma \\ 0 & -\sigma & \rho \end{pmatrix}.$$

Note that there are two ways to transform from cubic to monoclinic phases, which we label $\langle 110 \rangle$ polarized and $\langle 100 \rangle$ polarized. We should also remark that many martensitic transformations involve shuffling. In that case the crystal structures of austenite and martensite can each be viewed as the union of a set of identical interpenetrating Bravais lattices, translated with respect to each other. In that case the meaning of a distortion matrix is a matrix of a linear transformation (again, with respect to the cubic basis) that maps one of these Bravais lattices for austenite to the corresponding one for martensite. This definition is consistent with the measurements presented earlier for particular systems.

To describe the microstructure in Fig. 9.1, we consider two variants of martensite, described by two distortion matrices, say, $\mathbf{U}_1$ and $\mathbf{U}_2$. To describe the bands of martensite on the left of Fig. 9.1, we solve the "twinning equation,"

$$\mathbf{R}\mathbf{U}_2 - \mathbf{U}_1 = \mathbf{a} \otimes \mathbf{n}\,, \tag{9.4}$$

$\mathbf{R}$ being a rotation matrix. As above, we get two solutions $\mathbf{R}^{\mathrm{I}}, \mathbf{a}^{\mathrm{I}}, \mathbf{n}^{\mathrm{I}}$ and $\mathbf{R}^{\mathrm{II}}, \mathbf{a}^{\mathrm{II}}, \mathbf{n}^{\mathrm{II}}$, these being associated with Type I and Type II twins. We call a solution $(\mathbf{a}, \mathbf{n})$ of (9.4) a *twin system*. Taking one of these solutions, one can make a compatible layering of these distortions, $\mathbf{R}\mathbf{U}_2/\mathbf{U}_1/\mathbf{R}\mathbf{U}_2/\mathbf{U}_1$, etc., with a suitable volume fraction λ of say variant 2. This describes the structure on the left of Fig. 9.1. Introducing a transition layer between this layering and the austenite phase, one finds that the elastic energy in this transition layer can be made arbitrarily small by making the twins finer and finer, if and only if the following equation holds,

$$\hat{\mathbf{R}}\,(\lambda \mathbf{R}\mathbf{U}_2 + (1-\lambda)\mathbf{U}_1) = \mathbf{I} + \mathbf{b} \otimes \mathbf{m}\,, \tag{9.5}$$

for some rotation matrix $\hat{\mathbf{R}}$ and vectors $\mathbf{b}, \mathbf{m}$. Here $\mathbf{m}$ is the normal to the austenite/martensite interface, and $\hat{\mathbf{R}}$ is a suitable rigid body rotation of the martensite laminate needed to secure this approximate compatibility. Equations (9.4) and (9.5) comprise one form of the equations of the crystallographic theory of martensite.

Given a twin system, the calculation of the solution of (9.5) is quite rigid in the usual case $\lambda_2 \neq 1$. One finds [14] that given the twin system $(\mathbf{a}, \mathbf{n})$ there are four values of $\mathbf{b} \otimes \mathbf{m}$, that is, four austenite/martensite interfaces, corresponding to just two values[3] of the volume fraction λ. The shape changes, angles between boundaries, and volume fractions predicted by this calculation agree very well with those shown in Fig. 9.1, and with a great many other cases.

The crystallographic theory of martensite does not determine the fineness of microstructure. That is believed to involve a balance between the interfacial energy of the twin boundaries on the left of Fig. 9.1 and the elastic energy in the transition layer. In fact if one looks closely at Fig. 9.1 then one sees that there is branching of the twins near the interface. This is also understood (Kohn and Müller [16]) as a mechanism for reducing energy, in which the elastic energy of the transition layer becomes delocalized and the twins split into finer and finer arrays near the interface, but always with the volume fraction given by (9.5). In any case the energy of the austenite/martensite interface is the sum of bulk and interfacial energies arising from incompatibility of austenite and martensite. This energy has to be created both ways through the transformation. Any free energy decreasing path from one phase to the other must therefore be part of a hysteretic loop.

---

[3] Two interfaces have volume fraction, say, λ^*, and the other two have volume fraction $(1-\lambda^*)$.

However, if $\lambda_2 = 1$, then austenite *is* compatible with martensite and both elastic and interfacial energies are avoided, except for the single (likely atomically sharp) interface separating austenite and martensite. Since many millions of these austenite/martensite interfaces may be created in a macroscopic sample during transformation, one can imagine that $\lambda_2 = 1$ can be relevant for hysteresis, as noticed earlier.

We have discussed two conditions for reversibility: $\det \mathbf{U}_1 = 1$ and $\lambda_2 = 1$, λ_2 being the middle eigenvalue of $\mathbf{U}_1$. Due to the structure of distortion matrices [15], both the middle eigenvalue and the determinant of all distortion matrices corresponding to a given transformation (e.g., as listed earlier) are the same. We now propose to introduce a third set of conditions, we call the *cofactor conditions*, at which an even more spectacular "accident" of compatibility occurs. The cofactor conditions presuppose that $\lambda_2 = 1$, and they also depend on the choice of the twin system, $\mathbf{a}, \mathbf{n}$. These conditions can be easily extracted from the treatment of the crystallographic theory in [14], although one of the hypotheses was inadvertently omitted there. The cofactor conditions are

$$\lambda_2 = 1, \quad \operatorname{tr} \mathbf{U}_1^2 - \det \mathbf{U}_1^2 - 2 - \frac{1}{4}|\mathbf{a}|^2 > 0, \quad \mathbf{a} \cdot \mathbf{U}_1 \operatorname{cof} (\mathbf{U}_1^2 - \mathbf{I})\mathbf{n} = 0\,. \tag{9.6}$$

Here, cof A denotes the cofactor of the matrix A: $(\operatorname{cof} A)_{ij} = (-1)^{i+j} \det \hat{A}_{ij}$, where $\hat{A}$ is the 2×2 matrix obtained by deleting the ith row and jth column of A. If the cofactor conditions are satisfied, then, *in addition to the austenite single-variant interfaces arising from* $\lambda_2 = 1$*, it is possible to have austenite/martensite interfaces with any volume fraction*[4] *between* 0 *and* 1.

As an example, a distortion matrix belonging to a cubic to monoclinic transformation ($\langle 100 \rangle$ polarized) that satisfies exactly the cofactor conditions is

$$\mathbf{U}_1 = \begin{pmatrix} 1.09 & 0.030 & 0 \\ 0.030 & 1.010 & 0 \\ 0 & 0 & 0.93 \end{pmatrix}. \tag{9.7}$$

[Here, the chosen twin system is the Type I twin relating variants 1 and 12, the notation as above, which gives $\mathbf{a} = (-0.17182, -0.0572727, 0.145266)$, $\mathbf{n} = (101)$.] Notice that this matrix is not far away from the real measured transformation matrix of $Cu_{68}Zn_{15}Al_{17}$, Table 9.2. The best way to illustrate the result in italics just above is to plot a family of austenite/martensite interfaces corresponding to a sequence of volume fractions going from 0 to 1. This is done in Fig. 9.2. This should be contrasted with the restrictive results (4 interfaces, just 2 volume fractions) mentioned above in the usual case when the cofactor conditions are not satisfied.

---

[4] If the inequality in (9.6) is weakened to the statement $\operatorname{tr} \mathbf{U}_1^2 - \det \mathbf{U}_1^2 - 2 > 0$, then there is a limited range of volume fractions, given precisely by $[0, \lambda^*] \cup (1 - \lambda^*, 1]$, where $\lambda^* = \frac{1}{2}\left(1 - \sqrt{1 - 4(\mu/|\mathbf{a}|^2)}\right)$ and $\mu = \operatorname{tr} \mathbf{U}_1^2 - \det \mathbf{U}_1^2 - 2$, for which there are austenite/martensite interfaces.

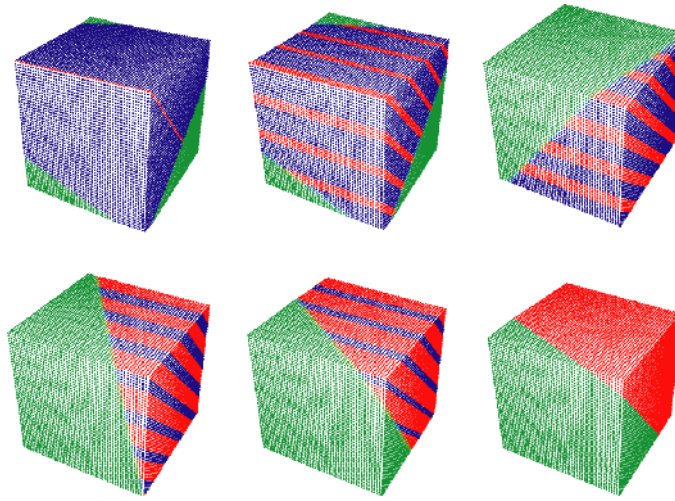

Fig. 9.2. Illustration of the continuous variation of volume fraction of martensite possible under the cofactor conditions. Distortions accurately drawn using the distortion matrix and twin system given in $(9.7)_{\text{ff}}$

Note the remarkable degree of flexibility indicated by these pictures. In fact, as the volume fraction of martensite goes from 0 to 1, the (perpendicular) directions of maximum and minimum principle strain in the martensite actually exchange places. Thus, these special conditions on lattice parameters do not mean that the martensite is compatible with the austenite because it does not deform with volume fraction changes. On the contrary, it undergoes large average deformations *while* remaining compatible with austenite.

One possible objection to the usefulness of the cofactor conditions is that they only appear to apply to one twin system. As we shall see later, this is not the case. In cubic to monoclinic transformations, if the cofactor conditions are satisfied for one twin system, then they are satisfied for many twin systems.

9.6 Specific Relationships Among Lattice Parameters for a High Degree of Reversibility

Here we answer the question of what precisely are the conditions on lattice parameters that imply the satisfaction of the proposed conditions for reversibility. It is easy to write down the conditions $\det \mathbf{U}_1 = 1$ and $\lambda_2 = 1$ in terms of the parameters in $\mathbf{U}_1$, so, instead, we concentrate on the most interesting case of satisfying simultaneously all of the conditions: $\det \mathbf{U}_1 = 1$, $\lambda_2 = 1$ and the cofactor conditions. We focus only on cases where the austenite is cubic, and the symmetries have a group/subgroup relationship. In this case it is easy to see that the full set of conditions cannot be satisfied if the distortion is

such that the martensite has tetragonal or trigonal (rhombohedral), symmetry, but can be satisfied for lower symmetry martensites, as discussed later. Later, when we discuss the variants of martensite, we refer to the numbering of distortion matrices given in Sect. 9.5.

9.6.1 Cubic to Orthorhombic Transformations

In the cubic to orthorhombic case there are precisely two matrices that satisfy all three conditions. These matrices are

$$\mathbf{U}_1^{\mathrm{I}} = \begin{pmatrix} \frac{1}{2}(1+\frac{1}{\sqrt{2}}) & \frac{1}{2}(1-\frac{1}{\sqrt{2}}) & 0 \\ \frac{1}{2}(1-\frac{1}{\sqrt{2}}) & \frac{1}{2}(1+\frac{1}{\sqrt{2}}) & 0 \\ 0 & 0 & \sqrt{2} \end{pmatrix}, \quad \mathbf{U}_1^{\mathrm{II}} = \begin{pmatrix} \frac{1}{2}(1+\sqrt{2}) & \frac{1}{2}(\sqrt{2}-1) & 0 \\ \frac{1}{2}(\sqrt{2}-1) & \frac{1}{2}(1+\sqrt{2}) & 0 \\ 0 & 0 & \frac{1}{\sqrt{2}} \end{pmatrix}.$$

Each of these matrices satisfies the cofactor conditions simultaneously for 12 twin systems, all Type I twins for the case of $\mathbf{U}_1^{\mathrm{I}}$ and all Type II twins for the case of $\mathbf{U}_1^{\mathrm{II}}$ (the compound twins never satisfy all three conditions). These are quite big matrices by any measure, and therefore unlikely to be realistic; they may also fall outside of the Ericksen–Pitteri neighborhood and therefore call into question the basic theory. Nevertheless, they are useful for the purpose of illustration.

9.6.2 Cubic to Monoclinic Transformations

⟨100⟩-Polarized

In the ⟨100⟩ polarized cubic to monoclinic case there are two one-parameter families of matrices satisfying all three conditions, given below.

$$\mathbf{U}_1^{\mathrm{I}} = \begin{pmatrix} \alpha+\alpha^2-\alpha^3 & \sqrt{\alpha^2(1+\alpha)(1-\alpha)^3} & 0 \\ \sqrt{\alpha^2(1+\alpha)(1-\alpha)^3} & 1-\alpha^2+\alpha^3 & 0 \\ 0 & 0 & \frac{1}{\alpha} \end{pmatrix}, \quad \alpha \le 1\,, \tag{9.8}$$

$$\mathbf{U}_1^{\mathrm{II}} = \begin{pmatrix} (\alpha^2+\alpha-1)/\alpha^2 & \frac{1}{\alpha^2}\sqrt{(\alpha-1)^3(\alpha+1)} & 0 \\ \frac{1}{\alpha^2}\sqrt{(\alpha-1)^3(\alpha+1)} & (\alpha^3-\alpha+1)/\alpha^2 & 0 \\ 0 & 0 & \frac{1}{\alpha} \end{pmatrix}, \quad \alpha \ge 1\,. \tag{9.9}$$

Each of these works simultaneously for 12 twin systems. These are Type I twins in case (9.8) and Type II twins in case (9.9), but not all are included (i.e., there are more than 12 Type I twins in this system). Note that both families begin at the identity, corresponding to no transformation, at $\alpha = 1$. The case (9.9) is particularly interesting in its proximity to real examples of distortion matrices.

There are also several one-parameter families corresponding to $\beta = 1$ in the notation above. These are less interesting because they do not seem to be close to any realistic cases that could provide starting points for alloy development. On the other hand, some of these cases apply to many twin systems.

⟨110⟩-Polarized

In the ⟨110⟩ polarized cubic to monoclinic case there are several one-parameter families of matrices satisfying all three conditions. We found seven such families, all passing through the identity, and all applying simultaneously to multiple twin systems. There is also a two-parameter family of matrices satisfying all three conditions, but only applying to a limited family of compound twins. While it is possible to write analytical expressions for the seven families matrices satisfying these conditions, these are somewhat complicated to write down so we do not give them here.

9.6.3 Relationships for Martensite/Martensite Transitions

The conditions we propose for reversibility are applicable to martensite–martensite transitions, such as the tetragonal to trigonal transformation that occurs at a morphotropic boundary. These should imply low hysteresis by the same reasoning that we have given for the austenite/martensite transitions. If $\mathbf{U}$ and $\mathbf{V}$ denote (positive-definite, symmetric) distortion matrices corresponding to two different martensites, the condition (1) of no volume change is $\det \mathbf{U} = \det \mathbf{V}$, (2) the exact compatibility is that the middle eigenvalue of $\mathbf{V}^{-1}\mathbf{U}^2\mathbf{V}^{-1}$ is 1. The cofactor conditions are (9.4) and (9.5) with $\mathbf{U}_1, \mathbf{U}_2$ replaced by $\mathbf{U}, \mathbf{V}$, respectively, and $\mathbf{I}$ replaced by either $\mathbf{U}$ or $\mathbf{V}$. It is also possible to pass from the description (9.4) and (9.5) to more compact conditions like (9.6) in the martensite/martensite case using the methods of [14]. There are also further conditions that would make two compatible laminates of martensite additionally flexible, that would likely also enhance the reversibility of transition.

9.7 Tuning Lattice Parameters to Satisfy Two of the Proposed Conditions in the NiTiCuPd System

We have recently put these ideas into practice in a special case, that of the NiTiCuPd system. It is known that a family of alloys in the system NiTiCu nearly satisfy the second condition $\lambda_2 = 1$, which suggested to us that this is a good starting place. We focused on trying to determine the alloys that satisfy just the first two conditions $\det \mathbf{U}_1 = 1$ and $\lambda_2 = 1$.

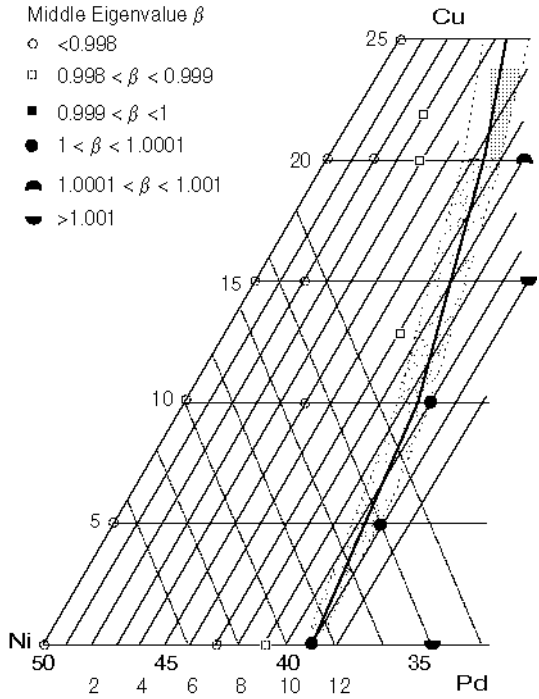

Fig. 9.3. A part of the compositional triangle NiCuPd at Ti = 50%. Compositions on the line satisfy the condition $\lambda_2 = \beta = 1$. A small subset of the measured samples is also shown. The *shaded region* indicates the error expected in this determination

Briefly, we measured lattice parameters of both austenite and martensite by X-ray diffraction and thereby established the mapping between composition and distortion matrices. (For a more detailed description of these experiments, see Zhang [17].)

Over a large compositional region we found that $\det \mathbf{U}_1 = 1$ within our error of measurement. However, the middle eigenvalue λ_2 was more sensitive to composition.[5] An example of our results is shown in Fig. 9.3. The compositional space NiTiCuPd is three-dimensional. Figure 9.3 shows a 2D slice through this surface at constant Ti composition of 50%.

9.8 Further Comparisons with Experiment

After determining the mapping between composition and distortion matrices as described in Sect. 9.7, we were informed of additional data on hysteresis in the literature for alloys of particular composition. (We are grateful to Wuttig, Quandt, and Berg for these references.)

---

[5]Also, the error of the measurement of λ_2 was smaller than that of $\det \mathbf{U}_1$.

We first describe measurements of Winzek and Quandt [18]. They measured thermal hysteresis in both free standing and stressed films, and both had similar trends, but, for definiteness, we compare with the measurements on the free standing films. Winzek and Quandt also measured hysteresis in two different ways: by using the width of a parallelogram approximation of the loop, and by using the thinnest place on the loop (some loops had a "waist"). We compare with the former method. In their measurements on NiTiCu, they found that an alloy with approximate composition $Ni_{34}Ti_{50}Cu_{16}$ exhibited the lowest hysteresis among alloys they studied. We did not find any alloys in the NiTiCu system that satisfy $\lambda_2 = 1$ within our experimental error. However, the alloy in the NiTiCu system that most closely satisfies $\lambda_2 = 1$ is $Ni_{30}Ti_{50}Cu_{20}$, which is quite close to that of Winzek and Quandt (in fact, the closest of those they measured). We believe that if they had measured the alloy $Ni_{30}Ti_{50}Cu_{20}$, it would have exhibited the lowest hysteresis.

More interestingly, Winzek and Quandt [18] also made similar measurements on NiTiPd films. They found that there was a rather sharp drop in the hysteresis at the composition $Ni_{40}Ti_{50}Pd_{10}$, among alloys they tested. This is very close to the crossing point of our surface $\lambda_2 = 1$, as can be seen from Fig. 9.3; in fact, the exact crossing is at $Ni_{39}Ti_{50}Pd_{11}$.

Also interesting is the data we have collected from the US Patent 5,951,793 shown in Table 9.3. Some of these alloys have small percentages of elements that we have not studied, and these can either be excluded from the comparison or else included (by, e.g., assigning their percent to the element for which they substitute). It is seen from Table 9.3 that there are dramatic differences in the size of the stress hysteresis. The closest alloy to our surface $\lambda_2 = 1$ is the alloy shown in bold and it is indeed very close. This is the one with the lowest hysteresis.

Table 9.3. Data on stress hysteresis vs. composition for various alloys collected from US Patent 5,951,793

Ti	Ni	Pd	Other	Width of the hysteresis (MPa)	A_f (°C)
49.5	43.5	0	Cu 7	236	25
50	40	0	Cu 10	172	60
50	47	2.5		263	55
49.5	47	3	Cr 0.5	148	5
49.5	46.5	4		137	5
50	42.5	7.5		95	25
50	42	7.5	Co 0.5	82	15
49.5	**40.5**	**10**		**54**	**−20**
49.5	38	12	V 0.5	106	30
49	36	13	Fe 2	103	−30
51	35	14		127	60
49	36	15		170	−50

9.9 Summary and Outlook: A General Method for Seeking New Classes of Functional Materials

We have proposed three relationships for reversibility: $\det \mathbf{U}_1 = 1$ (and, as many compatible variants of martensite as possible), $\lambda_2 = 1$, λ_2 being the middle eigenvalue of $\mathbf{U}_1$, and the cofactor conditions

$$\lambda_2 = 1, \quad \operatorname{tr} \mathbf{U}_1^2 - \det \mathbf{U}_1^2 - 2 - \frac{1}{4}|\mathbf{a}|^2 > 0, \quad \mathbf{a} \cdot \mathbf{U}_1 \operatorname{cof} (\mathbf{U}_1^2 - \mathbf{I})\mathbf{n} = 0\,. \quad (9.10)$$

The experimental evidence rather strongly suggests that the first two of these govern the main part of the hysteresis, while the third condition is a natural extension of these concepts. The standard ideas that are usually quoted as governing hysteresis in martensitic phase transitions do not seem to us to be the most influential factors.

More generally, our idea can be expressed as follows. *Arrange to have a big first order, reversible (martensitic, i.e., diffusionless) phase transformation that separates two phases with different electromagnetic properties.* This leads to the following advantageous situation. (1) Since the two phases have different lattice parameters, and different band structures, the possibilities for simultaneous unlikely properties are greatly improved. (2) If the phase transformation is reversible then the volume fraction of the two phases could be changed by using an electric field, a magnetic field, or a stress, depending on the shape change and electromagnetic properties of the two phases.

Besides ferroelectricity – ferromagnetism, there are many potential property pairs that exhibit lattice parameter sensitivity and are candidates for the proposed strategy: solubility–insolubility of H_2, high band gap–low band gap semiconductors, insulator–conductor (electrical or thermal), opaque–transparent (at various wavelengths), high–low index of refraction, luminescent–nonluminescent. Also possible according to this strategy are new kinds of thermoelectric and thermomagnetic materials, that utilize the lattice parameter sensitivity of electromagnetic properties together with the latent heat of transformation.

Acknowledgments

We are grateful to K. Rabe, M. Wuttig, E. Quandt, J.M. Ball, T. Shield, J. Cui and B. Berg for stimulating discussion of these ideas. This work was supported by MURI N00014-010100761 administered by ONR. The work also benefitted from the support of NSF-NIRT DMS-0304326.

References

1. N.A. Hill: J. Phys. Chem. B **104**, 6694 (2000)
2. N.A. Hill: Annu. Rev. Mater. **32**, 1 (2002)

3. N. Hill, K.M. Rabe: Phys. Rev. B **53**, 8759 (1999)
4. R.E. Cohen: J. Phys. Chem. Solids **61**, 139 (1999)
5. Y.C. Yang, X.D. Zhang, S.L. Ge, Q. Pan, L.S. Kong, H. Li, J.L. Yang, B.S. Zhang, Y.F. Ding, C.T. Ye: J. Appl. Phys. **70**, 6001 (1991)
6. J. Wang, J.B. Neaton, H. Zheng, V. Nagarajan, S.B. Ogale, B. Liu, D. Viehland, V. Vaithyanathan, D.G. Schlom, U.V. Waghmare, N.A. Spaldin, K.M. Rabe, M. Wuttig, R. Ramesh: Science **299**, 1719 (2003)
7. R. Tickle, R.D. James: J. Magn. Magn. Mater. **195**, 627 (1999)
8. H.A. Jahn, E. Teller: Proc. R. Soc. London **A161**, 220 (1937)
9. R.M. Tabanli, N.K. Simha, B.T. Berg: Metall. Mater. Trans. A **32**, 1866 (2001); Mater. Sci. Eng. A, **273**, 644 (1999)
10. K. Otsuka, H. Sakamoto, K. Shimizu: Acta Metall. **27**, 585 (1979)
11. S. Miyazaki, K. Otsuka: ISIJ Int. **29**, 353 (1989)
12. R.D. James, K. Hane: Acta Mater. **48**, 197 (2000)
13. K. Bhattacharya: Arch. Rational Mech. Anal. **120**, 201 (1992)
14. J.M. Ball, R.D. James: Arch. Rational Mech. Anal. **100**, 13 (1987)
15. J.M. Ball, R.D. James: Philos. Trans. R. Soc. London **A338**, 389 (1992)
16. R.V. Kohn, S. Müller: Philos. Mag. A **66**, 697 (1992); Commun. Pure Appl. Math. **47**, 405 (1994)
17. Z. Zhang: MS thesis, University of Minnesota (2004)
18. B. Winzek, E. Quandt: Proc. Mater. Res. Soc. Symp. **604**, 117 (2000)

10

Invar and Anti-Invar: Magnetovolume Effects in Fe-Based Alloys Revisited

E.F. Wassermann and M. Acet

10.1 Introduction

In search for a cheaper length standard than Pt–Ir, Guillaume found in 1897 "Invar," a ferromagnetic (FM) fcc $Fe_{65}Ni_{35}$ alloy showing small, almost temperature independent thermal expansion below the Curie temperature. After discovering "Elinvar," an FM fcc Fe–Ni–Cr alloy with constant elastic behavior, "revolutionizing" the watch industry with newly designed balance springs, Guillaume was honored with the Nobel Price in physics in 1920. In spite of worldwide research, understanding of Invar and Elinvar remained a centennial problem until the beginning of the 1990s, when ab initio calculations gave basic insights into the relations between lattice structure, atomic volume and magnetic properties. At that time, "anti-Invar" also was recognized, the effect being the enlargement of the atomic volume of fcc Fe and fcc Fe-rich alloys at high temperatures in the paramagnetic range by FM spin fluctuations. In this chapter we briefly review the basic experimental properties of Invar and anti-Invar and discuss the properties of Fe, the element inspiring Weiss to his historical 2γ-states model. We then revisit the theoretical situation and specifically discuss the models stressing the importance of charge transfer at the Fermi energy between electronic levels with different symmetry (e_g and t_{2g}) and nonbonding or antibonding character.

10.2 Invar

In spite of intensive research for more than a century, the Invar problem remains to be only partially solved. The actual knowledge at the time being, as well as the progress in the understanding of Invar, can be traced best in some review articles [1–5], in a recent book [6] and in some key experimental [7–9] and theoretical [10–12] papers. To date, the situation can be characterized by the statement that especially concerning the behavior at finite temperatures, there is appreciable disagreement between experiment and theory. The main

reason is the lack of appropriate theoretical "tools" to reliably describe the finite temperature behavior of itinerant magnets from first principles. This is, however, a prerequisite to fully explain the experimentally observed Invar typical features, most significantly the temperature dependence of the thermal expansion coefficient $\alpha(T)$. Invar materials show a volume increase in the magnetically ordered range below the ordering temperature, and therefore relative to a nonmagnetic lattice curve (Grüneisen curve) a *reduced* thermal expansion. In ferromagnetically ordered alloys below the Curie-temperature T_{C}, this is called "FM Invar-effect," in antiferromagnetically (AF) ordered systems below the Néel temperature T_{N} we get "AF Invar-effect". Figure 10.1 shows some typical experimental examples of the thermal expansion coefficient $\alpha(T)$ of fcc FM $Fe_{65}Ni_{35}$ Invar (open circles), FM Cementite Fe_3C+2 at% Cr (full circles), and AF $Ti_{35}Fe_{65}$ with hexagonal Laves phase C14 structure. Note that in all alloys, the FM or AF Invar effect vanishes for $T > T_{\mathrm{C}}$ or $T > T_{\mathrm{N}}$ and thus the reference curve ($\alpha_{\mathrm{lattice}}$) can be obtained by a Grüneisen analysis. The area between the Grüneisen curve and the experimental data give the maximum volume enhancement due to the Invar effect – the "spontaneous" volume magnetostriction at zero temperature ω_{so}. The values are $\omega_{\mathrm{so}} = 1.6\%$

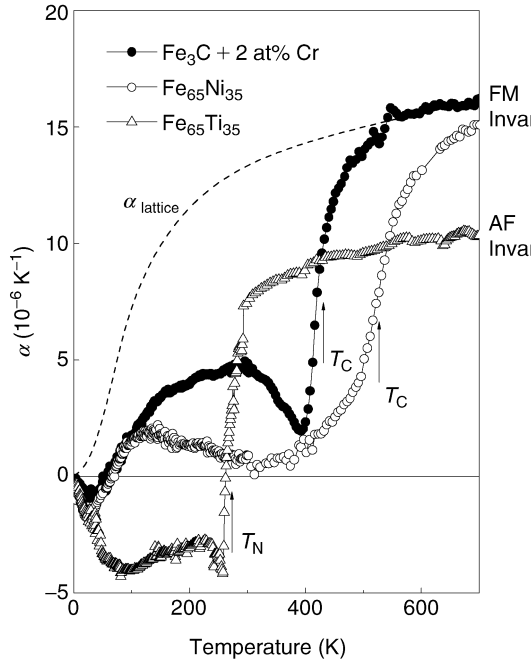

Fig. 10.1. Thermal expansion coefficient α vs. the temperature for fcc FM Invar $Fe_{65}Ni_{35}$, FM cementite $Fe_3C + 2$ at%Cr, and AF Invar $Ti_{35}Fe_{65}$ with Laves phase C14 hexagonal structure. *Dashed curve*: nonmagnetic Grüneisen reference $\alpha_{\mathrm{lattice}}(T)$. *Arrows* mark the magnetic ordering temperatures [6]

Table 10.1. Invar systems

Structure	Material	
fcc	Fe–Ni, Fe–Pt (ord.) Fe–Pt (disord.), Fe–Pd, Fe–Mn, Co–Mn, Fe–Ni–Mn, Fe–Ni–Cr, Fe–Ni–Co, Fe–Ni-Pt, Fe–Ni–Pd	
bcc	Cr–Fe, Cr–Mn, Fe–Cr–Mn	
hexagonal	Co–Cr	
amorphous	Fe–B, P	
	Fe–TE,	TE: Sc, Y, Zr, Hf
	(Fe–TE)X	TE: Mn, Co, Ni; X: Si, B, P
Laves phases	$TEFe_2$	TE: Ti, Zr
and compounds	$RECo_2$	RE: all except Eu
	RE_2Fe_{17}	RE: Y, Dy, La
	$Dy_2(FeCo)_{17}$, Fe_3C, $Fe_{14}Nd_2B$	

for FM Invar $Fe_{65}Ni_{35}$, $\omega_{so} \approx 1.0\%$ for cementite and $\omega_{so} \approx 0.6\%$ for AF Invar $Fe_{65}Ti_{35}$.

As shown in Table 10.1, Invar behavior (and often Elinvar behavior, the temperature independent elastic behavior) is not bound to fcc Fe-based systems alone. But, because of technical importance, Fe-based alloys are most widely investigated. Applications of Invar range from large scale, e.g., Fe–Ni for ship tanks for transportation of liquified natural gas at temperatures around 110 K [4] (Fig. 10.2), to small scale in e.g., chip base plates or bi-metals.

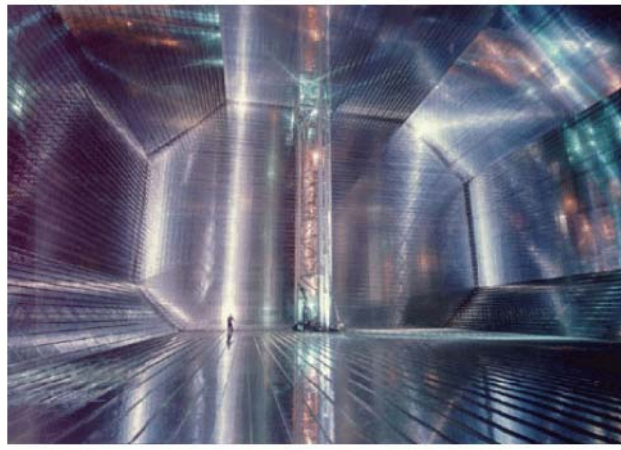

Fig. 10.2. Large scale application of iron–nickel Invar: View into a tank of a ship for transport of liquid natural gas (capacity $130,000\,m^3$, atm. pressure, $T = 110\,K$). The tank walls are made of weldable $Fe_{65}Ni_{35}$ Invar, specially treated to withstand repeated thermal cycling (Photo: Imphy Ugine Precision [4])

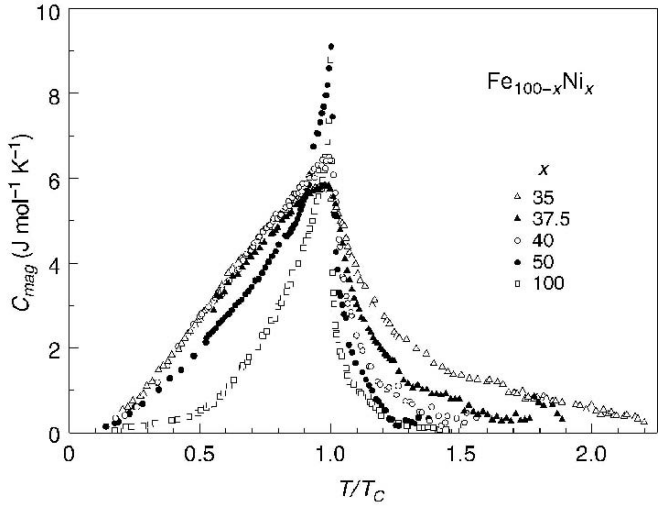

Fig. 10.3. Magnetic contribution c_{mag} to the specific heat as a function of the reduced temperature for pure Ni and $Fe_{100-x}Ni_x$ alloys with different composition [13]. For details see text

Most important on the world's Invar market, also by tonnage share, has been $Fe_{65}Ni_{35}$ Invar used for shadow masks in television tubes. With increasing spread of flat screens, this market section of Invar is, however, dying away, none the least because the current and voltage feedthroughs of the glass TV tubes are also made of Invar (an Fe–Ni–Co alloy known as "Kovar"). Guillaume's original Elinvar alloy ($Fe_{54}Ni_{34}Cr_{12}$) began losing its importance a long time ago too, when Invar balance springs in watches were replaced by quartz crystals. Today, Elinvar finds applications in RHEED contacts, relays, and frequency standards – a relatively small but a high-tech market.

Invar characteristic properties are by no means limited to the thermal expansion, but anomalies are found in all physical properties of the alloys mentioned, especially the magnetization $M(T, H)$ (in the context where the problem of the "hidden excitations" is still debated; see e.g. [1–5]), the elastic constants $C_{\mathrm{L,T}}(T)$ and the bulk and shear moduli $B(T)$ and $G(T)$, the latter three revealing the characteristics of the not fully understood "softness" of the Invar materials [1–6]. Invar-typical is also the behavior of the specific heat. This is depicted for Fe–Ni alloys in Fig. 10.3 [13] showing that relative to the reference behavior of pure FM Ni, there are appreciable magnetic contributions c_{mag} to the specific heat in FM fcc $Fe_{100-x}Ni_x$ alloys at temperatures below as well as above T_{C}. Starting from a composition $Fe_{50}Ni_{50}$, this excess contribution to c_{mag} finds its maximum at the Invar concentration $x = 35$. The excess magnetic specific heat is caused by thermal Invar-characteristic excitations – still debated concerning their nature as will be discussed below. These are known as moment–volume fluctuations and are also referred

to as "elasto-magnons". Figure 10.3 reveals that there is also an appreciable magnetic contribution to the specific heat in the paramagnetic temperature range for $T > T_C$, which is also maximum in $Fe_{65}Ni_{35}$ Invar. This excess is very likely caused by FM spin fluctuations [14], though, again, the physical nature of the underlying excitations is not understood.

10.3 From Invar to Anti-Invar

Our investigations [6–9] have shown that increasing the Fe-concentration in $Fe_{100-x}Ni_x$ alloys to above the Invar composition, $x > 65$ (electrons per atom, $e/a < 8.75$), results in a continuous transition to another magnetovolume effect called "anti-Invar" [15]. Anti-Invar is the opposite of Invar behavior and denotes the increase of the volume and the enhancement of the thermal expansion relative to a nonmagnetic reference. Anti-Invar is observed in γ-Fe [16] and fcc Fe-rich systems in the high temperature *paramagnetic* range. The relative volume increase through the anti-Invar effect can be determined quantitatively by plotting $T_m\alpha(T)$ as a function of T/T_m, where T_m is the melting temperature. For "normal" metals and alloys, such a plot results in an almost universal expansion curve, which we use as a Grüneisen-like reference for the thermal expansion of the magnetic alloys in question. Figure 10.4 shows such a plot for $Fe_{100-x}Ni_x$ alloys in the fcc stability range together with the data for pure γ-Fe above the A_3 point (1184 K) and $\alpha_{lattice}T_m$ vs. T/T_m, the Grüneisen reference curve mentioned. The Fe–Ni curves terminate at the martensite start temperatures M_s/T_m, where a transition from the high temperature austenitic fcc phase into the bcc (or bct) martensitic phase takes place on decreasing T. Very important in this context is the thermal expansion curve of $Fe_{77}Ni_{13}Mn_7C_3$ (open circles in Fig. 10.4). This paramagnetic alloy has fcc stability in the range $0 \leq T \leq T_m$, and thus can serve as an "anti-Invar reference" [17], i.e., it provides the course of the thermal expansion behavior $\alpha(T)$ for the Fe–Ni alloys in the temperature range where the fcc phase is not stable.

Note that the transition from Invar to anti-Invar behavior in Fig. 10.4 can be observed twice: *with increasing Fe-concentration* (at constant temperature) starting from pure fcc $Fe_{65}Ni_{35}$ FM Invar to pure fcc anti-Invar in $Fe_{77}Ni_{13}Mn_7C_3$, and *with increasing temperature* (at constant composition), as observed in, e.g., $Fe_{70}Ni_{30}$ through the "negative" deviation from the lattice reference at low temperatures changing to a "positive" deviation at higher temperatures. For $x > 75$ to pure γ-Fe, all the alloys in Fig. 10.4 are paramagnetic and show only anti-Invar behavior. Analogous transitions from Invar to Anti-Invar behavior with increasing Fe concentration as in Fig. 10.4 have also been found in Fe–Pt and Fe–Ni–Co alloys.

Anti-Invar typical anomalies can be found in other physical properties of the alloys mentioned above. However, since there is no magnetic long range order, and the anomalies occur at relatively high temperatures, the number of

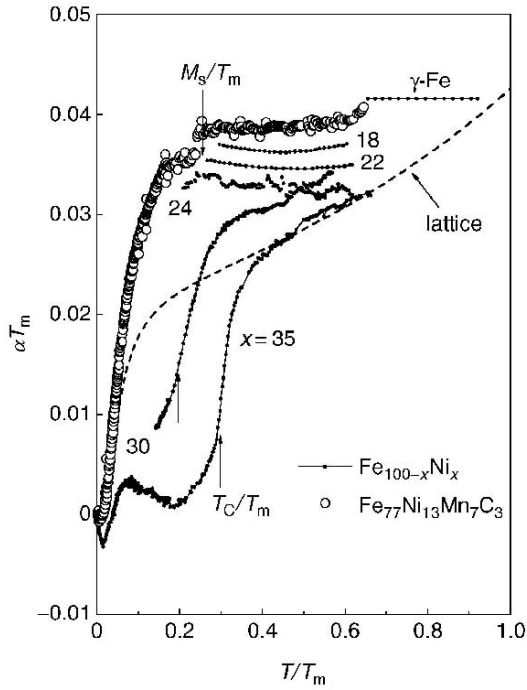

Fig. 10.4. αT_m vs. T_m (melting temperature) for Fe-rich Fe–Ni alloys. The curves for $0 \leq x \leq 30$ are measured down to their corresponding martensite start temperatures M_s/T_m. *Dashed*: lattice reference curve (Grüneisen). *Open circles*: anti-Invar alloy $Fe_{77}Ni_{13}Mn_7C_3$ [17]

available data is limited. Attempts to find anti-Invar typical behavior in, e.g., the elastic constants (e.g., [2]) have so far not been very successful. In Fig. 10.5, we present (analogous to Fig. 10.3) our recent data on the magnetic contribution c_{mag} to the specific heat through the anti-Invar effect for three alloys, $Fe_{80}Ni_{20}$, $Fe_{74}Ni_{26}$, and $Fe_{77}Ni_{13}Mn_7C_3$ [13] together with some theoretical data from Monte Carlo simulations of high-moment–low-moment transitions in Fe–Ni anti-Invar [18]. There is no room to discuss the details here, but it is obvious from the figure that there are very large magnetic anomalies in these alloys (the low temperature minimum in $Fe_{65}Ni_{35}Mn_7C_3$ results from a spin glass order), which can be described by a Schottky-type analysis that could follow from a low-spin–high-spin transition in a two level system (see also, Sects. 10.4 and 10.5).

Since the thermal expansion of almost all fcc Invar and anti-Invar alloys (besides those that are Co based) is isotropic, i.e., $3(\Delta l/l) = \Delta V/V$, using the Grüneisen lattice and the $Fe_{77}Ni_{13}Mn_7C_3$ anti-Invar references and the experimental $\alpha(T)$ data, one can work out a plot demonstrating the systematic transition from Invar to anti-Invar as a function of composition in very different alloy systems. Figure 10.6 gives the result in the form of maximum relative

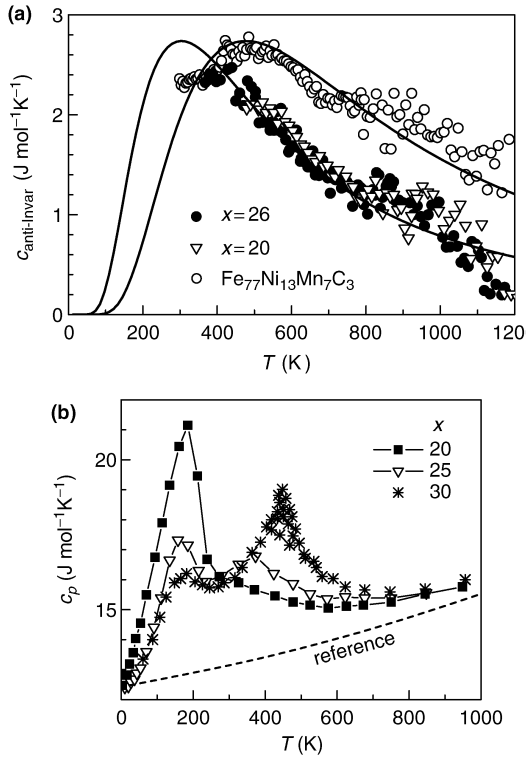

Fig. 10.5. (**a**) Anti-Invar contribution to the specific heat $c_{\text{anti-Invar}}$ vs. temperature determined experimentally [13] for $x = 20, 26$ and $Fe_{77}Ni_{13}Mn_7C_3$ anti-Invar alloys and (**b**) compared results of Monte Carlo simulations for a two level low-spin–high-spin transition system [18]

volume enhancement $(\Delta V/V)_{\max}$ vs. composition (in electrons per atom, e/a, counting s + d electrons) for a series of alloys (see symbols in Fig. 10.6). Invar behavior with a maximum volume increase of $(\Delta V/V)_{\max} \sim 1.6\%$ at $e/a = 8.75$ diminishes with decreasing electron concentration and vanishes for $e/a < 8.5$. There is Invar and anti-Invar simultaneously present (also as a function of temperature – which this plot does not show directly) in a small interval $8.5 < e/a < 8.8$. There is then the anti-Invar developing with decreasing e/a, with a maximum relative volume increase up to almost 6% in Fe–Mn. This relative volume increase by the anti-Invar effect occurs *in addition* to the relative volume increase of $(\Delta V/V) \sim 7\%$ all metals and alloys experience between 0 K and their melting temperature (Grüneisen law).

The continuous transition from Invar to anti-Invar when reducing the electron concentration e/a as shown in Fig. 10.6 is directly reflected in the ab initio ground state calculations [10, 11] of the total energy as a function of atomic volume in the Fe–Ni system. Simultaneously, the composition dependence of the electronic density of states (DOS) in these fcc alloys reveals typical features

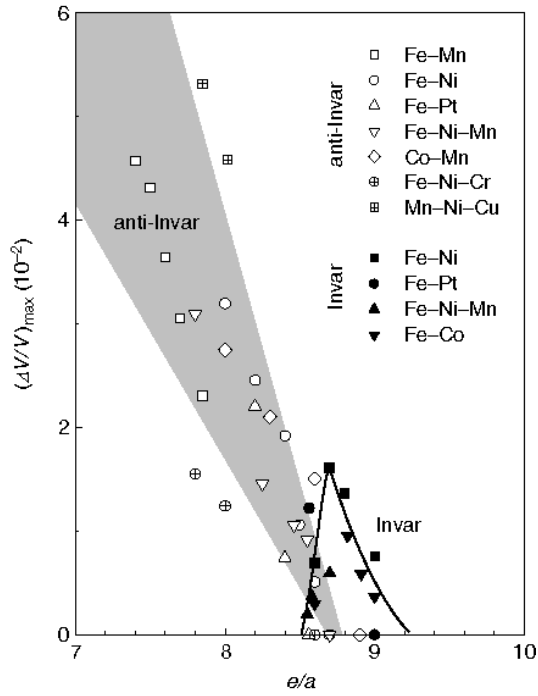

Fig. 10.6. Relative volume enhancement $(\Delta V/V)_{\max}$ as a function of the electron concentration per atom e/a for different Invar and anti-Invar alloys (see *symbols*)

at energies around the Fermi energy (see also below, Sect. 10.6), which can be interpreted in terms of the long debated high-spin (HS)–low-spin (LS) model, frequently used for the microscopic explanation of both, Invar and anti-Invar. Since the volume and temperature dependences of the total energy of pure iron already exhibit these HS–LS features, an understanding of elemental Fe is a prerequisite for the discussion of different Invar and anti-Invar (and also martensite) models. Iron will therefore be discussed in Sect. 10.4.

10.4 Allotropy of Pure Fe

Figure 10.7 shows the allotropy of elemental Fe in a plot of temperature vs. pressure. At atmospheric pressure, Fe solidifies in the bcc δ-phase and below 1665 K (A_4 point) structurally transforms on cooling, so that for 1184 K $<$ T $<$ 1665 K it has the fcc structure (γ-Fe). Yet, unexpected from entropic arguments, on further cooling below A_3, Fe does not become hexagonal close packed (hcp; ε-Fe), as one would also expect from its position in the periodic table (the elements Ru and Os below Fe in column VIII are hexagonal), but the bcc structure returns (α-Fe), and remains as the stable structure down to

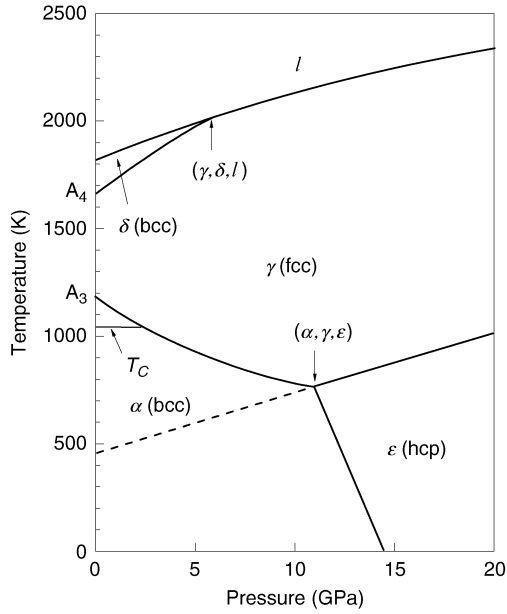

Fig. 10.7. Structural phase diagram of iron. For discussion see text

0 K. Thermodynamic considerations [19] show that the presence of strong FM correlations is a sufficient condition for the stability of the α-phase. Long range FM ordering, which occurs well below A_3 at the Curie-temperature $T_C = 1040$ K, is not a necessary condition. With respect to Invar and anti-Invar, the key feature of Fe is that the atomic volume of the high temperature fcc γ-phase is *smaller* than that of the low temperature bcc (α)-phase. Only ε-Fe occurring under high pressure is denser packed than γ-Fe, as the course of the γ–ε boundary line in Fig. 10.7 shows. If one extrapolates linearly this boundary line to zero pressure (dashed line), one obtains at ∼490 K the hypothetical γ–ε transition temperature, in the case that α-Fe were nonmagnetic (NM).

The allotropy of Fe can be understood from first principles ab initio band calculations [10–12], showing that magnetic coupling in the ground state of fcc Fe could be AF or FM depending on the volume, thereby also corroborating the 2γ-states model of Weiss [20]. In Fig. 10.8, we show a recent result [21] in plots of the total energy E (bottom panel) and the magnetic moment μ (top panel) vs. the atomic volume V_a for bcc, fcc, and hcp Fe.

In accordance with the phase diagram of Fig. 10.7, the most stable state, i.e., lowest in total energy, is the FM bcc ground state with the minimum at $V_a = 77.37$ a.u.^{3} (lattice constant $a = 2.84$ Å). This is about equal to the experimental value $V_a = 76.55$ a.u.^{3} ($a = 2.83$ Å). The bcc (FM) moment changes continuously with volume and has a value of about $\mu = 2.2\,\mu_B$ at equilibrium. Note that if the bcc state were NM, the total energy curve (not shown in Fig. 10.8) would have lied about 35 mRy higher than the bcc

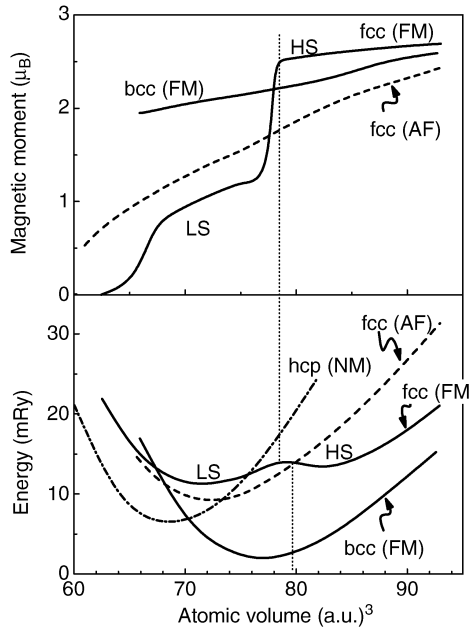

Fig. 10.8. Total energy and magnetic moment vs. volume at $T = 0\,\mathrm{K}$ of Fe in the bcc, fcc, and hcp structures [21]

state ($1\,\mathrm{mRy} = 150\,\mathrm{K}$), so that NM bcc Fe is never stable. The structure with the next highest energy is hcp (NM) (dashed-dotted), situated about 5 mRy above the bcc ground state. However, the minimum lies $\sim 10\,\mathrm{a.u.}^3$ lower in volume, so that this state can only be reached under high pressure, in agreement with Fig. 10.7. The next stable structure in Fig. 10.8 is fcc (AF) (dashed) with $\mu \sim 1.5\,\mu_\mathrm{B}$ at the equilibrium volume of $V_\mathrm{a} = 73\,\mathrm{a.u.}^3$ ($a = 3.51\,\mathrm{Å}$). The experimental values are $\mu \sim 0.7\,\mu_\mathrm{B}$ and $V_\mathrm{a} = 76.19\,\mathrm{a.u.}^3$ ($a = 3.56\,\mathrm{Å}$). This is the state with the small moment and small volume of fcc Fe – the LS state in the 2γ-states model of Weiss [20]. Energetically, this LS-state is 7.5 mRyd ($\sim$1125 K) above the bcc ground state, a value almost in quantitative agreement with $\mathrm{A}_3 = 1180\,\mathrm{K}$ in Fig. 10.7. If the volume of the fcc AF LS-state is enlarged, for $V > 80\,\mathrm{a.u.}^3$ ($a = 3.62\,\mathrm{Å}$), an fcc (FM) state is energetically favored. In agreement with the Weiss model [20], this is the FM HS state of γ-Fe with a magnetic moment of $\mu \sim 2.7\,\mu_\mathrm{B}$, a value close to $\mu = 2.8\,\mu_\mathrm{B}$ as extrapolated from the Slater–Pauling curve. An LS state solution also exists for the fcc (FM) curve having a minimum near the equilibrium volume of the AF solution with μ ranging between 0 and $1\,\mu_\mathrm{B}$, so that μ in the FM solution changes rapidly from small values to $2.7\,\mu_\mathrm{B}$. This is known as the moment–volume instability.

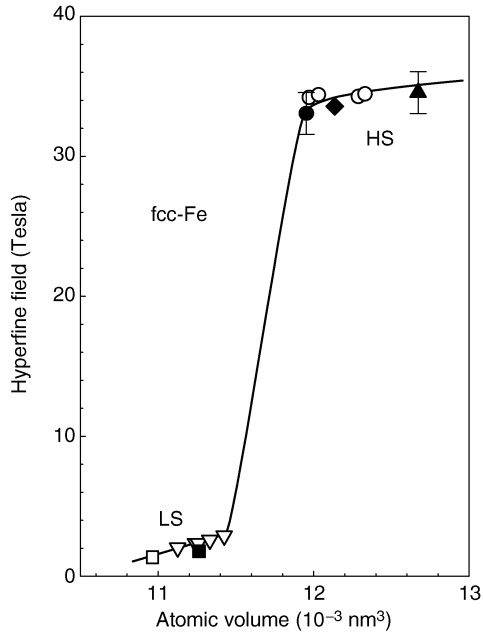

Fig. 10.9. Hyperfine field B_{hf} as a function of the atomic volume for fcc γ-Fe anti-Invar [22]. Data from Mössbauer experiments on epitaxial films grown on Cu (001) (*filled square*, *filled circle*), Cu_3Au (*filled triangle*), CuAu (*filled diamond*), and coherent precipitates in Cu–Al (*open down triangle*, *open square*)

The step-like behavior of the moment as a function of the atomic volume has been found experimentally for fcc Fe. Results are given in Fig. 10.9 showing the hyperfine field vs. the atomic volume from low temperature Mössbauer investigations on fcc Fe films epitaxially grown on substrates with different lattice constants: Cu(001) (filled square, filled circle), Cu_3Au (filled triangle), CuAu (filled diamond), and coherent precipitations of γ-Fe in Cu–Al alloys (open down triangle, open square) [22]. Since the hyperfine field is directly proportional to the magnetic moment, these data show in a convincing fashion the validity of the findings by Weiss [20]. We will demonstrate later (Sect. 10.6) that similar behavior can be detected in pressure experiments on Invar alloys.

10.5 Ground State Properties of Invar and Anti-Invar

Like for pure Fe, first principles ab initio band calculations of the total energy as a function of atomic volume, magnetic moment, and composition have given insight into the ground state properties of systems like Fe–Ni or Fe–Pt [10–12]. All important is that, independent of the system, the basic features in the total energy behavior are similar. In Fig. 10.10a–d, we give the results

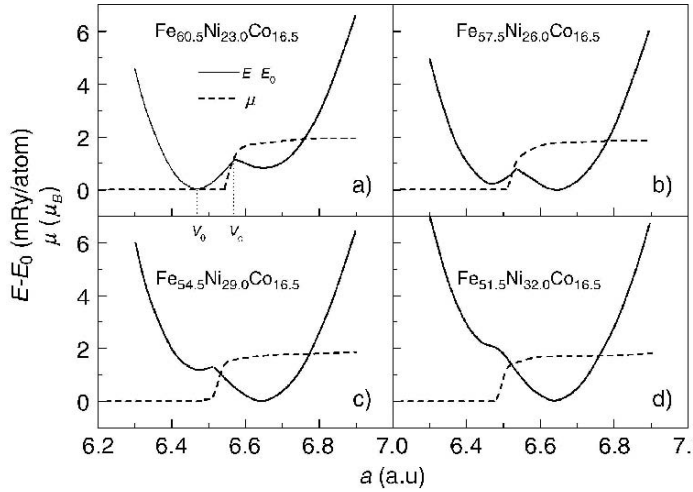

Fig. 10.10. Total energy E relative to a ground state energy E_0 (*full curves*), and magnetic moment (in μ_B/atom; *dashed*) as a function of the lattice constant (in atomic units a.u.) for fcc FM Fe–Ni–Co alloys with different compositions [23], showing anti-Invar properties in (**a**) and Invar in (**b**–**d**). For details see text

of the calculations for Fe–Ni–Co [23], a ternary system of technical importance, because it incorporates "Kovar" (composition around $Fe_{55}Ni_{29}Co_{16}$) and "Super-Invar" ($Fe_{64}Ni_{31}Co_5$), the alloy with the smallest known expansion coefficient of $\alpha = 0.2 \times 10^{-6}\,K^{-1}$ at room temperature. The plots in Fig. 10.10a–d give the total energy E (relative to the ground state energy E_0; full curves) and the magnetic moment μ (dashed curves) as a function of the lattice constant a (in a.u.) for four different compositions (Co content constant at 16.5 at%) in the transition range from anti-Invar (Fig. 10.10a; $e/a = 8.625$) to Invar (Fig. 10.10b–d; $8.685 \leq e/a \leq 8.805$). Typical for both anti-Invar and Invar is a "double well potential" in the total energy curve $E(a)$ and a "step-like" feature (moment–volume instability) in the magnetic moment. However, while in anti-Invar (Fig. 10.10a) the "anharmonicity" in $E(a)$ is found at *larger* volumes than the equilibrium value V_0, and this ground state is an NM state, in Invar (Fig. 10.10c–d), the "anharmonicity" occurs at *smaller* volumes than V_0. The ground state is always a HS state. The change from anti-Invar to Invar with increasing concentration e/a (cf. Fig. 10.6) at zero temperature is, therefore, characterized by a reversal of the transition from NM–HS in anti-Invar to HS–NM in Invar. The energetic difference $\Delta E = E_{NM} - E_{HS}$ is an almost linear function of e/a [11], changing sign around $e/a \sim 8.65$. The theoretical results in Fig. 10.10a–d almost agree with experiment. Only the anti-Invar behavior of the alloy in Fig. 10.10a is not very pronounced because of the occurrence of martensite [23].

The HS–NM transitions in $E(a)$ occur at saddle points (see dotted vertical lines in Fig. 10.10, where a third state, called the LS state with an intermediate value of the magnetic moment like in fcc Fe (cf. Fig. 10.8) might be involved. However, the presence of an LS state is not a necessary condition for the occurrence of Invar or anti-Invar behavior, a two level NM–HS scheme is sufficient. Moreover, for all Invar and anti-Invar alloys studied in ab initio calculations, the energetic differences between the HS and the LS or NM states turn out to be of the order of 1 mRy. It is thus tempting to assume that by raising the temperature, "excitations" – of whatever physical nature – from the large volume high moment ground state to the energetically elevated zero (or small) moment state at smaller volumes compensate the normal Grüneisen expansion and thus cause the Invar magnetovolume anomaly; and vice versa NM–HS transitions from small to large volumes cause anti-Invar. This scenario reminds us in many ways of the long standing widely debated 2γ-states (or HS–LS states) model of Weiss [20] introduced by him to understand fcc Fe and the Invar effect at finite temperatures in Fe–Ni (the vocabulary "anti-Invar" was not yet in use at that time).

10.6 Pressure Experiments: Evidence for High Spin to Low Spin State Transitions

While in anti-Invar a lattice expansion yields a step-like LS to HS state transition (see γ-Fe in Fig. 10.9), in Invar a lattice contraction with pressure should lead to the reverse, a HS to LS state transition. Abd-Elmeguid and Micklitz [24] were first to show in Mössbauer investigations under high pressure at 4.2 K that indeed such a behavior could be inferred from their results on ordered and disordered $Fe_{72}Pt_{28}$ as well as $Fe_{68.5}Ni_{31.5}$ Invar. Unfortunately, $Fe_{65}Ni_{35}$ cannot be investigated, because samples of this composition transform martensitically under pressure. For this reason, also recent investigations of the ac-susceptibility as a function of pressure and temperature were carried out on $Fe_{68.1}Ni_{31.9}$, also disordered $Fe_{72}Pt_{28}$ and $Fe_{70}Pt_{30}$, and $Fe_{66}Pd_{34}$ Invar alloys [25–27]. In Fig. 10.11a and b, we summarize all the data [24–27]. In Fig. 10.11a, the relative effective hyperfine fields $B_{\mathrm{eff}}(p)/B_{\mathrm{eff}}(0)$ and in Fig. 10.11b, the relative Curie temperatures are plotted as a function of the pressure with compositions as indicated in the figure. Especially in Fig. 10.11a, for ordered (filled triangle) and disordered (open triangle) $Fe_{72}Pt_{28}$ Invar, there is definitely a critical pressure necessary to induce a reduction of the magnetic moment. In $Fe_{66}Pd_{34}$ the moment even remains almost constant up to $p \sim 5$ GPa. There is also a change in slope in the $B_{\mathrm{eff}}(p)$ curves of all three Invar samples, $Fe_{68.5}Ni_{31.5}$ and $Fe_{72}Pt_{28}$ (ordered and disordered), with the tendency towards a second plateau at high pressures. This is, to some extent, supported by the plateaus occurring in the Curie-temperature curves $T_{\mathrm{C}}(p)$ in Fig. 10.11b. In disordered $Fe_{70}Pt_{30}$ (open square) and $Fe_{68.1}Ni_{31.9}$ (filled

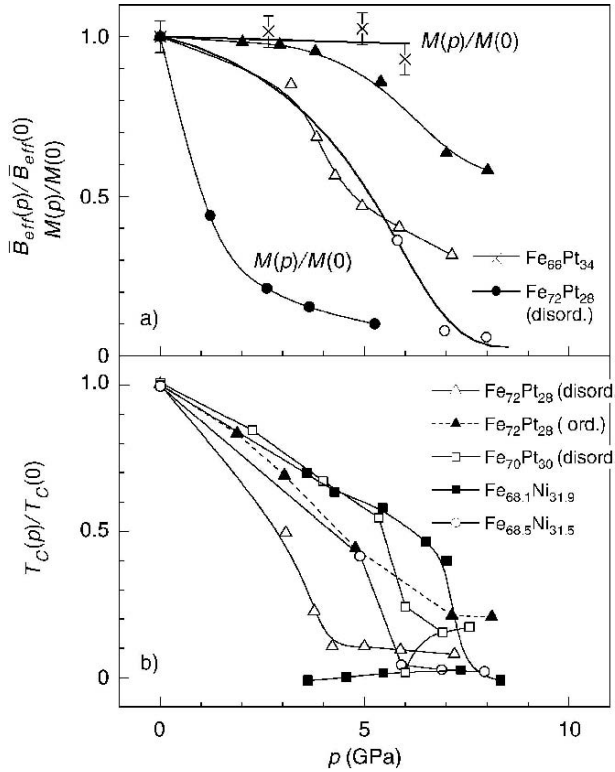

Fig. 10.11. (**a**) Normalized pressure dependence of the average effective hyperfine fields at 4.2 K, $B_{\rm eff}(p)/B_{\rm eff}(0)$ [24], and magnetization $M(p)/M(0)$ at room temperature [25]. (**b**) Normalized Curie-temperatures $T_{\rm C}(p)/T_{\rm C}(0)$ vs. pressure [24–27] for different Invar alloys as given indicated by various symbols

square), even AF components in a type of low magnetization reentrant spin glass state are found at high pressure. Though not in absolute clearness, all these data give strong support for the existence of HS and LS states and transitions within these states with pressure (at 4.2 K) in the sense of the model by Weiss [20]. Strong support for the Weiss hypothesis also stems from the pressure experiments by Odin et al. [28], who investigated $Fe_{72}Pt_{28}$ Invar at room temperature with X-ray Magnetic Circular Dichroism (XMCD) up to 20 GPa. The result for disordered Fe–Pt is shown in Fig. 10.12 in a plot of the relative XMCD signal vs. pressure. From these data, it is clear that on reduction of the volume with increasing pressure in disordered $Fe_{72}Pt_{28}$ Invar, there are two step-like transitions, from the initial HS state (admixed with LS states, as the authors claim) to a pure LS state and then to an NM state. This finding is in agreement with ab initio first principle calculations on Fe–Pt Invar by Podgorny [29]. However, it is to some extent in contradiction with the results of another group to what has been found on disordered $Fe_{72}Pt_{28}$

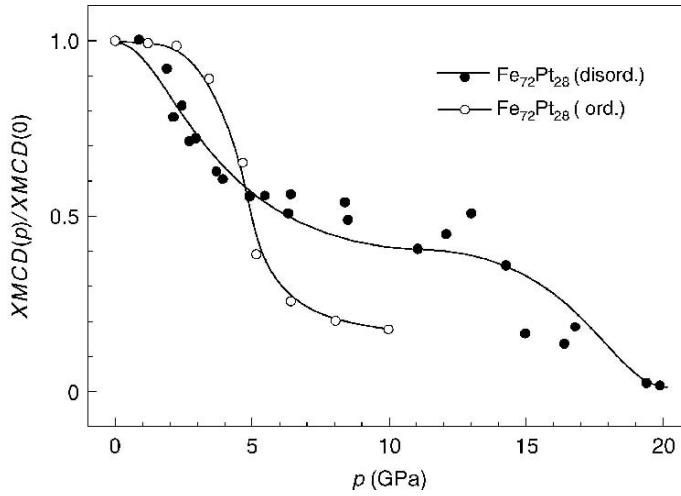

Fig. 10.12. Normalized X-ray magnetic circular dichroism signal, XMCD(p)/XMCD(0), vs. pressure as measured at room temperature for disordered $Fe_{72}Pt_{28}$ Invar [28]

Invar at room temperature in the pressure dependence of the magnetization (see Fig. 10.11a (filled circle)).

What are further *pros* and *cons* concerning the existence of different energetic "states" in the sense of Weiss [20] and the band structure results?

1. The calculations [10,11] predict the HS–LS (or NM) state transitions to be of first order. To some extent this is contradicted by the experiments, e.g., the temperature dependence of the specific heat or the magnetization [3–6] or the relatively smooth Invar to anti-Invar transition with composition (Fig. 10.6).
2. The LS state in Fe–Ni Invar in the Weiss model has AF order. AF order, however, is definitely not in play, neither in FM ordered $Fe_{72}Pt_{28}$ nor in FM cementite Fe_3C Invar. The existence of an AF LS state is not a necessary condition for the occurrence of Invar. This argument is in favor of some of the band calculations revealing HS and NM states without the presence of an LS state.
3. Models explaining specific "Invars" like Fe–Ni as a weak itinerant FM or Fe–Pt as a strong itinerant FM do not provide satisfactory solutions.
4. In this context, there has been a recent view claiming that the Invar behavior in the thermal expansion and the small bulk modulus B of $Fe_{65}Ni_{35}$ are associated with a noncollinear FM state, i.e., with canting of the moments [30, 31]. Canting, though earlier already introduced for γ-Fe and $Fe_{72}Pt_{28}$ Invar by Uhl et al. [32], in $Fe_{65}Ni_{35}$ Invar according to [24] led to a "wash-out" of the HS–LS features in the total energy, and to a smooth anharmonic $E(V)$ curve. In a recent neutron experiment with polarization

analysis by Cowlam and Wildes [33], it has been demonstrated, however, that $Fe_{65}Ni_{35}$ Invar alloys are collinear ferromagnets, supporting earlier inelastic polarized neutron scattering experiments of Lynn et al. [34], where there is no indication for the presence of noncollinearity. Furthermore, the presence of a clear discontinuity observed in the pressure dependence of the bulk modulus of $Fe_{64}Ni_{36}$ Invar in high pressure ultrasonic experiments [35] demonstrates that the HS–LS transition is more reliably explained in terms of the Weiss model rather than in terms of a smooth transition from a collinear to a noncollinear state.

5. The "softness" of Invar, i.e. the small bulk modulus as found experimentally [36] remains unexplained in the band calculations and is, thus, one of their main draw backs.

In general, there is ample experimental evidence for the existence of HS, LS, and NM states in anti-Invar and Invar materials. This provides the basis for the microscopic explanation of these effects as discussed in Sect 10.7.

10.7 HS–LS Transitions in a Microscopic Picture

A first idea not much recognized at its time of what could be the microscopic origin of the Invar effect was published in 1981 by Kaspar and Salahub [37]. From band structure calculations on fcc Fe–Ni clusters with different compositions, these authors predicted that in Invar, a charge transfer from antibonding (AB) majority to nonbonding (NB) minority electronic orbitals in the vicinity of the Fermi energy E_F could be the reason for the transition from a large volume, large moment HS state to a low volume, low moment LS state. This result was corroborated much later in calculations for ordered ($L1_2$) Fe_3Ni by Entel et al. [10]. These calculations revealed that in Invar, for large atomic volume in the HS state, there is a sharp peak in the majority density of states (DOS) just below E_F formed by electrons with $t_{2g\uparrow}$-symmetry (maximum charge density in [110] direction) and AB character. This peak faces a minimum in the DOS of the minority band at E_F formed by electrons with $e_{g\downarrow}$-symmetry (maximum charge densities in [100]-direction) and NB character. In the low volume LS state, the NB $e_{g\downarrow}$-minimum in the DOS remains at E_F, while the $t_{2g\uparrow}$-maximum shifts energetically to above E_F. Although introduction of structural disorder washes out the sharp peaks in the DOS [11], calculations for disordered Fe–Ni alloys [28] demonstrated that the important features survive. The results also demonstrated how the position of these DOS peaks relative to E_F varies as a function of composition, thus highlighting the differences in the DOS typical for Invar and anti-Invar when including the structural fcc to bcc transition even for martensite.

For a closer discussion of what to date is called the "$t_{2g\uparrow} \leftrightarrows e_{g\downarrow}$" scenario, we show in Fig. 10.13a and b examples of the electronic DOS [10, 11] typical

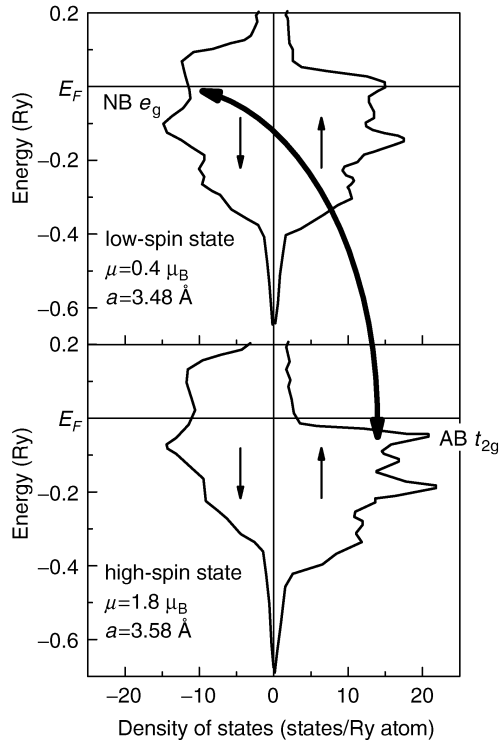

Fig. 10.13. Ab initio calculated electronic density of states for $Fe_{62.5}Ni_{37.5}$ in the high-spin and the low-spin state [10, 11]. The *arrow* indicates the $t_{2g\uparrow} \leftrightarrows e_{g\downarrow}$ transitions possibly taking place at finite temperatures

for a HS state (Fig. 10.13a) and LS (or NM) state (Fig. 10.13b). These DOS represent the ground state of Invar (Fig. 10.13a) and anti-Invar (Fig. 10.13b). The calculations [10,11] also revealed that in Fe_3Ni Invar, in a certain direction of the Brillouin zone at the equilibrium volume of the HS ground state, an AB $t_{2g\uparrow}$ spin band crosses with NB $e_{g\downarrow}$ bands right at E_F. Concerning the charge transfer as proposed by Kaspar and Salahub [37], the band calculations [10] revealed that at the critical volume V_c, where the HS to LS state transition takes place, there is a step in the occupation of levels, i.e. a charge transfer with a depopulation of the AB $t_{2g\uparrow}$ level at the expense of the NB $e_{g\downarrow}$ level when the volume is decreased. This AB $t_{2g\uparrow} \rightarrow$ NB $e_{g\downarrow}$ charge transfer causes the volume to shrink (Invar effect), because the internal electronic pressure favoring a large volume is reduced. The opposite, i.e., an NB $e_{g\downarrow} \rightarrow$ AB $t_{2g\uparrow}$ charge transfer, causes the pressure to rise and thus the volume to increase (anti-Invar effect).

Support for the validity of this $t_{2g\uparrow} \leftrightarrows e_{g\downarrow}$ scenario comes from various sources:

- First, within this picture, it is not necessary to differentiate between weak and strong itinerant FM Invar and to assume different and system specific physical reasons for the occurrence of Invar and anti-Invar behavior. The experimental systematics (cf. Fig. 10.6) demonstrating the continuous transition from Invar to anti-Invar with a variation of the electron concentration (e/a) is naturally explained by accompanying changes in the DOS features for *all* alloy systems.
- Second, the pressure experiments prove the existence of HS, LS and NM states, theoretically revealed in the ab initio ground state calculations. The experiments show that these states are even present at finite temperatures.
- Third, the $t_{2g\uparrow} \leftrightarrows e_{g\downarrow}$ scenario is corroborated by our [39] high temperature paramagnetic neutron scattering investigations on $Fe_{100-x}Ni_x$ alloys within the fcc stability range. Figure 10.14 shows the results in a plot of the magnetic moment μ_{norm} normalized to the value of fcc Fe given in [40] vs. the temperature T for compositions between $x = 35$ (Invar) through the anti-Invar range $(10 \leq x \leq 25)$ and to pure γ-Fe, for which we use earlier data from the literature [40]. Note that with increasing Fe concentration the slope of the curves in Fig. 10.14 changes its sign. While the

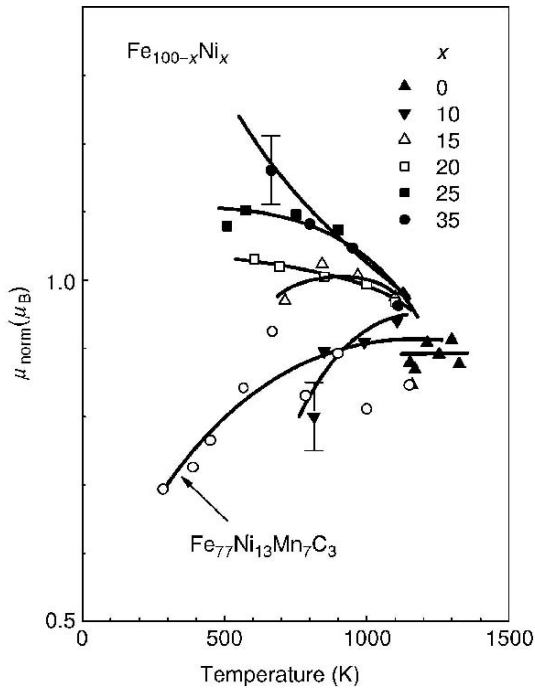

Fig. 10.14. Temperature dependence of the normalized magnetic moment as observed in Fe–Ni alloys in the paramagnetic range [39]

decrease of μ_{norm} with increasing T occurs in all FM materials, the *increase* of the average moment with temperature as observed for $Fe_{90}Ni_{10}$ and $Fe_{77}Ni_{13}Mn_7C_3$ anti-Invar is logically explained by an $e_{g\downarrow} \rightarrow t_{2g\uparrow}$ charge transfer. This enhances with rising temperature the DOS of the local band within the ferromagnetic short range correlations, thus enhancing the amplitude of the longitudinal FM spin fluctuations. This simultaneously supports the LS–HS transition picture.

- Fourth, we mention that recently, the zero thermal expansion of YbGaGe was found to be of electronic origin, a temperature-induced valence transition in the Yb atoms [41].

10.8 Questions and Outlook

The $t_{2g\uparrow} \leftrightarrows e_{g\downarrow}$ scenario as described has certain weaknesses and drawbacks raising doubts and further questions. On the one hand, recent polarized neutron experiments trying to find evidence for the $e_{g\downarrow} \leftrightarrows t_{2g\uparrow}$ charge transfer to take place with temperature in $Fe_{65}Ni_{35}$ [42] and ordered $Fe_{72}Pt_{28}$ [43, 44] Invar have not been successful. The changes in the e_g electron concentration in the temperature range from 100 to 600 K were found to be on the order of a percent in both systems, an amount probably not sufficient to explain the Invar effect on the basis of a charge transfer. On the other hand, these experiments for both alloys showed the existence of some additional excitation, a "forbidden" mode with the same dispersion as the $TA_1[110]$ phonon but with mixed phonon–magnon character. This could be what can be called the "elasto-magnon," the unknown HS to LS state excitation. Undoubtedly, it has been always one of the main drawbacks of the $t_{2g\uparrow} \leftrightarrows e_{g\downarrow}$ scenario that the explanation of the magnetovolume effects Invar and anti-Invar did not include phonons. Entel et al. [10] speculated about the electron–phonon coupling through the formation of a "pseudo-gap" pinning the $e_{g\downarrow}$-DOS minimum at the Fermi energy and holding it there when the temperature is increased. This has, however, not yet been confirmed experimentally.

Instead, theory revisited the disordered local moment (DLM) picture, which was earlier used to explain finite temperature properties of Fe–Ni alloys [45] and Invar [46]. Within this model, an originally binary alloy system such as $Fe_{100-x}Ni_x$ is turned into a pseudo ternary alloy by differentiating between Fe-spin up and Fe-spin down atoms, $(Fe_{1-c}\uparrow Fe_c\downarrow)_{100-x}Ni_x$, in a fashion that at $T = 0$ K, all spins are up ($c = 0$), while at $T = T_C$, 50% of the Fe-moments are pointing up and the other 50% point down ($c = 0.5$), which means that the magnetization has vanished [47]. Within this picture, a recent study [48] claims that the Invar effect and the "hidden" excitations are now understood, at least for disordered Fe–Pt Invar. For Fe–Ni alloys, where both types of atoms carry a moment, the LSD formalism is less straightforward. This led to the development of a magnetochemical model, in which the non-equilibrium local chemical order on an fcc Fe–Ni lattice gives rise to the Invar anomalies [49].

We think that as long as these models can neither explain the FM nature of the short range correlations found in the paramagnetic range in Fe–Ni Invar and anti-Invar [39] nor reveal the physical nature of the "elasto-magnons" [42–44] in a general picture for all Invar and anti-Invar type materials, more research from theoretical and experimental side is necessary to fully solve the "Invar problem," which is, concerning the time scale now, older than a century.

References

1. The physics and applications of invar alloys. In: Honda Memorial Series on Materials Science No. 3 (Marunzen, Tokyo 1978) p. 1
2. E.F. Wassermann: Invar, moment–volume-instabilities in transition metals and alloys. In: Ferromagnetic Materials, ed. by K.H.J. Buschow, E.P. Wohlfahrt, Vol. 5 (Elsevier, Amsterdam 1990) pp. 237–322
3. M. Shiga: Invar alloys. In: Materials Science and Technology, ed. by K.H.J. Buschow, E.P. Wohlfahrt, Vol. 3b (VCH, Weinheim 1994) pp. 159–210
4. G. Béranger et al. (Eds.): The Iron–Nickel Alloys (Lavoisier, Cachan, France, 1996)
5. J. Wittenauer (Ed.): The Invar Effect: A Centennial Symposium (TMS Society, Warrendale, PA, USA, 1997)
6. W. Pepperhoff, M. Acet: Constitution and Magnetism of Iron and its Alloys (Springer, Berlin Heidelberg New York 2001)
7. E.F. Wassermann, K. Usadel, D. Wagner (Eds.): Proceedings of the international symposium on magnetoelasticity ISOMES I (Duisburg, Germany, 1989) Physica B **161**, (1989)
8. E.F. Wassermann, M. Acet, P. Entel, W. Pepperhoff: J. Magn. Soc. Jpn. **23**, 385 (1999)
9. E.F. Wassermann (Ed.): Proceedings of the international symposium on magnetoelasticity ISOMES II (Duisburg, Germany, 1998), Philos. Mag. B **80**, (2000)
10. P. Entel, E. Hoffmann, P. Mohn, K. Schwarz, V.L. Moruzzi: Phys. Rev. B **47**, 8706 (1993)
11. M. Schroeter, H. Ebert, H. Akai, P. Entel, E. Hoffmann, G.G. Reddy: Phys. Rev. B **52**, 188 (1995)
12. H. Herper, E. Hoffmann, P. Entel: Phys. Rev. B **60**, 3839 (1999)
13. J. van Lier: Thesis, Universitaet Duisburg, Fak. IV (2002)
14. B. Rellinghaus, J. Kaestner, T. Schneider, E.F. Wassermann, P. Mohn: Phys. Rev. B **51**, 2983 (1995)
15. T. Schneider, M. Acet, B. Rellinghaus, E.F. Wassermann, W. Pepperhoff: Phys. Rev. B **51**, 8917 (1995)
16. M. Acet, H. Zaehres, E.F. Wassermann, W. Pepperhoff: Phys. Rev. B **49**, 6012 (1994)
17. M. Acet, T. Roessel, E.F. Wassermann, K.H. Andersen, J. Kulda, A.P. Murani, A. Wildes: J. Phys. Soc. Jpn. **69** (Suppl. A), 108 (2000)
18. M.E. Gruner, P. Entel: Comp. Mater. Sci. **10**, 230 (1998)
19. M. Acet, H. Herper, P. Entel, E.F. Wassermann: J. Phys. IV **11**, Pr8 (2001)
20. R.J. Weiss: Proc. Phys. Soc. London **82**, 281 (1963)

21. P. Entel, H. Herper, M. Schroeter, E. Hoffmann, K. Kadau, R. Meyer, in: Displacive Phase Transformations, ed. by K. Inoue, K. Mukharjee, K. Ohtsuka, H. Chen (The Minerals, Metals & Materials Society, 1998)
22. T. Shinjo, W. Keune: J. Mag. Magn. Mater. **200**, 598 (2000)
23. B. Gehrmann: Thesis, University of Duisburg, Fak. IV (1999)
24. M.M. Abd-Elmeguid, H. Micklitz: Physica B **161**, 17 (1989); Phys. Rev. B **40**, 7395 (1989)
25. M. Matsushita, T. Nishimura, S. Endo, M. Ishizuka, F. Ono: J. Phys.: Condens. Matter **14**, 10 753 (2002)
26. M. Matsushita, S. Endo, K. Miura, F. Ono: J. Mag. Magn. Mater. **260**, 371 (2003)
27. M. Matsushita, S. Endo, K. Miura, F. Ono: J. Mag. Magn. Mater. **265**, 352 (2003)
28. S. Odin, F. Baudelet, J.P. Itie, A. Polian, S. Pizzini, A. Fontaine, C. Giorgetti, E. Dartyge, J.P. Kappler: J. Appl. Phys. **83**, 7291 (1998)
29. M. Podgorny: Physica B **161**, 105 (1989)
30. M. van Schilfgaarde, I.A. Abrikosov, B. Johansson: Nature **400**, 46 (1999)
31. P. Mohn: Nature **400**, 18 (1999)
32. M. Uhl, L.M. Sandratskii, J. Kuebler: Phys. Rev. B **50**, 291 (1994)
33. N. Cowlam, A.R. Wildes: J. Phys.: Condens. Matter **15**, 521 (2003)
34. J.W. Lynn, N. Rosov, M. Acet, H. Bach: J. Appl. Phys. **75**, 60 069 (1994)
35. F. Decremps, L. Nataf: Phys. Rev. Lett. **92**, 157 204-1 (2004)
36. L. Mañosa, G.A. Saunders, H. Rahdi, U. Kawald, J. Pelzl, H. Bach: J. Phys.: Condens. Matter **3**, 2273 (1991)
37. J. Kaspar, D.R. Salahub: Phys. Rev. Lett. **47**, 54 (1981)
38. P. Entel, H.C. Herper, E. Hoffmann, G. Nepecks, E.F. Wassermann, M. Acet, V. Crisan, H. Akai: Phil. Mag. B **80**, 141 (2000)
39. M. Acet, E.F. Wassermann, K. Andersen, A. Murani, O. Schärpff: Europhys. Lett. **40**, 93 (1997)
40. P.J. Brown, I. Jassim, K.U. Neumann, K.R.A. Ziebeck: Physica B **16**, 9 (1989)
41. J.R. Salvador, F. Guo, T. Hogan, M.G. Kanatzidis: Nature **425**, 702 (2003)
42. P.J. Brown, K.U. Neumann, K.R.A. Ziebeck: J. Phys.: Condens. Matter **13**, 1563 (2001)
43. P.J. Brown, T. Kanomata, M. Matsumoto, K.U. Neumann, K.R.A. Ziebeck: J. Mag. Magn. Mater. **242–245**, 781 (2002)
44. P.J. Brown, T. Chaterji, J. Kaestner, K.R.A. Ziebeck: J. Phys.: Condens. Matter **16**, 5349 (2004)
45. H. Akai, P.H. Dederichs: Phys. Rev. B **47**, 8739 (1993)
46. D.D. Johnson, W.A. Shelton, in: The Invar Effect: A Centennial Symposium, ed. by J. Wittenauer (TMS Society, Warrendale, PA, USA, 1997) p. 63
47. S. Khmelevskyi, P. Mohn: Phys. Rev. B **68**, 214 412 (2003)
48. S. Khmelevskyi, I. Turek, P. Mohn: Phys. Rev. Lett. **91**, 037 201-1 (2003)
49. V. Crisan, P. Entel, H. Ebert, H. Akai, D.D. Johnson, J.B. Staunton: Phys. Rev. B **66**, 014 416 (2002)

11

Magnetocaloric Effect Associated with Magnetostructural Transitions

V.K. Pecharsky and K.A. Gschneidner, Jr.

11.1 Introduction

The discovery of the giant magnetocaloric effect in $Gd_5(Si_{4-x}Ge_x)$ in 1997 stimulated a considerable growth of research in order to both find new materials where the effect is just as potent and to understand the role magnetostructural transitions play in its enhancement. Results obtained to date indicate that the coupling between magnetic and crystal lattices is critical in achieving strong magnetothermal responses in weak magnetic fields and that advanced magnetocaloric materials should exist in solids where structural changes are linked to ferromagnetic ordering and disordering, and therefore, can be triggered by a magnetic field.

11.2 Magnetic Cooling or Why Having a Strong Magnetocaloric Effect in a Weak Magnetic Field Makes a Difference?

Magnetic cooling has a potential to reduce global energy consumption and eliminate or minimize the need for ozone depleting and greenhouse chemicals. It may soon become an alternative to vapor-compression technology. Instead of a working fluid undergoing a liquid–vapor transition in a conventional cooling system, a magnetic refrigerator (see Fig. 11.1) employs a solid, which heats up when magnetized and cools down when demagnetized. Originally measured in iron and reported by Warburg in 1881 [1], these magnetic field-induced temperature variations are known today as the magnetocaloric effect (MCE). Intrinsic to every magnetic solid, the MCE has exceptional fundamental importance because it bridges length, energy and time scales spanning over many orders of magnitude: from quantum mechanics to micromagnetics, from statistical to macroscopic thermodynamics and from spin dynamics to heat transfer [2–11].

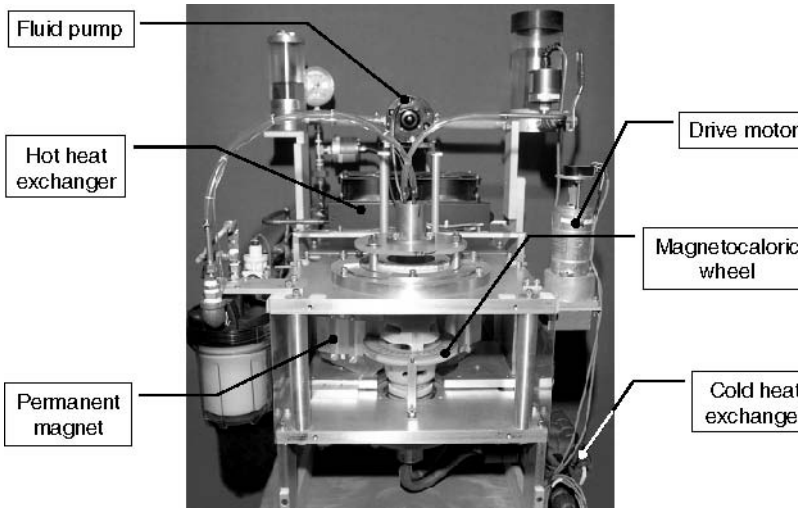

Fig. 11.1. Laboratory prototype magnetic refrigerator designed and constructed by the Astronautics Corporation of America in 2001 [18]. A ∼1.5 T magnetic field around the magnetocaloric wheel filled with Gd spheres is produced by a permanent magnet. The refrigerator operates at ambient conditions with a maximum temperature span of ∼20°C and maximum cooling power of 95 W. The photograph is courtesy of the Astronautics Corporation of America, 4115 N. Teutonia Avenue, Milwaukee, WI 53209

In addition to its role in basic science, the magnetocaloric effect has a substantial practical potential since its extent is one of the most critical parameters defining the performance of a magnetic refrigerator – the stronger the MCE, the higher the efficiency of the device all other things being equal [11–19]. As is often the case with emerging technologies, numerous applications of magnetic refrigeration may stem from a reliable foundation formed by advanced materials. For example, the availability of low-cost high-performance solids exhibiting enhanced MCE between ∼250 and ∼350 K is an important requirement in order to facilitate commercialization of magnetic refrigeration for a variety of consumer uses – from home appliances to climate control in motor vehicles. Also, when suitable magnetocaloric compounds supporting continuous magnetic cooling from ∼300 to ∼20 K are developed, the energy penalty incurred during hydrogen liquefaction using the conventional gas-compression approach may no longer be a limiting factor preventing the widespread use of liquid hydrogen fuel in transportation. The list of materials capable of satisfying future magnetocaloric requirements is, however, limited and if a solid is needed with a certain MCE to meet a set of specific constraints that lie beyond our current state of knowledge, one often relies on an accidental discovery rather than on design guided by a rational theory.

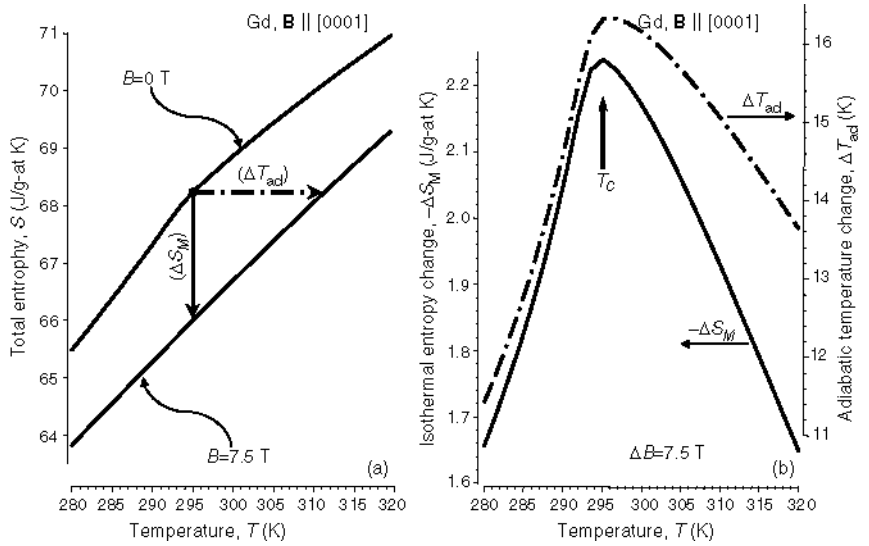

Fig. 11.2. The total entropy in zero and 7.5 T magnetic fields (**a**) and the magnetocaloric effect of the elemental Gd in the vicinity of its Curie temperature, T_{C}, for a magnetic field change from 0 to 7.5 T (**b**). The data are for a high purity single crystalline Gd with the magnetic field vector parallel to the [0001] crystallographic direction of the specimen

As illustrated in Fig. 11.2, the magnetocaloric effect can be expressed as either or both the isothermal entropy change, ΔS_{M} (an extensive quantity) or the adiabatic temperature change, ΔT_{ad} (an intensive parameter). For a given material at constant pressure, the two quantities are functions of absolute temperature (T) and magnetic field change ($\Delta B = B_{\mathrm{f}} - B_{\mathrm{i}}$), where B_{f} and B_{i} are the final and initial magnetic fields, respectively. The MCE can be easily computed (see [16, 20] and Fig. 11.2a) provided the behavior of the total entropy (S) of a compound is known as a function of temperature in both the initial and final magnetic fields

$$\Delta S_{\mathrm{M}}(T, \Delta B)_{\Delta B = B_{\mathrm{f}} - B_{\mathrm{i}}} = S(T, B)_{B = B_{\mathrm{f}}} - S(T, B)_{B = B_{\mathrm{i}}} \,, \tag{11.1}$$

$$\Delta T_{\mathrm{ad}}(T, \Delta B)_{\Delta B = B_{\mathrm{f}} - B_{\mathrm{i}}} = T(S, B)_{B = B_{\mathrm{f}}} - T(S, B)_{B = B_{\mathrm{i}}} \,. \tag{11.2}$$

Equation (11.2) is also straightforwardly employed in direct measurements of ΔT_{ad} [21–23]. At equilibrium, both ΔS_{M} and ΔT_{ad} are correlated with magnetization (M), magnetic flux density (B), heat capacity at constant pressure (C), and absolute temperature by one of the following fundamental

relationships [24]:

$$\Delta S_{\mathrm{M}}(T, \Delta B)_{\Delta B = B_{\mathrm{f}} - B_{\mathrm{i}}} = \int_{B_{\mathrm{i}}}^{B_{\mathrm{f}}} \left(\frac{\partial M(T, B)}{\partial T} \right)_B \mathrm{d}B \,, \tag{11.3}$$

$$\Delta T_{\mathrm{ad}}(T, \Delta B)_{\Delta B = B_{\mathrm{f}} - B_{\mathrm{i}}} = - \int_{B_{\mathrm{i}}}^{B_{\mathrm{f}}} \left(\frac{T}{C(T, B)} \times \frac{\partial M(T, B)}{\partial T} \right)_B \mathrm{d}B \,. \tag{11.4}$$

As immediately follows from (11.1) to (11.4), materials whose total entropy is sharply influenced by a magnetic field and where magnetization changes rapidly with temperature, are expected to exhibit enhanced MCE. The latter peaks when $|(\partial M(T, B)/\partial T)_B|$ is the greatest, i.e., around the Curie temperature (T_{C}) in a conventional ferromagnet or near the absolute zero temperature in a paramagnet. The MCE usually decreases both below and above the T_{C}, as clearly seen in Fig. 11.2b.

To amplify the MCE, conventional wisdom calls for increasing the magnetic field change in addition to maximizing both the derivative, $|(\partial M(T, B)/\partial T)_B|$, and the region of magnetic fields and temperatures where the magnetization remains highly sensitive to temperature. Considering the current state-of-the-art in permanent magnet materials, however, it is quite unlikely that magnetic fields in excess of about 2 T will become common in a foreseeable future. That is why maximizing the MCE by manipulating one or several most critical parameters of a compound appears to be the most realistic option in order to reach the strongest possible MCE's in readily available magnetic fields. Although it remains a formidable challenge for basic science, a better understanding, and therefore, the ability to control a variety of chemical, structural, and physical degrees of freedom that define the properties of complex solids may improve the existing materials and should eventually result in novel compounds exhibiting large magnetocaloric effects.

11.3 $Gd_5(Si_{4-x}Ge_x)$ System and the Giant Magnetocaloric Effect

The use of the term "giant" referring to the "magnetocaloric effect" can be traced back to 1973 [25], yet the phenomenon was not given much consideration before 1997 when Pecharsky and Gschneidner [26–28] observed the unusually potent MCE in $Gd_5(Si_2Ge_2)$ and other $Gd_5(Si_{4-x}Ge_x)$ alloys with $x \geq 2$, Fig. 11.3.

Between 1973 and 1997, there were a few accounts of a strong MCE, the most notable examples were FeRh [31, 32], $(Hf_{0.83}Ta_{0.17})Fe_{2\pm x}$ [33], and $(La_{1-x}Ca_x)MnO_3$ [34]. The larger than average MCE's reported before 1997 were primarily attributed to magnetic field induced transformations involving two magnetic states: low magnetic field antiferromagnetic and high magnetic field ferromagnetic (e.g., FeRh), or to large phase volume changes

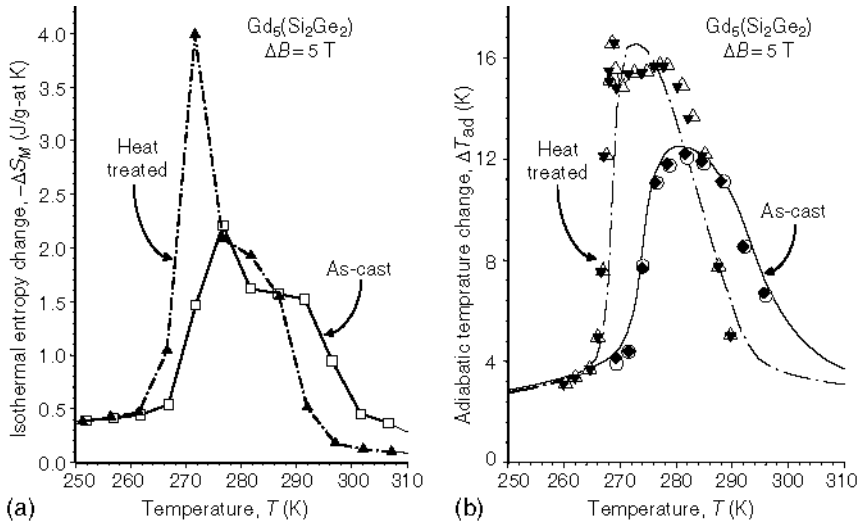

Fig. 11.3. The giant MCE of $Gd_5(Si_2Ge_2)$ in the as-prepared and annealed (1570 K, 1 h) states: (**a**) $-\Delta S_M$ calculated from magnetization data using Eq. (11.3) [29]; (**b**) $-\Delta T_{ad}$ calculated from heat capacity data using Eq. (11.2) (*lines*) and measured directly during increasing (*solid symbols*) and decreasing (*open symbols*) magnetic fields [30]

($La_{1-x}Ca_xMnO_3$). In addition to a tendency for irreversibility of the effect in FeRh, this and other systems available before 1997 were not flexible enough to enable easy tuning of the temperature range where the enhanced MCE was observed. Consequently, there was much uncertainty whether or not these materials could be used in a practical magnetic refrigerator in future.

The R_5T_4 compounds (R = rare earth metal and T = Si and/or Ge) have been known since 1966 [35–37]. For the next 30 years, they received little attention despite a striking observation made by Holtzberg et al. [37] that instead of the expected reduction of the Curie temperature of the elemental Gd ($T_C = 293$ K), the ferromagnetic ordering temperature of the intermetallic compound Gd_5Si_4, in which nearly half of magnetic Gd atoms have been replaced with nonmagnetic Si atoms, was increased by 43 K to $T_C = 336$ K. Among several other features noted by Holtzberg et al. [37], the following two were quite unusual: (i) the closely structurally related germanide, Gd_5Ge_4, orders antiferromagnetically at $T_N = 15$ K, while its paramagnetic Curie temperature ($\theta_p = 94$ K) was large and positive and (ii) upon substitution of Si for its electronic twin Ge in the pseudobinary $Gd_5(Si_{4-x}Ge_x)$ system, no continuous solubility was observed, instead, a new phase emerges for x between 2 and 2.8.

Studies performed 30 years later [38–40] indicated that the room temperature crystal structures of Gd_5Si_4 and Gd_5Ge_4 are different, yet they are intimately related to one another. The major difference is in the interactions

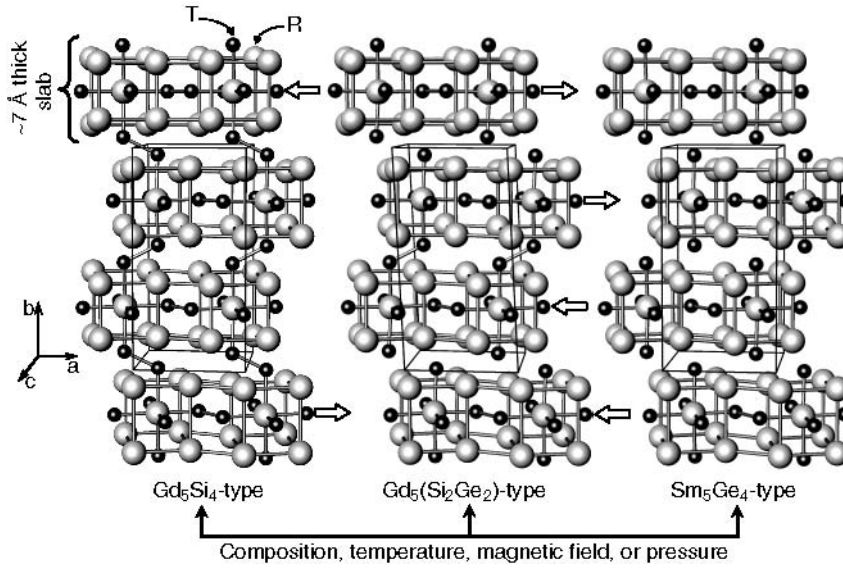

Fig. 11.4. Crystallography of the Gd_5T_4 system: the Gd_5Si_4-type where all slabs are linked via T–T bonds (the bonding distances shown as T–T dumbbells are ∼2.5 Å); the $Gd_5(Si_2Ge_2)$-type with the slabs connected into pairs, i.e., with half of the interslab T–T bonds broken; and the Sm_5Ge_4-type where no interslab T–T bonds exist. The interslab T–T distances increase from the bonding ∼2.5 Å to nonbonding ∼3.5 Å as the slabs slide by ∼0.2 to ∼0.4 Å in the directions indicated by short open arrows. To date, the $Gd_5(Si_2Ge_2)$-type ↔ Sm_5Ge_4-type transitions have been induced only by varying composition; the other two transformations can be triggered by any one or a combination of the listed thermodynamic variables

between the well-defined subnanometer-thick layers (or two-dimensional slabs) of tightly bound atoms as illustrated in Fig. 11.4. From $x = 0$ to $x \cong 2$, $Gd_5(Si_{4-x}Ge_x)$ alloys maintain orthorhombic Gd_5Si_4-type structure at room temperature [38]. When Ge concentration exceeds that of Si, half of the interslab T–T bonds break and monoclinic $Gd_5(Si_2Ge_2)$-type structure becomes stable at room temperature for x from ∼1.9 to ∼2.5 [38, 41]. Further increasing the Ge concentration eliminates all interslab T–T bonds and a different orthorhombic structure (Sm_5Ge_4-type) emerges at room temperature when $2.8 \leq x \leq 4$ [38, 42].

Soon after the original reports on the giant MCE of $Gd_5(Si_2Ge_2)$, Morellon et al. [43, 44] showed that a transition from the $Gd_5(Si_2Ge_2)$-type structure to the Gd_5Si_4-type structure coincides with the temperature-induced ferromagnetic ordering of the $Gd_5(Si_{4-x}Ge_x)$ alloy with $x = 2.2$. A number of studies that followed [39, 40, 45–53] confirmed that ferromagnetically ordered $Gd_5(Si_{4-x}Ge_x)$ alloys always adopt the Gd_5Si_4-type structure, while both the magnetically disordered and antiferromagnetically ordered compounds may exist in any of the three structure types illustrated in Fig. 11.4.

Although diffraction studies were only performed as functions of temperature in zero magnetic fields [39, 43, 45, 47, 52], thermal expansion and magnetostriction data measured as functions of temperature, magnetic field, and/or pressure [43, 49, 50, 53], were taken as indications that the same structural transition can be triggered by either or both magnetic field and pressure in addition to temperature (see Fig. 11.4). Hence, the existence of the giant magnetocaloric effect in $Gd_5(Si_{4-x}Ge_x)$ alloys has been implicitly related to the coupling of magnetic and crystallographic sublattices in these materials.

It is worth noting that the coupled magnetostructural transitions in the Gd_5T_4 system are thermodynamically first-order transformations, and therefore, the behavior of the MCE as a function of temperature is expected to be different from that illustrated in Fig. 11.2. We refer the reader to the analysis presented by Pecharsky et al. [54], although by comparing Fig. 11.2b with Fig. 11.3 it is easy to see that regardless of the differences in the magnetic field values and apart from sharp spikes[1] observed in the behavior of ΔS_M, the maximum MCE in $Gd_5(Si_2Ge_2)$ extends over a broader temperature range but then falls off more quickly when compared to the same in Gd. As ΔB increases, the temperature range over which the MCE remains large and nearly constant in first-order phase transition materials also increases, while the magnitude of the maximum magnetocaloric effect is affected to a much lesser degree [54].

As we noted above, the discovery of the giant magnetocaloric effect in $Gd_5(Si_{4-x}Ge_x)$ alloys catalyzed further research. As a result, several different families of materials have been recently reported to also exhibit the giant MCE. These include: a host of colossal magnetoresistive manganites (e.g., [17, 55]), MnAs and $MnAs_{1-x}Sb_x$ [56],[2] $MnFe(P_{1-x}As_x)$ [59], and $La(Fe_{13-x}Si_x)$ [60] compounds.[2] Changes of the magnetic structures in these materials are coupled with modifications of the crystal lattices. In manganites, crystallographic symmetry often varies similarly to that observed during the $Gd_5(Si_2Ge_2)$-type to the Gd_5Si_4-type transition, while in MnAs, $MnFe(P_{1-x}As_x)$, and $La(Fe_{13-x}Si_x)$, only unit cell volumes are altered. The latter, though comparable to the Sm_5Ge_4-type $\leftrightarrow$ Gd_5Si_4-type transition observed in Ge-rich Gd_5T_4 materials, is notably different because a martensitic-like structural transformation accompanies the unit cell volume changes without affecting symmetry in the $Gd_5(Si_{4-x}Ge_x)$ system (see Fig. 11.4 and [38, 40]). Reminiscent of R_5T_4 systems, structural changes in other materials exhibiting the giant MCE are normally assumed to be

[1] Spikes observed in Fig. 11.3a are experimental artifacts likely originating from a combination of data collection and processing errors, the greatest being numerical integration of magnetization data measured with finite temperature and magnetic field steps.

[2] We note that both the MCE and temperature-induced polymorphism in MnAs were reported as far back as 1958 [57]. Similarly to R_5T_4 materials, the $La(Fe_{13-x}Si_x)$ phases are known since 1968 [58], i.e., long before their magnetocaloric properties were measured.

triggered by a magnetic field as deduced from the combination of temperature-dependent zero magnetic field diffraction data and temperature- and magnetic field-dependent measurements of bulk physical properties, such as thermal expansion and/or magnetostriction.

The $Gd_5(Si_{4-x}Ge_x)$ system remains the most studied to date, both with respect to its magnetocaloric effect and understanding the interplay between structure, magnetic, and thermodynamic properties of these materials. Therefore, below we will concentrate on several different Gd_5T_4 stoichiometries in order to illustrate the role structural transitions play in enhancing the MCE in low magnetic fields. We will examine how the magnetic field alters the crystal structure of these materials, which by itself is an intriguing phenomenon that is not nearly as common as temperature or pressure induced polymorphism, and also evaluate the relative contributions from both crystallographic and magnetic phase changes into the appearance of the giant magnetocaloric effect in the $Gd_5(Si_{4-x}Ge_x)$ system.

11.4 Altering Crystal Structures with a Magnetic Field

One of the most interesting compounds in the $Gd_5(Si_{4-x}Ge_x)$ system is the germanide, Gd_5Ge_4. According to a variety of experimental data [38, 53, 61–68], it orders antiferromagnetically at $T_N \cong 130\,K$ and in low magnetic fields, the antiferromagnetic ground state is preserved down to 1.8 K. When Gd_5Ge_4 is exposed to a magnetic field exceeding ~1 T, however, a ferromagnetic state can be induced irreversibly below 10 K, partly reversibly between 10 and 20 K and fully reversibly above 20 K. Critical magnetic field, B_C, needed to induce the ferromagnetic state behaves differently in different temperature regions. Below 10 K it increases as temperature decreases; above 20 K, B_C rises with the increasing temperature, and the critical magnetic field remains constant from ~10 to ~20 K [65].

As shown recently by Pecharsky et al. [63], magnetism of Gd_5Ge_4 is closely related to its crystallography. As long as the compound remains antiferromagnetic, it maintains the Sm_5Ge_4-type structure and only lattice parameters of the material (see Fig. 11.5) are anisotropically reduced upon cooling from 300 to 5 K in a zero magnetic field. Between ~90 and 300 K, all unit cell dimensions vary nearly linearly with the following coefficients of linear thermal expansion: 6.90×10^{-6}, 1.18×10^{-5}, and $1.03 \times 10^{-5}\,K^{-1}$ along the *a*-, *b*-, and *c*-axis, respectively [69]. These values are in agreement with $\alpha_l = (dl/dT)/l = 1.03 \times 10^{-5}\,K^{-1}$ in the same temperature range as determined dilatometrically using polycrystalline Gd_5Ge_4 [53, 64, 70]. We note that along the *a*-axis, i.e., parallel to the direction along which the slabs slide during a structural change (see Fig. 11.4), thermal expansion is considerably smaller than that along either the *b*- or *c*-axis. The volumetric thermal expansion between ~90 and 300 K varies with $\alpha_V = (dV/dT)/V = 2.91 \times 10^{-5}\,K^{-1}$. Thermal expansion along the *a*-axis becomes nearly negligible below ~100 K,

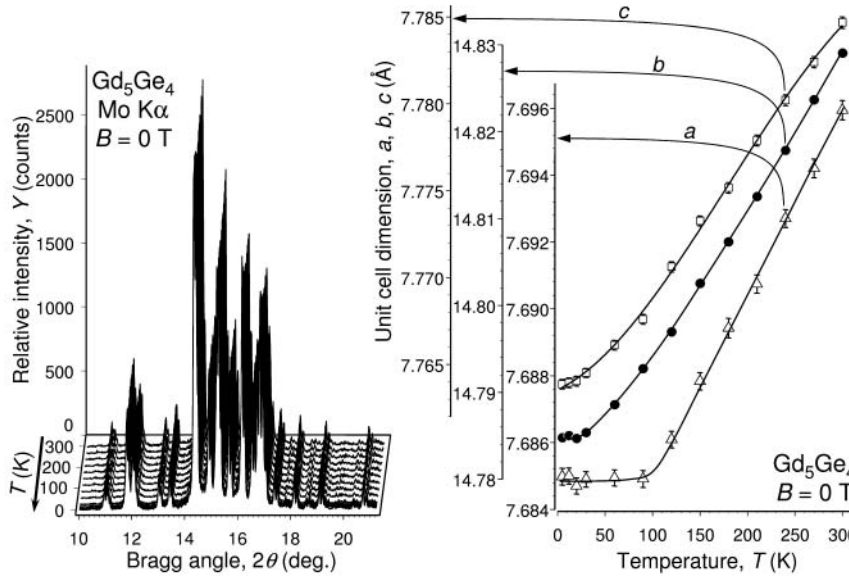

Fig. 11.5. Fragments of X-ray powder diffraction data of Gd_5Ge_4 collected using Mo Kα radiation during cooling from 300 to 5 K in a zero magnetic field (*left*) and temperature dependencies of the unit cell dimensions determined from X-ray powder diffraction data (*right*). The lines drawn through the data points on the right are guides to the eye

while it approaches zero only below ∼30 K along the other two principal crystallographic directions. No obvious anomalies of thermal expansion have been detected around the Néel temperature, $T_N =$ ∼130 K.

A magnetic field has a profound effect on the crystal structure of Gd_5Ge_4, as evidenced by the X-ray powder diffraction data depicted in Figs. 11.6 and 11.7. Isothermal exposure to an increasing magnetic field at 6.1 K results in a structural transition that begins around 1.5 T and is nearly complete at 2.5 T. The magnetic field-induced structural transition in Gd_5Ge_4 is irreversible at this temperature, as can be concluded from the powder patterns that barely change when the magnetic field is removed (Fig. 11.6).

Thus, after magnetizing and subsequent demagnetizing, Gd_5Ge_4 retains its high magnetic field crystal structure. When the magnetic field is cycled at this temperature again, the crystal structure of Gd_5Ge_4 remains unaffected, which is consistent with a variety of bulk physical property measurements, including magnetization [62, 64], electrical resistivity [61], thermal expansion [64], and magnetostriction [53]. Dependence of the Gd_5Ge_4 crystal structure on magnetic field is different from the above behavior when the magnetic field is cycled isothermally at 25 K. Just as at 6.1 K, the low magnetic field crystal structure transforms into the high magnetic field polymorph between 1.5 and 2.5 T (Fig. 11.7). But when the magnetic field is reduced at 25 K, the structural transformation becomes reversible and the zero magnetic field

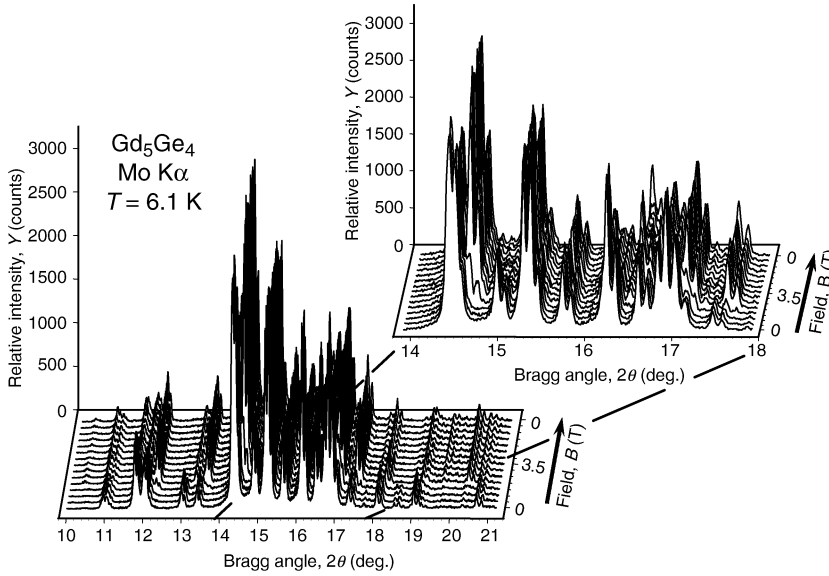

Fig. 11.6. Fragments of the X-ray powder diffraction patterns of Gd_5Ge_4 collected at 6.1 K with the magnetic field varying from 0 to 3.5 T and then back to 0 with a 0.5 T step

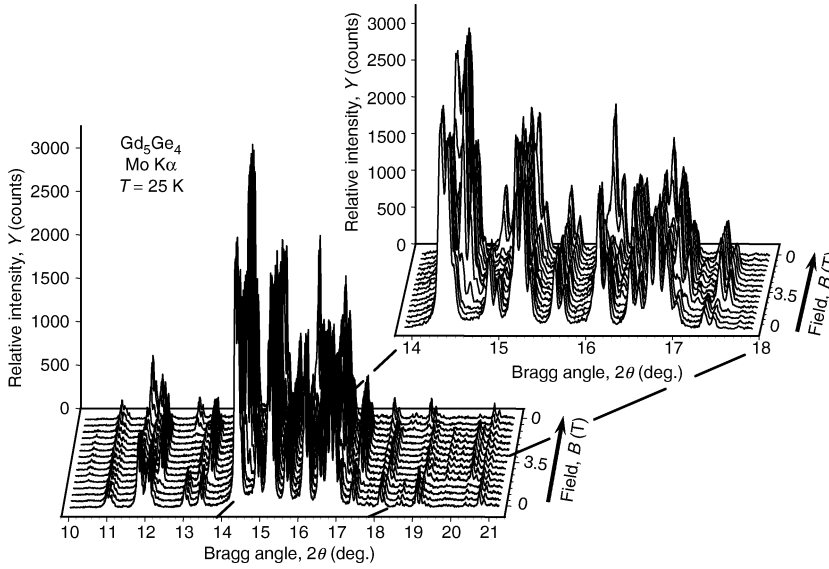

Fig. 11.7. Fragments of the X-ray powder diffraction patterns of Gd_5Ge_4 collected at 25 K with the magnetic field varying from 0 to 3.5 T and then back to 0 with a 0.5 T step

diffraction patterns are restored between 1.5 and 0.5 T (Fig. 11.7), displaying a ∼1 T hysteresis.

As follows from the results of the structure determination using powder diffraction data [63], the low magnetic field crystal structures of Gd_5Ge_4 observed at 6.1 and 25 K are identical to one another within the accuracy of the technique, and so are the high magnetic field polymorphs. The low field Gd_5Ge_4 adopts the Sm_5Ge_4-type structure, which is transformed into the Gd_5Si_4-type (see Fig. 11.4) by the magnetic field. The two crystal structures are related to one another via shear displacements of the neighboring layers by more than 0.2 Å each. These large shifts in opposite directions alter numerous interatomic distances (Fig. 11.8), and therefore, interactions among atoms from adjacent layers. The most prominent magnetic field induced change occurs in the interlayer Ge–Ge bonds. In the low field-Gd_5Ge_4 – the corresponding interatomic distances are $\delta_{Ge-Ge} = 3.62(1)$ Å – the bonds are weak but in the high field-Gd_5Ge_4, where $\delta_{Ge-Ge} = 2.62(1)$ Å, they become much stronger due to a 1 Å contraction. Despite substantial differences between the two structures, the layers themselves undergo little change, as evidenced by small variation of the interatomic distances inside each layer (see [63, 67], and Fig. 11.8).

The magnetic field, therefore, triggers a martensitic-like structural transition, which results in the breaking (in low magnetic fields) and the reforming (in high magnetic fields) of the covalent-like interlayer Ge–Ge bonds. This structural change is practically identical to that induced by the varying

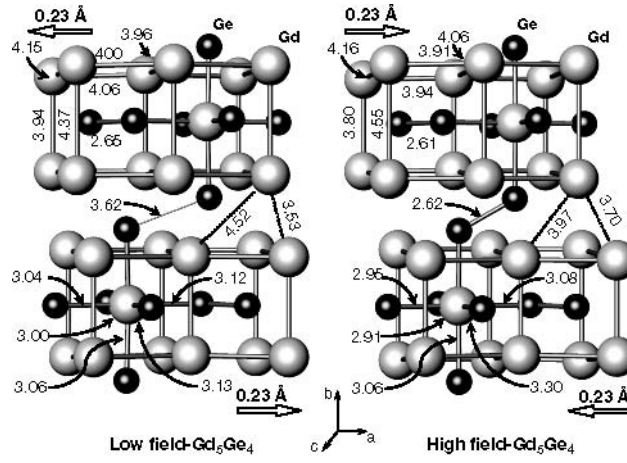

Fig. 11.8. Fragments of the low field (antiferromagnetic) and high field (ferromagnetic) crystal structures of Gd_5Ge_4 with selected distances labeled in Å (after [63]). The intraslab distances vary by a maximum of ∼5%, while the interslab distances change up to ∼28% during the transformation. The *open arrows* indicate the directions and the magnitudes of the shifts of the slabs during the respective transitions (from low to high field and vice versa)

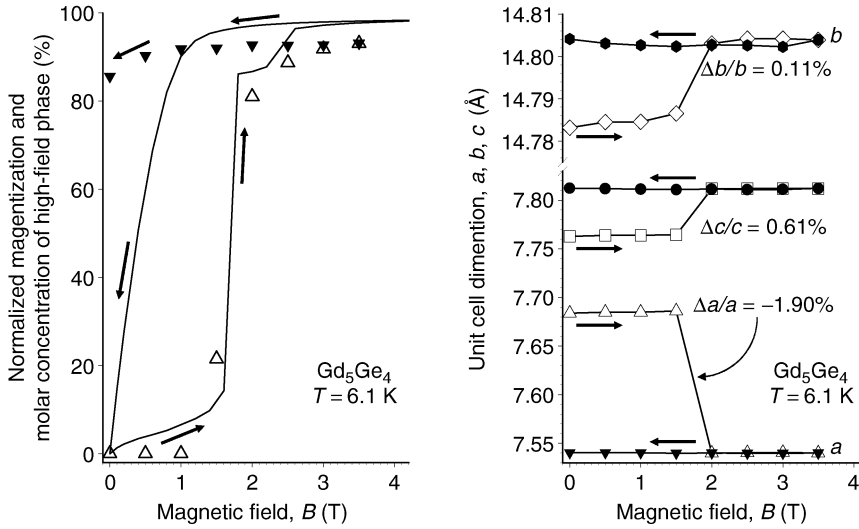

Fig. 11.9. *Left* – normalized magnetization (*lines*) and concentration of the high field Gd_5Ge_4 structure (*symbols*) [63]; *right* – unit cell dimensions of the majority phase at 6.1 K [69]. Short straight arrows indicate the direction of the magnetic field change

stoichiometry in the $Gd_5(Si_{4-x}Ge_x)$ system, i.e., when x decreases from $x = 4$ to $x = 0$ and the large germanium atoms are substituted with the smaller Si atoms. Hence, the application of the magnetic field in the case of Gd_5Ge_4 resembles chemical pressure effect when the phase volume, and consequently, interatomic distances are systematically reduced by chemical substitutions.

The irreversibility and reversibility of the magnetic field induced structural transition in Gd_5Ge_4 closely follows the irreversible and reversible behavior of the magnetization and the underlying magnetic structure changes of the compound. As illustrated in Fig. 11.9 (left), the fraction of the high field-Gd_5Ge_4 structure formed at 6.1 K by an increasing magnetic field follows the initial magnetization path. Upon removal of the magnetic field isothermally, Gd_5Ge_4 remains ferromagnetic at 6.1 K [62, 64]. Consistently with macroscopic magnetism, the system preserves the high magnetic field-Gd_5Ge_4 structure, which is ferromagnetic, and whose concentration is only slightly reduced from ∼93% to ∼86% when the magnetic field is lowered isothermally from 3.5 T to 0.

At 25 K, where the ferromagnetic–paramagnetic transformation becomes reversible, both the initial magnetization and the subsequent demagnetization paths are followed with high precision by the amount of the high magnetic field Gd_5Ge_4 structure formed in the specimen, see Fig. 11.10 (left). It is worth noting that no more than 93 mol. % of the sample has been transformed from the low magnetic field Gd_5Ge_4 to the high magnetic field Gd_5Ge_4 structure by a 3.5 T field at either temperature, even though at this magnetic field the

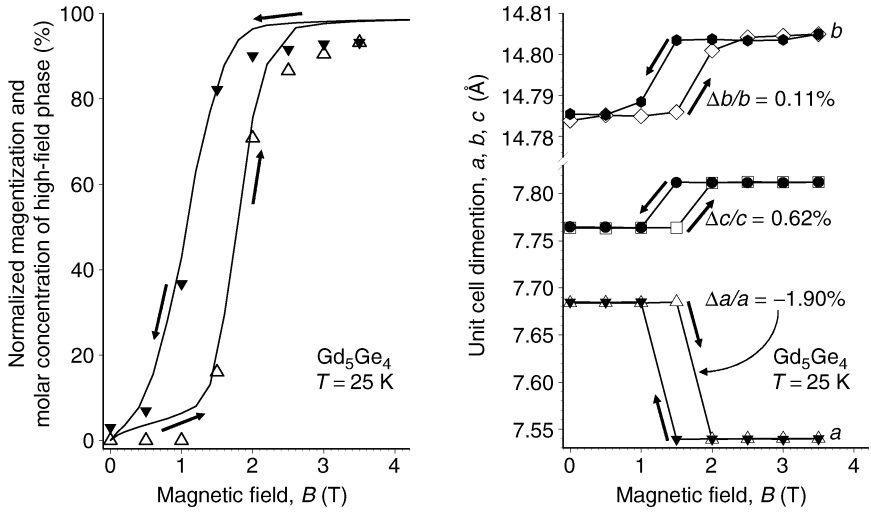

Fig. 11.10. *Left* – normalized magnetization (*lines*) and concentration of the high field Gd_5Ge_4 structure (*symbols*) [63]; *right* – unit cell dimensions of the majority phase at 25 K [69]. Short straight arrows indicate the direction of the magnetic field change

magnetization is at ∼99% of its saturation value of 7.5 μ_B/Gd atom, indicating a nearly complete collinearity of the spin structure.

The effect of the magnetic field on the crystal structure of Gd_5Ge_4 is, therefore, different from the effect of temperature on the crystal structures of the related $Gd_5Si_2Ge_2$ and $Gd_5Si_{0.4}Ge_{3.6}$ phases. In the latter two systems, the respective temperature induced structural transitions are complete [39,45], yet a small but measurable fraction of Gd_5Ge_4 retains its low field crystal structure while clearly ordering ferromagnetically. Even in a 3.5 T magnetic field, the crystallites of the ferromagnetic low field-Gd_5Ge_4 (Sm_5Ge_4-type) remain large enough to be discernible in the powder diffraction data.

As shown by Holm et al. [67], when Gd_5Ge_4 is magnetized and subsequently demagnetized at 15 K, i.e., where the antiferromagnetic–ferromagnetic transformation is partially reversible [53, 61, 62, 65], the structural transformation between the Sm_5Ge_4- (low magnetic field) and Gd_5Si_4-types (high magnetic field) of crystal structure is also partially reversible. Thus, 48 mol% of the Gd_5Ge_4 sample retains the high magnetic field crystal structure, while 52 mol% reversibly transforms into the low magnetic field polymorph after magnetizing and demagnetizing at 15 K [67]. According to Tang et al. [65], 49 mol% of the specimen retains the ferromagnetic state after magnetizing and demagnetizing at 15 K, while 51 mol% of the zero magnetic field antiferromagnetic state is recovered. The agreement between bulk magnetization and X-ray diffraction measurements, which were carried out independently, is excellent.

Our primary concern here is the role of magnetostructural transitions in the appearance of the giant magnetocaloric effect, yet we should also emphasize the significant variations of the unit cell dimensions of Gd_5Ge_4, and therefore, predictable magnetic field induced shape changes of the material in either a single crystalline or in a textured polycrystalline states. The magnitude of the forced magnetostriction along the [100] direction places Gd_5Ge_4 and other members of the R_5T_4 family prominently among the so-called ferromagnetic shape memory alloys – materials in which considerable shape changes can be controlled by a varying magnetic field. As seen in Fig. 11.10 (right), the a-axis of Gd_5Ge_4 reversibly contracts and expands by an enormous 1.9% (19,000 parts per million) upon, respectively, magnetizing and demagnetizing the material. For comparison, the largest magnetic field induced shape changes known today are those observed in stressed Ni_2MnGa single crystals [71,72]. Up to 6% (theoretical) strains in Ni_2MnGa that could be induced by the application of a magnetic field along the [001] direction, occur as a result of rearranging twin variants in a ferromagnetically distorted Heusler-type cubic structure. This rearrangement, which aligns the easy magnetization directions of all twin components with the external magnetic field vector, is however, not a true magnetic field-induced crystallographic phase transformation, as is the case in the R_5T_4 materials.

The ability of the magnetic field to induce a structural change in a material where spin–orbit contributions are negligible (Gd is an S-state ion), can be related to the coupling of the localized magnetic moments of the Gd atoms with the external magnetic field. The latter reverses the sign of magnetic exchange interactions and induces a metamagnetic transformation of the antiferromagnetic Gd_5Ge_4 (negative exchange parameter) into the ferromagnetically ordered system (positive exchange parameter). The increasing magnetic field causes a spin flip and the resulting collinear or nearly collinear spin system minimizes its free energy via a martensitic magnetic field-induced structural transition from the low field-Gd_5Ge_4 to the high field-Gd_5Ge_4 structures. The sample remains both structurally [63,67] and magnetically [61–65] inhomogeneous in a certain range of magnetic fields because the transition is magnetoelastic. Hence, work performed by the magnetic field to increase bulk magnetization is balanced by work required to overcome strain created by a 1.1% change of the phase volume. Since magnetic work ($B\,\mathrm{d}M$) becomes negligible near saturation as $\mathrm{d}M$ approaches zero but strain remains considerable, this may explain the presence of a small amount of the ferromagnetic low field-Gd_5Ge_4 structure in a nearly completely magnetically saturated sample.

The magnetocaloric effect of Gd_5Ge_4, calculated from magnetization data employing (11.3), is shown in Fig. 11.11. The isothermal magnetic entropy change of a virgin sample, i.e., when the material is in the antiferromagnetic state before the application of a magnetic field, is negligible as long as the field remains lower than the $\sim$1 T needed to induce the magnetostructural transition in Gd_5Ge_4. When B_f is 2 T and higher (B_i is 0 in all cases), the MCE rapidly increases in magnitude and extends towards the higher temperatures with increasing ΔB, consistent with the values of magnetic field

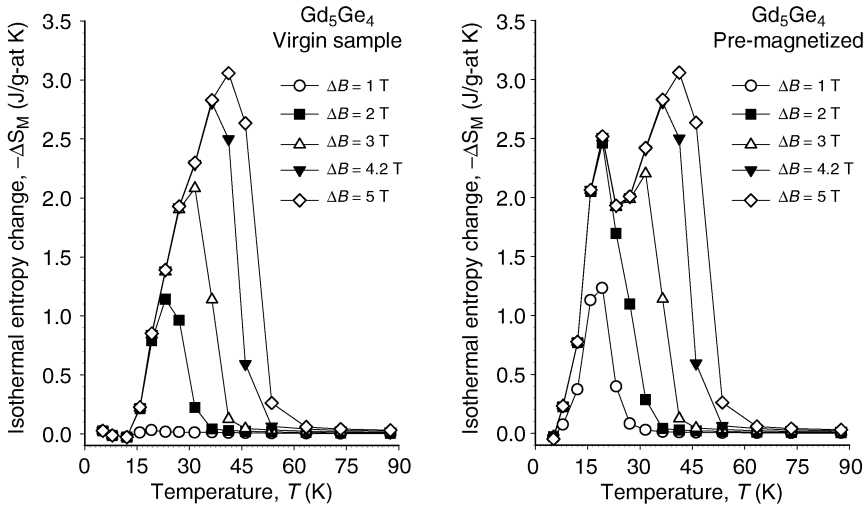

Fig. 11.11. The MCE of Gd_5Ge_4 calculated using (11.3). The plot on the left is obtained from $M(H)_{T=\text{const}}$ data measured during magnetizing a sample cooled in zero magnetic field from ∼150 K to each measurement temperature. The plot on the right is for $M(H)_{T=\text{const}}$ data measured after the same sample was magnetized by a 5 T field and then demagnetized

that are required to complete the magnetostructural transition in the compound [53, 61, 63, 65]. Conversely, when the sample was pre-magnetized by a 5 T magnetic field (the field, which is strong enough to induce the ferromagnetic state and complete the transformation below ∼30 K), an additional contribution to the MCE in the form of ΔS_M peak centered around 17 K becomes clearly visible. Except for this additional contribution, the MCE in the pre-magnetized Gd_5Ge_4 remains identical to that of the virgin sample.

The behavior of the low temperature ΔS_M peak in the pre-magnetized Gd_5Ge_4 sample is consistent with that of a conventional ferromagnet, while the high-temperature component of ΔS_M behaves as expected for a first-order phase transition material. Although quite unusual for a Gd-based compound, the dependence of the magnetocaloric effect on the magnetic history of the sample is in agreement with the existence of the ferromagnetic Gd_5Si_4-type structure induced either irreversibly (below ∼10 K) or partially reversibly (between ∼10 and ∼20 K) by a magnetic field.

Recently, Holm et al. [69] showed that magnetic field also triggers a structural transformation in $Gd_5(Si_{1.7}Ge_{2.3})$, which is another member of the same family of materials as Gd_5Ge_4, except that the former compound has the monoclinic $Gd_5(Si_2Ge_2)$-type crystal structure at room temperature. In the past, the structural transition to the orthorhombic Gd_5Si_4-type structure from the room temperature monoclinic phase of the $Gd_5(Si_{4-x}Ge_x)$ system was assumed from temperature dependent X-ray diffraction data [39,43] and from the magnetic field dependent physical property measurements

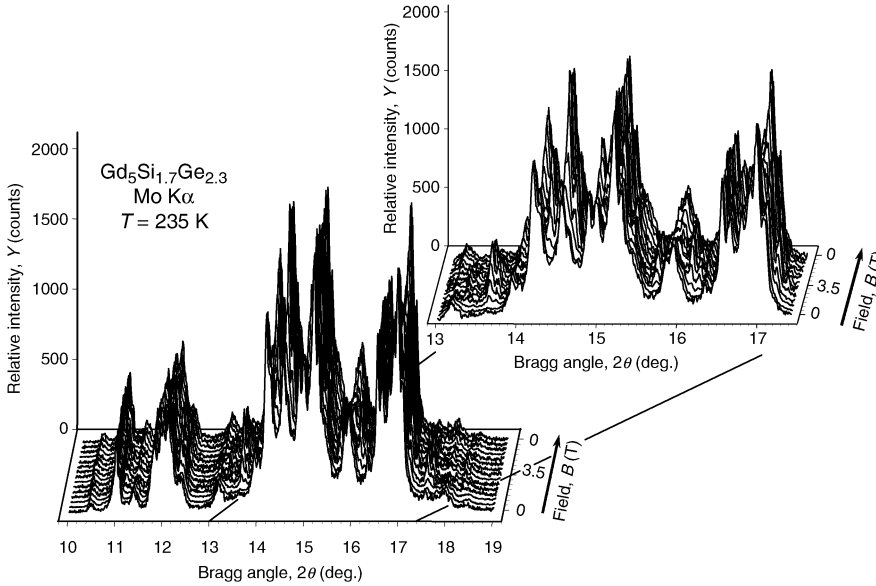

Fig. 11.12. Fragments of the X-ray powder diffraction patterns of $Gd_5(Si_{1.7}Ge_{2.3})$ collected at 235 K with the magnetic field varying from 0 to 3.5 T and then back to 0 with a 0.5 T step

(e.g., see [40,43]). As illustrated in Fig. 11.12, in situ X-ray powder diffraction demonstrates that when a $Gd_5(Si_{1.7}Ge_{2.3})$ sample is magnetized at $T = 235$ K, a structural transformation begins around 1.5 T and is nearly complete at 2.5 T. Upon subsequent isothermal demagnetization, the low magnetic field crystal structure begins to emerge at $\sim$1.5 T and the reverse transformation is complete at 0.5 T. Similar behavior is observed in $Gd_5(Si_{1.7}Ge_{2.3})$ at other temperatures above its zero magnetic field T_C. According to Holm et al. [69], the high magnetic field crystal structure of $Gd_5(Si_{1.7}Ge_{2.3})$ is identical to the high magnetic field crystal structure of Gd_5Ge_4. In other words, both ferromagnetically ordered materials belong to the Gd_5Si_4-type, in which all interslab T–T bonds are present. This result also confirms that the high magnetic field polymorphs are the same as the low temperature zero magnetic field crystal structures of materials in this phase region of the $Gd_5(Si_{4-x}Ge_x)$ system.

11.5 To What Extent a Structural Change Enhances the Giant Magnetocaloric Effect?

In the previous section, we provided sufficient evidence that in the $Gd_5(Si_{4-x}Ge_x)$ system, a martensitic-like structural transition follows ferromagnetic ordering/disordering when $x \gtrsim 2$ and that both the magnetic and crystallographic changes can be reversibly triggered by a magnetic field at

ambient pressure. Although magnetic field-induced polymorphism apparently occurs in other giant magnetocaloric effect systems, such as the manganites [55], the $Gd_5(Si_{4-x}Ge_x)$ alloys are unique because they enable one to obtain further insights on the role the structural transition plays in the enhancement of the magnetocaloric effect. This is especially true because alloys that have nearly identical stoichiometry, and therefore, closely spaced Curie temperatures around $x = 2$, can be prepared in two different crystal structures in the paramagnetic state [38, 41, 42]. When x is less than 1.91 [38], the paramagnetic $Gd_5(Si_{4-x}Ge_x)$ alloys crystallize in the Gd_5Si_4-type and their crystal structures are preserved when they become ferromagnetic. As a result, the magnetic ordering in these materials occurs via a second-order phase transformation, i.e., $Gd_5(Si_{4-x}Ge_x)$ alloys with $x < 1.91$ exhibit a conventional magnetocaloric effect, e.g., see Fig. 11.2. When x is 1.91 or greater, the paramagnetic $Gd_5(Si_{4-x}Ge_x)$ phases adopt the $Gd_5(Si_2Ge_2)$-type structure and they order ferromagnetically concurrently with a structural change to the Gd_5Si_4-type structure (Fig. 11.12), which results in a first-order paramagnetic to ferromagnetic transformation and the giant magnetocaloric effect, see Figs. 11.3 and 11.11.

Taking into consideration this difference in the thermodynamic nature of phase transitions occurring in closely related intermetallic phases, in Fig. 11.13 we illustrate the behavior of the total entropies of $Gd_5(Si_{2.5}Ge_{1.5})$ and $Gd_5(Si_2Ge_2)$ in a zero magnetic field.[3] The former orders ferromagnetically in a conventional (second-order) fashion at $T_C \cong 312\,K$, while the latter undergoes a first-order magnetostructural transition at $T_C \cong 270\,K$. Since the Curie temperatures of two materials are slightly different, all data in Fig. 11.13 are plotted as functions of the normalized temperature, $T - T_{tr}$, where T_{tr} is taken just above T_C as the temperature at which the magnetostructural transformation in $Gd_5(Si_2Ge_2)$ is complete. For clarity, the total entropy functions of $Gd_5(Si_{2.5}Ge_{1.5})$ were also normalized by subtracting a constant value of $\sim 5.5\,J\,g\text{-}at^{-1}\,K^{-1}$ to match the total zero magnetic field entropy of $Gd_5(Si_2Ge_2)$ just below the magnetostructural transition.

As expected from the similarity of the chemical compositions, identical crystallography and ferromagnetism, the total entropy functions of the two materials after normalization show nearly indistinguishable behavior in a zero magnetic field immediately below their respective Curie temperatures.

[3] When $x \cong 2$, either the monoclinic $Gd_5(Si_2Ge_2)$-type or the orthorhombic Gd_5Si_4-type structures can be retained in the paramagnetic state at constant x by heat treating $Gd_5(Si_{4-x}Ge_x)$ alloys at different temperatures [48, 51]. As we showed recently [73], it is conceivable, however, that the Gd_5Si_4-type structure in the paramagnetic state can be stabilized by oxygen as a result of heat treatment. Considering the martensitic-like mechanism of the structural transition (see Figs. 11.4 and 11.8) and the potential effect of oxygen, apparently located inside specific interslab voids [73], on the occurrence of the transformation, we will base our analysis on materials with close though different x but low and nearly the same amount of interstitial impurities, rather than on materials with the same x but different and usually uncontrolled impurity contents.

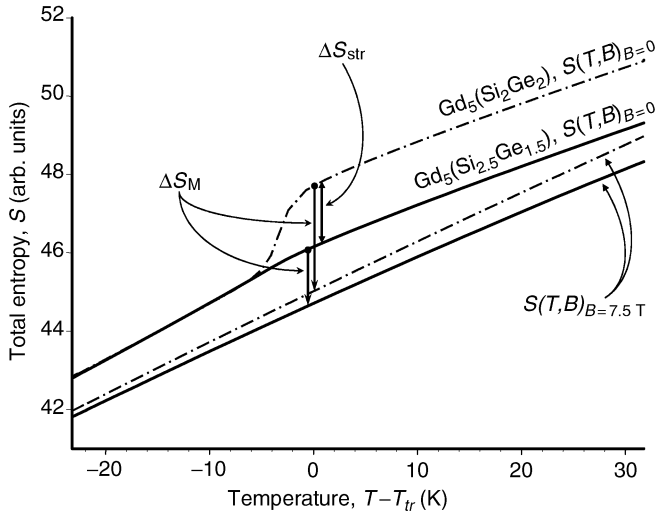

Fig. 11.13. The behavior of the total entropies of $Gd_5(Si_{2.5}Ge_{1.5})$, where ferromagnetic ordering at T_C is a second-order phase transformation (*solid lines*), and of $Gd_5(Si_2Ge_2)$ where ferromagnetic ordering is a first-order phase transformation (*dash-dotted lines*) in the vicinities of their respective Curie temperatures in 0 and 7.5 T magnetic fields. The three vertical arrows around T_{tr} indicate the magnitudes of the magnetocaloric effects of $Gd_5(Si_{2.5}Ge_{1.5})$ and $Gd_5(Si_2Ge_2)$, and entropy of the first-order phase transition in $Gd_5(Si_2Ge_2)$, all at $T = T_{tr}$

A major deviation occurs in the vicinity of T_C, where the entropy of $Gd_5(Si_2Ge_2)$ is increased by $\Delta S_{str} = \Delta H_{str}/T_{tr}$, ($\Delta H_{str}$ is enthalpy or latent heat of a first-order phase transformation). It is worth noting that in theory, the total entropy is expected to undergo a discontinuous change by ΔS_{str} at T_C, but in reality, this change occurs over a few Kelvin wide temperature range. As is easy to see from Fig. 11.13, the two zero magnetic field entropy functions continue to behave very similarly above the T_C, in fact, the difference between them remains nearly constant and equal to ΔS_{str}. Once again, we relate this similarity in the behavior of the two entropies to close relationships between crystallography and magnetism of these two compounds.

The total entropies of the two materials after the application of the magnetic field do not match as well as the zero magnetic field entropies do, as also clearly seen in Fig. 11.13. This mismatch can be related to different effects of the magnetic field on conventional ferromagnets, which $Gd_5(Si_{2.5}Ge_{1.5})$ is, when compared to $Gd_5(Si_2Ge_2)$, which is the system with a first-order magnetic-martensitic phase change. In fact, since the crystal structure is not coupled to a magnetic sublattice in the case of $Gd_5(Si_{2.5}Ge_{1.5})$, the magnetic field does not actually transform the system into a nearly collinear ferromagnet, nor does it raise the Curie temperature of the material.

Conversely, in the case of $Gd_5(Si_2Ge_2)$, where the magnetic field induces a magnetostructural phase change, the Curie temperature is increased nearly linearly with field [26]. Furthermore, the conventional ferromagnetic ordering of the orthorhombic paramagnetic $Gd_5(Si_2Ge_2)$ would occur at a much higher temperature than a conventional ferromagnetic ordering of the monoclinic paramagnetic $Gd_5(Si_2Ge_2)$ provided the latter crystal lattice can co-exist with a ferromagnetic sublattice [51]. This difference in Curie temperatures of the two structures nearly completely eliminates spin fluctuations and magnetic clustering in the case of $Gd_5(Si_2Ge_2)$, while both should be present in $Gd_5(Si_{2.5}Ge_{1.5})$.

The magnetocaloric effects at T_C are shown in Fig. 11.13 as arrows for both materials (the arrows are offset along the temperature axis for clarity). Obviously, the two MCE's are considerably different and the difference between them must be ascribed to the absence and the presence of a structural change in $Gd_5(Si_{2.5}Ge_{1.5})$ and $Gd_5(Si_2Ge_2)$, respectively. Even though the magnetic field has slightly different effect on the total entropies of the two compounds, the difference in ΔS_M at T_C is nearly identical to ΔS_{str}. The large magnetic field induced phase volume and chemical bonding changes, observed in Gd_5Ge_4, $Gd_5(Si_{1.7}Ge_{2.3})$, and other R_5T_4 materials, therefore, indicate that the giant MCE is achieved due to the concomitant change of the entropy during the structural transformation, designated in Fig. 11.13 as ΔS_{str}. As a result, it is possible to speculate that the observed giant magnetocaloric effect is the sum of the conventional magnetic entropy-driven process (11.3) and the difference in the entropies of the two crystallographic modifications (ΔS_{str}) of a solid

$$\Delta S_M(T, \Delta B)_{\Delta B = B_f - B_i} = \Delta S_{str} + \int_{B_i}^{B_f} \left(\frac{\partial M(T,B)}{\partial T} \right)_B \mathrm{d}B \,. \qquad (11.5)$$

Although the first factor in the right-hand side of (11.5) is a hidden parameter in conventional magnetization, heat capacity and direct magnetocaloric effect measurements because either property reflects both the magnetic and crystallographic states of the material [e.g., imagine the absence of the data for $Gd_5(Si_{2.5}Ge_{1.5})$ in Fig. 11.13], an estimate based on comparing the MCE's exhibited by these two members of the $Gd_5(Si_{4-x}Ge_x)$ family is possible. This is illustrated in Fig. 11.14, where we plot the isothermal magnetic entropy change of $Gd_5(Si_2Ge_2)$ taken from [29] and the same of $Gd_5(Si_{2.5}Ge_{1.5})$ [74] for ΔB varying from 2 to 10 T. Considering (11.5) and recalling that ΔS_{str} is independent of the magnetic field, provided the entire volume of the material retains the low magnetic field crystal structure at B_i and it is completely converted into the high magnetic field polymorph by B_f, the difference between the peak values of ΔS_M should remain constant (or nearly constant in view of Fig. 11.13) regardless of ΔB. This constant difference, indeed, is approximately equal to ΔS_{str}.

Numerical data representing the peak ΔS_M values for both materials are listed in Table 11.1. After recalling that the crystallographic phase change

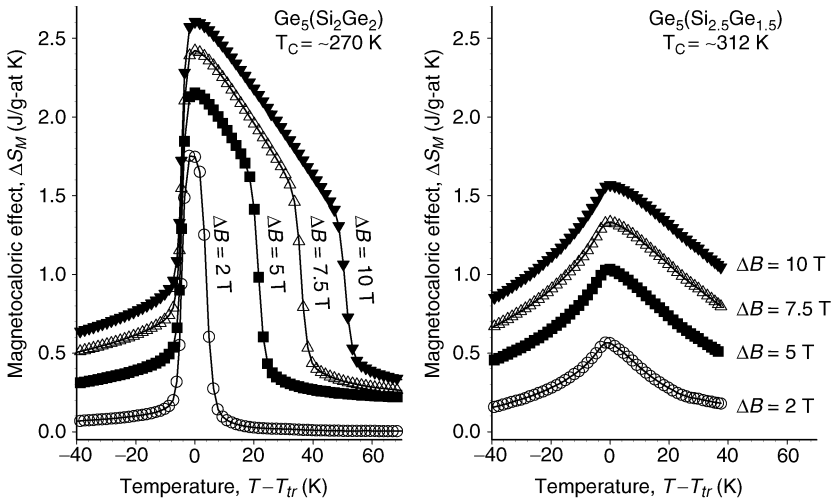

Fig. 11.14. The magnetocaloric effects of $Gd_5(Si_2Ge_2)$ (*left*) and Gd5($Si_{2.5}Ge_{1.5}$) (*right*) calculated from heat capacity measured in constant magnetic fields of 0, 2, 5, 7.5, and 10 T. In every case, $B_i = 0$

Table 11.1. Peak values of the magnetocaloric effect of $Gd_5(Si_2Ge_2)$ and $Gd_5(Si_{2.5}Ge_{1.5})$ for different ΔB (B_i is always 0) and ΔS_{str} estimated as the average difference between the peak ΔS_M values of the two compounds

Compound	Isothermal magnetic entropy change, $-\Delta S_M$ (J g-at^{-1} K^{-1})			
	$\Delta B = 2$ T	$\Delta B = 5$ T	$\Delta B = 7.5$ T	$\Delta B = 10$ T
$Gd_5(Si_2Ge_2)$	1.75	2.15	2.42	2.61
$Gd_5(Si_{2.5}Ge_{1.5})$	0.57	1.03	1.33	1.57
Difference	1.19	1.12	1.09	1.04
Average	(excluded)		$\Delta S_{str} = 1.08(4)$	

was not complete even in a 3.5 T magnetic field in Gd_5Ge_4 and assuming that similar effect is feasible in $Gd_5(Si_2Ge_2)$, it only makes sense to discard ΔS_M difference for the smallest ΔB, where $B_f = 2$ T. The values for the remaining three field changes are constant to within one standard deviation of the mean, which is $\Delta S_{str} = 1.08(4)$ J g-at^{-1} K^{-1}. The latter is of the same order of magnitude as the entropies of transformations of pure metals, which could be approximated [75] as $\Delta S_{str} = 0.75\nu$ J g-at^{-1} K^{-1} for an fcc → bcc transition (the actual values vary from 0.5 to 3.01 J g-at^{-1} K^{-1} for $\gamma \rightarrow \delta$ transitions in Fe and Ce, respectively), or as $\Delta S_{str} = 0.62 + 0.75\nu$ J g-at^{-1} K^{-1} for a hcp → bcc transition (the actual values vary from 0.56 J g-at^{-1} K^{-1} in Li to 3.68 J g-at^{-1} K^{-1} in Ti), where ν is the number of valence electrons.

Analysis of data presented in Fig. 11.14 and Table 11.1 indicates that ΔS_{str} accounts for 50% or more of the total extensive magnetocaloric effect

in magnetic fields below 5 T. Its relative contribution to ΔS_{M} increases as the magnetic field decreases as long as the final magnetic field (B_{f}) is strong enough to complete the magnetostructural transition. Advanced magnetocaloric materials should exist in other solid systems where structural changes are coupled with ferromagnetic ordering, and therefore, can be triggered by a magnetic field. Considering (11.5), the strongest MCEs in the weakest magnetic fields should be found in novel materials, engineered in order to maximize the difference in the entropies of the low magnetic field and high magnetic field phases, and therefore, the resulting entropy of a structural transformation, ΔS_{str}.

11.6 Conclusions

In summary, analysis of the magnetic-martensitic transformations and the magnetocaloric effects in a few representatives of the R_5T_4 family of intermetallic compounds – Gd_5Ge_4, $Gd_5(Si_{1.7}Ge_{2.3})$, $Gd_5(Si_2Ge_2)$, and $Gd_5(Si_{2.5}Ge_{1.5})$ – indicates that the coupling between the magnetic and crystal lattices is critical in bringing about the giant magnetocaloric effect. Although in general it is difficult to separate the contributions from either sublattice into the MCE, in the R_5T_4 series it was possible experimentally because these materials can be prepared in two different states: one that exhibits a conventional MCE and another where the magnetic and crystal lattices are coupled and the giant magnetocaloric effect is the result of a first-order magnetostructural transformation.

Especially the extensive measure of the magnetocaloric effect, i.e., the isothermal magnetic field-induced entropy change, can be strongly enhanced by the added entropy of a structural transition provided the magnetic field completes the polymorphic transformation. This additional entropy is magnetic field independent, and therefore, may account for more than a half of the observed magnetocaloric effect, especially in relatively weak magnetic fields. Design of novel materials exhibiting potent magnetocaloric effects in magnetic fields that can be created by using modern permanent magnets is, therefore, possible by ensuring that (i) a structural transition can be triggered and completed or nearly completed by a weak magnetic field; (ii) the transformation has low thermal and magnetic field hystereses, i.e., is reversible, and (iii) the difference between the total entropies of two polymorphic modifications, and therefore, ΔS_{str}, is maximized.

Acknowledgements

We thank Dr. A.P. Holm for allowing us to use some of his unpublished temperature and magnetic field dependent X-ray powder diffraction data and to Dr. A.O. Pecharsky for allowing us to use some of her unpublished heat capacity data collected as functions of temperature in magnetic fields ranging from

0 to 10 T. This work was supported by the Office of Basic Energy Sciences, Materials Sciences Division of the United States Department of Energy under Contract No. W-7405-ENG-82 with the Iowa State University of Science of Technology.

References

1. E. Warburg: Ann. Phys. (Leipzig) **13**, 141 (1881)
2. P. Debye: Ann. Phys. (Leipzig) **81**, 1154 (1926)
3. P. Weiss, R. Forrer: Ann. Phys. (Leipzig) **5**, 153 (1926)
4. W.F. Giauque: J. Am. Chem. Soc. **49**, 1864 (1927)
5. P.J. von Ranke, V.K. Pecharsky, K.A. Gschneidner Jr.: Phys. Rev. B **58**, 12 110 (1998)
6. A.M. Tishin, K.A. Gschneidner Jr., V.K. Pecharsky: Phys. Rev. B **59**, 503 (1999)
7. V.K. Pecharsky, K.A. Gschneidner Jr., A.O. Pecharsky, A.M. Tishin: Phys. Rev. B **64**, 144 406/1 (2001)
8. A.L. Lima, A.S. Oliveira, A.M. Gomes, P.J. von Ranke: Phys. Rev. B **65**, 172 411/1 (2002)
9. H. Yamada, T. Goto: Phys. Rev. B **68**, 184 417/1 (2003)
10. P.J. von Ranke, N.A. de Oliveira, S. Gama: Phys. Let. A **320**, 302 (2003)
11. A.M. Tishin, Y.I. Spichkin: The magnetocaloric effect and its applications (IOP, Bristol Philadelphia 2003)
12. W.F. Giauque, D.P. MacDougall: Phys. Rev. **43**, 768 (1933)
13. G.V. Brown: J. Appl. Phys. **47**, 3673 (1976)
14. C.B. Zimm, A. Jastrab, A. Sternberg, V.K. Pecharsky, K.A. Gschneidner Jr., M.G. Osborne, I.E. Anderson: Adv. Cryo. Engin. **43**, 1759 (1998)
15. K.A. Gschneidner Jr., V.K. Pecharsky, C.B. Zimm: Mater. Techn. **12**, 145 (1997)
16. V.K. Pecharsky, K.A. Gschneidner Jr.: J. Magn. Magn. Mater. **200**, 44 (1999)
17. K.A. Gschneidner Jr., V.K. Pecharsky: Ann. Rev. Mater. Sci. **30**, 387 (2000)
18. C.B. Zimm, A. Sternberg, A.G. Jastrab, A.M. Boeder, L.M. Lawton Jr., J.J. Chell: Rotating bed magnetic refrigeration apparatus. US Patent No. 6,526,759 (2003)
19. C.B. Zimm, A. Sternberg, A.G. Jastrab, A.M. Boeder, L.M. Lawton Jr.: Rotating magnet magnetic refrigerator. US Patent No. 6,668,560 (2003)
20. V.K. Pecharsky, K.A. Gschneidner Jr.: J. Appl. Phys. **86**, 565 (1999)
21. B.R. Gopal, R. Chahine, M. Földèaki, T.K. Bose: Rev. Sci. Instrum. **66**, 232 (1995)
22. B.R. Gopal, R. Chahine, T.K. Bose: Rev. Sci. Instrum. **68**, 1818 (1997)
23. S.Y. Dan'kov, A.M. Tishin, V.K. Pecharsky, K.A. Gschneidner Jr.: Rev. Sci. Instrum. **68**, 2432 (1997)
24. A.H. Morrish: The physical principles of magnetism (Wiley, New York 1965)
25. V.N. Belova, V.I. Nikolaev, V.M. Stuchebnikov: Fiz. Tv. Tela. (Leningrad) **15**, 909 (1973)
26. V.K. Pecharsky, K.A. Gschneidner Jr.: Phys. Rev. Lett. **78**, 4494 (1997)
27. V.K. Pecharsky, K.A. Gschneidner Jr.: Appl. Phys. Lett. **70**, 3299 (1997)
28. V.K. Pecharsky, K.A. Gschneidner Jr.: J. Magn. Magn. Mater. **167**, L179 (1997)
29. A.O. Pecharsky, K.A. Gschneidner Jr., V.K. Pecharsky: J. Appl. Phys. **93**, 4722 (2003)

30. K.A. Gschneidner Jr., V.K. Pecharsky, E. Brück, H.G.M. Duijn, E.M. Levin: Phys. Rev. Lett. **85**, 4190 (2000)
31. S.A. Nikitin, G. Myalikgulev, A.M. Tishin, M.P. Annaorazov, K.A. Asatryan, A.L. Tyurin: Phys. Lett. A **148**, 363 (1990)
32. M.P. Annaorazov, S.A. Nikitin, A.L. Tyurin, K.A. Asatryan, A.K. Dovletov: J. Appl. Phys. **79**, 1689 (1996)
33. J.F. Herbst, C.D. Fuerst, R.D. McMichael: J. Appl. Phys. **79**, 5998 (1996)
34. Z.B. Guo, Y.W. Du, J.S. Zhu, H. Huang, W.P. Ding, D. Feng: Phys. Rev. Lett. **78**, 1142 (1997)
35. G.S. Smith, A.G. Tharp, Q. Johnson: Nature (London) **210**, 1148 (1966)
36. G.S. Smith, A.G. Tharp, Q. Johnson: Act. Cryst. **22**, 940 (1967)
37. F. Holtzberg, R.J. Gambino, T.R. McGuire: J. Phys. Chem. Solids **28**, 2283 (1967)
38. V.K. Pecharsky, K.A. Gschneidner Jr.: J. Alloys Compds. **260**, 98 (1997)
39. W. Choe, V.K. Pecharsky, A.O. Pecharsky, K.A. Gschneidner Jr., V.G. Young Jr., G.J. Miller: Phys. Rev. Lett. **84**, 4617 (2000)
40. V.K. Pecharsky, K.A. Gschneidner Jr.: Adv. Mater. **13**, 683 (2001)
41. A.O. Pecharsky, K.A. Gschneidner Jr., V.K. Pecharsky: J. Magn. Magn. Mater. **267**, 60 (2003)
42. A.O. Pecharsky, K.A. Gschneidner Jr., V.K. Pecharsky, C.E. Schindler: J. Alloys Compds. **338**, 126 (2002)
43. L. Morellon, P.A. Algarabel, M.R. Ibarra, J. Blasco, B. García-Landa, Z. Arnold, F. Albertini: Phys. Rev. B **58**, R14 721 (1998)
44. L. Morellon, J. Stankiewicz, B. García-Landa, P.A. Algarabel, M.R. Ibarra: Appl. Phys. Lett. **73**, 3462 (1998)
45. L. Morellon, J. Blasco, P.A. Algarabel, M.R. Ibarra: Phys. Rev. B **62**, 1022 (2000)
46. Q.L. Liu, G.H. Rao, H.F. Yang, J.K. Liang: J. Alloys Compds. **325**, 50 (2001)
47. Q.L. Liu, G.H. Rao, J.K. Liang: Rigaku J. **18**, 46 (2001)
48. V.K. Pecharsky, A.O. Pecharsky, K.A. Gschneidner Jr.: J. Alloys Compds. **344**, 362 (2002)
49. M. Nazih, A. de Visser, L. Zhang, O. Tegus, E. Brück: Solid State Comm. **126**, 255 (2003)
50. M. Han, D.C. Jiles, J.E. Snyder, C.C.H. Lo, J.S. Leib, J.A. Paulsen, A.O. Pecharsky: J. Appl. Phys. **93**, 8486 (2003)
51. V.K. Pecharsky, G.D. Samolyuk, V.P. Antropov, A.O. Pecharsky, K.A. Gschneidner Jr.: J. Solid State Chem. **171**, 57 (2003)
52. J.S. Meyers, L.S. Chumbley, F. Laabs, A.O. Pecharsky: Acta Mater. **51**, 61 (2003)
53. C. Magen, L. Morellon, P.A. Algarabel, C. Marquina, M.R. Ibarra: J. Phys.: Cond. Mater. **15**, 2389 (2003)
54. V.K. Pecharsky, K.A. Gschneidner Jr., A.O. Pecharsky, A.M. Tishin: Phys. Rev. B **64**, 1444 406/1 (2001)
55. Z.M. Wang, G. Ni, Q.Y. Xu, H. Sang, Y.W. Du: J. Appl. Phys. **90**, 5689 (2001)
56. H. Wada, Y. Tanabe: Appl. Phys. Lett. **79**, 3302 (2001)
57. J.P. Meyer, P. Taglang: Compt. Rend. **264**, 1820 (1958)
58. P.I. Kripyakevich, O.S. Zarechnyuk, E.I. Gladyshevskii, O.I. Bodak: Z. Anorg. Allg. Chem. **358**, 90 (1968)
59. O. Tegus, E. Brück, K.H.J. Buschow, F.R. de Boer: Nature (London) **415**, 150 (2002)

60. X.X. Zhang, G.H. Wen, F.W. Wang, W.H. Wang, C.H. Yu, G.H. Wu: Appl. Phys. Lett. **77**, 3072 (2000)
61. E.M. Levin, V.K. Pecharsky, K.A. Gschneidner Jr., G.J. Miller: Phys. Rev. B **64**, 235 103/1 (2001)
62. E.M. Levin, K.A. Gschneidner Jr., V.K. Pecharsky: Phys. Rev. B **65**, 214 427/1 (2002)
63. V.K. Pecharsky, A.P. Holm, K.A. Gschneidner Jr., R. Rink: Phys. Rev. Lett. **91**, 197 204/1 (2003)
64. C. Magen, Z. Arnold, L. Morellon, Y. Skorokhod, P.A. Algarabel, M.R. Ibarra, J. Kamarad: Phys. Rev. Lett. **91**, 207 202/1 (2003)
65. H. Tang, V.K. Pecharsky, K.A. Gschneidner Jr., A.O. Pecharsky: Phys. Rev. B **65**, 064 410/1 (2004)
66. V. Hardy, S. Majumdar, S.J. Crowe, M.R. Lees, D. McK. Paul, L. Hervé, A. Maignan, S. Hébert, C. Martin, C. Yaicle, M. Hervieu, B. Raveau: Phys. Rev. B **69**, 020 407/1 (2004)
67. A.P. Holm, V.K. Pecharsky, K.A. Gschneidner Jr., R. Rink, M.N. Jirmanus: Rev. Sci. Instr. **75**, 1081 (2004)
68. E.M. Levin, K.A. Gschneidner Jr., T.A. Lograsso, D.L. Schlagel, V.K. Pecharsky: Phys. Rev. B **69**, 144 428/1 (2004)
69. A.P. Holm, V.K. Pecharsky, K.A. Gschneidner Jr.: (2003) unpublished
70. Numerical zero magnetic field linear thermal expansion data of polycrystalline Gd_5Ge_4 [53] measured using a strain gauge that were employed to compute the linear thermal expansion coefficient were kindly provided by Dr. L. Morellon
71. K. Ullakko, J.K. Huang, C. Kantner, R.C. O'Handley, V. Kokorin: Appl. Phys. Lett. **69**, 1966 (1996)
72. S.J. Murray, M. Marioni, S.M. Allen, R.C. O'Handley, T.A. Lograsso: Appl. Phys. Lett. **77**, 886 (2000)
73. Y. Mozharivskyj, A.O. Pecharsky, V.K. Pecharsky, G.J. Miller: J. Am. Chem. Soc. **127**, 317 (2005)
74. A.O. Pecharsky, K.A. Gschneidner Jr., V.K. Pecharsky: (2004) unpublished
75. K.A. Gschneidner Jr.: J. Less Common Metals **43**, 179 (1975)

12

Entropy Change and Magnetocaloric Effect in Magnetostructural Transformations

F. Casanova, X. Batlle, A. Labarta, J. Marcos, E. Vives, and
L. Mañosa, and A. Planes

12.1 Introduction

The physics of the magnetocaloric effect (MCE) is an old subject with renewed interest in the last decades owing to its potential application for refrigeration [1]. In fact, magnetic refrigeration offers the prospect of an energy-efficient and environment friendly alternative to the common vapor-cycle refrigeration technology in use today [2, 3]. The MCE is commonly defined as the heating or cooling (i.e., the temperature change) of a magnetic material due to the application of a magnetic field. This effect has been called adiabatic demagnetisation for years, though this phenomenon is one particular practical application of the MCE in magnetic materials. For excellent reviews on the magnetocaloric effect, see [1, 4, 5].

All magnetic materials exhibit MCE, which is an intrinsic phenomenon, although the intensity of this effect shows a large variation depending on the material. MCE originates from the coupling between the magnetic sublattice and the applied magnetic field, H, which produces an additional contribution to the entropy of the solid. Thus, the strength of the MCE in a particular solid can be characterised as the isothermal entropy change, ΔS_{iso}, or the adiabatic temperature change, ΔT_{ad}, arising from the application or removal of an external magnetic field. In particular, ΔS_{iso} induced in a system when the magnetic field is varied from H_{i} to H_{f} can be experimentally determined directly from calorimetric measurements or indirectly from magnetisation curves by numerical integration of the Maxwell relation:

$$\Delta S_{\mathrm{iso}}(H_{\mathrm{i}} \rightarrow H_{\mathrm{f}}) = \int_{H_{\mathrm{i}}}^{H_{\mathrm{f}}} \left(\frac{\partial M}{\partial T} \right)_{H} \mathrm{d}H \, . \tag{12.1}$$

According to this equation, the absolute value of the derivative of magnetisation with respect to temperature should be large to get a large entropy change. This occurs, for instance, when the system undergoes a magnetic transition. However, in second-order magnetic transitions, the existence of short-range

order and spin fluctuations above the ordering temperature brings about a reduction in the maximum value of $(\partial M/\partial T)_H$, and consequently the maximum MCE is reduced. In contrast, an ideal first-order phase transition takes place at constant temperature, so the value of $(\partial M/\partial T)_H$ should be infinitely large. Actually, in an ideal first-order magnetic transition, the discontinuities in both magnetisation and entropy make it possible that (12.1) can be rewritten in terms of the Clausius–Clapeyron equation as

$$\Delta S_{\mathrm{iso}} = -\Delta M \, \frac{\mathrm{d}H_{\mathrm{t}}}{\mathrm{d}T_{\mathrm{t}}} \, , \tag{12.2}$$

where H_{t} is the field at which the transition takes place and T_{t} is the transition temperature. Therefore, the MCE may be maximised in the vicinity of a first-order structural transition, when a large entropy change related to the crystallographic transformation, ΔS, can be field-induced through magnetoelastic coupling. The existence of a large ΔS associated with the first-order transition brings about an extra contribution to the MCE, yielding the so-called giant MCE. The use of this ΔS in practical applications is possible provided that the phase transition can be induced by an external magnetic field [6]. Extensive search for materials undergoing simultaneously structural and magnetic transitions (magnetostructural transformations) has recently been described in literature [7–9]. One of the most promising class of materials displaying a magnetostructural transformation comprises $Gd_5(Si_xGe_{1-x})_4$ alloys with $0 \leq x \leq 0.5$ [7, 10], in which ΔS_{iso} values at least twice larger than that of Gd near room temperature for $H = 50\,\mathrm{kOe}$ are observed. This enhanced MCE is due to a strong interplay between the magnetic and structural features in this system. These alloys have crystallographic structures made up of parallel nanometric slabs connected by covalent-like bonds [11]. Interestingly, the interslab connectivity does not only depend on x and the actual crystallographic structure, but also on the magnetic ordering. This makes it possible to field-induce a structural transformation in the system, driven by a shear mechanism between the parallel slabs, which adapts the interslab connectivity to the final magnetic state. Therefore, in these alloys, the magnetoelastic coupling responsible for the magnetostructural transformation is operating at the microscopic scale of the nanometric slabs.

However, in other materials undergoing magnetostructural transformations, magnetoelastic coupling may occur at multiple scales ranging from microscopic to mesoscopic lengths. Moreover, competing mechanisms of magnetoelastic coupling taking place at different scales may be present simultaneously. This is the case in a series of magnetic composition-related Ni–Mn–Ga shape-memory alloys undergoing a martensitic transformation. It is shown that the MCE, increasing the magnetic field in the vicinity of the martensitic transition, mainly originates from two contributions with opposite sign [12]: (i) magnetoelastic coupling on mesoscopic scale between the magnetic domains and the martensitic variants which gives a positive contribution to the MCE, and (ii) the microscopic spin–phonon coupling which produces a shift of T_{t}

with H and gives a negative contribution to the MCE. The relative importance of these two contributions has been shown to vary with composition. It is worth noting that, in the range of composition for which the mesoscopic mechanism becomes dominant, $(\partial M/\partial T)_H$ may be positive in the vicinity of the martensitic transformation when the magnetic field is increased. This is a very unusual behaviour for a magnetic system.

In this chapter, the magnetostructural transformations and the MCE exhibited by both families of alloys (Gd–Si–Ge and Ni–Mn–Ga) are studied, with a discussion of the different scales at which magnetoelastic coupling takes place.

12.2 Multiscale Origin of the MCE in Ni–Mn–Ga Alloys

Ni–Mn–Ga alloys are materials with twofold interest, as they display both magnetocaloric and magnetic shape-memory effects. The magnetic shape-memory property is a consequence of the coupling between structural and magnetic degrees of freedom in a ferromagnetic alloy undergoing a martensitic transformation at a temperature, T_{M}, below the Curie temperature (T_{C}). Ferromagnetic Ni–Mn–Ga alloys close to the stoichiometric Heusler composition are prototypical materials exhibiting this property, in which martensitic transformation occurs in the ferromagnetic state from a cubic structure (parent phase) to a tetragonal martensitic phase below T_{M}. One important feature to understand for the magnetic behaviour of this system is that, in the tetragonal phase, there are twin related structural domains with strong uniaxial anisotropy compared to that of the cubic phase, which can be rearranged by the application of moderate fields. Consequently, the martensitic transformation takes place between two ferromagnetic states with very different magnetic domain structures, being accompanied by a jump in the magnetisation of the system, which is mainly controlled by the magnetoelastic coupling at the mesoscopic scale of the martensitic variants. For certain compositions, this magnetisation jump may produce at moderate fields an MCE larger than that observed in Gd for a similar range of temperatures.

We present results for a single crystal of composition $Ni_{49.5}Mn_{25.4}Ga_{25.1}$. The sample exhibited an $L2_1$ structure at room temperature, a T_{C} of about 381 K and a martensitic transition on cooling at $T_{\mathrm{M}} \approx 177$ K to a modulated tetragonal structure ($5R$). The hysteresis for the martensitic transition was $\sim$10 K.

Isothermal magnetisation measurements were carried out in this specimen by the extraction technique in the range from 150 to 200 K, under magnetic fields up to 40 kOe. Figure 12.1a shows the obtained curves for selected temperatures, from which the field-induced entropy change, when the field increases from 0 to H, can be evaluated by numerical integration of (12.1). The results are plotted in Fig. 12.1b for selected values of H. The two peaks observed in the temperature dependence of $\Delta S_{\mathrm{iso}}(0 \rightarrow H)$ originate from unavoidable small composition inhomogeneities and impurities, which

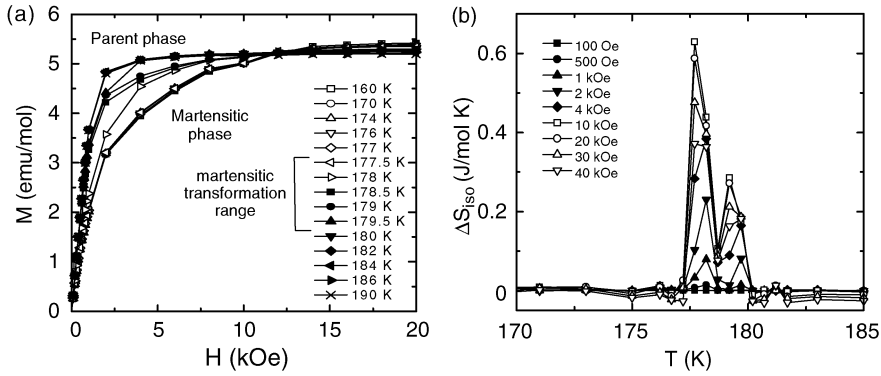

Fig. 12.1. (**a**) Magnetisation versus applied field at different temperatures around T_{M} for a $Ni_{49.5}Mn_{25.4}Ga_{25.1}$ sample. (**b**) Field-induced entropy change as a function of temperature for selected values of the maximum applied field, calculated from the data in (**a**)

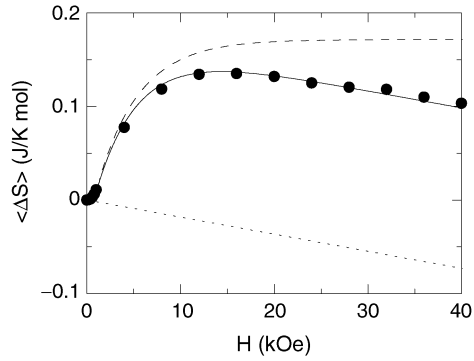

Fig. 12.2. Average field-induced entropy change $\langle \Delta S \rangle$ as a function of H for a $Ni_{49.5}Mn_{25.4}Ga_{25.1}$ sample. The continuous line is a fit of the experimental data to a phenomenogical model, which includes two contributions to the magnetoelastic coupling: the spin–phonon microscopic coupling (*dotted line*) and the martensite-variant mesoscopic coupling (*dashed line*)

are known to slightly affect the actual transition path [13]. In order to compare $\Delta S_{\mathrm{iso}}(0 \rightarrow H, T)$ for different samples it is convenient to calculate, for each field, the average of the field-induced entropy change over $\Delta T(H)$ (the temperature range at which the transition spreads) as

$$\langle \Delta S(H) \rangle = \frac{1}{\Delta T(H)} \int_{\Delta T} \Delta S_{\mathrm{iso}}(0 \rightarrow H, T)\, \mathrm{d}T\,. \tag{12.3}$$

This integral is performed numerically by taking a suitable baseline which permits elimination of any contribution arising from temperature variations of the magnetisation outside the transformation region. The obtained $\langle \Delta S(H) \rangle$ values as a function of the applied magnetic field are plotted in Fig. 12.2.

The average entropy change first increases, reaches a maximum at 13 kOe, and decreases linearly with H at higher fields. However, the most remarkable fact in these data is the positive value of entropy change originating from an increase in the applied field.

A deeper understanding of the magnetoelastic coupling in this system, which is at the origin of this peculiar magnetic behaviour, can be gained by analysing the temperature dependence of the magnetisation curves measured at a fixed value of the magnetic field around T_{M}, which are displayed in Fig. 12.3a. In the transition region, a jump in the magnetisation isofield curves is observed, which is positive or negative depending on the strength of the applied magnetic field. The magnitude of this jump ΔM (magnetisation difference between martensite and parent phase) displays a strong dependence on H, as shown in Fig. 12.3b. The different regions can be understood by taking into account the magnetic and structural domain patterns formed as a function of H [14, 15]. When the martensitic transformation takes place at zero field, nucleation gives rise to plates formed by parallel stripes of twin related variants with strong uniaxial anisotropy. The nucleation of the plates with such a microstructure is very advantageous, since it minimises the elastic (strain) energy arising from the crystal lattice misfit along the interfacial boundaries.

At low fields, magnetic domains are formed within each variant, in such a way that the magnetisation alternates between two values, which are parallel to the corresponding easy axes. This configuration ensures the absence of magnetic poles in the martensite phase giving rise to negative values of ΔM.

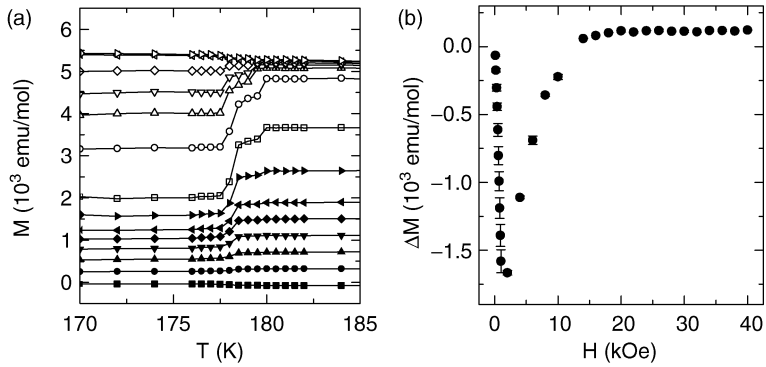

Fig. 12.3. (**a**) Magnetisation versus temperature curves at selected values of the magnetic field applied along the [100] direction of the cubic phase. Measurements were performed during heating. The different symbols correspond to the following fields: $H = 0$ (*filled square*), 100 Oe (*filled circle*), 200 Oe (*filled triangle*), 300 Oe (*filled down triangle*), 400 Oe (*filled diamond*), 500 Oe (*filled triangle left*), 700 Oe (*filled triangle right*), 1 kOe (*open square*), 2 kOe (*open circle*), 4 kOe (*open triangle*), 6 kOe(*open down triangle*), 10 kOe (*open diamond*), 20 kOe (*open triangle left*) and 50 kOe (*open triangle right*). (**b**) Magnetisation change at the phase transition, as a function of the magnetic field

In contrast, if the sample is cooled through the transition under a magnetic field larger than the saturation field of the parent phase, the twin related variants are magnetised. As the field is further increased, due to the strong uniaxial anisotropy of the tetragonal phase, the Zeeman energy is minimised by increasing the fraction of those variants with the easy magnetisation axis forming a smaller angle with the applied field. At high enough fields, transformation results in magnetically saturated single variant crystal, and ΔM becomes positive and constant. Interestingly, this magnetic behaviour is controlled by the same magnetoelastic coupling which causes the magnetic shape-memory effect [16, 17].

Consequently, ΔM and the field-induced entropy change through the transition are mainly controlled by the magnetoelastic coupling at the mesoscopic scale of the twin related variants. This contribution to the entropy change is positive and dominant at low fields. In fact, for moderate values of H, the field-induced entropy is not related to the entropy change of the structural transition. This is because of the weak spin–phonon coupling at the microscopic scale, as proven by the weak dependence of the phonon-dispersion curves and T_{M} on H [18, 19]. High fields are required to induce the transition even at temperatures very close to T_{M}. However, the magnetoelastic coupling at the microscopic scale is not entirely negligible in this material, giving rise to a negative contribution to the entropy change which becomes dominant at high fields and in turn gives rise to the linear decrease of $\langle \Delta S(H) \rangle$ shown in Fig. 12.2 above 13 kOe.

A simple phenomenological model including the interplay between both scales of magnetoelastic coupling accounts well for the observed experimental behaviour of $\langle \Delta S(H) \rangle$ [12], as shown in Fig. 12.2. In this model, the contribution coming from the magnetoelastic coupling at the mesoscopic scale of the martensite variants is evaluated assuming that, for the sake of simplicity, the system contains only two twin-related variants, whose relative population varies exponentially as H increases above the saturation field of the parent phase. The contribution arising from the spin–phonon coupling is calculated from (12.2), taking $(\mathrm{d}T_{\mathrm{M}}/\mathrm{d}H)H$ as a measure of the shift of T_{M} induced by the field. Both contributions are depicted separately in Fig. 12.2 to emphasise their different field dependence. Thus, the mesoscopic contribution is positive and increases monotonically to reach saturation, while the microscopic contribution is negative and decreases linearly as H increases. The relative importance of these two contributions changes with the actual composition of the alloy. In Fig. 12.4, $\langle \Delta S(H) \rangle$ obtained from magnetisation data [12] for five alloys of different compositions, including that of Fig. 12.2, are depicted. The continuous lines are the fits to the model of [12]. In alloys with a large difference between T_{C} and T_{M} (alloys 1 and 2 in Fig. 12.4), mesoscopic coupling is dominant and a negative giant MCE (decrease in temperature caused by an adiabatic increase of the magnetic field) is induced at moderate fields. In contrast, for alloys in which these temperatures are very close to one another (case 5 in Fig. 12.4), the microscopic coupling is the most relevant contribution

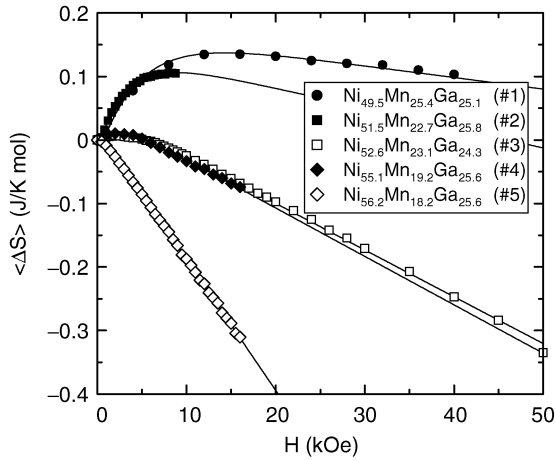

Fig. 12.4. Average field-induced entropy change $\langle \Delta S \rangle$ as a function of H for all the different analysed alloys. The continuous lines are the fits of the experimental data to a phenomenogical model

and gives rise to a positive giant magnetocaloric effect. This is in agreement with the decrease of the anisotropy of martensite phase as T_{M} approaches T_{C} [20]. Therefore, the maximum values of the field-induced entropy change in Ni–Mn–Ga alloys correspond to those with $T_{\mathrm{M}} \approx T_{\mathrm{C}}$ and are approximately $-30\,\mathrm{J\,kg^{-1}\,K^{-1}}$ for a field of 15 kOe [21]. These values are even larger than maximum values reported for prototypical materials displaying giant MCE at room temperature such as Gd–Si–Ge [22] and Mn–As [9] (of the order of $-15\,\mathrm{J\,kg^{-1}K^{-1}}$ for a field of 20 kOe).

12.3 Direct Determination of the Entropy Change at a First-Order Transformation

As has been discussed in Sect. 12.1, the MCE in a given magnetic material undergoing a first-order structural transition can be characterised by quantifying the field-induced ΔS_{iso} indirectly from magnetisation data, as it is the case for Ni–Mn–Ga in Sect. 12.2, or directly from calorimetric measurements. Differential scanning calorimeters (DSC) are well adapted to determine ΔS at a first-order transformation, since with this technique the heat flow exchanged by the sample and the surroundings is directly measured and a proper integration of the calibrated signal yields the latent heat of the transformation.

A DSC operating under magnetic field is particularly well suited to study magnetostructural transitions [23]. In these devices, the temperature is continuously scanned at a rate $\dot{T}$, while the heat flow, $\dot{Q}$, exchanged between the sample and the thermal block is measured by the thermobatteries. From $\dot{T}$ and $\dot{Q}$, the derivative of the heat with respect to the temperature can be

obtained (calorimetric signal). A proper integration of this signal subtracting the baseline leads to the latent heat or the entropy change of the transition.

It is worth noting that the calorimeter can also operate by sweeping the field maintaining a constant temperature. In this mode of operation, a magnetostructural transformation can be field-induced by setting a temperature above but sufficiently close to T_t. In this case, the calorimetric signal can be obtained from $\dot{Q}$ and $\dot{H}$ and a proper integration of this signal provides the field-induced entropy change. Consequently, this system permits a direct determination of the MCE, since ΔS induced in the sample by the application of an external magnetic field can be directly determined.

12.4 Magnetostructural Transformation in Gd–Si–Ge Alloys

$Gd_5(Si_xGe_{1-x})_4$ alloys are one of the most promising materials for practical applications of the MCE, which in these materials originates from a first-order magnetostructural transformation that appears in two compositional ranges. The phase diagram is complex [22, 24, 25], but the most relevant feature pertinent to the MCE is the existence of a structural transformation which takes place simultaneously with a magnetic transition from a high-temperature paramagnetic (PM) monoclinic phase to a low-temperature ferromagnetic (FM) Gd_5Si_4-type orthorhombic phase for $0.24 \leq x \leq 0.5$ [22, 24] and from a high temperature antiferromagnetic (AFM) Gd_5Ge_4-type orthorhombic phase to an isostructural low-temperature FM phase for $x \leq 0.2$ [25]. At higher temperature, a second-order transition occurs from the AFM to the PM state for $x \leq 0.2$. The giant MCE in these alloys is due to the existence of a strong coupling between the structure and the magnetic ordering which is governed by the interslab connectivity through the number of covalent-like bonds [11].

In this section, we present a direct determination of ΔS at the first-order transformation in $Gd_5(Si_xGe_{1-x})_4$ alloys. The samples were prepared by arc-melting and heat-treated for 9 h at 920°C under 10^{-5} mbar.

Figure 12.5 shows an example of the measured calorimetric curves by sweeping the temperature on cooling under different values of the magnetic field for samples with $x = 0.1$ (left panel) and $x = 0.3$ (right panel). The magnetostructural transformation corresponds to the sharp peak, which is present both for $x = 0.1$ and 0.3, and shifts significantly with the applied magnetic field, revealing a strong magnetoelastic coupling. The second-order transition appears only for samples with $x \leq 0.2$ as a small lambda peak, which shows weak field dependence. At high enough fields, the first- and second-order transitions collapse and the structural transformation takes place between the FM and PM states.

It is worth noting that the transition temperature of the structural transformation for moderate fields, lower than that at which the first- and second-order transitions collapse, varies linearly with the applied field. The reciprocal

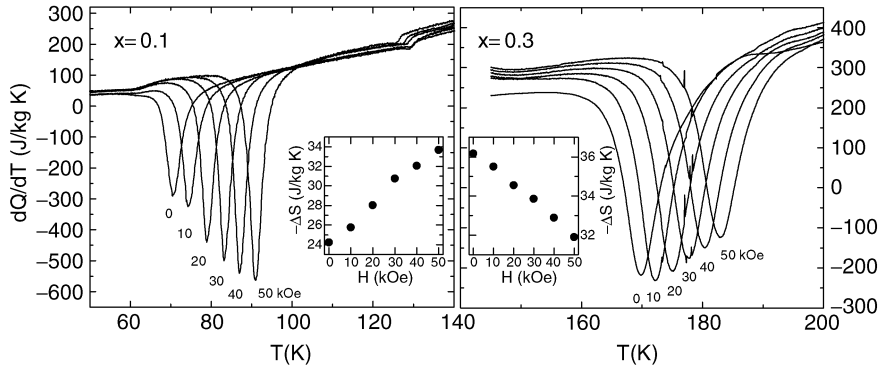

Fig. 12.5. Calorimetric curves recorded on cooling through the transitions of $Gd_5(Si_xGe_{1-x})_4$ samples ($x = 0.1$ and 0.3) for different applied magnetic fields. Insets show the entropy change as a function of magnetic field

of the slope of this linear dependence defined as dH_t/dT_t (H_t is the transition field, i.e., the field at which the transition takes place at T_t) is displayed in Fig. 12.6a as a function of the composition. These values are in agreement with those derived from magnetisation data [28]. In fact, dH_t/dT_t is related to the strength of the magnetoelastic coupling: in these compounds, the value of ΔS_{iso} measured when the transition is field-induced coincides with the value of ΔS_{iso} measured when the transition is induced by the application of pressure [24]. Therefore, through the Clausius–Clapeyron equation (12.2), it is shown that

$$\frac{\Delta M}{\Delta V} = -\frac{dT_t}{dH_t}\frac{dP_t}{dT_t} . \tag{12.4}$$

According to (12.4), a strong magnetoelastic coupling yields a small value of dH_t/dT_t. We stress the linear dependence of dH_t/dT_t on x (see Fig. 12.6a), which is decreasing for the PM-to-FM transition (solid line in Fig. 12.6a), while it is increasing for the AFM-to-FM transition (dashed line in Fig. 12.6a). Both lines intercept at the composition range where the second-order transition disappears ($0.2 < x < 0.24$), in agreement with the phase diagram for these alloys [22]. The decrease of dH_t/dT_t with increasing x for the PM–FM transition indicates a strengthening of the magnetoelastic coupling. This may be explained by taking into account that the FM exchange interactions are stronger for increasing x, as suggested by the magnetic phase diagram [22, 25], where T_t increases linearly with x. Concerning the AFM–FM transition, the increase of dH_t/dT_t with x may be related to the fact that the transition occurs between two ordered states. Figure 12.6a thus summarises the behaviour of the magnetostructural transformation as a function of x, T and H.

We have determined the field dependence of ΔS by proper integration of the calorimetric curves measured by sweeping T under fixed values of the magnetic field. Two examples which are representative of the obtained $\Delta S(H)$

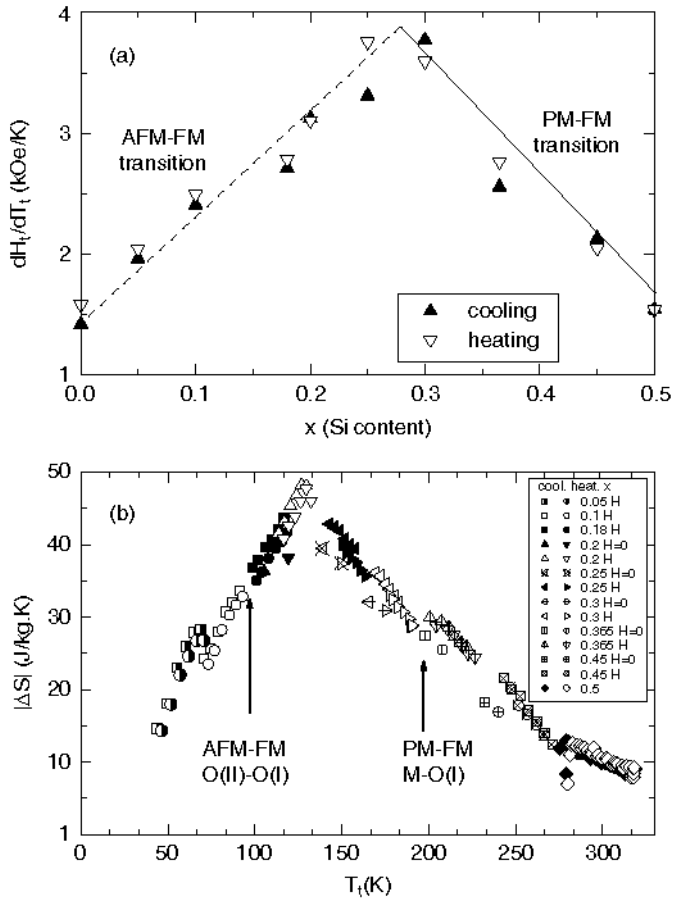

Fig. 12.6. (**a**) Slope of $H_{\rm t}(T_{\rm t})$ calculated from DSC data under H. *Solid line* corresponds to the PM–FM transition, while *dotted line* corresponds to the AFM–FM transition. (**b**) Scaling of $|\Delta S|$ at the first-order transition for the $Gd_5(Si_xGe_{1-x})_4$ alloys. Data corresponding to a large variety of applied fields and compositions are represented. *Solid and open diamonds* are from [26]. *Symbols labelled with an H* and $H = 0$ correspond, respectively, to measurements with/without magnetic field

curves are shown in the insets of Fig. 12.5 for samples with composition $x = 0.1$ and 0.3. For $x \leq 0.2$, $-\Delta S$ increases linearly with H, while for $0.24 \leq x \leq 0.5$, $-\Delta S$ decreases linearly with H. Interestingly, the absolute value of $\Delta S(H)$ curves corresponding to samples in the range of composition $0 \leq x \leq 0.5$ scale in two branches (one increasing and the other decreasing) when they are plotted as a function of $T_{\rm t}$, as shown in Fig. 12.6b. In this scaling there is only one parameter, $T_{\rm t}$, which is tuned by both x and H. This demonstrates that this is the relevant quantity in determining the magnitude of $|\Delta S|$ in

these alloys, and proves that the magnetovolume effects due to H are of the same nature as the volume effects caused by substitution [27]. Each one of the quasi-linear branches of the scaling corresponds to one of the two ranges of composition in which AFM–FM and PM–FM magnetostructural transformations occur in the phase diagram. As a matter of fact, the shape of the scaling is governed through the Clausius–Clapeyron equation (12.2) by the dependence of $\mathrm{d}H_\mathrm{t}/\mathrm{d}T_\mathrm{t}$ on x (see Fig. 12.6a) provided that ΔM decreases monotonically with T_t. Besides, the scaling is not a trivial consequence of the scaling of both ΔM and $\mathrm{d}H_\mathrm{t}/\mathrm{d}T_\mathrm{t}$, i.e., neither ΔM nor $\mathrm{d}H_\mathrm{t}/\mathrm{d}T_\mathrm{t}$ scale with T_t, which gives further relevance to the scaling of $|\Delta S|$ [27, 28]. Notice also that $|\Delta S|$ extrapolates to zero at $T_\mathrm{t} = 0$, as expected from the third law of the thermodynamics.

In systems with large magnetoelastic coupling, as it is the case for Gd–Si–Ge alloys, the magnetostructural transformation can easily be induced by the applied magnetic field. Figure 12.7 shows examples for $x = 0.1$ of the calorimetric curves measured by increasing and decreasing the field at constant temperatures above $T_\mathrm{t}(H = 0)$. As for the mode in which temperature is swept, a proper integration of the signal corresponding to each peak yields the entropy change of the transition. In Fig. 12.7, results are compared for two sweeping rates which differ by one order of magnitude. Neither the shape of the calorimetric curves nor the calculated ΔS values differ significantly when both sets of measurements are compared.

Figure 12.8a shows the evolution of the calorimetric curve when cycling repeatedly through the transition at 55 K with a sweeping rate of 1 kOe/min, in a sample with $x = 0.05$ in the virgin state at the start of the measuring

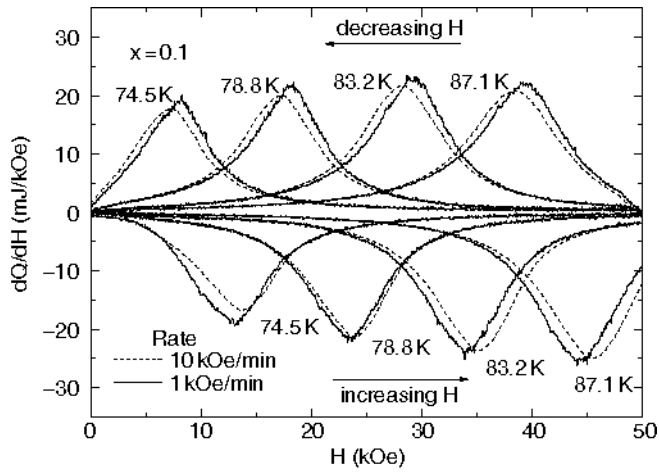

Fig. 12.7. Calorimetric curves recorded sweeping the magnetic field (increasing and decreasing H) in a $Gd_5(Si_{0.1}Ge_{0.9})_4$ sample at several fixed temperatures and for two different field rates

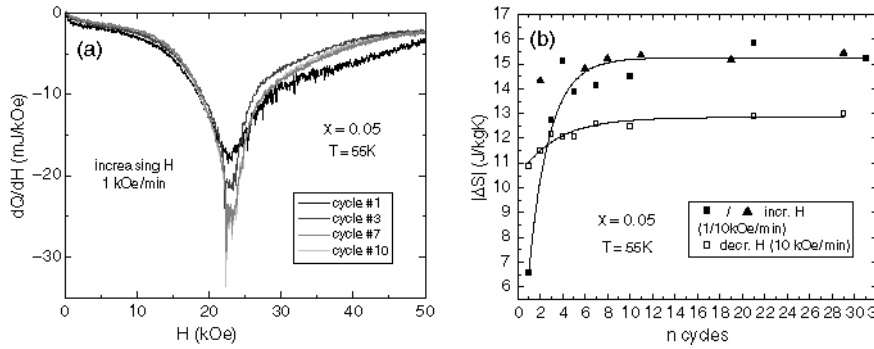

Fig. 12.8. (**a**) DSC curves recorded on increasing H at 1 kOe/min for different cycles in a $Gd_5(Si_{0.05}Ge_{0.95})_4$ sample. (**b**) Entropy change obtained from previous data, as a function of the number of cycle. Field rates, $\dot{H}$, are given in the plots. *Solid lines* are a guide to the eye

process. Even at first glance, it is clear that the curve corresponding to the first cycle encloses a smaller area than the subsequent ones. It is worth noting that the fine and sharp peaks superimposed on the broad peak of the transition are not a consequence of experimental noise. Actually, they reveal the jerky character of the transition for alloys with $x < 0.1$, for which magnetostructural transformation takes place at relatively low temperatures at which the thermal activation does not blur the discontinuous character of the transition. This discontinuous behaviour is associated with avalanche-type dynamics, which originates from collective jumps between metastable states at mesoscopic scale [29]. Similar results have also been detected in Gd_5Ge_4 from magnetisation measurements [30]. The superimposed peaks also evolve by cycling, reaching a pattern which is reproducible to some extent. This may be indicative of the athermal character of the transition [31]. That is to say, the transition is induced when the field reaches a critical value rather than being thermally activated. When a system is driven by an external parameter (the magnetic field in our case) through a first-order transition, the metastable-state path followed by the system depends on the disorder (microcracks, vacancies, dislocations). For an athermal transition the path can be reproduced from cycle to cycle provided that the disorder does not evolve [32].

Figure 12.8b shows the effect of cycling on $|\Delta S|$ of the transition in the same sample. $|\Delta S|$ increases strongly between first and fourth cycles and eventually gets saturated before the tenth cycle. This evolution is due to the formation of microcracks as a consequence of the continuous expansion/contraction of the crystallographic cell, until the system reaches a reproducible path. Besides, $|\Delta S|$ values with increasing H are systematically larger than those obtained with decreasing H. This might be due to the hysteresis effects between increasing and decreasing branches.

12.5 Conclusions

The MCE associated with magnetostructural transformations is controlled by the interplay between magnetic and structural degrees of freedom and occurs simultaneously at multiple length scales. In the vicinity of the martensitic transition of Ni–Mn–Ga, it is observed from the magnetisation measurements that the MCE originates from (i) the magnetoelastic coupling on the mesoscopic scale between the magnetic moments and the martensitic variants, and (ii) the microscopic spin–phonon coupling which gives rise to the shift of the transition temperature with the applied field. The contribution from these different scales to the MCE changes with the intensity of the applied field and the composition of the alloy. In Gd–Si–Ge alloys, the giant MCE is controlled by the microscopic spin–phonon coupling (which is proportional to $\mathrm{d}H_\mathrm{t}/\mathrm{d}T_\mathrm{t}$) since the transformation entropy change can be field-induced. ΔS can also be obtained directly from DSC operating under magnetic field. In these alloys, we observe that $|\Delta S|$ scales with the transition temperature, proving that the magnetovolume effects due to H are of the same nature as the volume effects caused by substitution. The jerky character of the calorimetric curves for alloys with low transition temperatures, which indicates an avalanche-type dynamics, evolves with cycling until a reproducible pattern is reached, evidencing the athermal character of the transition. Interestingly, it has been found that the avalanche size distribution evolves with cycling from a sub-critical distribution towards a critical (power-law) distribution [33]. $|\Delta S|$ also varies with the first cycles through the transformation.

Acknowledgements

The financial support of the Spanish CICYT (MAT2003-01124 and MAT2001-3251) and Catalan DURSI (2001SGR00066) are recognised. F.C. and J.M. acknowledge DURSI for Ph.D. grants.

References

1. A.M. Tishin, Y.I. Spichkin: The Magnetocaloric Effect and its Applications (Institute of Physics Publishing, Bristol and Philadelphia, 2003)
2. V.K. Pecharsky, K.A. Gschneidner Jr.: J. Appl. Phys. **85**, 5365 (1999)
3. K.A. Gschneidner Jr., V.K. Pecharsky: Annu. Rev. Mater. Sci. **30**, 387 (2000)
4. A.M. Tishin, in: Handbook of Magnetic Materials, ed. by K.H.J. Buschow, Vol. 12 (North Holland, Amsterdam 1999) pp. 395–524
5. V.K. Pecharsky, K.A. Gschneidner Jr.: J. Magn. Magn. Mater. **200**, 44 (1999)
6. F. Casanova, X. Batlle, A. Labarta, J. Marcos, L. Mañosa, A. Planes: Phys. Rev. B **66**, 100 401(R) (2002)
7. V.K. Pecharsky, K.A. Gschneidner Jr.: Phys. Rev. Lett. **78**, 4494 (1997)

8. H. Wada, Y. Tanabe: Appl. Phys. Lett. **79**, 3302 (2001)
9. O. Tegus, E. Brück, K.H.J. Buschow, F.R. de Boer: Nature **415**, 450 (2002)
10. V.K. Pecharsky, K.A. Gschneidner Jr.: Adv. Mater. **13**, 683 (2001) and references therein
11. W. Choe, V.K. Pecharsky, A.O. Pecharsky, K.A. Gschneidner Jr., V.G. Young Jr., G.J. Miller: Phys. Rev. Lett. **84**, 4617 (2000)
12. J. Marcos, L. Mañosa, A. Planes, F. Casanova, X. Batlle, A. Labarta: Phys. Rev. B **68**, 094 401 (2003)
13. F.C. Lovey, V. Torra: Prog. Mater. Sci. **44**, 189 (1999)
14. Q. Pan, R.D. James: J. Appl. Phys. **87**, 4702 (2000)
15. H.D. Chopra, C. Ji, V.V. Kokorin: Phys. Rev. B **61**, R14 913 (2000)
16. R.C. O'Handley: J. Appl. Phys. **83**, 3263 (1998)
17. S.Y. Chu, A. Cramb, M. De Graef, D. Laughlin, M.E. McHenry: J. Appl. Phys. **87**, 5777 (2000)
18. L. Mañosa, A. Planes, J. Zarestky, T. Lograsso, D.L. Schlagel, C. Stassis: Phys. Rev. B **64**, 024 305 (2001)
19. J. Marcos, L. Mañosa, A. Planes, F. Casanova, X. Batlle, A. Labarta, B. Martínez: Phys. Rev. B **66**, 224 413 (2002)
20. F. Albertini, L. Morellon, P.A. Algarabel, M.R. Ibarra, L. Pareti, Z. Arnold, G. Calestani: J. Appl. Phys. **89**(10), 5614 (2001)
21. L. Pareti, M. Solzi, F. Albertini, A. Paoluzi: Eur. Phys. J. B **32**, 303 (2003)
22. V.K. Pecharsky, K.A. Gschneidner Jr.: Appl. Phys. Lett. **70**, 3299 (1997)
23. J. Marcos, F. Casanova, X. Batlle, A. Labarta, A. Planes, L. Mañosa: Rev. Sci. Inst. **74**, 4768 (2003)
24. L. Morellon, P.A. Algarabel, M.R. Ibarra, J. Blasco, B. García-Landa, Z. Arnold, F. Albertini: Phys. Rev. B **58**, R14 721 (1998)
25. L. Morellon, J. Blasco, P.A. Algarabel, M.R. Ibarra: Phys. Rev. B **62**, 1022 (2000)
26. A. Giguère, M. Földeàki, B.R. Gopal, R. Chahine, T.K. Bose, A. Frydman, J.A. Barclay: Phys. Rev. Lett. **83**, 2262 (1999)
27. F. Casanova, X. Batlle, A. Labarta, J. Marcos, L. Mañosa, A. Planes: Phys. Rev. B **66**, 212 402 (2002)
28. F. Casanova, A. Labarta, X. Batlle, J. Marcos, L. Mañosa, A. Planes, S. de Brion: Phys. Rev. B **69**, 104 416 (2004)
29. F.J. Pérez-Reche, M. Stipcich, E. Vives, L. Mañosa, A. Planes, M. Morin: Phys. Rev. B **69**, 064 101 (2004)
30. V. Hardy, S. Majumdar, S.J. Crowe, M.R. Lees, D.M. Paul, L. Hervé, A. Maignan, S. Hébert, C. Martin, C. Yaicle, M. Hervieu, B. Raveau: Phys. Rev. B **69**, 020 407(R) (2004)
31. F.J. Pérez-Reche, E. Vives, L. Mañosa, A. Planes: Phys. Rev. Lett. **87**, 195 701 (2001)
32. J.P. Sethna, K. Dahmen, S. Kartha, J.A. Krumhansl, B.W. Roberts, J.D. Shore: Phys. Rev. Lett. **70**, 3347 (1993)
33. F. Casanova, A. Labarta, X. Batlle, J. Marcos, L. Mañosa, A. Planes: Eur. Phys. J. B **40**, 427 (2004)

13

Functional Magneto-Structural Materials: Summary and Perspectives

P.-A. Lindgård

The idea to bring many disciplines in physics and materials science together in a fruitful way is a bold and important one. This is manifested in the present book *Interplay of Magnetism and Structure in Functional Materials*. The common theme is in a sense the real and unavoidable complexity of the structural problems found in seemingly quite unrelated fields. In my task to give an overview, my attempt will be to concentrate on broader aspects and on the perspectives – instead of dealing with rather smaller technical details of interest mainly for specialists among specialists. For the readers interested in further studies – beyond the chapters in this book – let me mention related topics briefly and attempt to give some relevant references as a starting point.

It all began with the problem of understanding the martensitic phase transformation. When I was first introduced to that, now long time ago – coming from a field of statistical physics and critical phenomena – two things struck me (1) why was this considered as a special phase transition and (2) why did one not consider internal elastic strain modes, closely related to zone-boundary or other finite q-phonons, as variables in free energy expansions [1, 2]. Now, it is probably accepted by most that it is indeed a regular phase transition, displacive and diffusion less, usually weakly first order and with a lattice deformation as the order parameter. And it is the accommodation of that which is the problem because of the long-range character of the strain fields. This gives rise to the then usually much discussed precursor effects [3], which is not the main focus here. Neither is the remarkable nonmonotonous behavior of the hysteresis loop: the avalanche effect and self-organized critical phenomena, where analyses in terms of scaling laws and critical exponents come into play. Important progress has been made in this direction – in particular by the Barcelona group [4] – which I will not cover here. Part of this is covered in Chap. 2. In a paper by Hardy et al. [5] similar phenomena have been reported for manganites, of the type $Pr_{1-x}Ca_xMn_{1-y}M_yO_3$ (with $x \sim 0.5$, $y \sim 0.05$, and where M is a magnetic or nonmagnetic cation) in a field. A competition sets in between the magnetic energy promoting the ferromagnetic phase (FM) contrary to the antiferromagnetic (AFM) one, and the elastic energy

associated with strains created at the FM/AFM boundaries. In addition an incubation time phenomenon is observed, such that a given jump or avalanche can occur after a certain waiting time under constant external conditions. Vives et al. [6] reported on a new effect found in the Cu–Al–Mn alloys: a disorder induced critical point at low temperatures as a result of a competition between ferro- and antiferromagnetic interactions. However, the main focus here is not on the phase transition aspects.

The martensitic – or shape memory – transformation often occurs in quite complex alloys or nonstoichiometric materials. A physicist would rather study a model system to get a deep understanding of various problems – one at a time – if possible. In old times Zr served as such a model system [1, 2, 7] in which it was shown that the transition (from bcc to hcp) has to involve simultaneously both a uniform and an internal strain (corresponding to a transverse N-point [100] phonon). In other words the transition/reaction coordinate is (at least) two dimensional. It would come as no surprise that going from one point A in a mountainous landscape to another, B, can usually not be accomplished (without excessive efforts) following the straight line between A and B. One obviously would try to find a pass and be ready to make perhaps big detours – the bigger detour the smaller barrier. So there is a balance – and a transition path from A to B is not unique. One must even consider a distribution of possible paths. This fact is often overlooked in calculations of energy barriers in the martensitic problem, where we also deal with a rough "mountainous" energy landscape – or rather free-energy landscape. This resembles the situation found in nature's own much more complex, and much more functional materials: the proteins [8]. Perhaps complexity and functionality are interrelated.

However, there is still much work to do in understanding simple model systems – and a good candidate for a new system, AuZn, has been reported by Lashley et al. [9]. This has the advantage of being nonmagnetic – as Zr of course. It has a shape-memory transition from a cubic B2 (CsCl) to a trigonal P3 structure at $\sim$65 K, and may be ideal for studying the effects of nonstoichiometery on the martensitic transformation. It shows an essentially perfect second order transition with a λ-like specific heat, a transverse phonon softening at the N-point, etc. It can be obtained in perfect single crystals, which has allowed a de Haas–van Alphen determination of the Fermi surface [10]. This shows that there is a Fermi surface nesting feature matching the wave vector of the transition. That system seems to be nearly ideal – and understanding this in detail may be an important stepping stone toward understanding (also magnetic) shape memory alloys like NiTi [11] and Ni_xAl_{1-x} [12], and the fashionable $Ni_{2-x}Mn_{1-x}Ga$ [13], which all show large precursor effects at temperatures well above the martensitic transition temperature – as has been reported by Chernenko et al. [14], Pons et al. [15], and others. Shapiro et al. [16] performed numerous neutron scattering studies of systems in that family and other materials. And Ziebeck's group performed neutron studies of the intricate Invar-problem [17] and of the Ni–Mn–Ga system [21]. Description

of the neutron techniques and results obtained by these authors are reported in Chaps. 5 and 6, respectively. In the case of Zr, neutron scattering measurements of the phonon dispersion relations – and of soft modes – already gave very valuable insight into the transition mechanisms. Now, with the upcoming magneto-structural materials (promising for applications, because they can be influenced by a magnetic field), the neutrons will remain invaluable as a necessary experimental tool for gaining insight at the atomistic and the nanolevel. In addition, the possibilities are ripening to independently measure the spin and orbital components of the magnetic moment by X-ray/synchrotron methods, as discussed by Haskel et al. [18].

The magnetic shape memory systems come in two classes: those with uniaxial anisotropy, where the moment prefers a particular symmetry direction in the lattice; and those with planar anisotropy, which only confine the moments to certain preferred planes. For the shape memory effect to be useful it is important to control the development of the equivalent variants. For a transition from the bcc to hcp structure, there are six variants – and it can be more complicated as reported by Ahlers [19]. A selection can be made by a so-called "training process" of "smart" materials, during which deformation and transition are forced through a desired path, whereby certain variants can be promoted to nucleate earlier than others, in a complex process involving unknown features like defects, etc. in the structure. A much simpler control can be achieved by a magnetic field – in particular for the uniaxial materials. Kakeshita [20] reported on the uniaxial $Fe_{\sim 3}Pd$ system, which transforms from a cubic to a tetragonal structure at 230 K, with one variant expanding along the applied field direction. Also studied is the planar Fe_3Pt system, which contracts in the applied field direction into a divariant tetragonal phase at 85 K. The transformation path for the rearrangement of the variants by the magnetic field and by an applied stress has been found to be the same (with an energy dissipated during the rearrangements of the variants of 260 kJ m^{-3} for $Fe_{3.21}Pd$). The effect depends strongly on the magneto-crystalline anisotropy parameter in the Hamiltonian term of the form $-K S_z^2$. For $Fe_{\sim 3}Pd$ a value of $K \sim 350\,\mathrm{kJ\ m^{-3}}$ has been reported. It is highly important to theoretically understand the basic mechanisms behind the anisotropy, and to make accurate calculations. This, however, still represents a significant challenge.

This has become very apparent in the seemingly totally unrelated system of use for magnetic cooling by exploiting the magneto-caloric effect. This relies on the entropy change, ΔS, at the phase transition. Increasing the magnetic order reduces the entropy, and the corresponding energy is released as heat in the lattice – and vice versa. This can be used to cool other attached objects. Pecharsky et al. [21] showed that ΔS can be significantly enhanced by magneto-structural effects. In 1997 a giant magneto-caloric effect was found [22] in the Gd–Si–Ge materials (more precisely $R_5(Si_{4-x}Ge_x)$, where R is a rare earth element). This problem is discussed in Chap. 10. Although much is now understood – in particular that a shear between layers in the structure is important – a good deal of fundamental research remains to

be done before a basic understanding is achieved. It is thus very difficult to understand why $Gd_5(Si_{4-x}Ge_x)$ is one of the best materials – with as large an anisotropy constant as for Co. Gd, being an S-state ion, should on the contrary show only weak magneto-crystalline anisotropy. Here, clearly more theoretical foundation and quantitative calculations are needed. Perhaps a mechanism as that recently proposed for pure Gd applies here as well [23]. Labarta and collaborators [24] have reported on the influence that the composition x and the field H have on the phase transition and in particular on the entropy change ΔS. It has been concluded from the scaling behavior found for ΔS that the magneto-volume effects due to H are of the same nature as those due to atomic substitution, x. They further showed that the field induced maximum entropy change, $\Delta S_{\max}$, is even bigger per kg in the Ni–Mn–Ga systems ($\sim -30\,\mathrm{J\ K^{-1}}$ per kg at 1.5 T) than in the $Gd_5(Si_{4-x}Ge_x)$ materials ($\sim -15\,\mathrm{J\ K^{-1}}$ per kg at 2.0 T) [25]. These results are reported in Chap. 11.

When a material approaches the realm of applications, optimizations are called for – especially it seems necessary to reduce the magnetic field from the presently needed about 2 T (close to the maximum obtainable in permanent magnets) to lower values. An attempt to achieve that has been reported by Lewis et al. [26] who, by using thin films of $Gd_5(Si_{4-x}Ge_x)$ coated by either Fe or Al, can reduce the needed field and even increase ΔS – equally well with both coatings. The basic reason remains obscure, but a good guess might be that the first-order transition starts by nucleation events in which the surface properties obviously play a large role – hence strain effects produced by the add atoms may create nucleation sites – irrespective of their magnetic properties. Clearly, there is room for lots of improvements along those lines.

In a sense turning things upside down, Strässle et al. [27] reported on how one in many systems one can obtain the magneto-caloric effect by applying a hydrostatic pressure. The basic mechanism can be much more diversified than the above discussed "anisotropy mechanism" and might include mechanisms ranging from pressure induced structural ($Pr_xLa_{1-x}NiO_3$), magnetic (CeSb), valence [$EuNi_2(Si_xGe_{1-x})_2$] transitions, spin fluctuations (YMn_2) to electron hybridization in Kondo systems ($Ce_3Pd_{20}Ge_6$) – with potential effects as promising as in the above anisotropic magneto-caloric materials. Of course this cooling method is in principle the same as the conventional gas–liquid one. If one should make a choice between the various mechanisms, one tends to move into a space of – for physics – irrelevant variables like cost, efficiency, availability, noise, and other environmental effects, etc. Physics should be free to explore possibilities (not only avenues to prosperity, but also the impracticable paths) providing facts and inspiration for inventors. Unfortunately, the mentioned variables have a tendency to catch up with physics in the funding phase.

The magneto-volume problem is of course related to the Invar-problem, which has been much studied by Wassermann et al. [28]. This issue is reviewed in Chap. 9. The name indicates "invariant", namely an fcc $Fe_{65}Ni_{35}$ alloy, which does not show thermal expansion (because of a counteracting

volume magnetostriction) – an invention which brought the discoverer, C.E. Guillaume, the Nobel prize in 1920. However, in spite of almost 100 years of intensive research the basic mechanism has not been agreed upon – but Wassermann states that it most probably has to do with a charge transfer of electrons between orbitals of different symmetry (e_g and t_{2g} in ionic terms) and their nonbonding and antibonding characters; whereas a canting model of the moments cannot account for the phenomena [29]. Perhaps the meaning of "understanding" is relative: the more studies the stricter demands – now one might be able to solve some of the difficult (really metallic) problems with modern techniques and computers.

This brings us to the electronic theory part. Clearly, in most cases one must consider the behavior of the electrons along with the structural and magnetic changes – on the same footing, a very difficult problem. Harmon [30] is one of the pioneers in the field, who first used the "frozen phonon" method to elucidate the martensitic transformation in for example Zr [1, 31]. Harmon et al. [32] reported on the advances, using the local density approximation, augmented by a special treatment of the 4f-electrons for the electron exchange and correlation, for the calculation of the properties of complex magnetic materials as $Gd_5(Si_2Ge_2)$ and Ni_2MnGa. The intriguing behavior of a Zoo of precursor phases (with different periodicity) might be understood (at least partly) in terms of a Fermi surface nesting vector which moves with the degree of magnetization. In NiTi systems the soft phonon modes can be found quite accurately and in accordance with experiments using molecular dynamics methods. An impressive work has been performed by Ayuela et al. [33] on the efforts to calculate a number of properties, like the field dependent shape memory effect, the phonon curves, the anisotropy energies, and the transition temperatures in the Ni–Mn–Ga systems, in which a field can induce as much as 10% strain. They use a quite different, atomistic approach than the above mentioned. A good agreement with the anisotropy constant has been obtained, just by taking into account the orbital character of the electrons and calculating the energy differences. A similar calculation should be done for the $Gd_5(Si_2Ge_2)$ system. It is not clear if changes in the Fermi surface with magnetization or if the entropy part is properly taken into account in this treatment. Apropos entropy, it is quite important that the various contributions are theoretically estimated, whether originating from the changes in the electronic entropy or the vibrational (and disorder) entropy or other sources.

The again seemingly totally different subject of colossal magneto-resistance (CMR) materials of the manganite family, exemplified by $Bi_{1-x}Sr_xMnO_3$, has been investigated by Frontera et al. [34]. Here an intimate interplay between magnetic and structural properties exists. However, in these basically insulating materials, the theory seems to be on better grounds with the Goodenough rules [35] than in the metallic magneto-structural alloys. These rules go a long way in explaining the interplay between the magnetic ordering and the charge ordering – although one additionally may have to consider a strong coupling

between two neighboring Mn ions, which may then form a delocalized Zener polaron [36]. Many features of the effect of Bi substitution can be explained in terms of the Zener polaron model.

In similar materials, Ibarra's group [37] investigated the interplay between strong electron correlation and the lattice defects in mixed valence manganites. This is discussed in Chap. 3. They pointed out that an intrinsic inhomogeneous phase, even at the nanoscale, is found in which for example one would observe coexistence of ferromagnetic clusters in a paramagnetic insulating phase as well as coexistence of paramagnetic insulating regions and ferromagnetic metallic regions. A local disorder in these materials seems to be unavoidable. The balance is so delicate that one can observe pronounced isotope effects by exchanging ^{16}O by ^{18}O. This quite unexpected phenomenon has been shown by Egami [38], to occur both in the CMR ceramics and in the high temperature superconducting cuprates. It is a size not a phonon effect. He advocated for the importance of studying the ionic size effect on the CMR phenomena. To this a new – high-q – neutron scattering technique has been developed to very accurately determine the pair distribution function in solids. The general conclusion is that in these materials an intrinsic, unavoidable disorder occurs at the nanoscale level. If this – let us call it new – phase exists it requires rethinking of the thermodynamic treatment – namely an inclusion of the entropy corresponding to the intrinsic (static) disorder even at very low temperatures. This is an important challenge for theoreticians/statisticians in the years to come. This is covered in Chap. 4.

As a theoretician, I am always impressed by the advances made in experimental techniques. De Graef et al. [39] nicely demonstrated the progress made in imaging magnetic domains using the Lorentz transmission electron microscope, showing for example domain walls and domain pinning on lattice defects in Ni_2MnGa. He also looked into the prospects for in situ imaging. The technique is explained in Chap. 7. Similar studies by Tsuchiya et al. [40] allowed an imaging of the tetragonal, intermediate, and cubic phases in the Ni–Mn–Ga alloys. Additional use of electron holography has been discussed by Murakami et al. [41], with applications to the $Ni_{51}Fe_{22}Ga_{27}$ shape memory alloy and to the hole-doped manganites $La_{1-x}Sr_xMnO_3$. A complex interplay between the magnetic and the structural domain structure has been observed. In the manganites it is found that both ferro- and antiferromagnetic phases coexist. Clearly, the real space experimental methods provide very valuable, complementary information to that obtained by the reciprocal space scattering techniques.

To help putting some order into the complexity Shenoy et al. [42] formulated a classification of the disorder observed on various scales. He pointed out the importance of the different length scales and distinguishes among the macroscopic, the mesoscopic, the nanoscale, the atomic scale, and the electronic scale (as we saw one may need to go to even the nuclear scale – the O-isotope effect in manganites and cuprates). Using a Ginzburg–Landau approach he suggested a generic and elastic origin for the ubiquitous

inhomogeneity phenomena: stripes, droplets, channels, twins domains, etc. The energy is lowered by the interweaving of competing low-temperature structural variants. This is developed in Chap. 1. That may in fact be why the martensitic transition so long took a special position among phase transitions. It is very important to have these scales in mind when discussing phenomena in as diversified a field as encompassed by the interplay of magnetism and structure. In a sense we seem to face the opposite of a Babylonian confusion, having the same language for different things. Castán et al. [43] proposed a more detailed classification scheme for multistage displacive structural transformation in terms of the presence of, or absence of precursor modulated phases and applied it to the Ni–Mn–Ga, NiTi(Fe), Cu–Zn–Al and α-uranium systems. Classification schemes are good at creating new perspectives.

The accommodation problem of the structural transitions has been dealt with also at an abstract mathematical level. Lexellent et al. [44] used a scale free, mathematical approach to discuss the joint effect of external field and stress with the Ni–Mn–Ga systems in mind. James et al. [45] reported (Chap. 8) on the interrelations between various strain tensors – and has solved the problems by referring to the properties of the SU(n) symmetry groups. It is inspiring to see the martensitic problem discussed in terms usually joggled within elementary particle physics. Perhaps, the above classifications should be even further extended. And perhaps our materials have rich enough physics that they may be used as experimental testing ground for the more exotic theories of the Universe.

In conclusion, the chapters cover a wide area of materials science. They all bring something new or take a new angle on an old problem – and I have tried to amplify this principle, set out by the editors, by mentioning a couple of further, related investigations. Clearly the list of such works cannot be complete here. The feeling one is left with after the confrontation of the diverse phenomena is that physics is full of interesting phenomena and there is a lot to do, even at a very fundamental level. A particular flavor with all the materials covered here is further that apart from being intriguingly complex and of academic interest they are potentially useful for the society in a not too distant future.

Acknowledgment

I wish to thank the editors for bringing several of the discussed works to my attention, and also for useful comments.

References

1. Y.Y. Ye, Y. Chen, K.M. Ho, B.N. Harmon, P.A. Lindgård: Phys. Rev. Lett. **58**, 1769–1772 (1987)
2. P.A. Lindgård, O.G. Mouritsen: Phys. Rev. Lett. **57**, 2458–2461 (1986)
3. L.E. Tanner, A.R. Pelton, R. Gronsky: J. Phys. **43**, 169–172 (1982)

4. E. Vives, J. Ortín, Ll. Mañosa, I. Ràfols, R. Pérez-Magrané, A. Planes: Phys. Rev. Lett. **72**, 1694–1697 (1994)
5. V. Hardy, A. Maignan, S. Hebert, C. Martin: Phys. Rev. B **67**, 024401 (2003)
6. J. Marcos, E. Vives, Ll. Mañosa, M. Acet, E. Duman, M. Morin, V. Novák, A. Planes: Phys. Rev. B **67**, 224406 (2003)
7. C. Stassis, J. Zarestky, N. Wakabayashi: Phys. Rev. Lett. **41**, 1726–1729 (1978)
8. P.A. Lindgård: J. Phys.: Condens. Matter **15**, s1779–s1786 (2003); H. Frauenfelder, B.H. McMahon: Annal. Phys. **9**, 655–667 (2000)
9. J.C. Lashley, B.E. Lang, J. Boerio-Goates, B.F. Woodfield, T.W. Darling, A. Migliori, D. Thoma: J. Chem. Thermodyn. **34**, 251–261 (2000)
10. R.D. McDonald, J. Singleton, P.A. Goddard, F. Drymiotis, N. Harrison, H. Harima, M.-T. Suzuki, A. Saxena, T. Darling, A. Migliori, J.L. Smith, J.C. Lashley: J. Phys. Condens. Matter **17**, L69–L75 (2005)
11. N.B. Morgan, C.M. Friend: J. Phys. IV **11**, 325–332 (2001)
12. R.D. Noebe, R.R. Bowman, M.V. Nathal: Int. Mat. Rev. **38**(4), 193–232 (2001)
13. A. Sozinov, A.A. Likhachev, N. Lanska, K. Ullakko: Appl. Phys. Lett. **80**, 1746–1748 (2002)
14. P. Mullner, V.A. Chernenko, G. Kostorz: Scripta Matter. **49**, 129–133 (2003)
15. J. Pons, V.A. Chernenko, E. Cesari, V.A. L'vov: J. Phys. IV **112**, 939–942 (2003)
16. A. Zheludev, S.M. Shapiro, P. Wochner, A. Schwartz, M. Wall, L.E. Tanner: J. Phys. IV **5**, 1139–1144 (1995)
17. P.J. Brown, K.U. Neumann, K.R.A. Ziebeck: J. Phys.: Condens. Matter **13**, 1563–1569 (2001)
18. D.R. Lee, S.K. Sinha, D. Haskel, Y. Choi, J.C. Lang, S.A. Stepanov, G. Srajer: Phys. Rev. B **68**, 224409 (2003)
19. M. Ahlers: Philos. Mag. A – Phys. Condens. Matter Struct. Defects Mech. Prop. **82**, 1093–1114 (2002)
20. T. Kakeshita, K. Ullakko: MRS Bull. **27**, 105–109 (2002)
21. V.K. Pecharsky, A.P. Holm, K.A. Gschneidner Jr., R. Rink: Phys. Rev. Lett. **91**, 197204 (2003)
22. V.K. Pecharsky, K.A. Gschneidner Jr.: Phys. Rev. Lett. **78**, 4494–4497 (1997)
23. M. Colarieti-Tosti, S.I. Simak, R. Ahuja, L. Nordstrom, O. Eriksson, D. Aberg, S. Edvardsson, M.S.S. Brooks: Phys. Rev. Lett. **91**, 157201 (2003)
24. F. Casanova, X. Batlle, A. Labarta, J. Marcos, Ll. Mañosa, A. Planes: Phys. Rev. B **66**, 212402 (2002)
25. J. Marcos, Ll. Mañosa, A. Planes, F. Casanova, X. Batlle, A. Labarta: Phys. Rev. B **68**, 094401 (2003)
26. L.H. Lewis, M.H. Yu, R.J. Gambino: Appl. Phys. Lett. **83**, 515–517 (2003)
27. T. Strässle, A. Furrer, Z. Hossain, C. Geibel: Phys. Rev. B **67**, 054407 (2003)
28. P. Entel, H.C. Herper, E. Hoffmann, G. Nepecks, E.F. Wassermann, M. Acet, V. Crisan, H. Akai: Philos. Mag. B – Phys. Condens. Matter Stat. Mech. Electron. Opt. Magn. Prop. **80**, 141–153 (2000)
29. M. van Schilfgaarde, I.A. Abrikosov, B. Johansson: Nature **400**, 46–49 (1999)
30. B.N. Harmon, W. Weber, D.R. Hamann: J. Phys. **42**, 628–630 (1981)
31. Y. Chen, C.L. Fu, K.M. Ho, B.N. Harmon: Phys. Rev. B **31**, 6775–6778 (1985)
32. B.N. Harmon, V.N. Antonov: J. Appl. Phys. **93**, 4678–4685 (2003); Y. Lee, J.Y. Rhee, B.N. Harmon: Phys. Rev. B **66**, 054424 (2002)
33. A.T. Zayak, P. Entel, J. Enkovaara, A. Ayuela, R.M. Nieminen: Phys. Rev. B **68**, 132402 (2003)

34. C. Frontera, J.L. García-Muñoz, M.A.G. Aranda, M. Hervieu, C. Ritter, Ll. Mañosa, X.G. Capdevila, A. Calleja: Phys. Rev. B **68**, 134408 (2003)
35. J.S. Zhou, J.B. Goodenough: Phys. Rev. B **68**, 054403 (2003)
36. C. Zener: Phys. Rev. **82**, 403–405 (1951)
37. D. Rybicki, C. Kapusta, P.C. Ridi, C.J. Oates, M. Sikora, D. Zajac, J.M. De Teresa, C. Marquina, M.R. Ibarra: Acta Phys. Pol. A **105**, 183–188 (2004)
38. T. Egami: Physica C **364**, 441–445 (2001)
39. M. De Graef, Y. Kishi, Y. Zhu, M. Wuttig: J. Phys. IV **112**(2), 993–996 (2003)
40. K. Tsuchiya, A. Tsutsumi, H. Nakayama, S. Ishida, H. Ohtsuka, M. Umemoto: J. Phys. IV **112**(2), 907–910 (2003)
41. Y. Murakami, D. Shindo, K. Oikawa, R. Kainuma, K. Ishida: Appl. Phys. Lett. **82**, 3695–3697 (2003)
42. A.R. Bishop, T. Lookman, A. Saxena, S.R. Shenoy: Eur. Phys. Lett. **63**, 289–295 (2003); S.R. Shenoy, T. Lookman, A. Saxena, A.R. Bishop: Proceedings of the NATO Advanced Research Workshop (2004) and 30th International School of Solid State Physics, Erice, Sicily, 4–10 October 2003, in *Symmetry and heterogeneity in high-temperature superconductors*, ed. by A. Bianconi (Kluwer, Amsterdam, 2003)
43. T. Castán, A. Planes, A. Saxena: Phys. Rev. B **67**, 134113 (2003)
44. L. Hirsinger, C. Lexcellent: J. Phys. IV **112**(2), 977–980 (2003)
45. A. DeSimone, R.D. James: J. Phys. IV **112**(2), 969–972 (2003)

Index